UNIVERSITAT DE BARCELONA

Advanced strategies for high efficiency kesterite thin film solar cells

Sergio Giraldo Muñoz

UNIVERSITAT DE BARCELONA
University of Barcelona
Faculty of Physics

IREC
Institut de Recerca en Energia de Catalunya
Catalonia Institute for Energy Research
Advanced Materials for Energy
Solar Energy Materials and Systems Group

Advanced strategies for high efficiency kesterite thin film solar cells

Presented by:
Sergio Giraldo Muñoz

Thesis directors:
Dr. Edgardo Saucedo Silva
Prof. Alejandro Pérez Rodríguez

Thesis tutor:
Prof. Alejandro Pérez Rodríguez

Thesis submitted in January 2018
Doctorate Program: **Engineering and Applied Sciences**
Universitat de Barcelona

A mis yayos,
papá y mamá,
y mi tata.

Table of contents

List of acronyms and abbreviations

ARC – anti-reflective coating

CBD – chemical bath deposition

CIGS – $Cu(In_{1-x}Ga_x)Se_2$

CIS – $CuInSe_2$

CPV – concentrator photovoltaics

CV – capacitance-voltage

CZTS – Cu_2ZnSnS_4

CZTSe – $Cu_2ZnSnSe_4$

CZTSSe – $Cu_2ZnSn(S_xSe_{1-x})_4$

DDPP – Deep Decarbonization Pathways Project

DSSC – dye-sensitized solar cells

E_C – conduction band

EDX – energy dispersive X-ray spectroscopy

E_{EA} – electron affinity

EELS – electron energy loss spectroscopy

E_F – Fermi level

Eff – efficiency

E_g – band-gap

E_V – valence band

E_{vac} – vacuum level

FF – fill factor

GHG – greenhouse gas

IEA – International Energy Agency

IoT – Internet of Things

ITO – tin-doped indium oxide (In_2O_3:SnO_2)

J_{SC} – short-circuit current density

J-V – current density voltage

MJ – multi-junction

OPV – organic photovoltaics

PDA – post-deposition annealing

PDT – post-deposition treatment

PLD – pulsed laser deposition

PV – photovoltaic

PVD – physical vapor deposition

QD – quantum dot

RT – room temperature

SEM – scanning electron microscopy

SLG – soda-lime glass

TPV – thermo-photovoltaics

UNFCCC – United Nations Framework Convention on Climate Change

V_{OC} – open-circuit voltage

W – work function

XRD – X-ray diffraction

XRF – X-ray fluorescence

Preface

Publications and summary of the thesis

The work presented in this thesis was carried out at the Catalonia Institute for Energy Research (IREC) in Sant Adrià de Besòs (Barcelona), Spain, from 2015 to 2018, in the frame of SUNBEAM project (ENE2013-49136-C4-1-R) with an FPI fellowship (BES-2014-068533) from the Spanish Government. The main subject of the thesis is the development of high efficiency thin film photovoltaic technologies based on kesterite $Cu_2ZnSnSe_4$ absorbers, using a sequential process (sputtering of metallic stack precursors followed by reactive thermal annealing) through the implementation of innovative doping strategies.

Each chapter of the thesis is structured around several articles, which are published in high impact peer-reviewed journals. According to the requirements for the Doctor of Philosophy in Engineering and Applied Sciences at the University of Barcelona, this thesis is constituted of the following seven articles:

S. Giraldo, C. M. Ruiz, M. Espíndola-Rodríguez, Y. Sánchez, M. Placidi, D. Cozza, D. Barakel, L. Escoubas, A. Pérez-Rodríguez, and E. Saucedo, "Optical and electrical properties of In-doped $Cu_2ZnSnSe_4$," ***Sol. Energy Mater. Sol. Cells***, vol. 151, pp. 44–51, 2016. IMPACT FACTOR (IF): 4.784

S. Giraldo, M. Neuschitzer, T. Thersleff, S. López-Marino, Y. Sánchez, H. Xie, M. Colina, M. Placidi, P. Pistor, V. Izquierdo-Roca, K. Leifer, A. Pérez-Rodríguez, and E. Saucedo, "Large Efficiency Improvement in $Cu_2ZnSnSe_4$ Solar Cells by Introducing a Superficial Ge Nanolayer," ***Adv. Energy Mater.***, vol. 5, no. 21, p. 1501070, 2015. IMPACT FACTOR (IF): 16.721

S. Giraldo, T. Thersleff, G. Larramona, M. Neuschitzer, P. Pistor, K. Leifer, A. Pérez-Rodríguez, C. Moisan, G. Dennler, and E. Saucedo, "$Cu_2ZnSnSe_4$ solar cells with 10.6% efficiency through innovative absorber engineering with Ge superficial nanolayer," ***Prog. Photovoltaics Res. Appl.***, vol. 24, no. 10, pp. 1359-1367, 2016. IMPACT FACTOR (IF): 6.726

T. Thersleff, **S. Giraldo**, M. Neuschitzer, P. Pistor, E. Saucedo, and K. Leifer, "Chemically and morphologically distinct grain boundaries in Ge-doped $Cu_2ZnSnSe_4$ solar cells revealed with STEM-EELS," ***Mater. Des.***, vol. 122, pp. 102-109, 2017. IMPACT FACTOR (IF): 4.364

S. Giraldo, E. Saucedo, M. Neuschitzer, F. Oliva, M. Placidi, X. Alcobé, V. Izquierdo-Roca, S. Kim, H. Tampo, H. Shibata, A. Perez-Rodriguez and P. Pistor, "How small amounts of Ge modify the formation pathways and crystallization of kesterites," ***Energy Environ. Sci.***, 2017. DOI:10.1039/C7EE02318A. IMPACT FACTOR (IF): 29.518

S. Giraldo, M. Neuschitzer, M. Placidi, P. Pistor, A. Pérez-Rodríguez, and E. Saucedo, "$Cu_2ZnSnSe_4$-Based Solar Cells With Efficiency Exceeding 10% by

Adding a Superficial Ge Nanolayer: The Interaction Between Ge and Na," ***IEEE Journal of Photovoltaics***, vol. 6, no. 3, pp. 754-759, 2016. IMPACT FACTOR (IF): 3.712

M. Dimitrievska, **S. Giraldo**, P. Pistor, E. Saucedo, A. Pérez-Rodríguez, and V. Izquierdo-Roca, "Raman scattering analysis of the surface chemistry of kesterites: Impact of post-deposition annealing and Cu/Zn reordering on solar cell performance," ***Sol. Energy Mater. Sol. Cells***, vol. 157, pp. 462–467, 2016. IMPACT FACTOR (IF): 4.784

The thesis is constituted of five chapters. At the beginning of each chapter there is a short review of the literature and summary of the most important results presented in the articles on which that chapter is based. After that, each chapter concludes with the full text of the included articles.

The first chapter is a brief introduction into photovoltaics, centered on the importance of solar energy at this time, where the transition from traditional energy sources (fossil fuels) to cleaner and efficient technologies has become a matter of urgency. Following this, an explanation of the basic operation of photovoltaic devices is presented, along with relevant parameters and phenomena occurring in the p-n junction of a solar cell. Besides, this section describes the main photovoltaic technologies, including first generation (mainly based on silicon wafers, including mono-crystalline and multi-crystalline silicon), second generation (based on thin film materials), and third generation technologies (including emerging, novel technologies and more advanced concepts), and further discussion about strengths and weaknesses of the most relevant ones. The next sub-section is focused on kesterite thin film technologies, which are the main topic of this thesis. The emergence of kesterite as an absorber photovoltaic material overcomes the major limitations, regarding scarcity and/or toxicity issues of other chalcogenide thin films, like chalcopyrite CIGS and CdTe, since it is composed of low toxicity and earth abundant elements. In addition, there is a long list of advantages (described in the thesis) that make kesterites a suitable and very promising absorber photovoltaic material, although they still have some way to go due to their novelty and short history compared to more mature technologies. This chapter also presents a complete and updated review of the best reported kesterite solar cells as well as some of the current challenges of this material derived from its crystal structure and associated defects. Finally, the objectives of the thesis are presented.

The second chapter is focused on the study of selective doping strategies in kesterite $Cu_2ZnSnSe_4$. In the first sub-section, before going deeper into more advanced strategies, a previous optimization of the thermal processes for the synthesis of CZTSe absorbers is presented, by analyzing several critical selenization parameters (including temperature, total pressure, chalcogen quantity, ramp rates, etc.), and comparing one-, two-, and three-step annealing profiles. After that, a preliminary screening of doping

elements is presented, involving cation-substitution or doping with the elements: Ag, In, Si, Ge and Pb, as first candidates. The importance of studying these particular elements is discussed and why we decided to focus on Ge and In as dopants. This chapter includes the following three publications: “Optical and electrical properties of In-doped $Cu_2ZnSnSe_4$”, “Large efficiency improvement in $Cu_2ZnSnSe_4$ solar cells by introducing a superficial Ge nanolayer”, and “$Cu_2ZnSnSe_4$ solar cells with 10.6% efficiency through innovative absorber engineering with Ge superficial nanolayer” with a more exhaustive study about In and Ge elements as dopants in kesterite CZTSe.

The third chapter, in line with results presented in the previous chapter, is intended to shed light on the origin and the mechanisms underlying the beneficial effect of small amounts of Ge, and further explore the role of this element in high performing CZTSe solar cells. In the literature, the incorporation of Ge in kesterite-based solar cells has demonstrated a positive impact on several device properties, leading to significant performance improvements. A brief review from 2012, when IBM reported the first Ge-alloyed kesterite device, until now is presented. In summary, Ge incorporation has demonstrated: the possibility to increase the V_{OC} by widening the band-gap; the potential for graded band-gap concepts; remarkable improvements of grain growth and crystallinity; increased minority charge carrier lifetimes; and large potential to reduce the V_{OC} deficit in current kesterite technology. But, with the drawback of relying on large amounts of Ge (20-40% Ge-substitution), thus compromising the sustainability of the technology. In this context, the study of alternative strategies using small amounts of Ge becomes crucial to further develop long-term sustainable technologies, based mainly on earth-abundant elements. With regard to the origin of the beneficial effect of Ge doping in CZTSe solar cells, several hypotheses have been proposed and are discussed throughout the chapter; surface modification, formation of a flux agent, defect levels modification, interaction with Na, or the influence on grain boundaries nature are among them. This chapter includes the following two publications: “Chemically and morphologically distinct grain boundaries in Ge-doped $Cu_2ZnSnSe_4$ solar cells revealed with STEM-EELS”, and “How small amounts of Ge modify the formation pathways and crystallization of kesterites” with a detailed investigation of grain boundaries nature in Ge-doped CZTSe, the mechanisms underlying the Ge boost and how Ge affects the formation pathways of kesterite CZTSe.

The fourth chapter covers two of the most well-known factors that can clearly impact on device performance and are of great importance to obtain high efficiency solar cells: post-deposition treatments (PDT), and the presence and control of alkali elements during thermal processes. The text includes the main effects of alkalis in CIGS, in particular Na, essentially leading to an enhanced performance, reported systematically in several publications. Following this, the effect of alkalis in kesterite are reviewed, showing similar device properties improvements. Furthermore, an interesting complex interaction between group IV elements (Ge, Sn) and alkalis is revealed,

affecting the doping level of the absorbers and the optoelectronic properties of kesterite solar cells. Finally, post-deposition treatments, especially low temperature post-deposition annealing (PDA), are presented. In the literature, several groups have reported beneficial effects of these thermal treatments, either in air or inert atmosphere, to increase device efficiency, and have associated them with the well-known Cu-Zn interdiffusion. In particular, after PDA, the formation of a Cu-depleted and Zn-enriched absorber surface has proven to be mandatory for high device efficiency. This chapter includes the following two publications: "$Cu_2ZnSnSe_4$-based solar cells with efficiency exceeding 10% by adding a superficial Ge nanolayer: The interaction between Ge and Na", and "Raman scattering analysis of the surface chemistry of kesterites: Impact of post-deposition annealing and Cu/Zn reordering on solar cell performance" in which detailed information about the mentioned results is presented.

The final chapter of the thesis includes the conclusions and outlook of the work.

Finally, the following articles, which are co-authored by Sergio Giraldo, contributed to the preparation of this thesis, but are not included in the text:

I. Becerril-Romero, **S. Giraldo**, S. López-Marino, M. Placidi, Y. Sánchez, D. Sylla, A. Pérez-Rodríguez, E. Saucedo, and P. Pistor, "Vitreous enamel as sodium source for efficient kesterite solar cells on commercial ceramic tiles," ***Sol. Energy Mater. Sol. Cells***, vol. 154, pp. 11–17, 2016. IMPACT FACTOR (IF): 4.784

M. Neuschitzer, J. Marquez, **S. Giraldo**, M. Dimitrievska, M. Placidi, I. Forbes, V. Izquierdo-Roca, A. Pérez-Rodríguez, and E. Saucedo, "V_{OC} Boosting and Grain Growth Enhancing Ge-Doping Strategy for $Cu_2ZnSnSe_4$ Photovoltaic Absorbers," ***J. Phys. Chem. C***, vol. 120, no. 18, pp.9661-9670, 2016. IMPACT FACTOR (IF): 4.536

C. Ros, T. Andreu, **S. Giraldo**, Y. Sánchez, and J. R. Morante, "Conformal chalcopyrite based photocathode for solar refinery applications," ***Sol. Energy Mater. Sol. Cells***, vol. 158, pp. 184-188, 2016. IMPACT FACTOR (IF): 4.784

E. Kask, J. Krustok, **S. Giraldo**, M. Neuschitzer, S. López-Marino, and E. Saucedo, "Temperature dependent electrical characterization of thin film $Cu_2ZnSnSe_4$ solar cells," ***J. Phys. D. Appl. Phys***., vol. 49, no. 8, p. 085101, 2016. IMPACT FACTOR (IF): 2.588

M. Colina, I. Martín, **S. Giraldo**, Y. Sánchez, R. Kondrotas, F. Oliva, V. Izquierdo-Roca, A. Pérez-Rodríguez, A. Coll, R. Alcubilla, and E. Saucedo, "Influence of Amorphous Silicon Carbide Intermediate Layer in the Back-Contact Structure of $Cu_2ZnSnSe_4$ Solar Cells," ***IEEE Journal of Photovoltaics***, vol. 6, no. 5, pp. 1327-1332, 2016. IMPACT FACTOR (IF): 3.712

P. Schöppe, G. Gurieva, **S. Giraldo**, G. Martínez-Criado, C. Ronning, E. Saucedo, S. Schorr, and C. S. Schnohr, "Discrepancy between integral and local composition in off-stoichiometric $Cu_2ZnSnSe_4$ kesterites: A pitfall for classification," ***Appl. Phys. Lett.***, vol. 110, no. 4, p. 043901, 2017. IMPACT FACTOR (IF): 3.411

J. Krustok, T. Raadik, M. Grossberg, **S. Giraldo**, M. Neuschitzer, S. López-Marino, and E. Saucedo, "Temperature dependent electroreflectance study of $Cu_2ZnSnSe_4$ solar cells," ***Mater. Sci. Semicond. Process.***, vol. 39, pp. 251–254, 2015. IMPACT FACTOR (IF): 2.359

D. Cozza, C. M. Ruiz, D. Duché, **S. Giraldo**, E. Saucedo, J. J. Simon, and L. Escoubas, "Optical modeling and optimizations of $Cu_2ZnSnSe_4$solar cells using the modified transfer matrix method," **Optics Express**, vol. 24, no. 18, pp. A1201-A1209, 2016. IMPACT FACTOR (IF): 3.307

R. Kondrotas, M. Colina, M. Guc, M. Neuschitzer, **S. Giraldo**, X. Alcobé, F. Oliva, Y. Sánchez, P. Pistor, V. Izquierdo-Roca, A. Pérez-Rodriguez, and E. Saucedo, "Towards In-reduced photovoltaic absorbers: Evaluation of zinc-blende $CuInSe_2$-ZnSe solid solution," ***Sol. Energy Mater. Sol. Cells***, vol. 160, pp. 26–33, 2017. IMPACT FACTOR (IF): 4.784

M. Placidi, M. Espindola-Rodriguez, S. Lopez-Marino, Y. Sanchez, **S. Giraldo**, L. Acebo, M. Neuschitzer, X. Alcobé, A. Pérez-Rodríguez, and E. Saucedo, "Effect of rapid thermal annealing on the Mo back contact properties for $Cu_2ZnSnSe_4$ solar," ***J. Alloys Compd.***, vol. 675, pp. 158-162, 2016. IMPACT FACTOR (IF): 3.133

J. Marquez, H. Stange, C. J. Hages, N. Schaefer, S. Levcenko, **S. Giraldo**, E. Saucedo, K. Schwarzburg, D. Abou-Ras, A. Redinger, M. Klaus, C. Genzel, T. Unold and R. Mainz, "Chemistry and dynamics of Ge in kesterite: towards band gap graded absorbers," ***Chem. Mater.***, 2017. DOI: 10.1021/acs.chemmater.7b03416 IMPACT FACTOR (IF): 9.466

Y. Sánchez, M. Espíndola-Rodríguez, H. Xie, S. López-Marino, M. Neuschitzer, **S. Giraldo**, M. Dimitrievska, M. Placidi, V. Izquierdo-Roca, F. A. Pulgarín-Agudelo, O. Vigil-Galán, and E. Saucedo, "Ultra-thin CdS for highly performing chalcogenides thin film based solar cells," ***Sol. Energy Mater. Sol. Cells***, vol. 158, pp. 138-146, 2016. IMPACT FACTOR (IF): 4.784

S. López-Marino, Y. Sánchez, M. Espíndola-Rodríguez, X. Alcobé, H. Xie, M. Neuschitzer, I. Becerril, **S. Giraldo**, M. Dimitrievska, M. Placidi, L. Fourdrinier, V. Izquierdo-Roca, A. Pérez-Rodríguez, and E. Saucedo, "Alkali doping strategies for

flexible and light-weight $Cu_2ZnSnSe_4$ solar cells," ***J. Mater. Chem. A***, vol. 4, no. 5, pp. 1895–1907, 2016. IMPACT FACTOR (IF): 8.867

H. Xie, S. Lopez-Marino, T. Olar, Y. Sánchez González, M. Neuschitzer, F. Oliva, **S. Giraldo**, V. Izquierdo-Roca, I. Lauermann, A. Pérez-Rodríguez, and E. Saucedo, "Impact of Na Dynamics at the $Cu_2ZnSn(S,Se)_4$/CdS Interface During Post Low Temperature Treatment of Absorbers," ***ACS Appl. Mater. Interfaces***, vol. 8, no. 7, pp. 5017-5024, 2016. IMPACT FACTOR (IF): 7.504

E. Garcia-Llamas, J. M. Merino, R. Gunder, K. Neldner, D. Greiner, A. Steigert, **S. Giraldo**, V. Izquierdo-Roca, E. Saucedo, M. León, S. Schorr, and R. Caballero, "Cu_2ZnSnS_4 thin film solar cells grown by fast thermal evaporation and thermal treatment," ***Solar Energy***, vol. 141, pp. 236-241, 2017. IMPACT FACTOR (IF): 4.018

S. Lopez-Marino, M. Espíndola-Rodríguez, Y. Sánchez, X. Alcobé, F. Oliva, H. Xie, M. Neuschitzer, **S. Giraldo**, M. Placidi, R. Caballero, V. Izquierdo-Roca, A. Pérez-Rodríguez, and E. Saucedo, "The Importance of Back Contact Modification in $Cu_2ZnSnSe_4$ Solar Cells: the Role of a Thin MoO_2 Layer," ***Nano Energy***, vol. 26, pp. 708–721, 2016. IMPACT FACTOR (IF): 12.343

Contribution of the author to publications in the thesis

The author of this work, Sergio Giraldo, has been responsible for the design, coordination and execution of experiments as well as the analysis and interpretation of the experimental results included in this thesis.

Chapter 2:

(1) S. Giraldo, et al., "Optical and electrical properties of In-doped $Cu_2ZnSnSe_4$," ***Solar Energy Materials & Solar Cells***, vol. 151, pp. 44–51, 2016.

Impact Factor (IF): 4.784

1st quartile in categories: Electronic, Optical and Magnetic Materials; Renewable Energy, Sustainability and the Environment; Surfaces, Coatings and Films

This work investigates the effects of In doping in CZTSe thin films. Different In thicknesses were introduced (from 0 to 10 nm) corresponding to nominal In concentrations ranging from 0 to 2.6×10^{20} cm^{-3}. We demonstrate a uniform distribution of In throughout the CZTSe absorber, without affecting the main elements distribution, but impacting on the Na quantity at the surface. Additionally, remarkable changes in the morphology are observed, where the increasing In concentration leads to the formation of a bilayer structure. No deterioration of efficiencies was observed for In concentrations below 2.6×10^{19} cm^{-3}, while for higher doping levels, a significant drop in FF led to lower efficiencies. In the manuscript, we propose a phenomenological model supported by a complete characterization of absorbers and devices, showing that a conductive phase deteriorates devices properties that we associate with the possible presence of mixed Sn oxides and In oxides.

In this work, Sergio Giraldo was responsible for the synthesis of all absorber layers used in the study, the fabrication of solar cell devices as well as the optoelectronic characterization (J-V and EQE), and further analysis and interpretation of results.

(2) S. Giraldo, et al., "Large Efficiency Improvement in $Cu_2ZnSnSe_4$ Solar Cells by Introducing a Superficial Ge Nanolayer," ***Advanced Energy Materials***, vol. 5, no. 21, p. 1501070, 2015.

Impact Factor (IF): 16.721

1st quartile in categories: Materials Science; Renewable Energy, Sustainability and the Environment

In this publication, we present a remarkable improvement in $Cu_2ZnSnSe_4$ solar cell efficiency based on the introduction of a Ge superficial nanolayer. In particular, the use of 10 nm of Ge evaporated on top of metallic precursors leads to a paramount efficiency improvement, from about 7% for reference samples (Ge-free) to 10% for Ge-containing best cells, together with a markedly improved crystallinity. A detailed compositional and structural characterization demonstrates that Ge is barely incorporated in the CZTSe absorber, therefore we propose a mechanism how Ge could assist the crystallization via the formation of a liquid Ge-Se phase. Additionally, several reasons are presented that could explain the device performance improvement, including: (i) the formation of a Ge_3Se_7 phase that incongruently decomposes into volatile $GeSe_2$ and a Se-rich liquid phase, which assists the crystallization of CZTSe, improving the crystalline quality; (ii) the reduced formation of Sn +II species (commonly associated with the formation of harmful deep defects that deteriorate cell voltage) in presence of Ge, as suggested by preliminary XPS analysis; (iii) the presence of GeO_x nanoinclusions apparently associated with SnO_2 inclusions revealed by high resolution TEM/EELS analysis, which might have a passivation effect or somehow act as electron reflectors, enhancing the voltage of the solar cells.

This paper was published along with a frontispiece cover offered by the journal, included in the Appendix section.

In this work, Sergio Giraldo was responsible for the synthesis of CZTSe absorbers and subsequent fabrication of solar cells. Additionally, he performed the morphological SEM characterization as well as the optoelectronic characterization, including J-V characteristics, EQE and reflectance measurements.

(3) S. Giraldo, et al., "$Cu_2ZnSnSe_4$ solar cells with 10.6% efficiency through innovative absorber engineering with Ge superficial nanolayer," ***Progress in Photovoltaics: Research and Applications***, vol. 24, no. 10, pp. 1359-1367, 2016.

Impact Factor (IF): 6.726

1st quartile in categories: Condensed Matter Physics; Electrical and Electronic Engineering; Electronic, Optical and Magnetic Materials; Renewable Energy, Sustainability and the Environment

This work includes the complete optimization of the approach presented in the previous article, in which the positive effect of a Ge nanolayer introduced into the processing of CZTSe absorbers was demonstrated. In this publication, the optimum Ge thickness range is defined in order to achieve

an improved device performance, obtaining a record efficiency of 10.6% thanks to the international collaboration with IMRA in France. With this optimization, the V_{OC} is boosted for our pure selenium CZTSe up to 489 mV, leading to V_{OC} deficits among the lowest reported so far in kesterite technology. Additionally, first indications of the Ge-Na interaction and its effect on charge carrier density are shown. Finally, evidences pointing to the origin of the deterioration of devices properties for higher Ge amounts are presented.

In this work, Sergio Giraldo was responsible for the fabrication of the complete set of samples, including the synthesis of CZTSe absorbers and subsequent finishing of solar cells. With regard to characterization, he performed the optoelectronic characterization, J-V analysis and quantum efficiency measurements as wells as morphological/compositional analysis by SEM/EDX.

Chapter 3:

(4) T. Thersleff, S. Giraldo, et al., "Chemically and morphologically distinct grain boundaries in Ge-doped $Cu_2ZnSnSe_4$ solar cells revealed with STEM-EELS," ***Materials & Design***, vol. 122, pp. 102-109, 2017.

Impact Factor (IF): 4.364

1st quartile in categories: Materials Science; Mechanical Engineering; Mechanics of Materials

This publication presents a detailed analysis of structural, morphological and compositional trends in Ge-doped CZTSe samples with efficiencies over 10% (among the state-of-the-art for this material and fabrication route). Most relevant findings reveal the existence of at least two morphologically and distinct types of grain boundaries present in this system. These are concentrated in the upper and lower regions of the absorber layer, and the subsequent analytical STEM investigation reveals that they have different compositions. The deeper and more detailed EELS analysis of the lower grain boundaries shows that they contain large amounts of SnO_x and that Cu assumes a higher valence state, whereas the upper grain boundaries are slightly Cu-enriched and contain trace amounts of oxygen. Interestingly, we can also link the extent of these grain boundaries to a change in the overall composition of the absorber layer, which appears to have different stoichiometry in the upper and lower halves. Ultimately, the potential impact of both types of grain boundaries on the device performance and fabrication is discussed.

In this work, Sergio Giraldo was responsible for the fabrication of the samples and the experimental design to achieve high efficiencies. Additionally, he assisted with the TEM experimental design at Uppsala University in Sweden.

(5) S. Giraldo, et al., "How small amounts of Ge modify the formation pathways and crystallization of kesterites," ***Energy & Environmental Science***, 2017. DOI:10.1039/C7EE02318A

Impact Factor (IF): 29.518

1st quartile in categories: Environmental Chemistry; Nuclear Energy and Engineering; Pollution; Renewable Energy, Sustainability and the Environment

This work is an international cooperation between IREC, the University of Barcelona, AIST in Japan, and the Martin Luther University in Germany. This publication presents a deep investigation of the mechanisms underlying the Ge boost on kesterite solar cells and suggests an alternative mechanism based on the reaction scheme during selenization. Differences in the formation reaction of kesterite with and without Ge are analyzed in detail, by using EDX, XRF, XRD and Raman spectroscopy with multi-wavelength excitation for samples where the reactive annealing has been interrupted at different points in time. Interestingly, we observe that the presence of Ge strongly affects the in-depth elemental distribution, delaying and minimizing the fast Cu-out diffusion and the formation of Sn-Se volatile compounds, consequently avoiding Sn losses to a large extent. Further discussion about the implications on the reaction pathways is included in the publication. Finally, we also present a new methodology for obtaining high quality CZTSe absorbers, by introducing very thin Ge layers above and below the metallic stack precursor, leading to a record 11.8% conversion efficiency.

This article has been highlighted among the hottest works published in this journal, being part of the themed collection: *2017 Energy and Environmental Science HOT articles*.

In this work, Sergio Giraldo was responsible for the fabrication of CZTSe absorber layers and resulting devices. He performed the annealing break-off experiment and analyzed the experimental results. He also carried out the morphological SEM characterization as well as the in-depth elemental distribution analysis by EDX. Finally, best performing solar cell devices were finished during his stay at AIST in Japan.

Chapter 4:

(6) S. Giraldo, et al., "$Cu_2ZnSnSe_4$-Based Solar Cells With Efficiency Exceeding 10% by Adding a Superficial Ge Nanolayer: The Interaction Between Ge and Na," ***IEEE Journal of Photovoltaics***, vol. 6, no. 3, pp. 754-759, 2016.

Impact Factor (IF): 3.712

1st quartile in categories: Condensed Matter Physics; Electrical and Electronic Engineering; Electronic, Optical and Magnetic Materials

This work investigates the complex Ge-Na interaction, which has shown to be crucial to further understand the harmful effect of thicker Ge nanolayers (≥25 nm) introduced in the CZTSe absorbers. In this publication, we explain how Ge concentration can have a significant impact on the Na content and, thus, modify the doping level of the kesterite. Additionally, the possible mechanism by which this interaction occurs is presented as well as the expected formation of point defects. Moreover, we support our Ge-Na interaction model with experiments using Na-free substrates, demonstrating the importance of accurately controlling the Na content when Ge is used to increase the efficiency of kesterite CZTSe solar cells, with special attention to the proper doping level and the optimum composition of the absorbers.

In this work, Sergio Giraldo was responsible for the synthesis of analyzed CZTSe absorbers and fabrication of solar cell devices on SLG substrates. He performed the complete morphological SEM characterization, compositional EDX analysis, XRF measurements, and subsequent optoelectronic characterization of the finished devices.

(7) M. Dimitrievska, S. Giraldo, et al., "Raman scattering analysis of the surface chemistry of kesterites: Impact of post-deposition annealing and Cu/Zn reordering on solar cell performance," ***Solar Energy Materials & Solar Cells***, vol. 157, pp. 462–467, 2016.

Impact Factor (IF): 4.784

1st quartile in categories: Electronic, Optical and Magnetic Materials; Renewable Energy, Sustainability and the Environment; Surfaces, Coatings and Films

This work explores the structure-function relationships of post-deposition annealing (PDA) at different temperatures in $Cu_2ZnSnSe_4$ kesterite-based solar cells. Diffusion and recrystallization phenomena at the absorber/buffer interface during the PDA are investigated using multi-wavelength Raman spectroscopy and photoluminescence, and correlated to the optoelectronic properties of the devices. The obtained results show that PDA treatments of

completed devices induce a redistribution of atoms (Cu and Zn) within the surface and sub-surface of the absorber layer. In particular, the absorber surface becomes more Cu-depleted and Zn-enriched, creating optoelectronically beneficial defects V_{Cu} and Zn_{Cu}, which can partly explain the performance improvement. Additionally, recrystallization effects of the CdS buffer layer are observed, leading to a better absorber/buffer interface and potentially a better band alignment.

In this work, Sergio Giraldo was responsible for the fabrication of kesterite solar cells, he performed the different temperature post-deposition annealings and the optoelectronic characterization, including J-V and EQE measurements. Additionally, he carried out the morphological SEM characterization.

None of these articles have been previously used by other co-authors for their doctoral thesis.

Barcelona, 02/01/2018

Dr. Edgardo Saucedo Silva

Prof. Alejandro Pérez Rodríguez

Prefacio

Publicaciones y resumen de la tesis

El trabajo presentado en esta tesis fue realizado en el *Institut de Recerca en Energia de Catalunya* (IREC) en Sant Adrià de Besòs (Barcelona), España, desde el año 2015 hasta el 2018, dentro del proyecto SUNBEAM (ENE2013-49136-C4-1-R) con una beca FPI (BES-2014-068533) del Gobierno de España. El tema principal de la tesis se centra en el desarrollo de tecnologías fotovoltaicas de capa fina de alta eficiencia basadas en absorbedores de kesterita $Cu_2ZnSnSe_4$, utilizando un proceso secuencial (pulverización catódica de precursores metálicos seguida de tratamiento térmico reactivo), mediante la implementación de novedosas estrategias de dopado.

Cada capítulo de la tesis está estructurado en torno a varios artículos publicados en revistas de alto impacto. De acuerdo con los requisitos dentro del programa de doctorado de Ingeniería y Ciencias Aplicadas de la Universidad de Barcelona, esta tesis está constituida por los siguientes siete artículos:

S. Giraldo, C. M. Ruiz, M. Espíndola-Rodríguez, Y. Sánchez, M. Placidi, D. Cozza, D. Barakel, L. Escoubas, A. Pérez-Rodríguez, and E. Saucedo, "Optical and electrical properties of In-doped $Cu_2ZnSnSe_4$," ***Sol. Energy Mater. Sol. Cells***, vol. 151, pp. 44–51, 2016. IMPACT FACTOR (IF): 4.784

S. Giraldo, M. Neuschitzer, T. Thersleff, S. López-Marino, Y. Sánchez, H. Xie, M. Colina, M. Placidi, P. Pistor, V. Izquierdo-Roca, K. Leifer, A. Pérez-Rodríguez, and E. Saucedo, "Large Efficiency Improvement in $Cu_2ZnSnSe_4$ Solar Cells by Introducing a Superficial Ge Nanolayer," ***Adv. Energy Mater.***, vol. 5, no. 21, p. 1501070, 2015. IMPACT FACTOR (IF): 16.721

S. Giraldo, T. Thersleff, G. Larramona, M. Neuschitzer, P. Pistor, K. Leifer, A. Pérez-Rodríguez, C. Moisan, G. Dennler, and E. Saucedo, "$Cu_2ZnSnSe_4$ solar cells with 10.6% efficiency through innovative absorber engineering with Ge superficial nanolayer," ***Prog. Photovoltaics Res. Appl.***, vol. 24, no. 10, pp. 1359-1367, 2016. IMPACT FACTOR (IF): 6.726

T. Thersleff, **S. Giraldo**, M. Neuschitzer, P. Pistor, E. Saucedo, and K. Leifer, "Chemically and morphologically distinct grain boundaries in Ge-doped $Cu_2ZnSnSe_4$ solar cells revealed with STEM-EELS," ***Mater. Des.***, vol. 122, pp. 102-109, 2017. IMPACT FACTOR (IF): 4.364

S. Giraldo, E. Saucedo, M. Neuschitzer, F. Oliva, M. Placidi, X. Alcobé, V. Izquierdo-Roca, S. Kim, H. Tampo, H. Shibata, A. Perez-Rodriguez and P. Pistor, "How small amounts of Ge modify the formation pathways and crystallization of kesterites," ***Energy Environ. Sci.***, 2017. DOI:10.1039/C7EE02318A. IMPACT FACTOR (IF): 29.518

S. Giraldo, M. Neuschitzer, M. Placidi, P. Pistor, A. Pérez-Rodríguez, and E. Saucedo, "$Cu_2ZnSnSe_4$-Based Solar Cells With Efficiency Exceeding 10% by

Adding a Superficial Ge Nanolayer: The Interaction Between Ge and Na," ***IEEE Journal of Photovoltaics***, vol. 6, no. 3, pp. 754-759, 2016. IMPACT FACTOR (IF): 3.712

M. Dimitrievska, **S. Giraldo**, P. Pistor, E. Saucedo, A. Pérez-Rodríguez, and V. Izquierdo-Roca, "Raman scattering analysis of the surface chemistry of kesterites: Impact of post-deposition annealing and Cu/Zn reordering on solar cell performance," ***Sol. Energy Mater. Sol. Cells***, vol. 157, pp. 462–467, 2016. IMPACT FACTOR (IF): 4.784

La tesis está estructurada en cinco capítulos. Cada capítulo comienza con una breve revisión de la literatura y un resumen de los resultados más relevantes presentados en los artículos en los cuales se basa dicho capítulo. A continuación, cada capítulo concluye con el texto completo de los artículos correspondientes.

El primer capítulo consiste en una breve introducción a la tecnología fotovoltaica, enfocada en la importancia de la energía solar en la actualidad, donde la transición de las fuentes tradicionales de energía (combustibles fósiles) a tecnologías más limpias y eficientes se ha convertido en un tema urgente. Seguidamente, se explica el funcionamiento básico de dispositivos fotovoltaicos, junto con los parámetros más relevantes y los fenómenos que ocurren en la unión p-n de una célula solar. Además, esta sección describe las principales tecnologías fotovoltaicas, incluyendo primera generación (principalmente basada en obleas de silicio, incluyendo silicio mono-cristalino y multi-cristalino), segunda generación (basada en materiales de capa fina) y tercera generación (incluyendo nuevas tecnologías emergentes y conceptos avanzados), y una discusión posterior sobre las ventajas e inconvenientes de las más relevantes. La siguiente subsección se centra en las tecnologías de capa fina de kesterita, siendo el tema principal de esta tesis. La aparición de la kesterita como material absorbedor fotovoltaico supera las principales limitaciones en cuanto escasez y/o toxicidad de otros calcogenuros de capa fina, como la calcopirita CIGS y el CdTe, ya que está compuesta de elementos de baja toxicidad y abundantes en la corteza terrestre. Además, existe una larga lista de ventajas (descritas en la tesis) que hacen de la kesterita un material absorbedor fotovoltaico ideal y muy prometedor, aunque todavía tiene camino por recorrer debido a su novedad y corta trayectoria en comparación con tecnologías más maduras. Este capítulo también presenta una revisión completa y actualizada con las mejores células solares de kesterita reportadas en la literatura, así como algunos de los desafíos actuales de este material derivados de su propia composición y estructura cristalina, y los defectos asociados. Finalmente, se describen los objetivos de la tesis.

El segundo capítulo se centra en el estudio de estrategias de dopaje selectivas en kesterita $Cu_2ZnSnSe_4$. En la primera subsección, antes de profundizar en estrategias más avanzadas, se presenta una optimización previa de los procesos térmicos para la síntesis de absorbedores CZTSe, mediante el análisis de varios parámetros críticos

durante la selenización (incluyendo temperatura, presión total, cantidad de calcógeno, rampas de temperatura, etc.) y comparando perfiles de proceso en una, dos y tres etapas. A continuación, se presenta un examen preliminar de los elementos dopantes, mediante el estudio de los elementos: Ag, In, Si, Ge y Pb, como primeros candidatos. Se discute la importancia de estudiar estos elementos en particular y por qué decidimos centrarnos en el Ge y el In como dopantes. Este capítulo incluye las siguientes tres publicaciones: "Optical and electrical properties of In-doped $Cu_2ZnSnSe_4$", "Large efficiency improvement in $Cu_2ZnSnSe_4$ solar cells by introducing a superficial Ge nanolayer" y "$Cu_2ZnSnSe_4$ solar cells with 10.6% efficiency through innovative absorber engineering with Ge superficial nanolayer" con un estudio más exhaustivo sobre los elementos In y Ge como dopantes en kesterita CZTSe.

El tercer capítulo, en línea con los resultados presentados en el capítulo anterior, pretende arrojar luz sobre el origen y los mecanismos que subyacen al efecto beneficioso de pequeñas cantidades de Ge y explorar más a fondo el papel de este elemento en células solares CZTSe de alto rendimiento. En la literatura, la incorporación de Ge en células solares basadas en kesterita ha demostrado un impacto positivo en varias propiedades de los dispositivos, lo que lleva a mejoras significativas en el rendimiento de los mismos. Conjuntamente, se presenta una breve revisión desde 2012, cuando IBM presentó el primer dispositivo de kesterita aleado con Ge, hasta la actualidad. En resumen, la incorporación de Ge ha demostrado: la posibilidad de aumentar el V_{OC} incrementando la banda prohibida o band-gap; el potencial en conceptos de gradiente de band-gap; notables mejoras en el tamaño de grano y la cristalinidad de los absorbedores; aumento del tiempo de vida de los portadores de carga minoritarios; y un gran potencial para reducir el déficit de voltaje en la tecnología de kesterita actual. Pero con el inconveniente de depender de grandes cantidades de Ge (20-40% de sustitución con Ge), comprometiendo la sostenibilidad de esta tecnología. En este contexto, el estudio de estrategias alternativas utilizando pequeñas cantidades de Ge resulta crucial para continuar con el desarrollo de tecnologías sostenibles a largo plazo, basadas principalmente en elementos abundantes en la corteza terrestre. Con respecto al origen del efecto beneficioso del dopaje con Ge en células solares de CZTSe, se han propuesto varias hipótesis que se discuten a lo largo del capítulo; la modificación de la superficie, la formación de un agente fundente, la modificación de los niveles de defectos, la interacción con el Na, o la influencia en la naturaleza de las fronteras de grano se encuentran entre ellas. Este capítulo incluye las siguientes dos publicaciones: "Chemically and morphologically distinct grain boundaries in Ge-doped $Cu_2ZnSnSe_4$ solar cells revealed with STEM-EELS" y "How small amounts of Ge modify the formation pathways and crystallization of kesterites" con una investigación detallada sobre la naturaleza de las fronteras de grano en CZTSe dopado con Ge, los mecanismos subyacentes al efecto beneficioso del Ge y cómo este afecta a los procesos de formación de la kesterita CZTSe.

El cuarto capítulo abarca dos de los factores más conocidos que pueden afectar claramente al rendimiento de los dispositivos y son de gran importancia para obtener células solares de alta eficiencia: tratamientos posdeposición (PDT) y la presencia y control de elementos alcalinos durante los procesos térmicos. El texto incluye los principales efectos de los álcalis en CIGS, en particular el Na, que esencialmente conducen a una mejora del rendimiento, reportado sistemáticamente en varias publicaciones. A continuación, se revisa el efecto de los álcalis en kesterita, mostrando mejoras similares en las propiedades de los dispositivos. Además, se observa una interesante y compleja interacción entre los elementos del grupo IV (Ge, Sn) y los álcalis, que afecta al nivel de dopaje de los absorbedores y las propiedades optoelectrónicas de las células solares de kesterita. Finalmente, se presentan los tratamientos posteriores a la deposición, especialmente los recocidos a baja temperatura (PDA). En la literatura, varios grupos han reportado los efectos beneficiosos de estos tratamientos térmicos, ya sea en aire o en atmósfera inerte, para aumentar la eficiencia de los dispositivos, asociándolos con la bien conocida interdifusión de Cu-Zn. En particular, después del PDA, la formación de una superficie en el absorbedor pobre en Cu y rica en Zn ha demostrado ser imprescindible para lograr altas eficiencias. Este capítulo incluye las dos publicaciones siguientes: "$Cu_2ZnSnSe_4$-based solar cells with efficiency exceeding 10% by adding a superficial Ge nanolayer: The interaction between Ge and Na" y "Raman scattering analysis of the surface chemistry of kesterites: Impact of post-deposition annealing and Cu/Zn reordering on solar cell performance" en las que se presenta información detallada sobre los resultados mencionados.

En el último capítulo de la tesis se incluyen las conclusiones del trabajo.

Por último, los siguientes artículos, de los cuales Sergio Giraldo es coautor, han contribuido a la preparación de esta tesis, aunque no están incluidos en el texto:

I. Becerril-Romero, **S. Giraldo**, S. López-Marino, M. Placidi, Y. Sánchez, D. Sylla, A. Pérez-Rodríguez, E. Saucedo, and P. Pistor, "Vitreous enamel as sodium source for efficient kesterite solar cells on commercial ceramic tiles," ***Sol. Energy Mater. Sol. Cells***, vol. 154, pp. 11–17, 2016. IMPACT FACTOR (IF): 4.784

M. Neuschitzer, J. Marquez, **S. Giraldo**, M. Dimitrievska, M. Placidi, I. Forbes, V. Izquierdo-Roca, A. Pérez-Rodríguez, and E. Saucedo, "V_{OC} Boosting and Grain Growth Enhancing Ge-Doping Strategy for $Cu_2ZnSnSe_4$ Photovoltaic Absorbers," ***J. Phys. Chem. C***, vol. 120, no. 18, pp.9661-9670, 2016. IMPACT FACTOR (IF): 4.536

C. Ros, T. Andreu, **S. Giraldo**, Y. Sánchez, and J. R. Morante, "Conformal chalcopyrite based photocathode for solar refinery applications," ***Sol. Energy Mater. Sol. Cells***, vol. 158, pp. 184-188, 2016. IMPACT FACTOR (IF): 4.784

E. Kask, J. Krustok, **S. Giraldo**, M. Neuschitzer, S. López-Marino, and E. Saucedo, "Temperature dependent electrical characterization of thin film $Cu_2ZnSnSe_4$ solar cells," ***J. Phys. D. Appl. Phys***., vol. 49, no. 8, p. 085101, 2016. IMPACT FACTOR (IF): 2.588

M. Colina, I. Martín, **S. Giraldo**, Y. Sánchez, R. Kondrotas, F. Oliva, V. Izquierdo-Roca, A. Pérez-Rodríguez, A. Coll, R. Alcubilla, and E. Saucedo, "Influence of Amorphous Silicon Carbide Intermediate Layer in the Back-Contact Structure of $Cu_2ZnSnSe_4$ Solar Cells," ***IEEE Journal of Photovoltaics***, vol. 6, no. 5, pp. 1327-1332, 2016. IMPACT FACTOR (IF): 3.712

P. Schöppe, G. Gurieva, **S. Giraldo**, G. Martínez-Criado, C. Ronning, E. Saucedo, S. Schorr, and C. S. Schnohr, "Discrepancy between integral and local composition in off-stoichiometric $Cu_2ZnSnSe_4$ kesterites: A pitfall for classification," ***Appl. Phys. Lett.***, vol. 110, no. 4, p. 043901, 2017. IMPACT FACTOR (IF): 3.411

J. Krustok, T. Raadik, M. Grossberg, **S. Giraldo**, M. Neuschitzer, S. López-Marino, and E. Saucedo, "Temperature dependent electroreflectance study of $Cu_2ZnSnSe_4$ solar cells," ***Mater. Sci. Semicond. Process.***, vol. 39, pp. 251–254, 2015. IMPACT FACTOR (IF): 2.359

D. Cozza, C. M. Ruiz, D. Duché, **S. Giraldo**, E. Saucedo, J. J. Simon, and L. Escoubas, "Optical modeling and optimizations of $Cu_2ZnSnSe_4$solar cells using the modified transfer matrix method," **Optics Express**, vol. 24, no. 18, pp. A1201-A1209, 2016. IMPACT FACTOR (IF): 3.307

R. Kondrotas, M. Colina, M. Guc, M. Neuschitzer, **S. Giraldo**, X. Alcobé, F. Oliva, Y. Sánchez, P. Pistor, V. Izquierdo-Roca, A. Pérez-Rodriguez, and E. Saucedo, "Towards In-reduced photovoltaic absorbers: Evaluation of zinc-blende $CuInSe_2$-ZnSe solid solution," ***Sol. Energy Mater. Sol. Cells***, vol. 160, pp. 26–33, 2017. IMPACT FACTOR (IF): 4.784

M. Placidi, M. Espindola-Rodriguez, S. Lopez-Marino, Y. Sanchez, **S. Giraldo**, L. Acebo, M. Neuschitzer, X. Alcobé, A. Pérez-Rodríguez, and E. Saucedo, "Effect of rapid thermal annealing on the Mo back contact properties for $Cu_2ZnSnSe_4$ solar," ***J. Alloys Compd.***, vol. 675, pp. 158-162, 2016. IMPACT FACTOR (IF): 3.133

J. Marquez, H. Stange, C. J. Hages, N. Schaefer, S. Levcenko, **S. Giraldo**, E. Saucedo, K. Schwarzburg, D. Abou-Ras, A. Redinger, M. Klaus, C. Genzel, T. Unold and R. Mainz, "Chemistry and dynamics of Ge in kesterite: towards band gap graded absorbers," ***Chem. Mater.***, 2017. DOI: 10.1021/acs.chemmater.7b03416 IMPACT FACTOR (IF): 9.466

Y. Sánchez, M. Espíndola-Rodríguez, H. Xie, S. López-Marino, M. Neuschitzer, **S. Giraldo**, M. Dimitrievska, M. Placidi, V. Izquierdo-Roca, F. A. Pulgarín-Agudelo, O. Vigil-Galán, and E. Saucedo, "Ultra-thin CdS for highly performing chalcogenides thin film based solar cells," ***Sol. Energy Mater. Sol. Cells***, vol. 158, pp. 138-146, 2016. IMPACT FACTOR (IF): 4.784

S. López-Marino, Y. Sánchez, M. Espíndola-Rodríguez, X. Alcobé, H. Xie, M. Neuschitzer, I. Becerril, **S. Giraldo**, M. Dimitrievska, M. Placidi, L. Fourdrinier, V. Izquierdo-Roca, A. Pérez-Rodríguez, and E. Saucedo, "Alkali doping strategies for flexible and light-weight $Cu_2ZnSnSe_4$ solar cells," ***J. Mater. Chem. A***, vol. 4, no. 5, pp. 1895–1907, 2016. IMPACT FACTOR (IF): 8.867

H. Xie, S. Lopez-Marino, T. Olar, Y. Sánchez González, M. Neuschitzer, F. Oliva, **S. Giraldo**, V. Izquierdo-Roca, I. Lauermann, A. Pérez-Rodríguez, and E. Saucedo, "Impact of Na Dynamics at the $Cu_2ZnSn(S,Se)_4$/CdS Interface During Post Low Temperature Treatment of Absorbers," ***ACS Appl. Mater. Interfaces***, vol. 8, no. 7, pp. 5017-5024, 2016. IMPACT FACTOR (IF): 7.504

E. Garcia-Llamas, J. M. Merino, R. Gunder, K. Neldner, D. Greiner, A. Steigert, **S. Giraldo**, V. Izquierdo-Roca, E. Saucedo, M. León, S. Schorr, and R. Caballero, "Cu_2ZnSnS_4 thin film solar cells grown by fast thermal evaporation and thermal treatment," ***Solar Energy***, vol. 141, pp. 236-241, 2017. IMPACT FACTOR (IF): 4.018

S. Lopez-Marino, M. Espíndola-Rodríguez, Y. Sánchez, X. Alcobé, F. Oliva, H. Xie, M. Neuschitzer, **S. Giraldo**, M. Placidi, R. Caballero, V. Izquierdo-Roca, A. Pérez-Rodríguez, and E. Saucedo, "The Importance of Back Contact Modification in $Cu_2ZnSnSe_4$ Solar Cells: the Role of a Thin MoO_2 Layer," ***Nano Energy***, vol. 26, pp. 708–721, 2016. IMPACT FACTOR (IF): 12.343

Contribución del autor a publicaciones de la tesis

El autor de este trabajo, Sergio Giraldo, ha sido responsable del diseño, coordinación y realización de los experimentos, además del análisis e interpretación de los resultados experimentales incluidos en esta tesis.

Capítulo 2:

(1) S. Giraldo, et al., "Optical and electrical properties of In-doped $Cu_2ZnSnSe_4$," ***Solar Energy Materials & Solar Cells***, vol. 151, pp. 44–51, 2016.

Factor de impacto (IF): 4.784

1.er cuartil en las categorías: *Electronic, Optical and Magnetic Materials; Renewable Energy, Sustainability and the Environment; Surfaces, Coatings and Films*

Este trabajo investiga los efectos del dopado con In en películas delgadas de CZTSe. Se introdujeron diferentes espesores (de 0 a 10 nm) correspondientes a concentraciones nominales de In de 0 a 2.6×10^{20} cm^{-3}. Demostramos una distribución uniforme de In en todo el absorbedor CZTSe, sin afectar a la distribución de los elementos principales, pero que sí impacta en la cantidad de Na en la superficie. Además, se observan cambios notables en la morfología, donde el aumento de la concentración de In conduce a la formación de una estructura bicapa. No se observó deterioro de las eficiencias para concentraciones inferiores a 2.6×10^{19} cm^{-3}, mientras que para niveles de dopaje más altos, una caída significativa del FF condujo a una disminución de la eficiencia. En el manuscrito, proponemos un modelo fenomenológico respaldado por una completa caracterización de absorbedores y dispositivos, que muestra cómo una fase conductora deteriora las propiedades de los dispositivos y que asociamos con la posible presencia de compuestos formados por óxidos de In y Sn.

En este trabajo, Sergio Giraldo fue responsable de la síntesis de todos los absorbedores utilizados en el estudio, la fabricación de dispositivos de células solares, así como la caracterización optoelectrónica (J-V y EQE), y el posterior análisis e interpretación de los resultados.

(2) S. Giraldo, et al., "Large Efficiency Improvement in $Cu_2ZnSnSe_4$ Solar Cells by Introducing a Superficial Ge Nanolayer," ***Advanced Energy Materials***, vol. 5, no. 21, p. 1501070, 2015.

Factor de impacto (IF): 16.721

1.er cuartil en las categorías: *Materials Science; Renewable Energy, Sustainability and the Environment*

En esta publicación, presentamos una notable mejora en la eficiencia de células solares de kesterita $Cu_2ZnSnSe_4$, basada en la incorporación de una nanocapa superficial de Ge. En particular, el uso de 10 nm de Ge evaporados sobre precursores metálicos conduce a una significativa mejora de la eficiencia, desde aproximadamente 7% para muestras de referencia (sin Ge) hasta el 10% para las mejores células que contienen Ge, junto con una mejora notable de la cristalinidad. Una detallada caracterización composicional y estructural demuestra que el Ge apenas se incorpora en el absorbedor CZTSe, por lo que proponemos un mecanismo que explicaría cómo el Ge podría ayudar a la cristalización mediante la formación de una fase líquida Ge-Se. Además, se presentan varias razones que podrían explicar esta mejora del rendimiento de los dispositivos, que incluyen: (i) la formación de una fase Ge_3Se_7 que se descompone de forma incongruente en $GeSe_2$ (volátil) y una fase líquida rica en Se, que ayudaría a la cristalización del CZTSe, mejorando la calidad cristalina; (ii) la menor formación de especies Sn + II (comúnmente asociadas con la formación de defectos profundos nocivos que deterioran el voltaje de las células) en presencia de Ge, tal y como sugiere el análisis preliminar de XPS; (iii) la presencia de nanoinclusiones de GeO_x, aparentemente asociadas con inclusiones de SnO_2, detectada por el análisis TEM/EELS de alta resolución, que podría tener un efecto de pasivación o actuar de algún modo como reflectores de electrones, mejorando el voltaje de las células solares.

Este artículo se publicó junto con una portada concedida por la revista, incluida en la sección *Appendix*.

En este trabajo, Sergio Giraldo fue responsable de la síntesis de los absorbedores CZTSe y la posterior fabricación de células solares. Además, realizó la caracterización morfológica por SEM así como la caracterización optoelectrónica, incluyendo medidas de eficiencia cuántica (EQE), J-V y medidas de reflectancia.

(3) S. Giraldo, et al., "$Cu_2ZnSnSe_4$ solar cells with 10.6% efficiency through innovative absorber engineering with Ge superficial nanolayer," ***Progress in Photovoltaics: Research and Applications***, vol. 24, no. 10, pp. 1359-1367, 2016.

Factor de impacto (IF): 6.726

1.er cuartil en las categorías: *Condensed Matter Physics; Electrical and Electronic Engineering; Electronic, Optical and Magnetic Materials; Renewable Energy, Sustainability and the Environment*

Este trabajo incluye la optimización completa de la estrategia presentada en el artículo anterior, en el cual se demostró el efecto positivo de incorporar una nanocapa de Ge en el procesamiento de los absorbedores CZTSe. En esta publicación, se define el rango de espesor de Ge óptimo para lograr una mejora del rendimiento de los dispositivos, obteniendo una eficiencia récord del 10.6% gracias a la colaboración internacional con IMRA en Francia. Con esta optimización, el V_{OC} de nuestro CZTSe de puro de selenio aumenta hasta 489 mV, lo que implica un déficit de voltaje entre los más bajos reportados hasta la fecha en tecnologías de kesterita. Además, se muestran primeros indicios de la interacción Ge-Na y su efecto en la densidad de portadores de carga. Finalmente, se presentan evidencias que apuntan a la causa del deterioro de las propiedades de los dispositivos con mayor cantidad de Ge.

En este trabajo, Sergio Giraldo fue responsable de la realización del conjunto completo de muestras, incluida la síntesis de los absorbedores CZTSe y la posterior fabricación de células solares. Posteriormente, realizó la caracterización optoelectrónica, análisis J-V y mediciones de eficiencia cuántica, así como el análisis morfológico/composicional por SEM/EDX.

Capítulo 3:

(4) T. Thersleff, S. Giraldo, et al., "Chemically and morphologically distinct grain boundaries in Ge-doped $Cu_2ZnSnSe_4$ solar cells revealed with STEM-EELS," ***Materials & Design***, vol. 122, pp. 102-109, 2017.

Factor de impacto (IF): 4.364

1.er cuartil en las categorías: *Materials Science; Mechanical Engineering; Mechanics of Materials*

Esta publicación presenta un análisis detallado de las características estructurales, morfológicas y de composición en muestras de CZTSe dopadas con Ge con eficiencias superiores al 10% (entre las mejores reportadas para este material y método de fabricación). Los hallazgos más relevantes revelan la existencia de al menos dos tipos morfológicamente distintos de fronteras de grano presentes en este sistema. Estas se concentran en las regiones superior e inferior de la capa absorbedora, y la posterior investigación analítica por STEM revela que tienen diferentes composiciones. El análisis más profundo y detallado por EELS de las fronteras de grano inferiores muestra que contienen grandes cantidades de SnO_x y que el Cu asume un

estado de valencia mayor, mientras que las fronteras de grano superiores están ligeramente enriquecidas en Cu y contienen trazas de oxígeno. Curiosamente, también podemos vincular la extensión de estas fronteras de grano a un cambio en la composición del absorbedor, el cual parece tener una estequiometría diferente en las mitades superior e inferior. En última instancia, se discute el impacto potencial de ambos tipos de fronteras de grano en el rendimiento y la fabricación de los dispositivos.

En este trabajo, Sergio Giraldo fue responsable de la fabricación de las muestras y el diseño experimental para lograr altas eficiencias. Además, ayudó con el diseño experimental de TEM en la Universidad de Uppsala en Suecia.

(5) S. Giraldo, et al., "How small amounts of Ge modify the formation pathways and crystallization of kesterites," ***Energy & Environmental Science***, 2017. DOI:10.1039/C7EE02318A

Factor de impacto (IF): 29.518

1.^{er} cuartil en las categorías: *Environmental Chemistry; Nuclear Energy and Engineering; Pollution; Renewable Energy, Sustainability and the Environment*

Este trabajo es una colaboración internacional entre IREC, la Universidad de Barcelona, AIST en Japón y la Universidad Martin Luther en Alemania. Esta publicación presenta una detallada investigación de los mecanismos que subyacen al efecto beneficioso del Ge en células solares de kesterita y sugiere un mecanismo alternativo basado en el esquema de reacción durante la selenización. Se analizan en detalle las diferencias en la reacción de formación de la kesterita con y sin Ge, utilizando EDX, XRF, XRD y espectroscopía Raman con múltiples longitudes de onda para muestras en las que el tratamiento térmico reactivo se ha interrumpido en diferentes momentos del proceso. Curiosamente, observamos que la presencia de Ge afecta considerablemente a la distribución elemental en profundidad, retrasando y minimizando la rápida difusión del Cu y la formación de compuestos volátiles de Sn-Se, evitando en consecuencia las pérdidas de Sn en gran medida. En la publicación se incluye una discusión adicional sobre las implicaciones en los esquemas de reacción. Finalmente, también presentamos una nueva metodología para la obtención de absorbedores CZTSe de alta calidad, mediante la introducción de nanocapas de Ge muy finas encima y debajo del precursor metálico, que nos permite obtener una eficiencia récord del 11.8%.

Este artículo ha sido destacado entre los mejores trabajos publicados en esta revista y forma parte de la colección: *2017 Energy and Environmental Science HOT articles*.

En este trabajo, Sergio Giraldo fue responsable de la fabricación de los absorbedores CZTSe y los dispositivos resultantes. Realizó los experimentos de interrupción del tratamiento térmico reactivo y analizó los resultados experimentales. También llevó a cabo la caracterización morfológica por SEM, así como el análisis de la distribución elemental en profundidad por EDX. Finalmente, los dispositivos de células solares de mayor rendimiento fueron terminados durante su estancia en el centro de investigación AIST en Japón.

Capítulo 4:

(6) S. Giraldo, et al., "$Cu_2ZnSnSe_4$-Based Solar Cells With Efficiency Exceeding 10% by Adding a Superficial Ge Nanolayer: The Interaction Between Ge and Na," ***IEEE Journal of Photovoltaics***, vol. 6, no. 3, pp. 754-759, 2016.

Factor de impacto (IF): 3.712

1.er cuartil en las categorías: *Condensed Matter Physics; Electrical and Electronic Engineering; Electronic, Optical and Magnetic Materials*

Este trabajo investiga la compleja interacción Ge-Na, que ha demostrado ser crucial para comprender mejor el efecto perjudicial de nanocapas de Ge de espesores mayores (≥25 nm) introducidas en los absorbedores de CZTSe. En esta publicación, explicamos cómo la concentración de Ge puede tener un impacto significativo en el contenido de Na y, por lo tanto, modificar el nivel de dopaje de la kesterita. Además, se presenta el posible mecanismo por el cual ocurre esta interacción, así como la formación esperada de defectos puntuales. Asimismo, apoyamos nuestro modelo de interacción Ge-Na con experimentos utilizando sustratos libres de Na, demostrando la importancia de controlar con precisión el contenido de Na cuando se usa Ge para aumentar la eficiencia en células solares de kesterita CZTSe, poniendo especial atención al nivel de dopaje adecuado y la composición óptima de los absorbedores.

En este trabajo, Sergio Giraldo fue responsable de la síntesis de los absorbedores CZTSe analizados y la fabricación de dispositivos sobre sustratos de vidrio SLG. Realizó la completa caracterización morfológica por SEM, el análisis composicional por EDX, las mediciones de XRF y la posterior caracterización optoelectrónica de los dispositivos terminados.

(7) M. Dimitrievska, S. Giraldo, et al., "Raman scattering analysis of the surface chemistry of kesterites: Impact of post-deposition annealing and Cu/Zn reordering on solar cell performance," ***Solar Energy Materials & Solar Cells***, vol. 157, pp. 462–467, 2016.

Factor de impacto (IF): 4.784

1.er cuartil en las categorías: *Electronic, Optical and Magnetic Materials; Renewable Energy, Sustainability and the Environment; Surfaces, Coatings and Films*

Este trabajo investiga las relaciones estructura-función de los tratamientos térmicos posdeposición (PDA) a diferentes temperaturas en células solares de kesterita $Cu_2ZnSnSe_4$. Se investigan los fenómenos de difusión y recristalización en la interfaz absorbedor/buffer durante el PDA, usando espectroscopía Raman con múltiples longitudes de onda y fotoluminiscencia, y se correlacionan con las propiedades optoelectrónicas de los dispositivos. Los resultados obtenidos muestran que los tratamientos PDA en dispositivos completos inducen una redistribución de átomos (Cu y Zn) en la superficie y subsuperficie del absorbedor. En particular, la superficie del absorbedor se vuelve más pobre en Cu y rica en Zn, creando defectos beneficiosos V_{Cu} y Zn_{Cu}, que pueden explicar en parte la mejora del rendimiento. Además, se observan efectos de recristalización de la capa buffer de CdS, lo que conduce a una mejor interfaz absorbedor/buffer y potencialmente a un mejor alineamiento de bandas.

En este trabajo, Sergio Giraldo fue responsable de la fabricación de las células solares de kesterita, realizó los tratamientos térmicos posdeposición a diferentes temperaturas, así como la caracterización optoelectrónica, incluidas las mediciones J-V y EQE. También llevó a cabo la caracterización morfológica de SEM.

Ninguno de estos artículos ha sido utilizado previamente por los coautores para su tesis doctoral.

Barcelona, 02/01/2018

Dr. Edgardo Saucedo Silva Prof. Alejandro Pérez Rodríguez

Chapter 1

Introduction

Nowadays, the greenhouse gas (GHG) emissions have become a serious concern due to their dramatic effect on the global warming and the climate change. About two-thirds of these emissions stem from energy production and use, thus placing the energy sector at the center of attention as one of the keys for their necessary reduction and to fight against climate change.[1] The transition from traditional energy sources based on fossil fuels combustion to a cleaner and efficient energy system is a crucial policy goal, not only for developed countries but also for developing nations. The first concerted effort of the international community to confront the problem of climate change was the birth of the United Nations Framework Convention on Climate Change (UNFCCC) in 1992 (entered into force in 1994).[2,3] The UNFCCC established a framework for action to control and stabilize concentrations of GHG in earth's atmosphere. Later on, in 1997, the participants established the Kyoto Protocol, which entered into force in 2005, including legally binding obligations to reduce GHG emissions for developed countries, on the basis that they are historically responsible for the current levels of GHG in the atmosphere.[4] More recently, the Paris Agreement adopted in 2015 was created with the central aim of strengthening the global response to the threat of climate change by holding a global average temperature increase this century well below 2°C above pre-industrial levels, and to pursue efforts to limit the temperature rise to 1.5°C.[5] In order to provide a clear and tangible understanding of what will be required for different countries to reduce GHG emissions and achieve the goal of limiting global warming to less than 2°C, the organization DDPP (Deep Decarbonization Pathways Project) emerged in 2013. According to DDPP, the deep decarbonization is technically feasible while accommodating economic and population growth, and analyzing the different modeled scenarios, the energy-related CO_2 emissions would be reduced by 46% - 56% (or 9.9 - 12.1 Gt CO_2) below 2010 levels, as shown in Figure 1.1 for some of the highest emitting countries.[6]

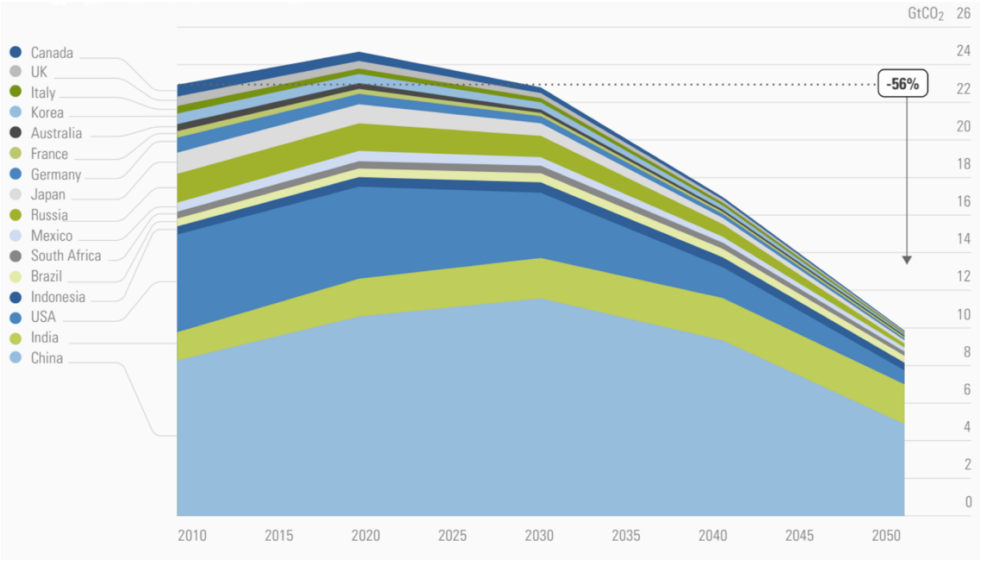

Figure 1.1. Emissions evolution for energy CO_2, 2010-2050 forecast, showing most ambitious reduction scenarios for several high emitting countries.[6]

In this context, renewable energy can play an important role in the transition to a less carbon-intensive and more sustainable energy system, allowing a significant reduction of GHG emissions. Renewables have grown significantly in the last years, especially solar photovoltaics (PV) with a remarkable cost reduction. PV module prices have fallen by around 80% since 2010, and the global weighted average cost of electricity from solar PV plants commissioned between the years 2010-2016 have also fallen 69%, even reaching the range of estimated fossil fuel-fired power generation costs (see Figure 1.2).[1,7] According to the International Energy Agency (IEA), renewables accounted for almost two-thirds of net power capacity around the world in 2016, with almost 165 gigawatts (GW) coming online. Last year, new solar PV capacity grew by 50% (over 74 GW), and for the first time, it increased faster than any other fuel.

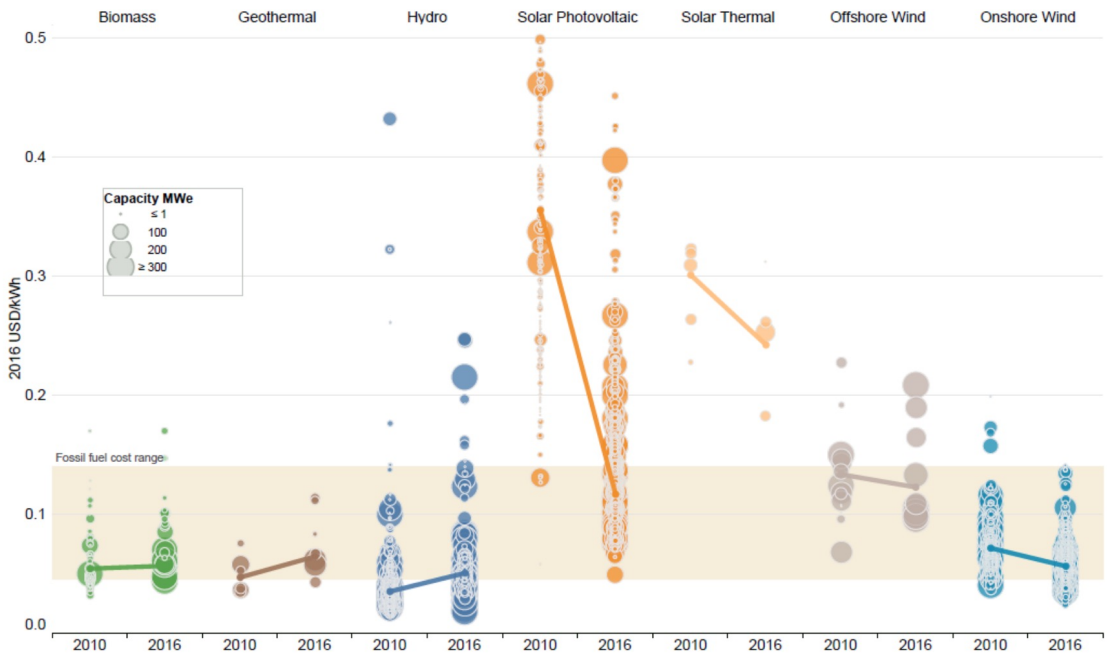

Figure 1.2. Levelized cost of electricity from utility-scale renewable technologies (ranges and average).[1]

In view of the foregoing, there is no doubt that solar energy is getting a lot of attention as one of the key renewable energy sources around the world for keeping a gradual decarbonization of the power sector and ensure a sustainable future. In the following section, the main photovoltaic technologies and their current status will be described.

1.1. Photovoltaic technologies

Essentially, PV is the technology that converts light directly into electricity. This phenomenon, known as PV effect, occurs when photons strike and are absorbed by a semiconductor material, and this energy from the photons is transferred to the electrons (- charge) in the material, making them jump to a higher state (conduction band) where they can freely move. Actually, this jump of the electron leaves behind a "hole" (+ charge) in the valence band, generating two charge carriers, the so-called electron-hole pair. A typical PV device is formed by joining a p-type (excess of holes) with an n-type (excess of electrons) semiconductor material, creating an electric field (p-n junction), and thus making holes move in the opposite direction from electrons, producing an electric current. In Figure 1.3, the conventional structure of a solar cell device is presented for clarification together with the band diagram of the p-n junction and the relevant electronic properties. Among these different properties or parameters, the E_g or band-gap is the minimum amount of energy required to excite an electron that is in its bound state into a free state where it can move and participate in the conduction. The lower energy level for an electron is called the valence band (E_V), and the energy level at which the electron is considered free is the conduction band (E_C). Therefore, the gap in energy between both states, i.e. between the valence band and conduction band, is the band-gap of the material. The work function (W) of the material is defined as the minimum required energy to transfer an electron from the Fermi level (E_F) to the vacuum level (E_{vac}), while the electron affinity (E_{EA}) is the energy needed to transfer an electron from the conduction band to the vacuum level.

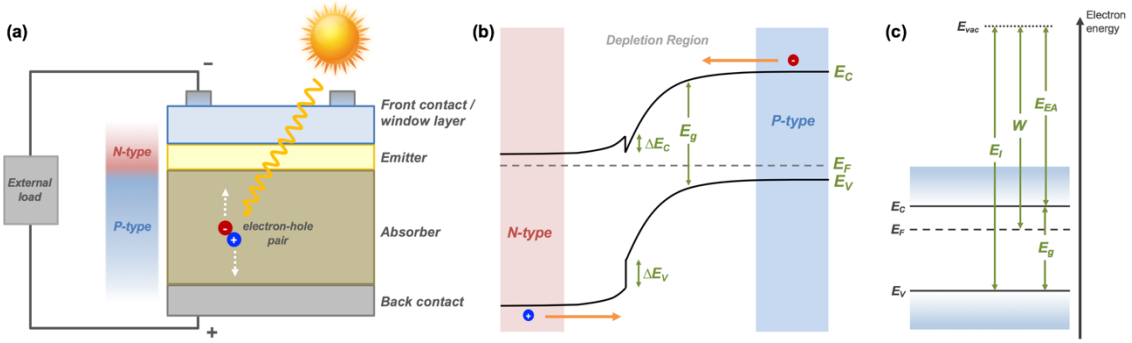

Figure 1.3. (a) Schematic of the typical solar cell structure, (b) band diagram of the p-n junction (E_g: band-gap energy, E_C: conduction band energy, E_V: valence band energy, E_F: Fermi level), (c) relevant electronic properties of semiconductor materials in a p-n junction (E_{EA}: electron affinity, W: work function, EI: ionization energy, E_g: band-gap energy).

In a p-n junction, since the n-type material has a high electron concentration and the p-type a high hole concentration, electrons diffuse from the n-type region to the p-type region. When the electrons and holes move to the other side of the junction, they leave behind exposed charges; on the n-type side, positive charges are exposed, while

on the p-type side, negative ion cores are exposed. Then, an electric field forms between both sides, forming the “depletion region” or “space charge region” (since the electric field quickly sweeps free carriers out, the region becomes depleted of free carriers).

There are different types of p-n junctions and they can be made of different semiconductor materials. On the following pages, the main photovoltaic technologies will be presented. Traditionally, solar cell technologies are divided into three different generations: first generation PV, based mainly on crystalline and multi-crystalline silicon; second generation PV, based on thin film materials; and third generation PV, which includes emerging, novel technologies and more advanced and complex concepts.

First generation solar cells are mainly based on silicon wafers, including mono-crystalline (single-crystal) and multi-crystalline (poly-crystalline) Si-based devices. These are the most common solar cells used in commercially available solar panels, and have been developed and optimized for decades now, representing about 94% of the total PV production in 2016.[8] Crystalline silicon solar cells have achieved laboratory energy conversion efficiencies over 26% for mono-crystalline cells and over 21% for multi-crystalline ones.[9] Advantages of this technology includes: maturity, since there is a substantial amount of information on evaluating robustness and reliability of the design; performance, since a standard industrially produced silicon solar cell offers higher efficiency than any other single-junction device, thus reducing the number of cells needed and cost of the final installation; reliability, since it has been proven that crystalline silicon cells reach lifetimes of more than 25 years with rather low long-term degradation; and abundance, since silicon is the second most abundant element in Earth’s crust.[10] However, they are slowly reaching their theoretical efficiency limit, so further improvements are becoming more and more challenging. Furthermore, since silicon has an indirect band-gap, leading to a low absorption coefficient, thicker absorber layers are required (about 200 μm), increasing the cost and the material usage, and also limiting their potential applications in flexible PV devices.

Second generation solar cells are based on thin film technologies. This not only significantly reduces the semiconductor material content of the final device (over 100 times less material), it also allows for higher throughput commercial production. Since the required thickness of the semiconductor material may only be of the order of 1-5 μm, almost any semiconductor is inexpensive enough to be a candidate for use in a solar cell.[11] The main thin film technologies include amorphous silicon (a-Si), which has demonstrated efficiencies of 14%, cadmium telluride (CdTe), which has achieved 21% efficiency cells, and the chalcopyrite materials like CIS ($CuInSe_2$) or the most commonly used CIGS ($Cu(In_{1-x}Ga_x)Se_2$), which has reached 21.7% efficiency (class record).[9] In Figure 1.4, efficiencies of the main second generation technologies compared to Si-based ones are shown for comparison. On the other hand, one of the major drawbacks of these technologies is the use of relatively scarce and/or toxic elements (In, Ga, Cd, Te).

Regarding the market share of all thin film technologies, in 2016, it only amounted to about 6% of the total annual production.[8]

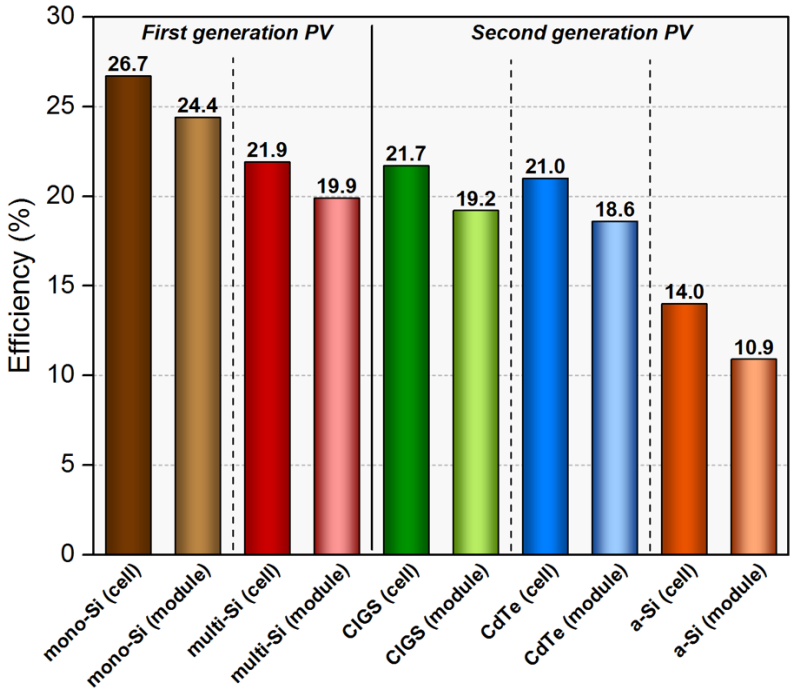

Figure 1.4. Efficiency comparison of first generation and second generation PV technologies. Best class record cell efficiencies and best module efficiencies are shown (values obtained from Ref. [9]).

Third generation technologies appear with the aim of boosting the efficiency of the previous PV concepts (even beyond the maximum theoretical 30-33% efficiency for a single junction device under 1 Sun illumination, known as the Shockley-Queisser limit[12,13]), maintaining the economic and environmental cost advantages of thin film deposition techniques. Third generation PV exploit emerging and novel materials as well as concentrator photovoltaics (CPV). In this group, one of the main technologies are the multi-junction (MJ) or tandem solar cells that have the potential for achieving efficiencies over 50%.[14] The emerging technologies include organic photovoltaics (OPV), advanced inorganic thin films and thermo-photovoltaics (TPV), although one of the most representative nowadays are perovskite-based solar cells, which despite some instability issues have achieved efficiencies above 20%, within a very short time of research.[9] Within all these technologies, several advanced concepts and approaches are being investigated including intermediate level devices, up/down conversion, hot carrier cells among others.[15,16] In Figure 1.5, the more common classification of the different available PV technologies are shown (wafer-based Si; thin film PV; and emerging PV), summarizing their main features with some illustrative examples.

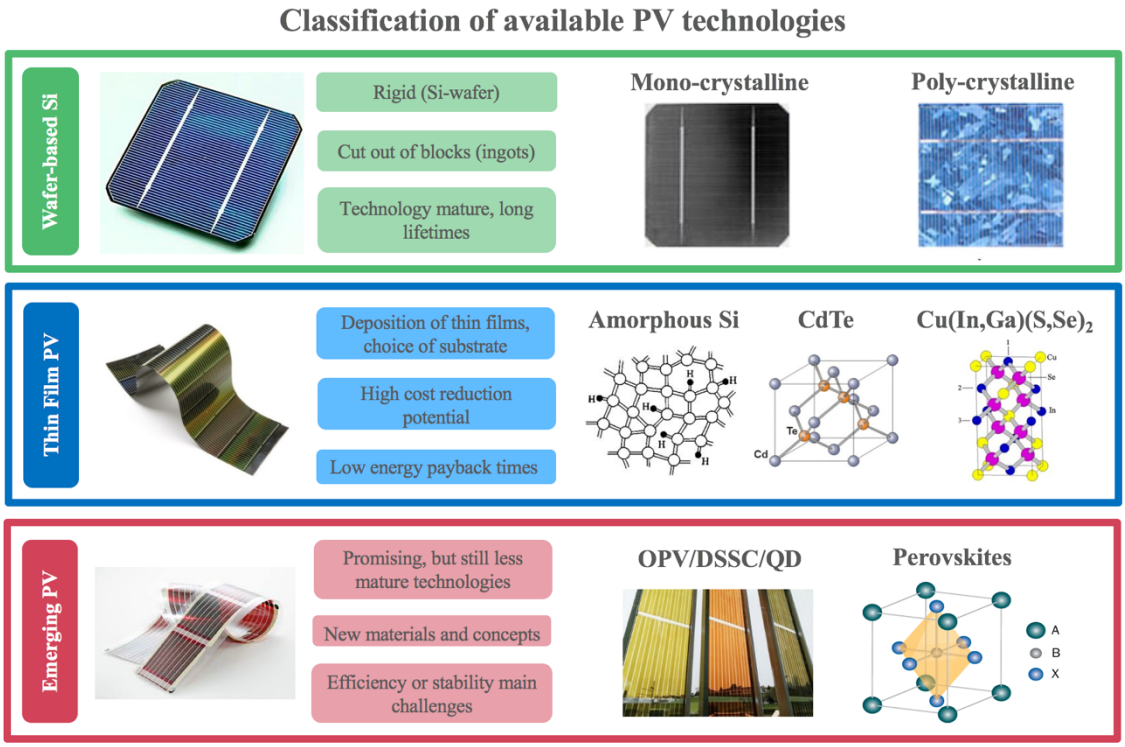

Figure 1.5. Classification and main characteristics of the available PV technologies.

Looking at the record research-cell efficiencies for all different PV technologies (see Figure 1.6), without considering MJ or GaAs solar cells, it is clear that crystalline Si technology offers much higher performance (with efficiency values almost touching 28%) than emerging thin films, for example compared to the promising kesterite $Cu_2ZnSn(S_xSe_{1-x})_4$ (CZTSSe) (with efficiencies below 13%). But we must not forget that Si technology has been investigated for a long time, and especially in PV, since the 1950's when Bell Labs demonstrated the first practical silicon solar cell.[17] On the other hand, kesterite thin films began to be investigated quite recently, about 20 years ago, but they have demonstrated to be a promising PV material due to several features that make it a very attractive and, theoretically, an ideal material to fabricate solar cells. The next subsection will be focused on kesterite semiconductor materials.

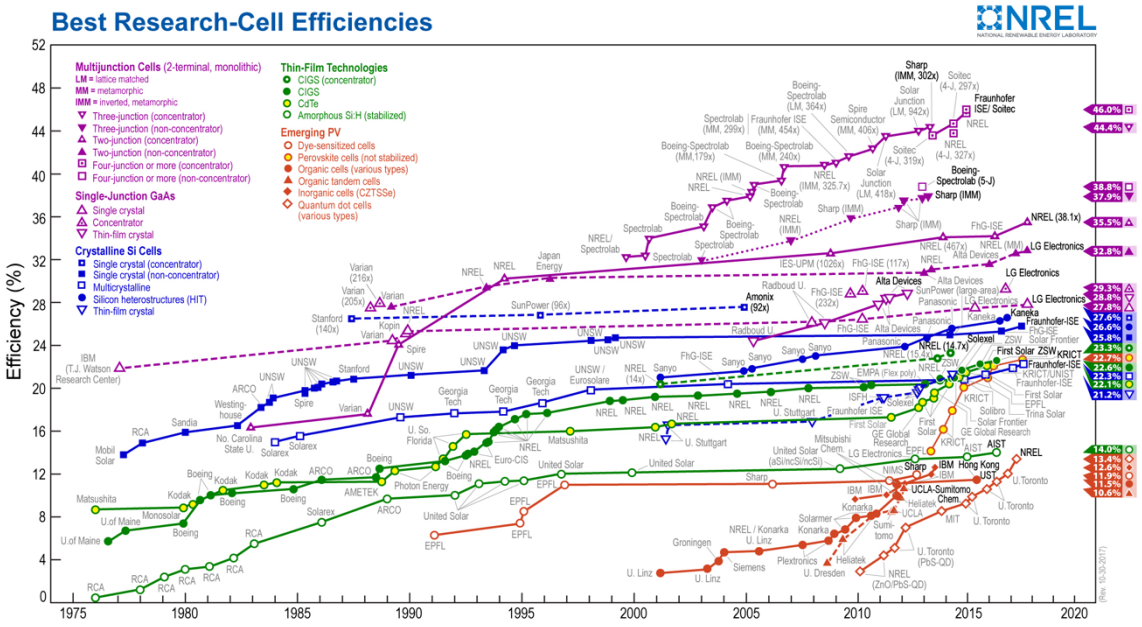

Figure 1.6. Best research-cell efficiencies for the different PV technologies (This plot is courtesy of the National Renewable Energy Laboratory, Golden, CO).[18]

1.2. Kesterite

In the field of thin film PV technologies, as mentioned previously, a-Si and the chalcogenides CdTe and CIGS are the most representative absorber materials, the latter being the most efficient ones. Chalcopyrite CIGS thin film solar cells have proven to be among the best performing devices of the second generation PV technology, achieving efficiencies as high as 22.6%.[19] Compared to silicon, chalcogenide based solar cells like CIGS have some key advantages; the direct optical band-gap that leads to a high absorption coefficient, or the possibility to accurately tune the band-gap either by metal or chalcogenide substitutions allowing for a better matching with the solar spectrum.[20,21] However, the use of tellurium and cadmium, in CdTe cells, and the use of gallium and indium, in CIGS cells, are the main constraints of these technologies for their sustainability, due to scarcity and/or toxicity concerns.[22,23] Additionally, indium has a large demand from the flat panel displays industry, which consumes over 70% of the world output of indium, making the prices higher.[24]

The emergence of kesterite Cu_2ZnSnS_4 (CZTS) as an absorber PV material overcomes the above-mentioned limitations, since it is composed of non-toxic and earth abundant elements (by replacing the scarce In and Ga of CIGS with Zn and Sn).[10,25,26] Therefore, CZTS and its related compounds $Cu_2ZnSnSe_4$ (CZTSe) and the solid solution $Cu_2ZnSn(S_xSe_{1-x})_4$ (CZTSSe) have attracted a lot of attention in recent years, as can be deduced from Figure 1.7, where the number of publications about kesterite (including the key words “kesterite solar cell”) has significantly increased in the last 10 years.

Although CZTS compound was identified for the first time as a suitable absorber material in 1988,[27] it was not until 1996 that Katagiri et al. fabricated the first CZTS solar cell (0.66% efficiency).[28] Subsequent optimizations of the materials and deposition techniques allowed a paramount increase of the efficiency up to 6.77% in 2008.[29] At this point, several groups started to further investigate this promising material, and in 2010, IBM published a 9.66% efficiency cell through solution-based process,[30] which was improved up to 10.1% efficiency just one year later.[31] The current certified record CZTSSe cell efficiency of 12.6% was reported in 2013, also from Mitzi group at IBM.[32]

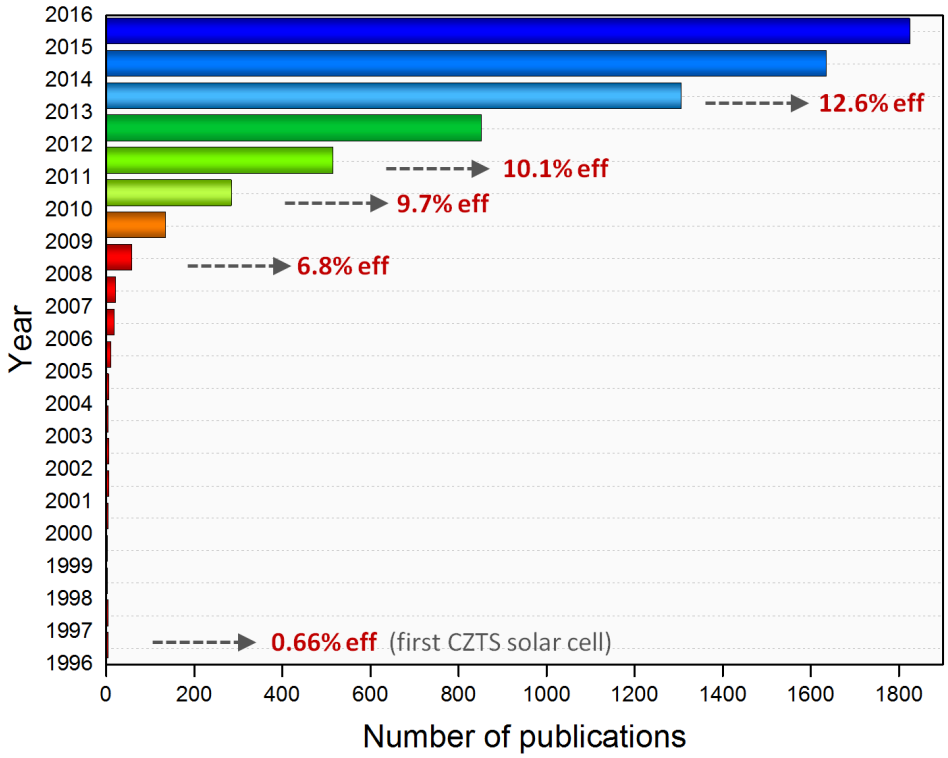

Figure 1.7. Number of publications including the key words "kesterite solar cell" for the different years since the first CZTS device was fabricated in 1996. Qualitative leaps in efficiency are also indicated with arrows and values.

There is a quite long list of advantages that make kesterites a suitable and also a very promising absorber material:

- It is exclusively formed by non-toxic and earth abundant elements.
- It has p-type conductivity naturally due to intrinsic point defects.
- It is a direct band-gap semiconductor with a high absorption coefficient (~10^4 cm^{-1}).[33]
- Its band-gap can be easily tuned with the ratio S/Se, from 1.0 eV, for the pure selenium CZTSe compound, to 1.5 eV, for the pure sulfur CZTS.[34,35] Moreover, cation substitution can also be used for tuning the band-gap, e.g. with Ge-

alloying (in Sn position),[36] Cd-alloying (in Zn position),[37] Ag-alloying,[38] or Li-alloying (in Cu position).[39]

- It is highly compatible with CIGS technology, so almost all the know-how previously acquired for chalcopyrites can be applied in kesterites. In particular, the knowledge gathered on buffer layers, window layers or back contacts has been directly utilized in kesterite solar cells, although for high efficiency kesterite devices some adjustments are indispensable. The standard structure of the CZTSe solar cells presented in this thesis is shown in Figure 1.8: these cells are grown in substrate configuration onto soda-lime glass (SLG); ~800 nm of sputtered molybdenum as back contact; about 1.6 μm of kesterite CZTSe absorber, synthesized by a sequential process (sputtered metallic stack precursor + reactive annealing under Se + Sn atmosphere); 50 nm of CdS as n-type emitter/buffer layer by chemical bath deposition (CBD); and about 250 nm window layer, composed of ~50 nm of intrinsic ZnO (i-ZnO) and ~200 nm of In_2O_3:SnO_2 (ITO), which acts as front contact. Occasionally, silver or Ni/Al metallic grids are deposited on top as a front electrode to improve the electric contact and current collection, and MgF_2 anti-reflective coating (ARC).

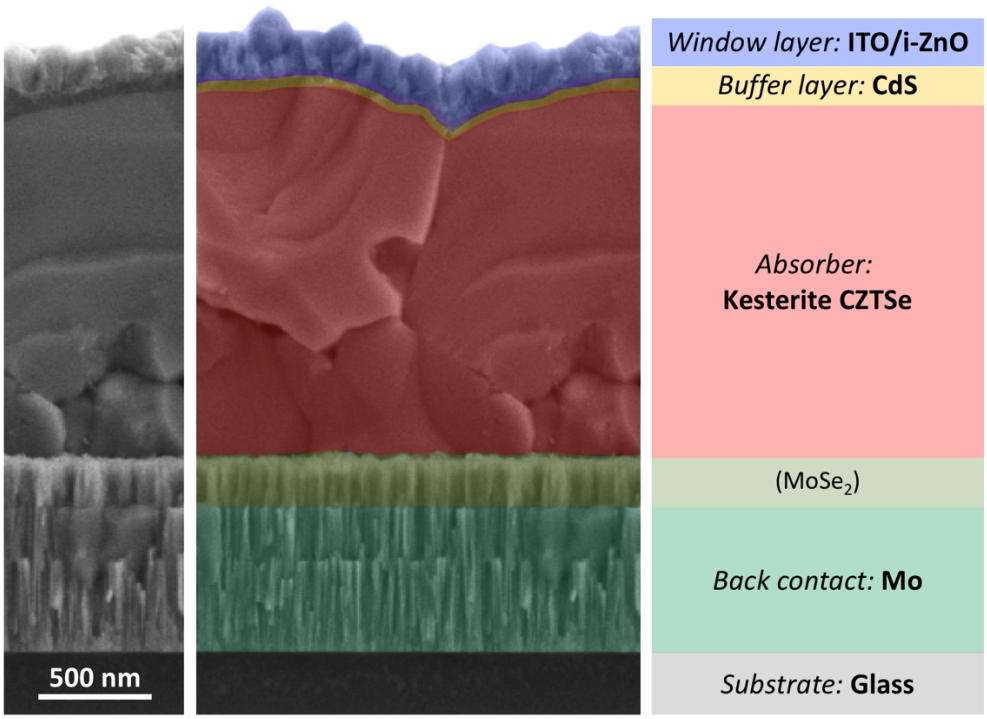

Figure 1.8. Cross-sectional scanning electron microscopy (SEM) picture of a kesterite solar cell device with its typical structure.

Besides all these good properties of kesterite, the fact that it can be synthesized with a large variety of techniques is another advantage to take into account. In general, these methods are divided into vacuum-based (mostly physical vapor deposition (PVD)-based) and non-vacuum deposition techniques. Vacuum-based methods include thermal evaporation, e-beam evaporation, sputtering, or pulsed laser deposition (PLD), among the most widely used. While non-vacuum techniques include solution processing via spin-coating/dip-coating/doctor-blade-coating/spray of the precursor, chemically synthesizing CZTS nanoparticle solution, or electrochemical deposition.

Currently, the highest efficiency (12.7%) has been achieved using hydrazine-based solution approach, although the wide variety of deposition techniques, like co-evaporation, sputtering, spray, spin-coating or doctor-blade coating, have also given efficiencies above 10% (see Table 1.1 with a selection of the best reported kesterite solar cell devices).

Table 1.1. Selection of the best reported kesterite solar cells, including pure selenium CZTSe, solid solution CZTSSe, pure sulfur CZTS, and several alloys (Ge, Cd and Ag). Corresponding references: a,[40] b,[41] c,[42] d,[43] e,[44] f,[45] g,[46] h,[47] i,[32] j,[48] k,[49] l,[50] m,[51] n,[52] o,[53] p,[9] q,[54] r,[55] s,[56] t,[57] u,[58] v.[59]

	Material (E_g, eV)	Affiliation	Eff (%)	V_{oc} (mV)	J_{sc} (mA/cm²)	FF (%)	Cell Area (cm²)	Technique	Further Details	Ref
Se	CZTSe (1.0)	IBM	11.6	423	40.6	67.3	0.43	Co-evaporation + Hot plate	Na doping	*a*
	CZTSe (1.0)	IMEC	10.4	395	39.7	66.2	0.52	Sputtering + H_2Se	-	*b*
	CZTSe (1.03)	Nankai University	10.4	419	38.5	64.8	0.345	Sputtering + Se vapor	w/o ARC	*c*
	CZTSe (0.97)	NREL	9.8	380	37.5	68.9	0.42	Co-evaporation	Certified	*d*
	CZTSe (1.07)	AIST	9.6	425	34.9	64.5	0.519	Co-evaporation + CTP	Na doping	*e*
	CZTSe (1.06)	EMPA	9.4	440	34.0	63.0	0.346	Co-sputtering + RTP	Se capping layer, w/o ARC	*f*
	CZTSe (1.06)	Purdue University	9.3	400	35.2	66.2	0.47	Nanoparticle-based + RTP	-	*g*
	CZTSe (1.04)	**IREC**	10.1	453	33.3	66.8	0.09	Sputtering + CTP	Ge doping, w/o ARC	
	CZTSe (1.05)	**IREC**	10.6	473	34.4	65.4	0.228	Sputtering + CTP	Ge doping	
	CZTSe (1.04)	**IREC**	11.8	463	38.3	66.3	0.487	Sputtering + CTP	Ge doping	
S,Se	CZTSSe (1.07)	IBM	12.7	466	38.9	69.8	0.45	Hydrazine-based	Hybrid In_2S_3/CdS buffer	*h*
	CZTSSe (1.13)	IBM	12.6	513	35.2	69.8	0.42	Hydrazine-based	Certified	*i*
	CZTSSe (1.04)	University of Washington	11.8	449	38.8	68.1	0.10	Spray	Li doping	*j*
	CZTSSe	Solar Frontier	11.8	503	35.1	66.8	10.6	Sputtering + SAS (Se→S)	Hybrid In_2S_3/CdS buffer, Submodule	*k*
	CZTSSe (1.11)	EMPA	11.5	496	35.2	65.8	0.30	Spin-coating + RTP	Li doping (high)	*l*
	CZTSSe (1.17)	IMRA	10.9	520	32.2	65.0	0.25	Spray + N_2→Se	Hybrid In_2S_3/CdS buffer	*m*
	CZTSSe (1.07)	ZSW	10.3	471	31.6	69.6	0.25	Doctor-blade coating	Certified	*n*
	CZTSSe (1.05)	NCK University	10.1	450	36.5	61.9	0.141	Spin-coating + SBS (S→Se)	w/o ARC	*o*
S	CZTS (1.5)	UNSW	11.0	731	21.7	69.3	0.234	Co-sputtering + RTP	(Zn,Cd)S buffer, Certified	*p*
Ge	CZTGSe (1.11)	AIST	12.3	527	32.3	72.7	0.519	Co-evaporation + CTP	Ge/(Ge+Sn)=22%	*q*
	CZTGSSe (1.2)	University of Washington	11.0	583	33.6	55.9	0.11	Spray + CTP	Ge/(Ge+Sn)=25%, w/o ARC	*r*
Cd	CZCTS (1.38)	UNSW	11.5	650	26.7	66.1	0.22	Sputtering + RTP	Cd/(Cd+Zn)=40%	*s*
	CZCTS (1.36)	NTU	9.2	581	24.1	66.0	0.25	Spin-coating	Cd/(Cd+Zn)=40%, w/o ARC	*t*
Ag	ACZTSSe (1.07)	Henan University	10.4	448	35.2	65.7	0.21	Spin-coating	Ag/(Ag+Cu)=3%, w/o ARC	*u*
	ACZTSe (1.0)	IBM	10.2	423	38.4	62.9	0.43	Co-evaporation + Hot plate	Ag/(Ag+Cu)≈10%	*v*

Historically, most record kesterite devices have been achieved using solution-based film deposition routes, contradicting the generalized idea that these techniques usually yield lower performing devices compared to PVD-based ones. Nowadays, both vacuum and non-vacuum based processes are able to produce high performance solar cells, with comparable efficiencies, as shown in Table 1.1. Additionally, in the last few years and as illustrated in Figure 1.9, there has been a remarkable improvement of devices fabricated through PVD-based approaches like sputtering and co-evaporation, which is of great importance from the industrial point of view. In terms of scalability, in

general, these vacuum-based processes are more interesting since they can be easily scaled-up with high reproducibility.

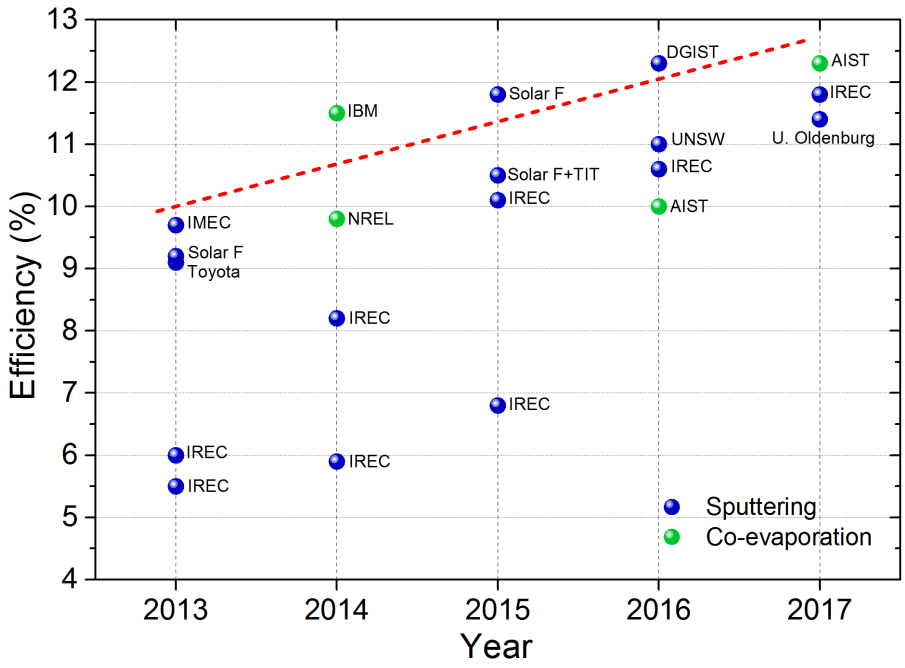

Figure 1.9. Evolution of efficiency for selected kesterite solar cells fabricated by PVD-based processes in different institutions.

Crystal structure and associated defects

The mineral kesterite belongs to the family of $A^{I}_{2}B^{II}C^{IV}X^{VI}_{4}$ compounds, which are known to exist in two main tetragonal crystal structure types: the kesterite type structure and the stannite type structure.[60] These structures are closely related but assigned to different space groups due to distinct distributions of the cations A^{I} and B^{II}. Each anion X^{VI} in both structures is surrounded by two A^{I}, one B^{II}, and one C^{IV}, and every cation is tetrahedrally coordinated by X^{VI} (Figure 1.10 shows the unit cell of both structure types for CZTSe). Therefore, due to their structural similarities it has been proven not to be trivial to distinguish between them without a careful crystal structural analysis. Nevertheless, there are several studies that using first-principle calculations determined, for CZTS and CZTSe, that the kesterite structure is energetically more stable than the stannite structure.[61–63] Besides, neutron powder diffraction as well as high-resolution XRD studies also support that both CZTS and CZTSe crystallize in kesterite structure.[64,65] More recently, polarized Raman spectroscopy has also succeeded to confirm that kesterite type structure is mostly present in these compounds.[66]

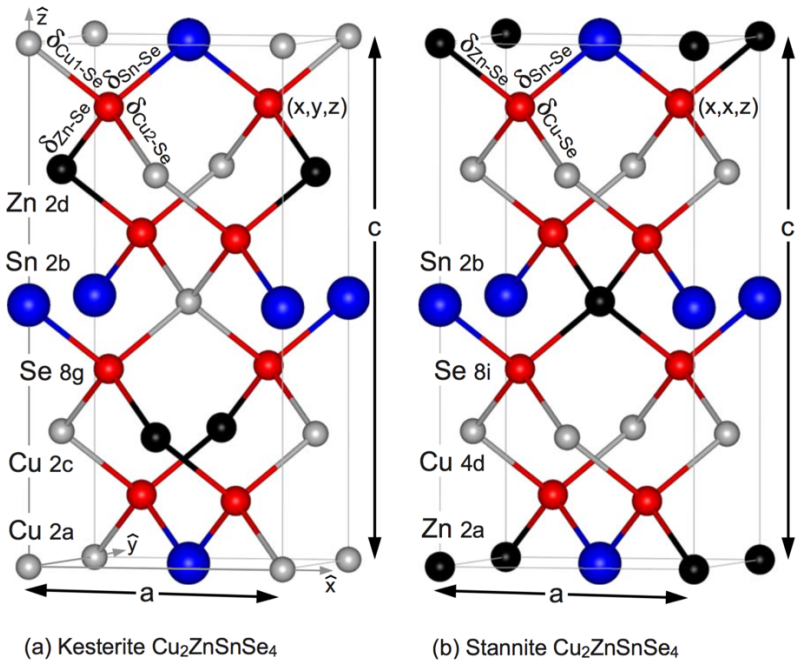

Figure 1.10. Conventional unit cells of (a) the kesterite structure and (b) the stannite structure for CZTSe, having four Cu atoms (light gray), two Zn atoms (black), two Sn atoms (blue), and eight Se atoms (red) per conventional unit cell. Reproduced from Persson.[67]

Consequently, the specific arrangement of the atoms in the kesterite structure (specifically the presence of Cu-Zn planes), the similar ionic radii of Cu and Zn and the fact that both are isoelectronic, make Cu and Zn atoms very likely to interchange, leading to the well-known Cu/Zn disorder.[64,68] Thus, promoting the formation of the common Cu_{Zn} and Zn_{Cu} antisites defects. Although these defects are partially compensated by the typical targeted Cu-poor and Zn-rich composition to obtain high performing devices,[69,70] they are not completely eliminated and can contribute to increase the band tailing (basically, by the formation of trap states that arise due to electrostatic potential fluctuations), ultimately limiting the open-circuit voltage (V_{OC}) and the efficiency of the solar cells.[46,71–73]

Figure 1.11 shows theoretically calculated ionization levels of different intrinsic defects in the CZTSe band gap, i.e. cation antisites and vacancy defects. The shallower V_{Cu} and Cu_{Zn} acceptor defects have the lowest formation energies, and are expected to contribute to the p-type conductivity of the CZTSe.[74,75] Conversely, deep defects are detrimental to device performance since they can act as recombination centers for electron-hole pairs. In particular, most of the Sn-related defects, V_{Sn} and Sn-antisites, according to these theoretical estimations, lead to the formation of deep levels in the band-gap that will degrade solar cell performance. In addition, Sn atom in the kesterite structure has been identified to adopt different oxidation states (+II and +IV), which can also contribute to the formation of harmful defects, specifically Sn_{Zn} has shown to be a

deep recombination center when Sn adopts state +II.[76] Therefore, this multivalent behavior of Sn makes the introduction of other elements in its position a very interesting and challenging approach in order to further improve the device performance of kesterite-based solar cells, as will be presented in detail in the following chapters of this thesis.

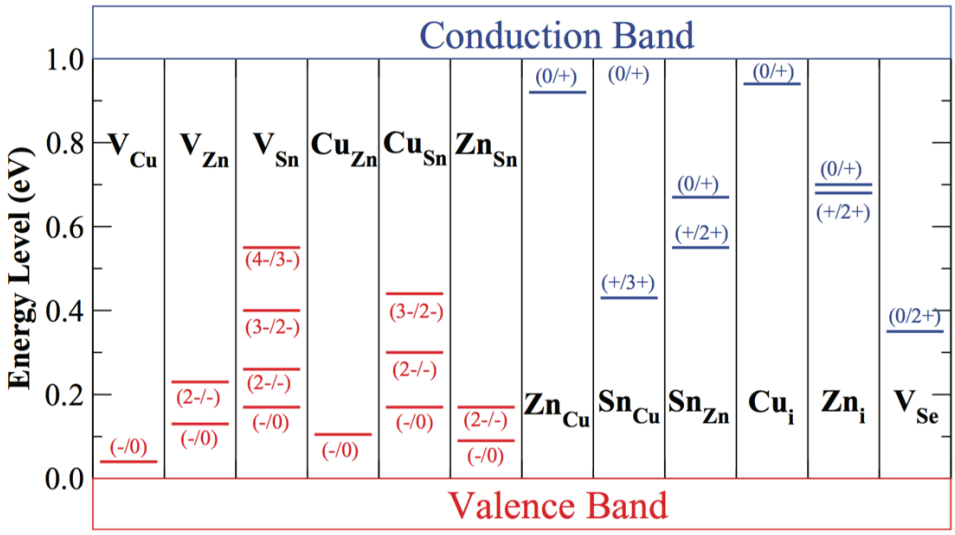

Figure 1.11. Ionization levels of intrinsic defects in the band-gap of Cu2ZnSnSe4. Red bars show acceptor levels, while blue bars show donor levels, with initial and final charge states labeled in parentheses. Reproduced from Chen et al.[75]

Regarding elements' substitution/addition in the kesterite material, two main strategies can be distinguished: doping or alloying. In the case of the doping approach, and on the contrary to alloying, there is no or slight modification of the band-gap and structural parameters, and it has little impact on fundamental optical properties. On the other hand, the doping can modify the electrical properties, transport charge properties, interfaces' characteristics, it can impact on the morphology, and even affect other elements' distribution during the synthesis. Thus, doping strategies can be a very interesting point in order to explore the effect of additional elements in the kesterite system, hopefully with a positive impact without changing its fundamental properties. This topic will be further discussed in the papers included in this thesis.

To conclude this introduction chapter, special mention should be made of the possible real-life applications of kesterite PV devices, although, as previously mentioned, kesterite is still considered an emerging and young PV technology with much room for improvement. Nevertheless, most recently, Haight and colleagues reported an encouraging work, demonstrating that kesterite devices can represent a worthwhile alternative to be used in small autonomous household electronics.[77,78] In that work, the researchers succeeded to fabricate a serially connected device capable of reaching 5.7

V at 1 Sun illumination (and ~2 V under low light conditions, below 10^{-3} Suns), and described an integration approach with a battery capable of powering autonomous electronic devices. Furthermore, the approach used in that study, by removing and depositing a new back contact in the final processing stages, may allow for facile integration with batteries, sensors and microprocessors, providing the energy harvesting and storage required to allow a system of distributed electronics for the Internet of Things (IoT). This kind of works can bring a breath of fresh air and hope for researchers who still believe in the promising future of kesterite and the clear promise of efficient, inexpensive, scalable and eco-friendly power generation.

1.3. Objectives of the thesis

The main objective of this thesis is to develop high efficiency thin film photovoltaic technologies based on sustainable kesterite ($Cu_2ZnSnSe_4$) absorbers, using a sequential process (sputtering of metallic stack precursors followed by reactive thermal annealing) through the implementation of innovative doping strategies, for advanced photovoltaic applications. To fulfil this general objective, the following sub-objectives are proposed:

1. Optimization of sequential processes for the synthesis of $Cu_2ZnSnSe_4$ thin films, consisting in the sputtering deposition of Cu/Sn/Cu/Zn metallic stacks onto Mo-coated soda-lime glass substrates, followed by a reactive thermal annealing under Se + Sn atmosphere, using a semi-closed graphite box in a conventional tubular furnace.

2. Screening of possible doping elements to improve CZTSe properties for obtaining high efficiency solar cell devices. This involves the analysis and preliminary optimizations of different dopants, including Ag, In, Si, Ge and Pb.

3. Study and identification of the main loss mechanisms that can degrade the efficiency of kesterite CZTSe-based solar cells, including surface engineering to compensate and mitigate these losses.

4. Analysis of the possible interaction between relevant dopants and alkali elements (Na in particular), and the impact of post-deposition annealing treatments on the device properties.

Chapter 2

Selective doping strategies in Sn position in kesterite $Cu_2ZnSnSe_4$: Indium and Germanium

2.1. Fine tuning of thermal processes

In this section, before going deeper into more advanced strategies, a previous study and optimization of the thermal processes for the synthesis of kesterite CZTSe absorbers are presented.

Historically, CIGS record efficiencies have been obtained with absorbers synthesized by co-evaporation technique, which includes a Cu-rich stage.[79] Conversely, for kesterite, sequential processes (precursor deposition + thermal annealing) have led to the best efficiencies (as can be seen in previous Table 1.1), where reactive thermal processes become a crucial step. This reactive annealing, typically performed in a semi-closed graphite box under chalcogen atmosphere, is mainly controlled by several thermodynamic and kinetic-related parameters, like temperature, total pressure or chalcogen partial pressure, and dwelling times or ramp rates, respectively. Additionally, synthesis catalysts and crystallization fluxes can have a strong impact on the annealing process, but they have been barely investigated in kesterites. This topic will be covered in following sections.

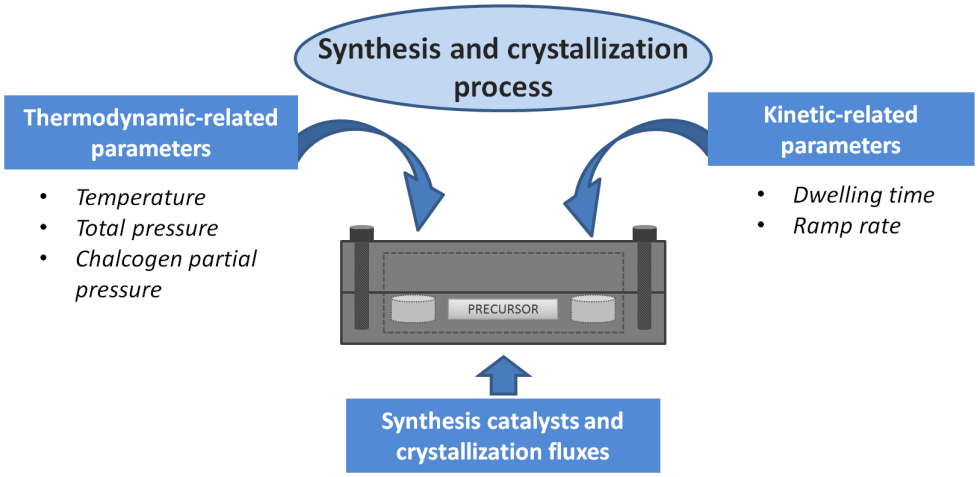

Figure 2.1. Sketch of a typical semi-closed graphite box with the main parameters controlling the synthesis and crystallization processes.

This preliminary study of the thermal annealing process consisted in a conservative and slight variation of some critical selenization parameters, comparing one-, two-, and three-step annealing profiles. All these modifications were performed using a conventional three-zone tubular furnace and commonly used graphite boxes (69 cm^3 of volume). For the standard selenization, 100 mg of Se powder and 5 mg of Sn powder were placed into the graphite boxes.

First of all, single one-step thermal annealing was implemented using our standard annealing temperature (550°C), but changing the heating ramp rate from

5°C/min to 20°C/min. As displayed in Figure 2.2, at first glance both samples show large inhomogeneities after selenization, which are also observed at micron-scale by morphological SEM characterization with contrasted roughness. Additionally, solar cell devices were fabricated with these absorbers leading to same expected inhomogeneities on the cells parameters.

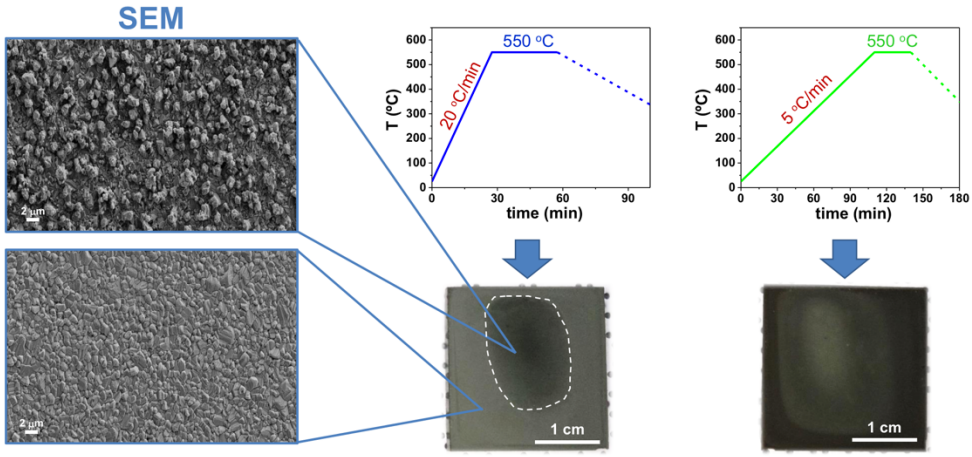

Figure 2.2. Morphological characterization (top-view SEM) of one-step annealing processes varying the heating ramp rate from 5°C/min to 20°C/min.

Two-step annealing profiles were also explored by modifying the second-step temperature (mainly related to a crystallization stage) from 550°C to 600°C as well as the ramp rate from 20°C/min to 50°C/min. As clearly observed in Figure 2.3(a), on the contrary to one-step annealings, the sample fabricated with a two-step process does not show macroscopic inhomogeneities due to a more controlled incorporation of selenium during the first step, when the different binary selenide compounds start to form. In Figure 2.3(b), the SEM characterization shows a moderate improvement in the grain size and a positive impact on the bilayer structure by increasing the temperature. Nevertheless, neither crystalline quality nor secondary phases formation are affected, as corroborated by Raman spectroscopy (see Figure 2.3(c)). Apparently, temperatures (thermodynamic parameter) and heating ramp rates (kinetic parameter) are not affecting the crystalline quality of the CZTSe and the formation of undesired secondary phases, but mainly promote slight morphology changes.

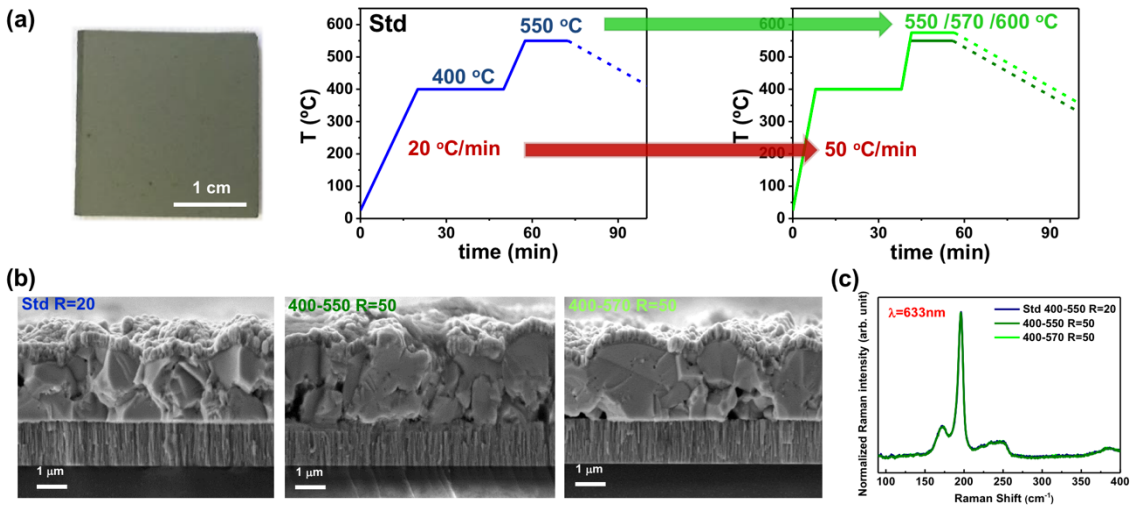

Figure 2.3. (a) Top-view of CZTSe sample synthesized with the standard (Std) two-step annealing process, and temperature profiles of the studied two-step processes; (b) cross-sectional SEM pictures of samples fabricated with different two-step annealing processes; (c) Raman spectroscopy analysis of the same previously characterized samples.

Photovoltaic parameters of representative devices fabricated with these CZTSe layers are shown in Figure 2.4(a). While the ramp rate variation barely affects the optoelectronic parameters of the cells, the temperature increase (up to 570°C) seems to improve to some extent the cell efficiency because of an increase in V_{OC}, although it cannot be related to a doping level modification, as shown in Figure 2.4(b). Most probably, this slight performance improvement is due to the enhanced crystallization.

(a)

	J_{SC} (mA/cm²)	V_{OC} (mV)	FF (%)	Eff (%)
Std. 550 (R=20)	30.1	466	63.3	**8.9**
550 (R=50)	30.3	457	64.9	**9.0**
570 (R=50)	30.3	477	64.2	**9.3**
600 (R=50)	28.7	444	59.0	**7.5**

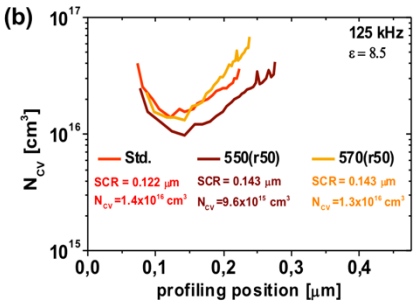

Figure 2.4. (a) Photovoltaic parameters of solar cells fabricated with different two-step annealing processes; (b) doping profiles as obtained from CV measurements for the different samples.

Additionally, selenium partial pressure during the annealing was also investigated by varying the selenium quantity from 100 mg to 400 mg for the best previously analyzed two-step processes. These results (not shown here) did not reveal any remarkable impact in terms of morphology or crystalline quality, as verified by SEM and Raman spectroscopy. Resulting devices from these absorber layers gave

comparable efficiencies in all cases, probably indicating that in our standard annealing conditions the atmosphere is already saturated of Se.

Finally, a preliminary experiment with three-step selenization processes was carried out, where the temperatures used for the different steps were 400°C, for the first step, 500°C, for the second step, and 550°C, 570°C or 600°C, for the last short crystallization step. Unfortunately, all fabricated devices showed very similar performance and slightly lower efficiencies compared to two-step annealing processes.

In summary, the fine tuning of the selenization process developed at IREC, and based on reported parameters for some of the best devices available in the literature, can be summarize as follows:

- Annealing profile (one- vs two- vs three-step): two-step profile shows the best results regarding homogeneity and device conversion efficiency.
- Temperatures around 570°C lead to a general improvement of the morphology with a slight increase of the efficiency (<0.5%), mainly due to a V_{OC} increase.
- Ramp rates have a negligible impact on the analyzed properties in our annealing system.
- Selenium quantity barely affects the morphology and device properties.

With this study, the standard thermal process that will be further used in most of the studies performed in this thesis is defined. The following table summarizes the most relevant parameters that have been defined as the optimal:

Table 2.1. Summary of relevant thermal annealing parameters optimized in the first stages of the thesis, and used in most of the work presented in the next chapters.

Annealing profile	Temperature (°C)	Se quantity (mg)	Sn quantity (mg)	Pressure (mbar)	Ramp rate (°C/min)	Duration (min)
2-steps	1) 400°C 2) 550°C	100 mg	5 mg	1) 1.5 mbar 2) 1000 mbar	20°C/min	1) 30 min 2) 15 min

Therefore, additional strategies need to be developed in order to further improve kesterite devices performance. Customized solutions and innovative approaches are crucial for the development of kesterite-based technologies.

2.2. Screening of doping elements

As was introduced in the previous chapter, the addition of extrinsic elements in the kesterite system either by alloying or doping approaches may lead to a significant impact on the material properties. A very simplistic way to differentiate both strategies is the quantity of the element that is introduced in the material, where doping typically involves concentrations below 1%, and alloying above 1%. Thus, this sub-section will include the screening of possible beneficial dopants for kesterite CZTSe absorbers.

Alkali doping in CZTSe is the most widely studied, in particular Na doping, being essential to increase conversion efficiency (as in CIGS).[44,80–83] However, the work carried out here was focused on cation-substitution or doping, with the elements: Ag, In, Si, Ge and Pb, as first candidates, all of them somehow related to kesterite-constituting elements. Figure 2.5 highlights the elements tested in this study with their location in the periodic table.

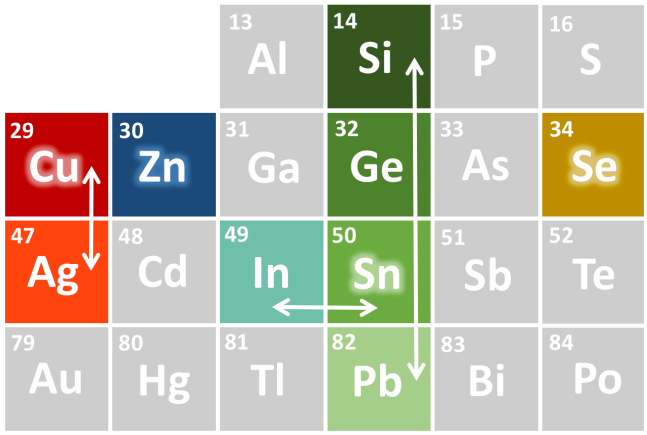

Figure 2.5. Part of the periodic table highlighting CZTSe-constituting elements and the different assessed dopants.

Regarding doping in Cu position, Ag was selected for a preliminary investigation. It is known that high Ag content (>50%) inverts the kesterite conductivity to n-type, so we might expect a lower doping level for intermediate concentrations.[59] Additionally, Ag is an interesting candidate for replacement of Cu since it possesses a larger atomic radius, which could potentially suppress Cu-Zn antisites defects to some extent, i.e. decreasing Cu-Zn disorder. Theoretical calculations have demonstrated that Ag_{Zn} defects have much higher formation energy than Cu_{Zn} defects.[84] Therefore, Ag could decrease the harmful band tailing and improve minority carrier lifetimes.

On the other hand, another interesting strategy is the selective doping in Sn position. As it is widely known, the presence of Sn in kesterite is one of the most challenging issues since it can induce compositional imbalances due to formation of

volatile $SnSe_2$ compounds and the consequent Sn loss, as well as detrimental effects owing to the multivalence of this element (Sn +II or Sn +IV are the most stable). Moreover, as was introduced in the first chapter, all Sn-related defects promote the formation of deep-level traps within the CZTSe band-gap with negative consequences for device performance. In this sense, elements from the same group in the periodic table like Si, Ge and Pb were assessed as possible cationic dopants. Additionally, In was studied since it could potentially increase the doping level of the CZTSe (In +III oxidation state is the most stable), and also to investigate its possible "contaminating" effect since it is frequently present in other layers of the device structure, like buffer layers (e.g. In_2S_3) or window layers (e.g. ITO).

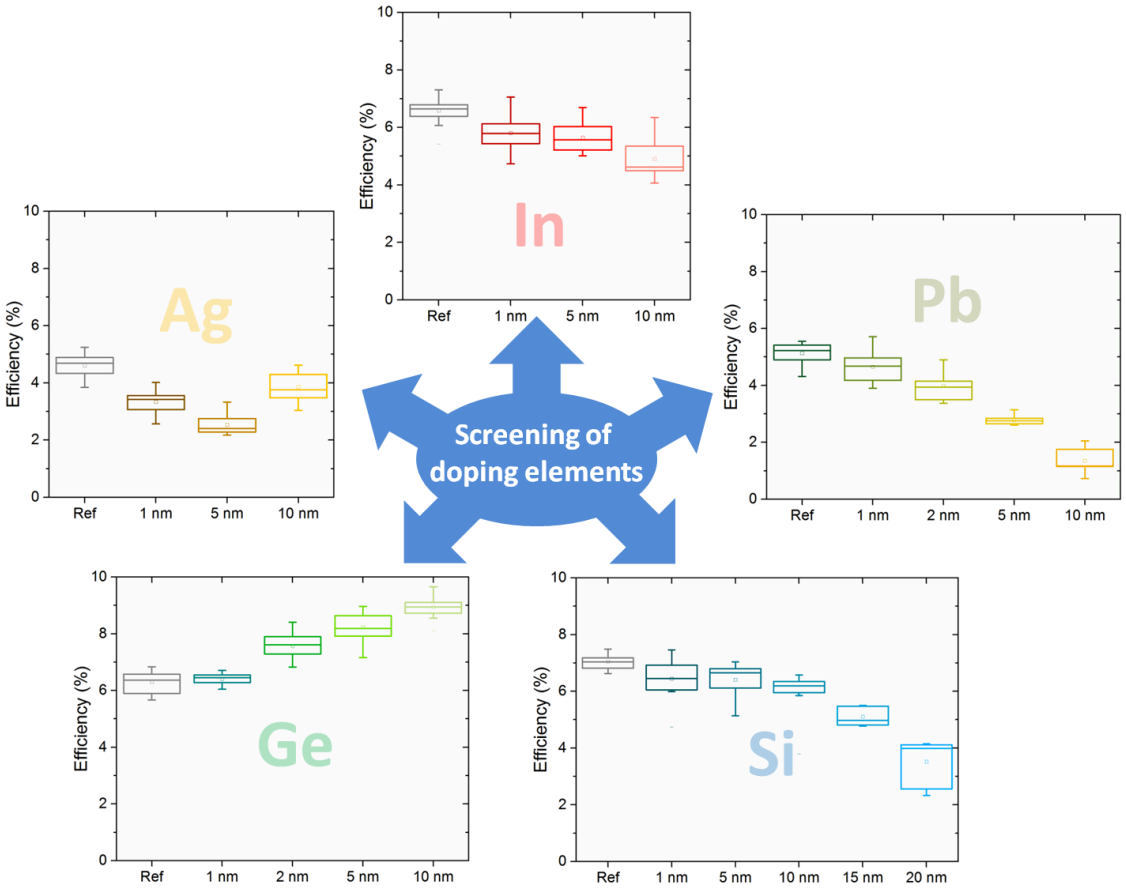

Figure 2.6. Evolution of efficiency in CZTSe solar cells for different concentrations (thicknesses) of selected dopants: Ag, In, Pb, Ge and Si.

In order to study the effect of different dopants, CZTSe absorbers were synthesized adding extremely thin layers of Ag, In, Ge, Si or Pb on top of the metallic Cu/Sn/Cu/Zn stack precursor with the standard kesterite composition, and later made into solar cell devices. Figure 2.6 shows the efficiencies of devices fabricated with several amounts (from 1 nm to 10/20 nm thickness) of the screened dopants. In the case of Ag, this preliminary experiment did not show a clear tendency, being all Ag-doped devices

less efficient compared to non-doped samples. On the other hand, Si- and Pb-doped samples showed a clear trend, where the efficiency was gradually degraded with the increasing dopant thickness. The introduction of Si into CZTSe has demonstrated to be rather challenging and so far, no successful results have been achieved. Besides, first-principle calculations of the structural and electronic properties of Si-incorporated CZTSe have revealed that the formation energy of this compound is larger compared to CZTSe, probably requiring higher temperatures to be properly synthesized.[85] Regarding Pb-containing CZTSe, the harmful effect is even more pronounced since 10 nm of Pb are sufficient to practically kill the cell efficiency (<2%). Some reasons for this may be related to its most stable oxidation state, Pb +II, since it could be inducing the formation of deep defects as in the case of Sn +II.[76] With regard to In-doped samples, a slight gradual deterioration of devices was firstly observed with the increasing In content, although rather less evident than with previous dopants. However, a remarkable efficiency improvement was achieved by introducing small amounts of Ge (10 nm) with a clear trend, as shown in first screening results presented in Figure 2.6.

Finally, In and Ge were both selected to further analyze their doping properties on CZTSe absorbers through a complete characterization, including compositional, morphological, structural, optical and electrical properties of the layers and the resulting solar cell devices.

The importance of studying In, as was highlighted before, lies in the fact that this element may be present in different layers of the devices, like ITO window layers, or hybrid In_2S_3/CdS buffers, both used in high efficiency solar cells.[47,86,87] Therefore, during CZTSe synthesis, In could be a potential contaminant diffusing from other layers. Moreover, In is an interesting doping element since kesterite comes from the substitution of two In atoms in the chalcopyrite structure by one Zn and one Sn atoms, meaning that In might substitute either Zn or Sn forming charged defects. Additionally, In_{Cu} defects in CIGSe have been proven to form benign complexes with V_{Cu}.[88] Conversely, in CZTSe this has not been extensively studied, although there are some published results that point to an increase of the carrier concentration and mobility, which could potentially improve the electrical properties of the absorber.[89]

Regarding the use of Ge in kesterite, it is known that Ge, partially replacing Sn in the lattice, allows tuning the band-gap of the absorber material from about 1.0 to 1.35-1.5 eV in the case of pure selenide kesterite (CZTSe), or from about 1.5 to 1.9 eV using sulfide kesterite (CZTS).[85,90,91] Although Ge-incorporated kesterite has not been deeply investigated yet, the few already published works show promising improvements. First studies including devices fabrication had shown small or moderate improvements, achieving efficiency values below 10%.[92,93] Nevertheless, more recently it has been reported better performances, reaching efficiencies of 11% and above 12%, lowering the voltage deficit to record values.[54,55,94] Therefore, together with our preliminary

promising results at doping level, Ge seems an obvious candidate for further investigations. Moreover, the doping strategy implies the advantage of using much less Ge, thus it would not compromise the sustainability of these processes, as it may be considered a scarce element.

This chapter includes the following three publications: "Optical and electrical properties of In-doped $Cu_2ZnSnSe_4$", "Large efficiency improvement in $Cu_2ZnSnSe_4$ solar cells by introducing a superficial Ge nanolayer", and "$Cu_2ZnSnSe_4$ solar cells with 10.6% efficiency through innovative absorber engineering with Ge superficial nanolayer" with a more exhaustive study about In and Ge elements as dopants in kesterite CZTSe.

Solar Energy Materials & Solar Cells 151 (2016) 44–51

Contents lists available at ScienceDirect

Solar Energy Materials & Solar Cells

journal homepage: www.elsevier.com/locate/solmat

Optical and electrical properties of In-doped $Cu_2ZnSnSe_4$

S. Giraldo [a,*], C.M. Ruiz [b], M. Espíndola-Rodríguez [a], Y. Sánchez [a], M. Placidi [a], D. Cozza [b], D. Barakel [b], L. Escoubas [b], A. Pérez-Rodríguez [a,c], E. Saucedo [a]

[a] Catalonia Institute for Energy Research (IREC), Jardins de les Dones de Negre 1, 08930 Sant Adrià de Besòs, Spain
[b] Aix-Marseille University – IM2NP, CNRS (UMR 7334), France
[c] IN2UB, Universitat de Barcelona, C. Martí Franquès 1, 08028 Barcelona, Spain

ARTICLE INFO

Article history:
Received 31 July 2015
Received in revised form
9 November 2015
Accepted 28 February 2016

Keywords:
$Cu_2ZnSnSe_4$
In doping, Thin film solar cells
Kesterite

ABSTRACT

$Cu_2ZnSnSe_4$ (CZTSe) is a very promising material as absorber layer for low cost and earth abundant thin film solar cells. Currently in this technology we can find indium in different layers, including the transparent window layer In_2O_3:SnO_2 (ITO), and the In_2S_3/CdS double emitter, both used in high efficiency devices. Therefore, during devices fabrication processes, In could be a potential contaminant and consequently, it is very interesting to investigate its possible impact in the solar cells performance. Besides this, a key factor in the control of material properties lies in the doping. Extrinsic doping has been barely studied for CZTSe and among the possible doping elements, In is one of the most interesting candidates, because it has the possibility to occupy either Sn or Cu/Zn positions.

In this work we investigate the indium doping of CZTSe thin films. For this purpose, CZTSe was synthesized by a sequential process with different nominal In concentrations ranging from 0 to 2.6×10^{20} cm^{-3}. We demonstrate that In is uniformly introduced in CZTSe, not affecting the main elements distribution, but impacting in the Na quantity at the surface. Drastic changes on the morphology are observed, where the increasing indium concentration leads to the formation of a bilayer structure. Efficiencies in the range of 7–7.5% or 8.5–9.2% were obtained for In concentrations below 2.6×10^{19} cm^{-3} for pure CZTSe and CZTSe:Ge respectively, decreasing for further doping levels mainly due to the deterioration of the fill factor, while the other optoelectronic parameters are less affected. We propose a phenomenological model supported by the complete electrical characterization of the material and devices, showing that a conductive phase deteriorates the properties of the system that we associate to the possible presence of mixed Sn-oxides and In-oxides.

1. Introduction

$Cu_2ZnSnSe_4$ (CZTSe) is a promising compound as an absorber layer for low cost thin film solar cells owing to many advantages such as direct band gap, high light absorption coefficient, and because is formed by relative earth abundant elements [1–3], having demonstrated efficiencies exceeding 11% [4]. Currently in this technology (and as standard in many others thin films photovoltaic technologies), we can find indium in different layers, including the transparent window layer In_2O_3:SnO_2 (ITO), and the In_2S_3/CdS double emitter, used in high efficiency CZTSSe solar cells as buffer layer [5,6]. Therefore, during solar cells synthesis processes and under normal operation, indium could be a potential contaminant diffusing from these layers towards the absorber, and consequently it is very interesting to investigate its possible impact in the solar cells performance.

Besides this, a key factor in the control of material properties lies in the doping, either by varying the stoichiometry or by adding other elements. Nowadays, required electrical properties of CZTSe to achieve high efficiency devices are mainly controlled by intrinsic defects (Cu-poor and Zn-rich conditions) [2,3,5]. Unfortunately, this implies the management of three atoms, extremely complicating the accurate control of doping level. The study of doping on this material has been mainly limited to alkaline elements (mostly Na and K), which have demonstrated to have a remarkable impact on the optoelectronic properties of the kesterite based devices [7–10]. Learning from the close cousin $CuIn_{1-x}Ga_xSe_2$ (CIGSe) technology, alkaline elements are mainly occupying isoelectronic Cu^+ positions [11–13], and could probably prevent to a certain extent the formation of detrimental Zn_{Cu} anti-sites. So, alkaline doping has already demonstrated to be useful for controlling doping level, improving crystalline quality and modifying the atomic lattice dynamic interacting mainly with the Cu-site positions. Aside the

* Corresponding author.
E-mail address: sgiraldo@irec.cat (S. Giraldo).

http://dx.doi.org/10.1016/j.solmat.2016.02.024
0927-0248/

alkaline doping that has been studied in some extent, only few reports have been published with other dopants like Cd, Fe and Ge [14,15].

In this sense, In is one of the most interesting dopants, since kesterite comes from the substitution of two In in the chalcopyrite structure by one Zn and one Sn, meaning that probably In can substitute both Zn and Sn forming charged defects (In has +3 charge, while Sn has +4 and Zn has +2). Additionally, In has shown that it is thermodynamically possible the formation of In_{Cu} defects in CIGSe that form benign complexes with V_{Cu} [12]. Nevertheless, In doping in CZTSe has not been properly studied, and only the properties of $Cu_{1.75}Zn(Sn_{1-x}In_x)Se_4$ (with $0 \leq x \leq 0.6$) alloys, i.e. with high In quantity have been reported [16]. It was shown that increasing the In concentration the carrier concentration also increases, and the mobility first increases for relatively low In concentration and then decreases [16], suggesting that In can improve the electrical properties of CZTSe. Nevertheless, the impact on the optoelectronic properties of the solar cells was not studied at all.

Taking into account the non-negligible possible In contamination in processes required for the fabrication of kesterite based solar cells, as well as the potential of this atom as electrically active dopant, in this work we study the effect of In doping on the compositional, structural, morphological, optical and electrical properties of CZTSe. We demonstrate that In is effectively introduced into the CZTSe layer at doping level, having a uniform in-depth distribution independently on their concentration. CZTSe exhibits a good tolerance to In, where the efficiency of the devices is barely affected till relatively high doping levels, deteriorating then. We present a phenomenological approach suggesting that the deterioration is due to the formation of a conductive phase (probably SnO_2–In_2O_3 alloy) in the grain boundaries, that is supported by capacitive and Kelvin probe atomic force microscopy.

2. Materials and methods

CZTSe doped with In was synthesized onto Mo coated soda lime glass (800 nm, 0.5 Ω/□) by a sequential process, based on the deposition of Cu/Sn/Cu/Zn metallic stacks by DC-magnetron sputtering technique (Alliance Concepts AC450), and subsequent reactive annealing. The metal thicknesses were selected in order to achieve Cu-poor and Zn-rich conditions (Cu/(Zn+Sn)=0.75 and Zn/Sn=1.20). Afterwards, different In thicknesses (0 nm -undoped-, 1 nm -In1-, 5 nm -In5-and 10 nm -In10-, corresponding to non-intentionally doped, 2.6×10^{19} at/cm^3, 1.3×10^{20} at/cm^3 and 2.6×10^{20} at/cm^3 nominal In concentration respectively) were evaporated on top by thermal evaporation (Univex 250 Oerlikon Leybold Vacuum). Some experiments were also performed onto CZTSe:Ge layers, since it has been reported as route to achieve high efficiency CZTSe based solar cells [15]. Following, we performed a reactive annealing in a graphite box (69 cm^3 in volume) under Se (100 mg) and Sn (5 mg) containing atmosphere to form the kesterite absorber in a conventional tubular furnace. The selenization was performed with a 2-step process; the first one at 400 °C (heating ramp 20 °C/min) during 30 min and 1.5 mbar Ar pressure, and the second one at 550 °C (heating ramp 20 °C/min) during 15 min and 1 bar Ar pressure, as has been reported elsewhere [17].

Precursors and absorbers composition was characterized using X-ray fluorescence (XRF Fisherscope XVD), and time-of-flight secondary ion mass spectrometry (TOF-SIMS) with a TOF-SIMS IV instrument from Ion-Tof GmbH Germany, using the following conditions: Bi_3 at 25 keV pulsed beam at 45° of incidence, rastered over 200×200 μm^2; O_2 gun at 2 kV rastered over 350×350 μm^2, flood gun active, Bi^{+3} current of 420 nA, positive polarity and bismuth liquid metal ion gun mode (BiHCBU). All the samples were analyzed in the same experimental conditions, selecting the following elements: $16O^+$, $23Na^+$, $28Si^+$, $39K^+$, $63Cu^+$, $64Zn^+$, $80Se^+$, 98Mo, $115In^+$, $120Sn^+$. In-depth scanning electron microscope (SEM) images were obtained with a ZEISS Series Auriga microscope using 5 kV accelerating voltage. Photoluminescence (PL) was performed at room temperature using a 532 nm diode laser with a power flux of 16 W/cm^2 as an excitation probe. For detection, a liquid nitrogen refrigerated InGaAs diode was coupled to a iHR320 Horiba monochromator. *C–V* and impendance spectroscopy measurements were performed using an Agilent E4980A LCR meter coupled to an Agilent E3641A DC power source. Kelvin probe atomic force microscopy images were obtained using a Nano-Observer AFM from CSInstruments (CSI – France) using HD-KFM mode. The scanning was performed on 3×3 μm^2 surfaces for guaranteeing the presence of grain boundaries. X-ray diffraction (XRD) measurements were performed using an Advance D8 diffractometer (Bruker, CuKα radiation, λ=1.5406 Å, 40 kV, 40 mA). Typical $\theta-2\theta$ measurements were carried out from 10° to 60° with step size of 0.010°.

Solar cells were fabricated using the standard configuration (Glass/Mo/CZTSe:In/CdS/i-ZnO/ZnO:Al), depositing CdS (50 nm) by chemical bath deposition and i-ZnO/ZnO:Al (50 nm/350 nm – 40 Ω/□) by DC-pulsed magnetron sputtering technique (Alliance Concepts CT100). *J–V* dark and illuminated curves (AM1.5 illumination conditions) were obtained using a pre-calibrated Sun 3000 Class AAA solar simulator from Abet Technologies. Complete solar cells were submitted to a 200 °C soft annealing in air during 30 min before the measurement of the illuminated *J–V* curve [18]. The spectral response was measured in a pre-calibrated Bentham PVE300 system, allowing us to obtain the external quantum efficiency (EQE) of the cells. We avoid the use of In in the solar cell structure (with the exception of the In doping intentionally introduced in the CZTSe absorber), to prevent possible interferences and to have an accurate control of the doping. Thus, as was presented before, we deposit ZnO:Al instead of ITO as window layer, and we use CdS (instead the In_2S_3/CdS double emitter) as buffer layer.

3. Results and discussion

In Fig. 1 representative cross-section SEM images of the different layers under study in this work are shown. Our standard CZTSe (undoped) exhibits large grains, with several microns in size, that extends all alongside the cross section as is clearly seen in Fig. 1a, similar to those reported for high efficiency devices in the literature [see for example Refs. [4,15]]. Even after the introduction of small In quantities, some degradation of the grain structure of the absorber is observed. A bi-layer type structure starts to appear, which is mainly composed of larger grains at the top and smaller grains at the bottom. Comparing Fig. 1b–d with Fig. 1a it is evident that the higher the indium concentration, the thicker the bottom layer with small grains and the thinner the up-most layer with big grains. Thus, indium seems to negatively affect the crystallization process, reducing the grain size mainly at the back region, although at the surface also a reduction of the size is clearly observed.

The possible mechanisms behind this degradation are not yet clear, but according to preliminary XRD and Raman analysis the presence of secondary phases is almost unaffected by the indium doping. This is in agreement with the reported phase formation of $Cu_2ZnSnSe_4$–$CuInSe_2$ alloys that have shown a high miscibility in a wide compositional range [19]. We think that this phenomenon is most probably related to modifications of selenium diffusion processes. Following by using TOF-SIMS we will show that indium introduction modifies the alkaline profile, in particular increasing the alkaline concentration at the very surface. The strong interaction of selenium with alkaline elements (mainly sodium and potassium) avoids to some extent the right selenium diffusion towards the back region, impeding its correct crystallization. This

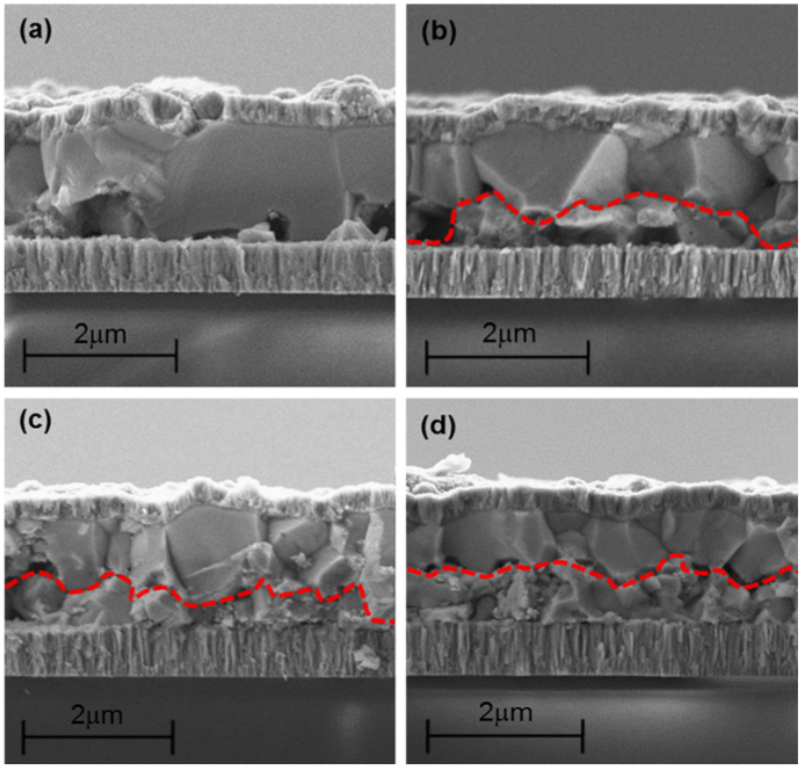

Fig. 1. In-depth SEM images of samples doped with different In quantities: undoped (a), In1 (b), In5 (c) and In10 (d).

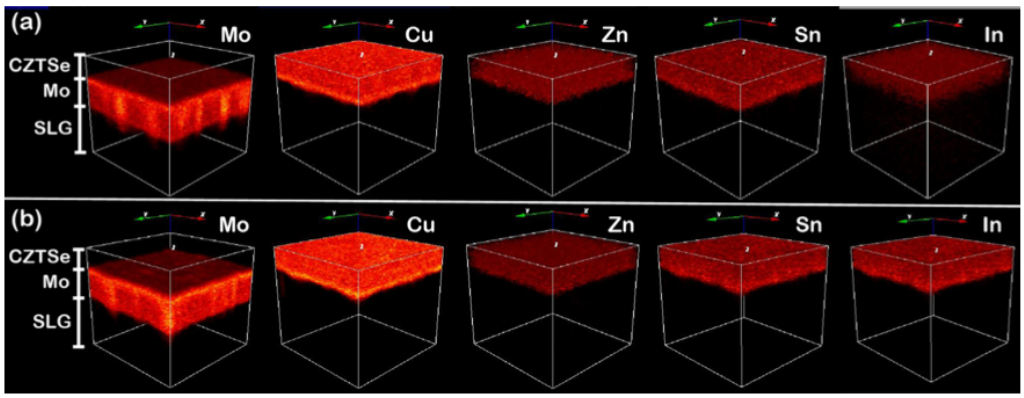

Fig. 2. TOF-SIMS 3D volume maps showing the distribution of Mo, Cu, Zn, Sn and In, for the undoped (a) and In10 (b) samples.

is in agreement with the observed out-diffusion of Se accompanying the out-diffusion of Na [20].

To evaluate whether the In was or not effectively incorporated, together with the corresponding in-depth distribution of this element, TOF-SIMS analysis were performed. Fig. 2 shows the 3D elemental distribution of Mo, Cu, Zn, Sn, and In (see Supporting information for additional 3D TOF-SIMS profiles corresponding to samples with other In concentrations) for undoped, as well as In10 samples. In the Figure, substrate (SLG), back contact (Mo) and absorber (CZTSe) are indicated for better clarity. A rough comparison between the figures suggests that neither Cu, nor Zn and Sn distributions are affected by the presence of In at this concentration levels. The three cations show very similar distribution and intensity as is complementary shown in the Supporting information. Conversely, a large increase in the In concentration is clearly observed in the whole CZTSe volume. The figure also indicates that In is distributed quite uniformly through the whole absorber. This behavior is markedly different than the typical distribution observed for alkaline doping in chalcogenides (mainly Na and K), which use to be accumulated at the interfaces giving a "V" like in-depth profile as has been reported for CIGSe [21]; or even than the Ge reported one which is barely incorporated into the CZTSe matrix due to the inherent volatility of Ge–Se compounds [15].

To better understand this behavior, Fig. 3 shows the 2D TOF-SIMS compositional profiles of In and Na for the different samples. Fig. 3a confirms the effective In incorporation into the CZTSe matrix, with an almost constant in-depth distribution as was predicted with the 3D profiles in Fig. 2. As is expected, TOF-SIMS intensity monotonically increases with the increase of the nominal In doping

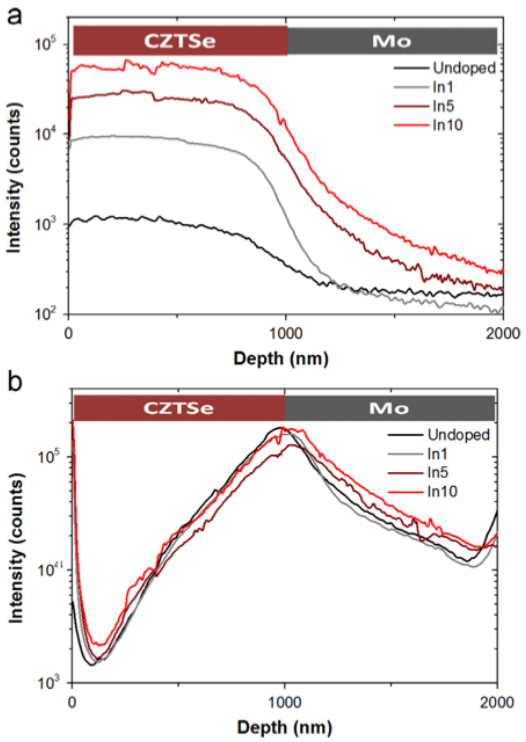

Fig. 3. In (a) and Na (b) TOF-SIMS in-depth profiles of the complete set of samples.

concentration, suggesting that almost all the In was incorporated during the reactive annealing process. Apparently, there is no accumulation of In neither at the surface nor at the back region. As was previously suggested, the dopant is almost no affecting the distribution of Cu, Zn and Sn, at least at this low concentration level (see Supporting information). Due to the importance of Na doping, we have also analyzed the evolution of this element as a function of the In concentration, as is presented in Fig. 3b. In all cases we observe the typical "V" like profile of Na [21], that is not modified by the In incorporation. At this stage, we can conclude that at the back and in the bulk of the material, the Na concentration can be considered independent of the In doping level. Nevertheless, the increase of the In concentration apparently slightly increases the Na content at the very surface. Similar trend is observed for K distribution as is presented in the Fig. S3 of the Supporting information. There is a slight tendency to accumulate more Na (and K) at this interface with the increasing In doping. It is well known that alkaline elements tend to accumulate at the interfaces and grain boundaries [11,12] as is clearly seen in Fig. 3b, that is usually associated with the easily oxidation of these alkaline elements [22]. Thus, we can suppose that the very thin up-most In layer is oxidized and can contribute to the accumulation of Na at the front surface. Also, this suggests that In could be combined with oxygen (note that the In thickness is 10 nm or less, implying a high probability of oxidation), that can have a further impact on the properties of this element as dopant.

Additionally, X-ray diffraction (XRD) of the Ref, In5 and In10 samples was analyzed (see Supporting information) in order to assess the In incorporation into the CZTSe lattice, the evolution of the XRD pattern as a function of In concentration, as well as the possible formation of oxidized species. Indeed, XRD patterns for the In doped samples show a slight shift of the kesterite identified peaks to lower angles, reconfirming the In-incorporation into CZTSe as has been reported previously [19]. Neither remarkable changes in the texture nor in the crystalline quality (estimated by the FWHM of the (112) plane) are observed. Concerning the formation of oxidized species it is very difficult to draw any firm conclusions from this kind of XRD analysis due to the probably rather small quantities of these species present in the material compared to all the bulk kesterite material, though we cannot rule out their formation.

To evaluate the impact of the doping on the optical and electrical properties of the absorber, PL and *C–V* measurements were performed. Fig. 4 presents the room temperature PL spectra of the four samples. The spectrum is characterized by two sub band-gap contributions, a main peak centered at 0.87–0.90 eV that has been attributed to an acceptor defect [22] (probably Cu_{Zn} – [23]) or recombination involving localized states related to QDAP defects [24]; and a second low intensity peak at approximately 0.98 eV, that has been related to shallow defects involving band tails states [24]. The main peak slightly shifts to higher energy only for sample In1, and afterwards, its position is almost constant with the increased In concentration. The slight changes observed in this QDAP emission suggests that In is not affecting significantly the shallow acceptors and donors involved in this transition, i.e. it seems that In is not directly introducing shallow defects. Conversely, the peak at higher energy seems to slightly increase with the In doping level. As was shown, the distribution of Cu, Zn and Sn is almost unaffected by the presence of In. Nevertheless, Na concentration tends to increase at the surface (see Fig. 3b). A sub band-gap band at approximately the same energy than those reported here has been associated to the presence of Na [24], correlating with the increase of the Na content detected by TOF-SIMS. Even though this explanation is based on reported findings that relate this higher PL peak to Na, regarding its origin we cannot exclude that could be also associated with In-related defects, thereby additional investigations will be carried out on this issue. In the end, these observations could imply that Na distribution can be affected by the presence of In, and could be possibly related to the presence of In–O species.

C–V measurements corroborate that the In doping do not have a remarkable impact on the carrier concentration (see Table in Fig. 5), confirming that In seems to not introduce shallow defects easily ionisable at room temperature that can contribute to increase this parameter. In fact, p is in the range of $6–9 \times 10^{16}$ cm^{-3} independently on the nominal In doping concentration. Additionally, using Impedance Spectroscopy measurements we can separate and estimate the grain boundary and grain contributions to the resistance, namely R_{GB} and R_G respectively, as well as the capacitance of the grain boundary (C) [25]. The evolution of all these parameters is presented in the Supporting information. In particular, R_G and C are slightly or even unaffected by the In concentration, correlating with the uniform in-depth distribution of this element and the small variation of the carrier concentration. On the contrary, R_{GB} is strongly affected by the introduction of In, firstly increasing for very small In quantities, and then remarkably decreasing for higher doping levels. We can define a figure of merit (FM) to determine the electrical quality of the grain boundary as the ratio between its ability to conduct charges (i.e. its resistance) and its capacity to store chargers (the capacitance): $FM = R_{GB}/C$. The higher the value of this figure of merit, the smaller the impact of the grain boundaries in the electrical recombination in the layer. Fig. 5 shows the obtained FM values as a function of In concentration. Clearly, the FM follows the same tendency as R_{GB}, increasing for low In doping levels and decreasing then. This suggests that to some extent, when In thickness is equal or higher than 5 nm, the dopant starts to deteriorate the grain boundaries, reducing their resistance and creating shortcuts through the layer for the carriers and thus degrading the F.F. of the device.

To understand the impact of In doping on the device properties, solar cells were prepared with all the absorbers and the results are presented in Fig. 6, including a statistical analysis based in 9 different devices of the efficiency, fill factor (F.F.), open circuit voltage

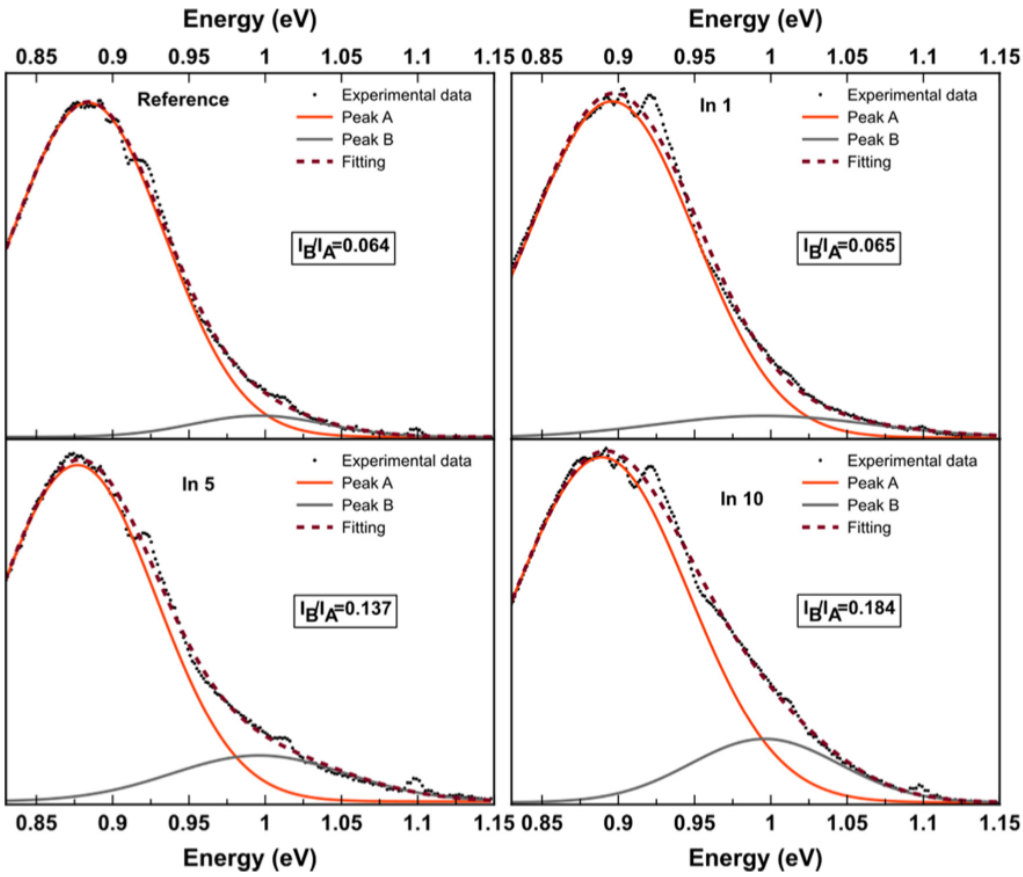

Fig. 4. Room temperature photoluminescence spectra of samples with different In content. The fitting of the PL spectra with two emissions is also displayed, showing the increasing intensity of the peak at higher energy with the increasing In concentration.

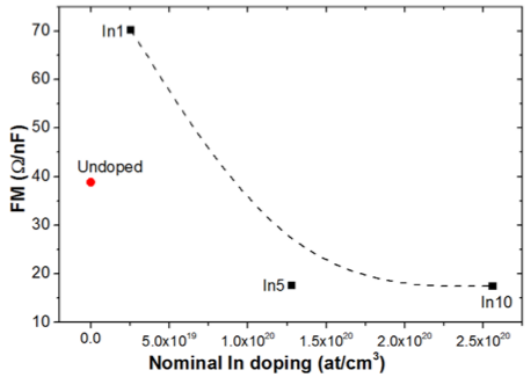

Sample	Nom. [In] (at./cm³)	E_G (eV)	p (cm⁻³)
Undoped	0	0.92	6x10¹⁶
In1	2.6x10¹⁹	0.93	7x10¹⁶
In5	1.3x10²⁰	0.92	9x10¹⁶
In10	2.6x10²⁰	0.92	7x10¹⁶

Fig. 5. Figure of merit obtained from Impedance Spectroscopy for the different samples. The table summarizes the band gap (E_G) and carrier concentration obtained by C–V for the different layers.

(V_{OC}) and short circuit current density (J_{SC}). Representative J–V curves as well as series (R_S) and shunt (R_{Sh}) resistances are presented in the Supporting Information. As is clear from Fig. 6a, the efficiency starts to be deteriorated for In concentration about 1×10^{20} cm^{-3}. This trend is confirmed by both, the evolution of the average as well as the maximum efficiencies obtained for the different experiments. Regarding the other optoelectronic parameters, the F.F. is largely affected by In concentration, in fact this parameter decreases monotonically with the increasing doping level. The V_{OC} of the cells seems to be less affected by the presence of In, being deteriorated by In concentrations as high as 2.6×10^{20} cm^{-3}. Conversely, the J_{SC} seems to be barely affected by the presence of In, and could be considered almost constant in the whole concentrations range. This is in agreement with the R_S and R_{Sh} values presented in the S.I. The series resistance is almost unaffected by the dopant, explaining the low effect on the V_{OC}. Nevertheless, the R_{Sh} is strongly reduced mainly for samples In5 and In10, in close agreement with the diminution of the R_{GB} presented in Fig. 5 and in the S.I., and with the degradation of the F.F. without affecting to a large extent the other optoelectronic parameters. This strongly suggests that In is modifying in somehow the properties of the grain boundaries, affecting mainly the fill factor.

Fig. 7 shows the E.Q.E. of the best cells reported in Fig. 6. At a first glance, all the curves look very similar, in close agreement with almost constant J_{SC} presented in Fig. 6b. But, observing deeply the different wavelength regions, some small differences are detected at low and high wavelength values. The inset presented at the left hand of Fig. 7 shows a small increase of the E.Q.E. values in the 480–600 nm region, i.e. in the region close to the junction. This suggests an improved carrier collection in this region. This can correlates with the increased Na concentration at the surface

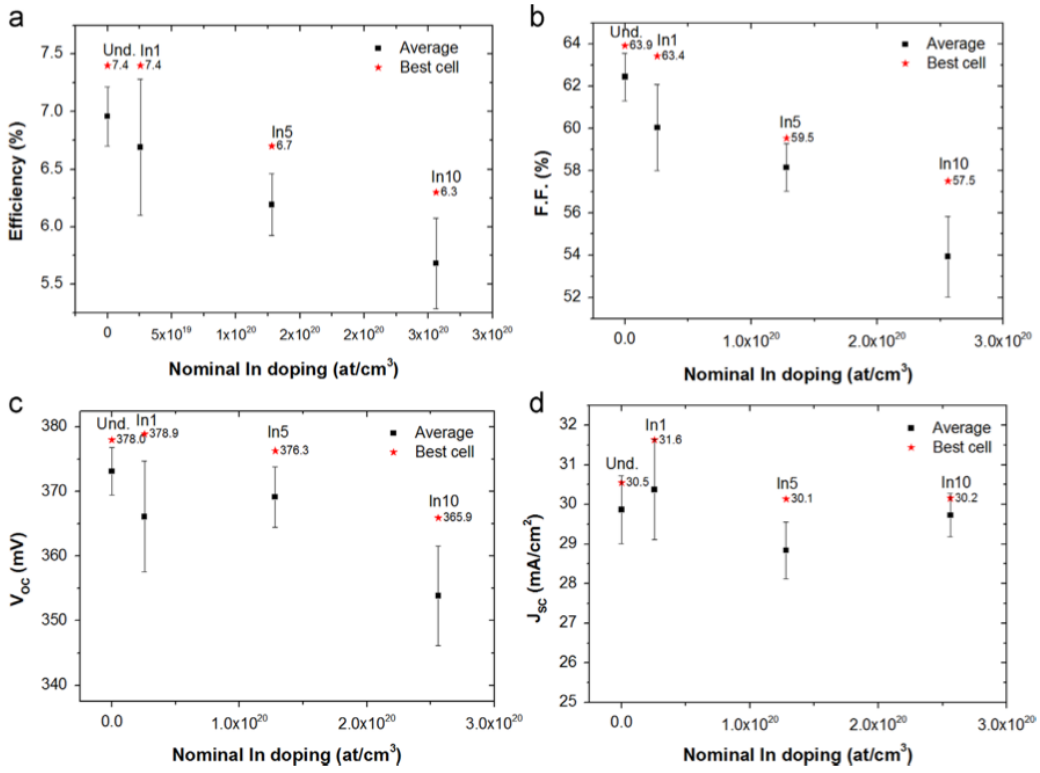

Fig. 6. Evolution of the optoelectronic parameters as a function of the In doping level: conversion efficiency (a), F.F. (b), V_{OC} (c) and J_{SC} (d).

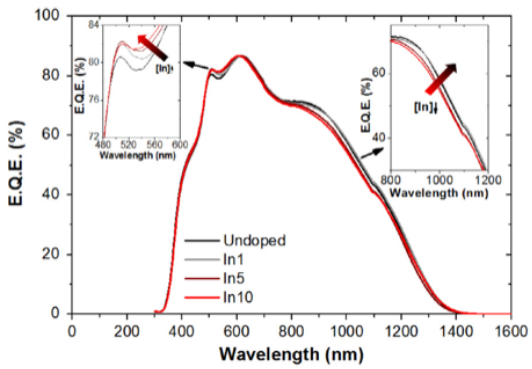

Fig. 7. E.Q.E. spectra of the different devices. Detail of the short and long wavelengths regions of E.Q.E. spectra.

observed by TOF-SIMS that can contribute to keep the V_{OC} almost unaffected for samples In1 and In5, although the properties of the grains and grain boundaries are becoming to be deteriorated. The adequate Na content in the absorber has shown to be very positive for the improvement of the V_{OC} [24–26].

Conversely, as is shown in the right inset of Fig. 7, at large wavelengths the higher the In concentration, the lower the E.Q.E. values. Although the origin can be complex, this can be an indication of a deterioration of the carrier collection properties, probably related to the deterioration of the grain structure as has been presented in Fig. 1. The smaller grains observed by SEM can be at the origin of the E.Q.E. losses in the 800–1200 nm wavelength range. Thus, the balance between the better carrier collection for short wavelengths because the higher Na concentration at the surface and the worse carrier collection for long wavelengths because of the deterioration of the grain structure, can be the explanation for the rather small impact of In doping on the current density of the devices.

To shed light on the peculiar effect of In doping on the optoelectronic parameters of the CZTSe based devices, complementary Kelvin probe atomic force microscopy (KP-AFM) analysis was performed. Fig. 8 shows the AFM images of the surface of In1 and In10 samples (undoped sample behaves very similar to In1), and the corresponding KP-AFM images. The topography of the samples already confirms the results from the SEM analysis, showing big grains for the sample In1, while the surface of In10 is formed by accumulations of small grains. Nevertheless, the most interesting result is given by the surface potential corresponding to these surfaces. While in the sample In1 there is a clear correlation between the presence of grain boundaries and strong potential variations, it is not the case for the In10. These differences in potential with the grain boundaries have always been accounted as one of the main responsibles of the correct performance of thin film polycrystalline solar cells despite their poor structural quality [27]. These results are comparable with the values obtained by Impedance Spectroscopy, where the resistance from the bulk and the grain boundaries are comparable for sample In10; while in the case of In1 the grain boundary resistance was several times higher than the one from the bulk.

Finally, to corroborate the observed effect on the grain boundaries of the In doping, we prepared devices using CZTSe:Ge doped samples. CZTSe:Ge has shown high efficiencies, since Ge doping seems to effectively passivate the grain boundaries giving high R_{Sh} and F.F. values [15]. Fig. 9 presents the illuminated J–V curves for devices prepared with CZTSe:Ge, using a 10 nm Ge superficial layer as is reported in Ref. [15], and by adding also 1 nm, 5 nm and 10 nm of In. The reference cell (only CZTSe with 10 nm of Ge) exhibits a conversion efficiency of 9.1% with a F.F. of 64% and R_{Sh} of 312 Ω cm^2. Once In is introduced, the device properties start to deteriorate. The R_{Sh} is markedly reduced as the

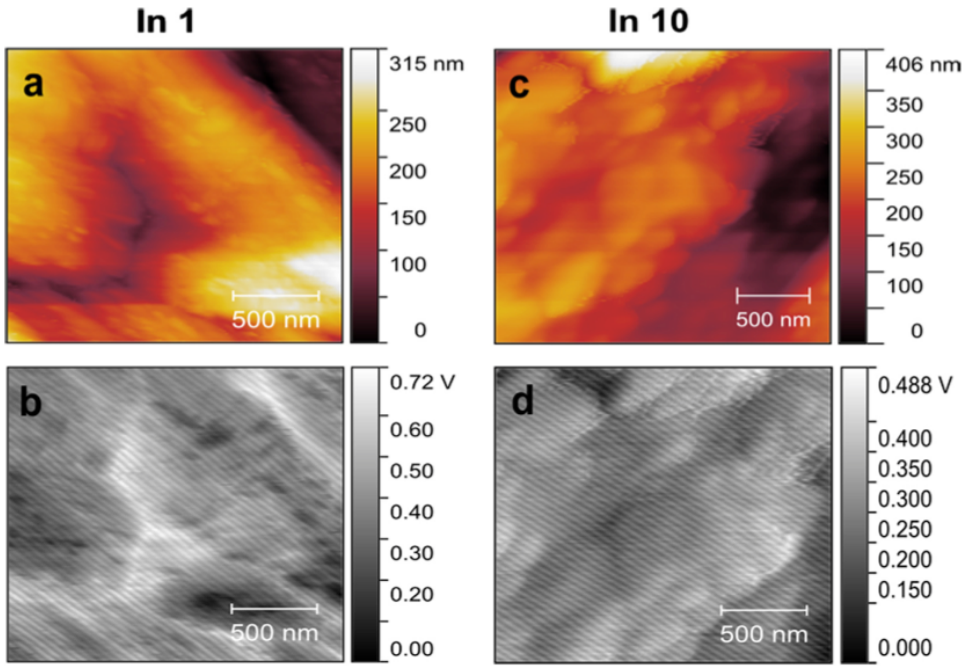

Fig. 8. At the top, topography AFM images for In1 (a) and In10 (c), below the corresponding potential mappings for In1 (b) and In10 (d).

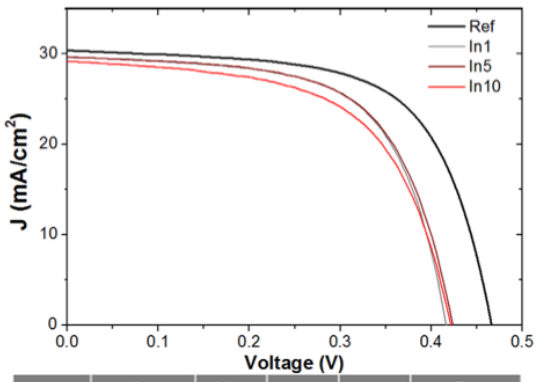

	J_{SC} (mA/cm²)	V_{OC} (mV)	FF (%)	Eff (%)	R_{Sh} (Ohm.cm²)
Ref.	30.3	466	64.1	9.1	312
In1	29.6	416	63.1	7.8	250
In5	29.6	423	62.1	7.8	250
In10	29.1	421	59.3	7.3	188

Fig. 9. *J–V* illuminated curves of CZTSe:Ge devices doped with different In concentrations and the corresponding summary of the optoelectronic properties.

In concentration increases, and concomitantly the F.F. drops. The tendency is very similar to those presented before, corroborating that the In doping seems to deteriorate the grain boundaries properties by the formation of a conductive phase, that mainly affects the R_{Sh} and F.F. of the solar cells.

4. Conclusions

The systematic doping of CZTSe with In was studied at doping levels equal or below 2.6×10^{20} cm^{-3}. CZTSe seems to have a good tolerance to In doping. We clearly demonstrate that In is effectively incorporated into the CZTSe matrix, impacting in the following way in the different properties of the system:

i. *Morphology*: large concentrations of In deteriorate the grain structure, forming a typical bi-layer structure with small grains at the back region.
ii. *Composition*: In is effectively incorporated in the CZTSe matrix and uniformly distributed alongside the thickness. The cationic distribution (Cu, Zn and Sn) is almost unaffected, while In seems to play a role on the Na distribution, observing an accumulation of this alkaline element towards the surface. This can be correlated with the possible oxidized state of the In dopant.
iii. *Optical properties*: at the concentration levels studied in this work, the band gap of the material is not changed at all. Shallow defects analyzed by PL study show that typical DAP defect observed for CZTSe at 0.87 eV is not modified, while an emission at higher energies (1.0 eV approximately) and related with an increased Na content is largely enhanced. This perfectly correlates with the observed TOF-SIMS Na profiles.
iv. *Electrical properties*: carrier concentration is almost constant with the increasing In content, suggesting that either, In forms neutral charged defects and/or complex defects; or In introduces a deep defect that is not significantly ionized at room temperature. Additionally, an increased In concentration seems to deteriorate the grain boundaries properties, making them more conductive.
v. *Optoelectronic properties of devices*: for relatively low In concentrations the conversion efficiency is barely affected, starting to be reduced for concentrations further on 1.2×10^{20} cm^{-3}. This deterioration is mainly explained by large changes in the F. F. of the devices, while the V_{OC} is only affected by high In doping quantities, and the J_{SC} is almost constant with the In concentration. This suggests that the grain boundaries passivation is affecting to a large extent the quality of the devices.
vi. *Grain boundaries properties*: with increasing In doping, the grain boundaries become more conductive, or even change their potential, correlating with the electrical characterization,

and strongly supporting that the deterioration of the device properties for high In doping concentrations is mainly related to the modification of the grain boundaries, by the introduction of a conductive phase.

In summary, CZTSe can tolerate rather high quantities of In without a significant modification of its properties, confirming the possibility of using In containing layers in the CZTSe based devices, like ITO as window and In_2S_3 as buffer layer. If happens, the diffusion of In from this layer can be harmless for the solar cells. We propose that the deterioration of the devices properties for high In concentration levels is due to the presence of a conductive phase at the grain boundaries, that we associate to the formation of SnO_2–In_2O_3 conductive specie. Although In doping seems not to be especially positive for further increasing the solar cells efficiency, this work demonstrates the possibility to safely use In-containing layers in the CZTSe solar cells structure without deteriorating its properties.

Acknowledgments

This research was supported by MINECO (Ministerio de Economía y Competitividad de España) under the SUNBEAM project (ENE2013-49136-C4-1-R) and by European Regional Development Funds (ERDF, FEDER Programa Competitivitat de Catalunya 2007–2013). Authors from IREC and the University of Barcelona belong to the M-2E (Electronic Materials for Energy) Consolidated Research Group and the XaRMAE Network of Excellence on Materials for Energy of the "Generalitat de Catalunya". S.G. thanks the Government of Spain for the FPI fellowship (BES-2014-068533), M.E-R. thanks for the FPI-MINECO (BES-2011-045774), Y.S. for the PTA fellowship (PTA2012-7852-A), M.P. for the MINECO postdoctoral fellow (FPDI-2013-18968), and E.S. for the "Ramón y Cajal" fellowship (RYC-2011-09212). D.C. thanks project KESTCELLS (FP7-PEOPLE-2012-ITN-316488)

Appendix A. Supplementary material

Supplementary data associated with this article can be found in the online version at http://dx.doi.org/10.1016/j.solmat.2016.02.024.

References

[1] S. Siebentritt, S. Schorr, Kesterites—a challenging material for solar cells, Progress Photovolt. Res. Appl. 20 (2012) 512–519.
[2] S. Delbos, Këesterite thin films for photovoltaics: a review, EPJ Photovolt. 3 (2012) 35004.
[3] A. Fairbrother, E. García-Hemme, V. Izquierdo-Roca, X. Fontané, F.A. Pulgarín-Agudelo, O. Vigil-Galán, A. Pérez-Rodríguez, E. Saucedo, Development of a selective chemical etch to improve the conversion efficiency of Zn-rich Cu_2ZnSnS_4 solar cells, J. Am. Chem. Soc. 134 (2012) 8018–8021.
[4] Y.S. Lee, T. Gershon, O. Gunawan, T.K. Todorov, T. Gokmen, Y. Virgus, S. Guha, $Cu_2ZnSnSe_4$ thin-film solar cells by thermal co-evaporation with 11.6% efficiency and improved minority carrier diffusion length, Adv. Energy Mater. 5 (2014) 1401372–1401375.
[5] L. Vauche, L. Risch, Y. Sánchez, M. Dimitrievska, M. Pasquinelli, T. Goislard de Monsabert, P.-P. Grand, S. Jaime-Ferrer, E. Saucedo, 8.2% pure selenide kesterite thin-film solar cells from large-area electrodeposited precursors, Progress Photovolt. Res. Appl. (2015), http://dx.doi.org/10.1002/pip.2643.
[6] J. Kim, H. Hiroi, T.K. Todorov, O. Gunawan, M. Kuwahara, T. Gokmen, D. Nair, M. Hopstaken, B. Shin, Y. Seog Lee, W. Wang, H. Sugimoto, D.B. Mitzi, High efficiency $Cu_2ZnSn(S,Se)_4$ solar cells by applying a double In_2S_3/CdS emitter, Adv. Mater. 26 (2014) 7427–7431.
[7] Z. Tong, C. Yan, Z. Su, F. Zeng, J. Yang, Y. Li, L. Jiang, Y. Lai, F. Liu, Effects of potassium doping on solution processed kesterite Cu_2ZnSnS_4 thin film solar cells, Appl. Phys. Lett. 105 (2014) 223903.
[8] L.Q. Phuong, M. Okano, G. Yamashita, M. Nagai, M. Ashida, A. Nagaoka, K. Yoshino, Y. Kanemitsu, Photocarrier dynamics in undoped and Na-doped Cu_2ZnSnS_4 single crystals revealed by ultrafast time-resolved terahertz spectroscopy, Appl. Phys. Express 8 (2015) 062303.
[9] T. Ma, G. Jiang, W. Liu, C. Zhu, Sodium doping effects on the crystalline and electrical properties of $Cu_2ZnSnSe_4$ thin films, Sol. Energy 115 (2015) 413–418.
[10] H. Zhou, T.-B. Song, W.-C. Hsu, S. Luo, S. Ye, H.-S. Duan, C.-J. Hsu, W. Yang, Y. Yang, Rational defect passivation of $Cu_2ZnSn(S,Se)_4$ photovoltaics with solution-processed Cu_2ZnSnS_4:Na nanocrystals, J. Am. Chem. Soc. 135 (2013) 15998–16001.
[11] R. Caballero, C.A. Kaufmann, T. Eisenbarth, M. Cancela, R. Hesse, T. Unold, A. Eicke, R. Klenk, H.W. Schock, The influence of Na on low temperature growth of CIGS thin film solar cells on polyimide substrates, Thin Solid Films 517 (2009) 2187–2190.
[12] R. Caballero, C.A. Kaufmann, T. Eisenbarth, T. Unold, R. Klenk, H.W. Schock, High efficiency low temperature grown $Cu(In,Ga)Se_2$ thin film solar cells on flexible substrates using NaF precursor layers, Progress Photovolt. Res. Appl. 19 (2011) 547–551.
[13] V. Izquierdo-Roca, R. Caballero, X. Fontané, C.A. Kaufmann, J. Álvarez-García, L. Calvo-Barrio, E. Saucedo, A. Pérez-Rodríguez, J.R. Morante, H.W. Schock, Raman scattering analysis of Cu-poor $Cu(In,Ga)Se_2$ cells fabricated on polyimide substrates: effect of Na content on microstructure and phase structure, Thin Solid Films 519 (2011) 7300–7303.
[14] A.D. Collord, H. Xin, H.W. Hillhouse, Combinatorial exploration of the effects of intrinsic and extrinsic defects in $Cu_2ZnSn(S,Se)_4$, IEEE J. Photovolt. 5 (2015) 288–298.
[15] S. Giraldo, M. Neuschitzer, T. Thersleff, S. López-Marino, Y. Sánchez, H. Xie, M. Colina, M. Placidi, P. Pistor, V. Izquierdo-Roca, K. Leifer, A. Pérez-Rodríguez, E. Saucedo, Adv. Energy Mater. 5 (2015) 1501070.
[16] D.-H. Kuo, M. Tsega, Electrical conduction and mobility enhancement in p-type In-doped $Cu_2ZnSnSe_4$ bulks, Jpn. J. Appl. Phys. 53 (2014) 035801.
[17] M. Neuschitzer, Y. Sanchez, S. López-Marino, H. Xie, A. Fairbrother, M. Placidi, S. Haass, V. Izquierdo-Roca, A. Perez-Rodriguez, E. Saucedo, Progress Photovolt. Res. Appl. 23 (2015) 1660–1667.
[18] M. Neuschitzer, Y. Sánchez, T. Olar, T. Thersleff, S. López-Marino, F. Oliva, M. Espíndola-Rodríguez, H. Xie, M. Placidi, V. Izquierdo-Roca, I. Lauermann, K. Leifer, A. Pérez-Rodríguez, E. Saucedo, Chem. Mater. 27 (2015) 5279–5287.
[19] S. Hartnauer, L.A. Wägele, E. Jarzembowski, R. Scheer, In-situ XRD study of alloyed $Cu_2ZnSnSe_4$–$CuInSe_2$ thin films for solar cells, Thin Solid Films 582 (2015) 272–275.
[20] D. Braunger, D. Hariskos, G. Bilger, U. Rau, H.W. Schock, Influence of sodium on the growth of polycrystalline $Cu(In,Ga)Se_2$ thin films, Thin Solid Films 361–362 (2000) 161–166.
[21] A. Rockett, J.S. Britt, T. Gillespie, C. Marshall, M.M. Al Jassim, F. Hasoon, R. Matson, B. Basol, Na in selenized $Cu(In,Ga)Se_2$ on Na-containing and Na-free glasses: distribution, grain structure, and device performances, Thin Solid Films 372 (2000) 212–217.
[22] M. Grossberg, J. Krustok, K. Timmo, M. Altosaar, Radiative recombination in $Cu_2ZnSnSe_4$ monograins studied by photoluminescence spectroscopy, Thin Solid Films 517 (2009) 2489–2492.
[23] E. Kask, M. Grossberg, R. Josepson, P. Salu, K. Timmo, J. Krustok, Defect studies in $Cu_2ZnSnSe_4$ and $Cu_2ZnSn(Se_{0.75}S_{0.25})_4$ by admittance and photoluminescence spectroscopy, Mater. Sci. Semicond. Process. 16 (2013) 992–996.
[24] T. Gershon, Y.S. Lee, R. Mankad, O. Gunawan, T. Gokmen, D. Bishop, B. McCandless, S. Guha, The impact of sodium on the sub-bandgap states in CZTSe and CZTS, Appl. Phys. Lett. 106 (2015) 123905.
[25] A.S. Gilmore, Studies of the Basic Electronic Properties of CdTe Thin Films and Completed CdTe/CdS Solar Cells (Ph.D. thesis), Colorado School of Mines, USA, 2003.
[26] J.V. Li, D. Kuciauskas, M.R. Young, I.L. Repins, Effects of sodium incorporation in co-evaporated $Cu_2ZnSnSe_4$ thin-film solar cells, Appl. Phys. Lett. 102 (2013) 163905.
[27] I. Visoly-Fisher, S.R. Cohen, K. Gartsman, A. Ruzin, D. Cahen, Understanding the beneficial role of grain boundaries in polycrystalline solar cells from single-grain-boundary scanning probe microscopy, Adv. Funct. Mater. 16 (2006) 649–660.

SUPPORTING INFORMATION

Optical and electrical properties of In-doped $Cu_2ZnSnSe_4$

S. Giraldo[1]*, C.M. Ruiz[2], M. Espíndola-Rodríguez[1], Y. Sánchez[1], M. Placidi[1], D. Cozza[2], D. Barakel[2], L. Escoubas[2], A. Pérez-Rodríguez[1,3], E. Saucedo[1]

[1] Catalonia Institute for Energy Research (IREC), Jardins de les Dones de Negre 1, 2pl, 08930 Sant Adrià de Besòs, Spain

[2] Aix-Marseille University - IM2NP, CNRS (UMR 7334), France

[3] IN2UB, Universitat de Barcelona, C. Martí Franquès 1, 08028 Barcelona, Spain

* Corresponding author e-mail: sgiraldo@irec.cat

In the manuscript, 3D TOF-SIMS profiles of undoped and In10 samples were shown. Figure S1 shows the corresponding ones to samples In1 and In5, corroborating the negligible impact of In doping on the Cu, Zn and Sn distribution, as well as the increasing In concentration on the layer as was demonstrated in the Figure 3a of the manuscript.

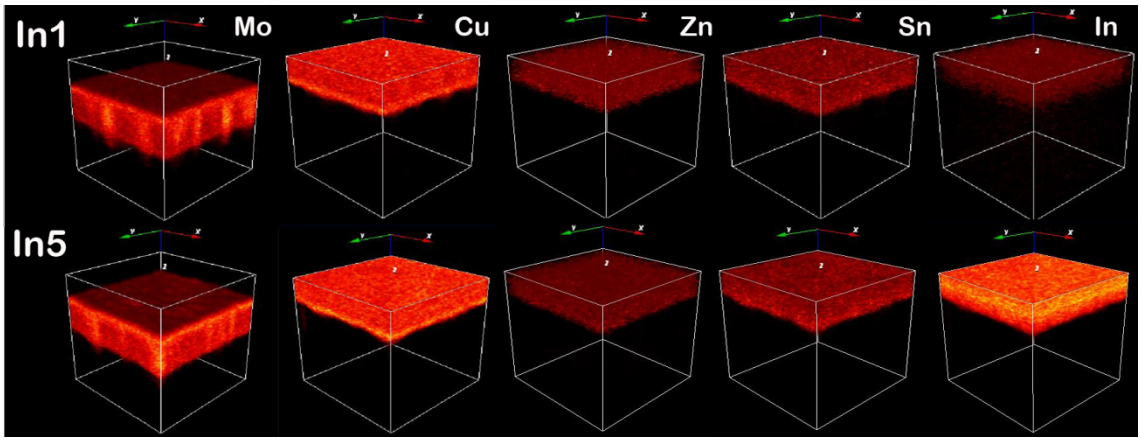

Figure S1. TOF-SIMS 3D volume maps showing the distribution of Mo, Cu, Zn, Sn and In, for the In1 (a) and In5 (b) samples.

To better support that the introduction of In in the CZTSe lattice does not modify the distribution of the other elements, Figure S2 shows the 2D profiles of Cu, Zn and Sn. Clearly, the variation of the 3 cations profile could be considered negligible, and any special trend is observed, corroborating that In in such low concentration is not affecting in principle the macroscopic composition distribution of the main elements.

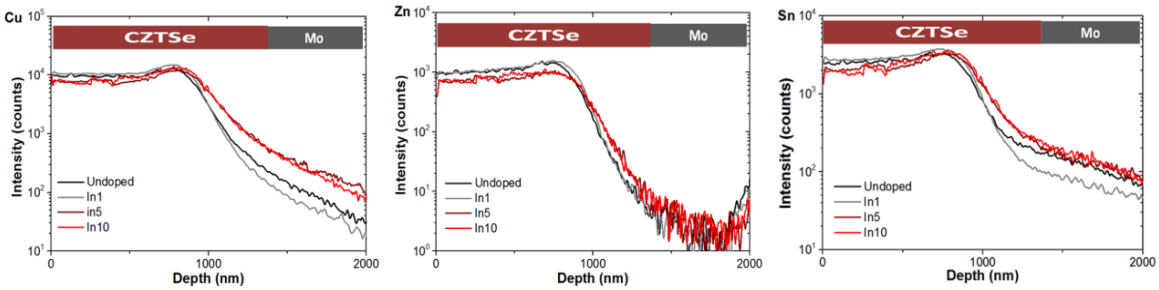

Figure S2. TOF-SIMS in-depth profiles of Cu, Zn and Sn, for undoped, In1, In5 and In10 samples.

Additionally, K distribution along the absorber layer is analysed in Figure S3 showing an increasing tendency of this element close to the CZTSe/CdS interface. As was explained in the manuscript, the presence of alkaline elements like K and Na has been associated with the presence of its oxidized related compounds, being an indirect method to confirm the possible presence of higher oxygen concentrations with increasing In doping.

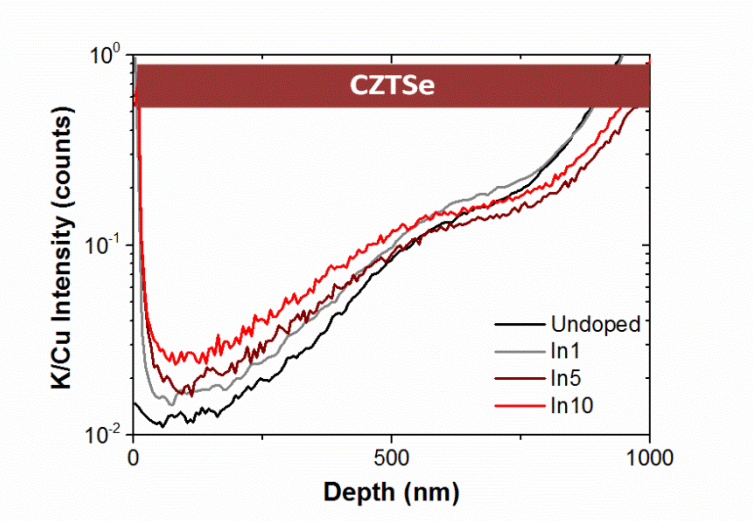

Figure S3. TOF-SIMS in-depth profiles of K/Cu for undoped, In1, In5 and In10 samples.

In order to assess structural changes because of the In incorporation as well as detect the presence of possible oxidised species, Figure S4 shows the XRD patterns of the Ref, In5 and In10 samples. As is clearly observed there is a small shift towards lower angles of the kesterite identified peaks for the doped samples, corresponding to the In-incorporation in the lattice (as has been demonstrated in the manuscript). The relative intensity of the diffraction peaks corresponding to the CZTSe kesterite phase is unaffected by the presence of In. Additionally, by fitting the (112) of the CZTSe phase (using Gaussian fit), we estimate the FWHM obtaining the following values: 0.069° (Ref), 0.067° (In5) and 0.066° (In10). This suggests that the In incorporation, at least at the level used in this work, is not modifying the crystalline quality of the CZTSe main phase. Nevertheless, concerning the formation of additional oxidised phases it is very difficult to detect since the quantity of these species present in the material compared to all the kesterite bulk kesterite material is very low, though we cannot rule out their formation.

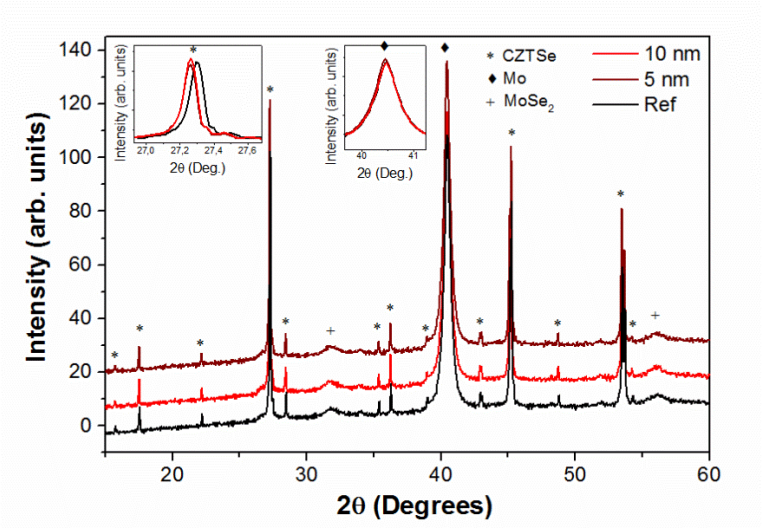

Figure S4. XRD pattern of the Ref, In5 and In10 samples.

Figure of merit defined in the manuscript after the C-V characterization was obtained through the determination of grain boundaries and grain resistance, as well as grain boundaries capacity. As is observed, the bulk resistance and the grain boundaries capacitance are slightly affected by the presence of the dopant. Conversely, grain boundaries resistance is severely affected by the introduction of In, decreasing by a factor of 2 for high In concentrations.

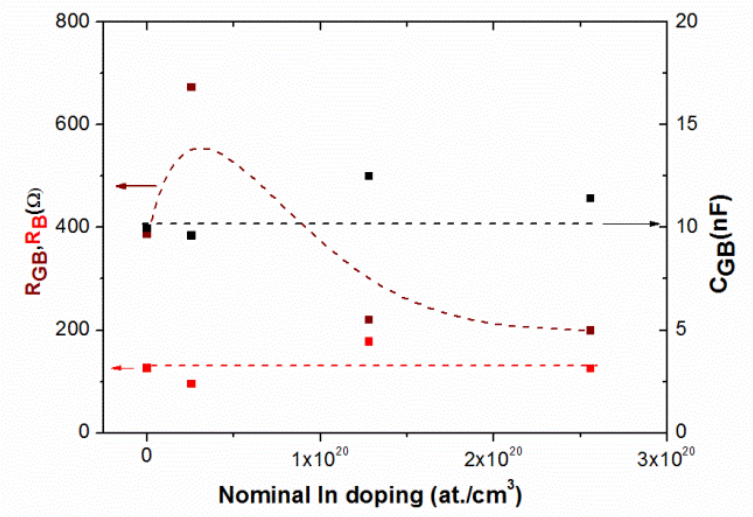

Figure S5. Evolution of the rain boundary resistance (R_{GB}), the bulk resistance (R_B) and the grain boundaries capacitance (c_{GB}), with the In concentration.

Figure S6 shows the J-V illuminated curves for the best cells obtained for each doping level. As is clear, mainly the V_{OC} and the F.F. are deteriorated with the increasing In concentration. In Table S1, we summarize the shunt resistance (R_{SH}) and series resistance (R_S) of the same devices. In agreement with the CV and the AFM potential mappings presented in the manuscript, while the series resistance of the devices is almost unaffected, the shunt resistance decreases significantly for high doping concentrations, supporting that the deterioration is related to some modification mainly at the grain boundaries.

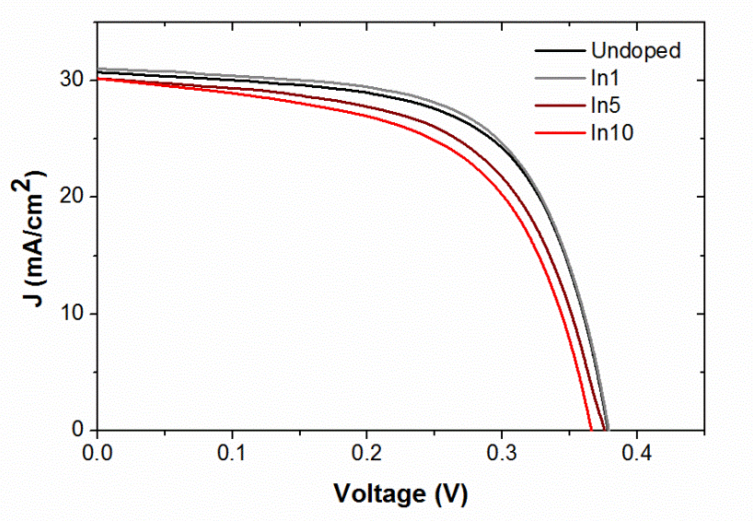

Figure S6. J-V illuminated curves of the best cells presented in Figure 6 of the manuscript.

Table S1. Summary of the shunt and series resistance of the devices presented in Figure S6 of the S.I. and Figure 6 of the manuscript.

Sample	R_{SH} ($\Omega.cm^2$)	R_S ($\Omega.cm^2$)
Undoped	176	0.2
In1	206	0.3
In5	136	0.3
In10	84	0.4

Materials Views
www.MaterialsViews.com

ADVANCED ENERGY MATERIALS
www.advenergymat.de

COMMUNICATION

Large Efficiency Improvement in $Cu_2ZnSnSe_4$ Solar Cells by Introducing a Superficial Ge Nanolayer

*Sergio Giraldo, Markus Neuschitzer, Thomas Thersleff, Simón López-Marino, Yudania Sánchez, Haibing Xie, Mónica Colina, Marcel Placidi, Paul Pistor, Victor Izquierdo-Roca, Klaus Leifer, Alejandro Pérez-Rodríguez, and Edgardo Saucedo**

As the knowledge on kesterite photovoltaic absorbers increases, the factors limiting the efficiency of solar cells based on this family of materials become more and more evident.[1] Comparing the best efficiencies obtained using $Cu_2ZnSn(S,Se)_4$ (CZTSSe) as absorber with more mature CdTe and $Cu(In,Ga)Se_2$ (CIGSe) technologies, it is clear that the voltage deficit is the major challenge that kesterite devices have to face in the near future.[2] Recently, the pure selenide $Cu_2ZnSnSe_4$ (CZTSe) compound has demonstrated efficiencies exceeding 11%, with an open circuit voltage (V_{OC}) of 423 mV.[3] Commonly, the highest efficiencies were reported for kesterites with Se-rich sulfo-selenide solid solutions, which generally lead to a higher V_{OC}. This highlights the importance to identify and reduce the voltage losses for these materials.[2,4] In this sense, and with the aim to solve the inherent problems of kesterites, the substitution of cations has been explored to some extent.[5–8] In particular, Sn exhibits an intrinsic multicharge character and thus the Sn-site substitution is probably the most interesting.[5,9] This is because multicharge atoms commonly introduce deep defects that increase the nonradiative charge carrier recombination. This has an especially severe impact on the degradation of V_{OC}.[5,9]

For this reason, one of the most interesting approaches is to substitute Sn by other cations such as Ge. By alloying CZTSe with Ge, the band gap can be tuned from 1.0 (pure Sn/Zn kesterite) to 1.35 eV (pure Ge/Zn kesterite).[10,11] Additionally, several other beneficial effects have been associated with the use of Ge, such as the increase of carrier lifetime and the suppression of Sn^{+2} state formation.[5,6] Nevertheless till now, the use of Ge has demonstrated rather limited device improvements with respect to the pure Sn kesterite. Furthermore, all reports published so far are based on the use of large Ge amounts, which may compromise the viability of this technological approach, as Ge has been identified not only as a critical raw material with an earth crust abundance about 1.6 ppm, but also as a scattered material disabling the extraction by mining.[12] For example, Kim et al. reported an increase in the device efficiency from 4.6% to 6.0% using a graded band gap by alloying Cu_2ZnSnS_4 with Ge, observing a Ge/(Sn+Ge) ratio about 0.50 at the surface and an almost pure Ge phase at the back.[7] The efficiency improvement is mainly explained by an increase in the J_{SC}, and the reported values are far from the state-of-the-art efficiencies reported for kesterite solar cells. Bag et al. reported the Ge substitution in CZTSe solar cells too, obtaining a rather small efficiency improvement (from 9.07% for the pure Sn kesterite to 9.14% for the Sn–Ge alloyed with 40% of Ge), but observing a remarkable increase in V_{OC} of more than 50 mV.[5] Finally, Hages et al. reported an improved performance of Ge-alloyed $Cu_2Zn(Sn,Ge)(S,Se)_4$ solar cells, increasing the efficiency from 8.4% (no Ge) to 9.4% (with 30% of Ge), mainly explained by an increase of 50 mV in V_{OC}.[6] This shows that till now although very promising, attempts of alloying kesterite with large amounts of Ge have demonstrated rather small improvements in the solar cell performance.

In this work, we report a breakthrough in kesterite-based technologies. We demonstrate that high-voltage and high-efficiency devices can be easily achieved using small quantities of Ge, leading to efficiencies higher than 10%. The Ge-based approach presented here is based on the evaporation of a 10 nm thick Ge layer on top of the Cu/Sn/Cu/Zn metallic precursor stack prior to the selenization step, using a sequential process to synthesize CZTSe absorbers.[13] As will be shown later, this leads to a substitution of less than 1.6% of Sn in the final kesterite structure, ensuring the sustainability of the developed processes.

To analyze the impact of Ge on the optoelectronic properties of the devices, in the following we first present the impact of the superficial Ge nanolayer on the device parameters in a *J–V* and external quantum efficiency (EQE) comparison. The morphology, elemental composition, and distribution of the resulting absorber layers will be evaluated by scanning electron microscopy (SEM), by time-of-flight secondary ion mass spectroscopy (TOF-SIMS), and by combining transmission electron microscopy (TEM) with electron energy loss spectroscopy (EELS). Finally, in the Supporting Information, we present a

S. Giraldo, M. Neuschitzer, S. López-Marino, Y. Sánchez, H. Xie, Dr. M. Colina, Dr. M. Placidi, Dr. P. Pistor, Dr. V. Izquierdo-Roca, Prof. A. Pérez-Rodríguez, Dr. E. Saucedo
Catalonia Institute for Energy Research, (IREC)
Jardins de les Dones de Negre 1
08930, Sant Adrià de Besòs, Barcelona, Spain
E-mail: esaucedo@irec.cat
Dr. T. Thersleff, Prof. K. Leifer
The Ångström Laboratory
Department of Engineering Sciences
Uppsala University
Box 534, 75121, Uppsala, Sweden
Prof. A. Pérez-Rodríguez
IN2UB
Universitat de Barcelona
c. Martí i Franquès 1, 08028 Barcelona, Spain

DOI: 10.1002/aenm.201501070

ADVANCED ENERGY MATERIALS
www.advenergymat.de

www.MaterialsViews.com

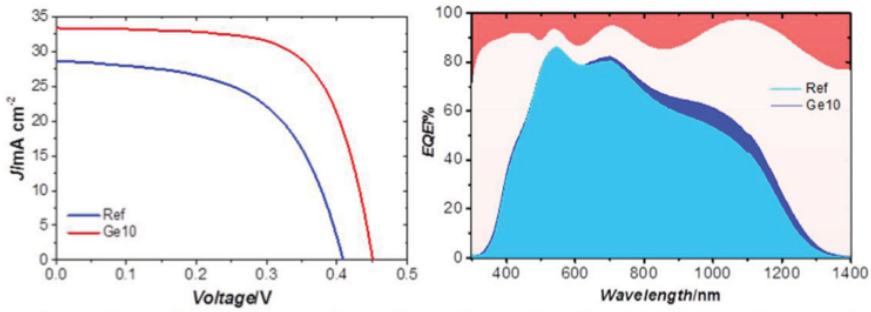

Sample	V_{OC} /mV	J_{SC} /mA cm^{-2}	FF/%	Eff/%	R_s /Ω cm^2	R_{sh} /Ω cm^2	A	J_0 /mA cm^{-2}	E_G/eV	$E_g q^{-1} - V_{OC}$ /eV
Ref	408	29.1	59.2	7.0	0.23	265	1.86	9.9x10^{-3}	1.04	0.632
Ge10	453	33.3	66.8	10.1	0.52	712	1.70	6x10^{-4}	1.04	0.587

Figure 1. *J–V* curves and the corresponding optoelectronic parameters of reference and Ge10 solar cells (left), and EQE plot of both samples (right). In the EQE plot, the upper orange area represents the reflectance of both solar cells.

detailed characterization of the back and front surfaces of the CZTSe absorbers with and without Ge layer by Raman spectroscopy, and of the surface with X-ray photoemission spectroscopy (XPS).

Figure 1 (left) presents the *J–V* illuminated curves of the reference cell (Sn-pure CZTSe) and those produced introducing a 10 nm thick Ge layer on top of the precursor (Ge10) as is described in the Experimental Section. This corresponds to a Ge/(Ge+Sn) ratio of 0.044, i.e., a 4.4% of nominal Sn substitution by Ge. In the right-hand side of Figure 1, the corresponding EQE is plotted, including the reflectance of the complete devices. Notably, the efficiency increases from 7% (reference CZTSe) to 10.1% (Ge10) representing the highest efficiency reported till now for a Ge-containing cell, with a remarkable improvement of all the optoelectronic parameters (see the table in Figure 1). In fact, the maximum efficiency was achieved with a 10 nm thick Ge nanolayer on top, but the whole range between 0 and 25 nm has been explored in a first optimization as is presented in the Supporting Information. It is important to remark the large improvement in V_{OC}, from 409 mV for the reference cell to 453 mV for the record one, although some cells produced in other rounds have achieved a V_{OC} as high as 469 mV (with efficiencies easily exceeding 9.5%, see Tables S1 and S2 and Figure S1 in the Supporting Information, which include the best, average, and standard deviation of the most relevant optoelectronic parameters). Additionally, the J_{SC} exhibits a slight increase while the fill factor (F.F.) and the shunt resistance (R_{SH}) are remarkably increased. This implies that the Ge incorporation in rather small quantities into the CZTSe matrix has an unexpected complex behavior, impacting on several properties of the material.

To better support the electrical characterization of the devices, the dark *J–V* curves were also analyzed and the diode quality factor (A) and reverse saturation current (J_0) were extracted, together with the band gap E_G and the ($E_G/q - V_{OC}$) parameters. As is clear, the addition of the Ge superficial nanolayer improves both diode parameters, indicating that the quality of the p–n junction was improved and the carrier recombination in the Ge10 device reduced. It is important to remark that a deep electrical characterization of the samples is being performed and will be reported elsewhere, but preliminary results including V_{OC} versus temperature plots show that for both, reference and Ge10 devices, the activation energy (E_a) of this plot is closer to the determined band-gap values. This suggests that the device properties are mainly controlled by bulk recombination, and that the addition of Ge is probably reducing it. Additionally, the carrier density seems not to be affected by the presence of Ge at this level and is about 4–6 × 10^{16} cm^{-3} for reference and Ge10 samples.

The improvements in the photogenerated current collection are also reflected in the EQE spectra as are shown in Figure 1. The EQE is almost unaffected in the 300–620 nm wavelength region being markedly higher for longer wavelengths, indicating an enhanced collection of charge carrier generated deep within the absorber.[14] Additionally, the E_G of the absorbers was estimated with the EQE by the derivative method (see Figure 1 and Table S1 in the Supporting Information). Clearly, the band gap is unaffected by Ge, but we must consider that with these measurements only the effective minimum E_G is proved. Complementary PL measurements were performed as is shown in Figure S2 in the Supporting Information, showing no changes in the PL spectra in agreement with the almost constant band gap estimated by EQE. Finally, the $E_G/q - V_{OC}$ (voltage deficit) is also presented, where it is clear that the voltage deficit is reduced for the Ge10 device. In fact, we estimate a value of the voltage deficit of 587 mV, comparable or even better than the best results reported in the literature for the record devices.[3,13] Although the origin can be complex, we expect this to be related to an increased diffusion length due to an improved crystalline quality. The questions now are (i) where is the Ge located? and (ii) why can such low amount of Ge lead to this large efficiency improvement?

To evaluate the presence of Ge in the absorber, we performed TEM and SEM studies. Left-hand side of **Figure 2** presents the High-Angle Annular Dark-Field (HAADF; Z-contrast) overview of a lamella produced from the Ge10 sample, together with an enlargement of nanoscale features observed in the bulk. After a careful compositional analysis of several representative areas of the lamella (including back and surface interfaces and grain boundaries) with EELS, neither at the surface nor at the back

Materials Views
www.MaterialsViews.com

ADVANCED ENERGY MATERIALS
www.advenergymat.de

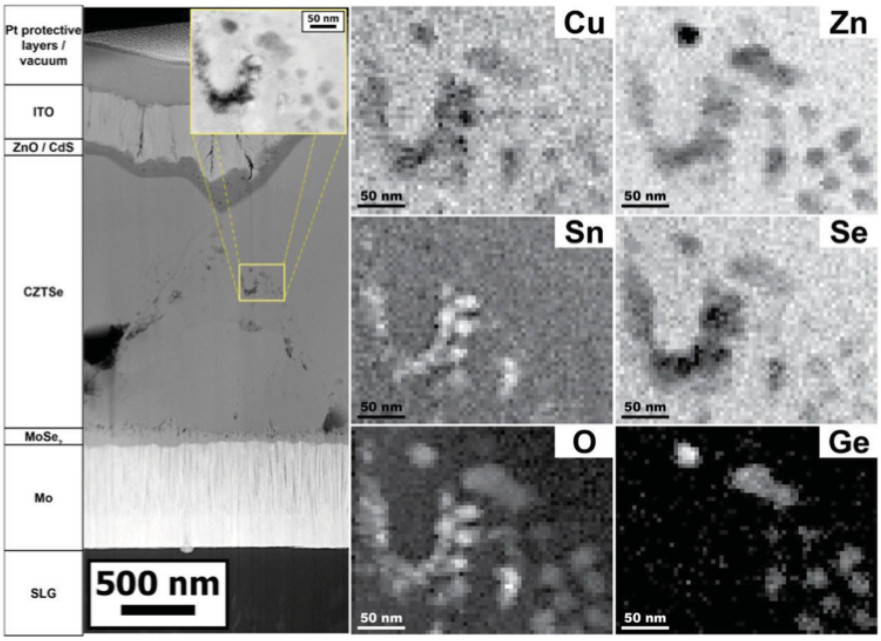

Figure 2. TEM/EELS analysis of Ge10 sample. High-Angle Annular Dark Field (HAADF; Z-contrast) overview of the lamella (left hand). EELS analysis of the nanostructures observed in the TEM image, including the signal of Cu, Zn, Sn, Se, O, and Ge (right hand).

of the CZTSe absorber was Ge detected. Based on the experimental parameters, scattering cross-sectional shape, and equipment used for this experiment, we estimate that the minimum atomic fraction of Ge necessary for detection would be 0.2%, corresponding to a Ge/(Ge+Sn) ratio of 1.6%.[16,17] This is significantly smaller than the 4.4% ratio in the initial precursors. Thus, the V_{OC} increase (up to 469 mV as is shown in the Supporting Information) is even more impressive taking into account that the absorber can be considered almost Ge-free $Cu_2ZnSnSe_4$. This leads to the conclusion that the V_{OC} increase is not related to a band-gap increase at the surface as was originally assumed.

Analyzing the lamella in detail, we found that the CZTSe absorber layer exhibits an unexpected substructure. This substructure consists of a large number of nanoscale inclusions of a very different chemical composition. These show up as regions of different intensity level in the HAADF (Z-contrast) overview image presented in Figure 2. These inclusions appear to be on the order of 1–10 nm in diameter and are concentrated around the CZTSe grain boundaries, but it is important to note that some of them were found embedded within large grains as well (it is important to remark that these inclusions are also observed in samples with higher Ge quantities). A more detailed EELS analysis of these nanostructures is presented in the right-hand part of Figure 2. Clearly, these inclusions are formed by two types of materials. First, GeO_x inclusions with a diameter ranging from some 2 to 5 nm are identified, being the only EELS evidence of the presence of Ge in the layer (see Figure S3 in the Supporting Information for a detailed description of the evaluation of the nanostructures). Intriguingly, these GeO_x inclusions appear to be Sn-neutral with respect to the bulk, while they are also clearly Cu, Zn, and Se-poor. On the other hand, SnO_2 inclusions are also observed in the neighboring areas.

Figure 3 shows comparative cross-sectional SEM images of reference and Ge10 solar cells, where large grains and reduced density of grain boundaries are observed in the later. It is important to highlight that these samples are representative for both processes, and were selected among several cross-sectional studies (see also Figure S4 in the Supporting Information), supporting the observed improvement of the crystalline quality for the Ge containing samples. To understand this behavior, we consider the complex Ge–Se phase diagram. Under the conditions used in our reactive thermal annealing (P = 1 bar, T = 550 °C), we expect the Ge precursor layer to form a Ge_3Se_7 phase which melts incongruently at 385 °C and is decomposed into a volatile $GeSe_2$ and a liquid phase with high selenium content (≈85 at% of Se).[18] The liquid phases can assist the crystal growth which offers an explanation for the enlarged grains observed by SEM. The lower density of grain boundaries and associated defects in turn might contribute to a general reduction of recombination paths and an improvement in the solar cell performance. The formation of a volatile $GeSe_2$ phase would lead to a Ge loss as is observed, similar to the well-documented Sn loss in kesterite.[19]

The following reaction is then proposed to explain both the crystallization assisted for a Ge liquid phase and the already observed Ge loss:

$$3Ge_{(s)} + 7/2Se_{2(g)} \leftrightarrow Ge_3Se_{7(s)} \xrightarrow{*} GeSe_{2(g)} + Ge_xSe_{y(l)}\,(\sim 85\ \text{at.\%}\ Se) \quad (1)$$

Equation (1) is a proposed reaction for the formation of a Ge–Se volatile specie ($GeSe_2$) plus a Se-rich liquid phase that

ADVANCED ENERGY MATERIALS
www.advenergymat.de

www.MaterialsViews.com

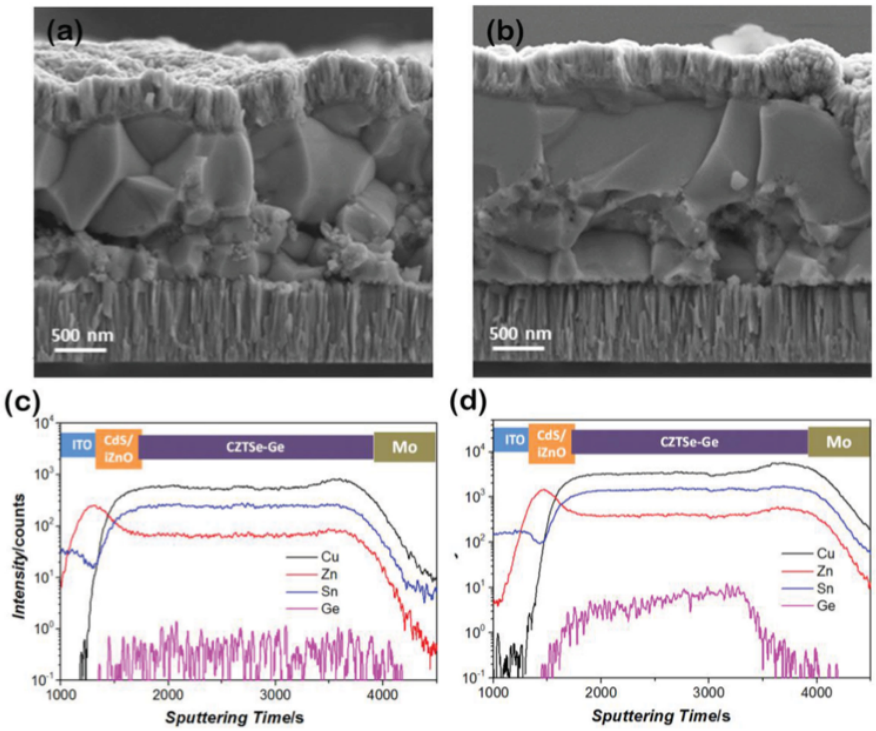

Figure 3. Comparative cross-sectional SEM views of a) reference and b) Ge10 samples. TOF-SIMS profile of c) reference and d) Ge10 samples, showing the metallic in-depth distribution.

assists the absorber crystallization. Note that the last equation is not balanced (indicated by the *).

Figure 3 also presents TOF-SIMS in-depth profiles of reference and Ge10 samples, confirming the very low Ge concentration throughout the absorber thickness. In particular, the comparison of both samples shows that Cu, Zn, and Sn profiles are practically unaffected by the presence of Ge. Apparently, the rather small nominal concentrations used in this work are insufficient to modify the distribution of the cations. According to the TOF-SIMS results, the low Ge signal is mainly concentrated in the top-half part of the sample in agreement with the TEM analysis, which shows that most of the GeO_x nanoinclusions are also in the upper part. In the bottom-half part of the sample, the Ge signal is reduced to the noise level. The Ge amount in the reference sample is below the detection limit.

In addition, a structural analysis of the front and back regions was carried out with Raman spectroscopy, which is sensitive to detect little amounts of Ge in the structure (Figure S5 in the Supporting Information).[20,21] As is observed, the main A^1 mode at the surface region of the Ge10 sample is only slightly blueshifted with respect to the reference sample by only 0.26 cm^{-1}. This shift can be originated by either rather small Ge quantity incorporation in the lattice or the improvement of the crystalline quality.[21,22] By supposing that the shift is completely related to the Sn substitution by Ge, the Ge/(Ge+Sn) ratio in the surface region can be estimated to be lower than 2%. Despite the low Ge incorporation, the decreased full width at half maximum (FWHM) of the A^1 modes recorded at the surface clearly evidences the increased crystalline quality of Ge10. In fact, the observed blueshift of the A^1 mode for the Ge10 sample could also be interpreted as a result of a reduction of the crystal lattice disorder.[22]

The situation is markedly different at the back region of both samples, where very similar Raman shift and FWHMs are obtained suggesting that the Ge surface approach has a limited impact on this region. In fact, combining SEM and TEM analysis we estimate that the $MoSe_2$ thickness is about 80–100 nm independently of the Ge quantity used as capping nanolayer. We therefore conclude that the most important changes introduced by the Ge addition are located at the surface and in the near bulk.

Finally, in the Supporting Information, a preliminary XPS characterization of reference and Ge10 absorbers is presented (see Figure S6) in order to evaluate the impact of the Ge nanolayer on the Sn^{+2} and Sn^{+4} valence state formation.[23] Our first results show a clear shift of the Sn3d5 peak toward higher binding energies when Ge is introduced, suggesting that the Sn^{+4} oxidation state prevails over Sn^{+2}. This strongly supports that the presence of Ge prevents to some extent the formation of reduced Sn species like Sn^{+2}, which could be detrimental for the solar cell performance.[6]

In summary, we report here a breakthrough in the kesterite solar cell technology based on the introduction of a nanometric Ge layer, which dramatically improves the solar cell efficiency, from 7% for the reference sample (Ge-free) to 10.1% with an optimized Ge quantity. With a detailed compositional and

www.MaterialsViews.com

ADVANCED ENERGY MATERIALS
www.advenergymat.de

structural characterization, we demonstrate that surprisingly Ge is barely incorporated into the CZTSe layer, and propose a mechanism how Ge might assist the crystallization via the formation of a liquid phase. A large amount of Ge is expected to be re-evaporated during the decomposition of the Ge_3Se_7 phase. Despite the Ge loss, the remarkable improvement of the device performance can be explained by one or several of the following reasons:

1. The formation of Ge_3Se_7 phase that incongruently decomposes into volatile $GeSe_2$ and a Se-rich liquid phase which assists the crystallization of CZTSe, improving the crystalline quality and helping to obtain large grains.
2. The presence of Ge reduces the probability of formation of Sn-reduced species like Sn^{+2} that are commonly associated with deep defects that deteriorate the cell voltage, as is suggested by preliminary XPS analysis.
3. The only evidence we found for an incorporation of Ge into the CZTSe absorber is the presence of GeO_x nanoinclusions inserted in the grains bulk, apparently associated with the formation of SnO_2 inclusions as well. Although we are analyzing the impact of these nanoinclusions, one hypothesis under study is that these structures might act as electron back reflectors, which might largely enhance the voltage of the solar cells.

Further investigations on the origin of these effects are currently underway applying advanced characterization methodologies. This communication demonstrates that the application of rather small quantities of Ge onto the CZTSe precursors dramatically increases the voltage and the efficiency of the resulting devices. This opens new paths to strongly reduce the voltage deficit problem of kesterite solar cells, since this methodology can be applied to many different process technologies, leading the way toward high-efficiency devices.

Experimental Section

CZTSe Absorber Synthesis: CZTSe films were prepared by a sequential process onto Mo-coated soda lime glass substrates, consisting in a metallic stack deposition followed by a reactive annealing process. Cu/Sn/Cu/Zn metallic stacks were tuned in order to obtain Zn-rich and Cu-poor conditions (Cu/(Zn+Sn) = 0.75 and Zn/Sn = 1.20 determined with a calibrated X-ray fluorescence (XRF, Fischerscope XVD)) and deposited using DC magnetron sputtering (Alliance Ac450), as has been reported elsewhere.[10] Additionally, Ge nanolayers with different thicknesses were thermally evaporated on top of the precursors (1, 2, 5, 10, 15, and 25 nm, Oerlikon Univex 250). The whole precursor stack (5×5 cm^2 in area) was subsequently annealed in an Se + Sn containing atmosphere (100 mg of Se (Alfa-Aesar powder, 200 mesh, 99.999%) and 5 mg of Sn (Alfa-Aesar powder, 100 mesh, 99.995%)), using graphite boxes (69 cm^3 in volume) in a conventional tubular furnace. The selenization was performed in a two-step process, the first one at 400 °C (heating ramp 20 °C min^{-1}) during 30 min and 1.5 mbar Ar pressure, followed by the second step at 550 °C (heating ramp 20 °C min^{-1}) during 15 min and 1 bar Ar pressure, with a natural cooling down to room temperature.

Solar Cell Fabrication: To complete the devices, a CdS buffer layer (50 nm) was deposited by chemical bath deposition (CBD), preceded by several chemical etchings in order to remove secondary phases on the surface of the absorber and to passivate it.[13,24] First, an oxidizing etching was performed by using $KMnO_4$ + H_2SO_4 solution, followed by a chemical etching in $(NH_4)_2S$ solution, and finally a diluted KCN solution was used to etch the absorber.[24,25] Immediately after CdS growth, the solar cells were completed by DC-pulsed sputtering deposition of i-ZnO (50 nm) and In_2O_3-SnO_2 (ITO, 350 nm) as transparent conductive window layer (Alliance CT100). Afterward, for the optoelectronic characterization, 3×3 mm^2 cells were mechanically scribed using a manual microdiamond scriber MR200 OEG. Neither antireflective coating nor metallic grids were used for the optoelectronic characterization of the devices.

Film and Device Characterization: Dark and illuminated *J–V* curves were measured using a calibrated Sun 3000 class AAA solar simulator (Abet Technologies, 25 °C, AM1.5G illumination). The spectral response was measured using a Bentham PVE300 system calibrated with Si and Ge photodiodes in order to obtain the EQE of the solar cells. TEM analysis was carried out using a Tecnai F30 from FEI company operated at 300 kV and equipped with a Tridiem image filter from Gatan, Inc for EELS measurements. The lamellae were prepared for TEM investigation using the focused ion Beam (FIB) in situ lift-out method and thinned to a final thickness of less than 100 nm using a 5 kV Ga+ beam. The sample preparation method that we employed is particularly well-suited to correlating macroscale behavior to nanoscale effects (we had more than 10 µm of the full stack in cross section available). SEM images were obtained with a ZEISS Series Auriga microscope using 5 kV accelerating voltage. Raman spectra were obtained using a Horiba Jobin Yvon LabRam HR800-UV coupled with an Olympus metallographic microscope. Backscattering measurements were performed using a 532 nm excitation wavelength (penetration depth below 100 nm). All Raman measurements were carried out in an area of 30×30 μm^2 in a dual-scan mode. The laser spot diameter was about 1 µm. For avoiding possible thermal effects in the Raman experiments, the power density was kept below 16 kW cm^{-2}. The Raman spectra have been calibrated using an Si monocrystal reference and imposing the Raman shift for the main Si band at 520 cm^{-1}. In order to evaluate the Raman shift and FWHM errors, several Raman experiments on the same position of the samples were performed. The same setup was used to record the PL spectra of the samples. TOF-SIMS measurements were performed in an ION-TOF IV equipment, equipped with 25 kV Bi cluster primary ion gun for analysis, and O_2 and Cs ion guns for sputtering in depth profiling modes. The analyzed area was 50×50 μm^2 with a cycle time of 100 µs and a time to digital converter (TDC) resolution of 200 ps. XPS measurements were performed in a PHI 5500 Multitechnique System (from Physical Electronics) with a monochromatic X-ray source (Aluminium Kα line of 1486.6 eV energy and 350 W), placed perpendicular to the analyzer axis and calibrated using the 3d5/2 line of Ag with an FWHM of 0.8 eV.

Supporting Information

Supporting Information is available from the Wiley Online Library or from the author.

Acknowledgements

This research was supported by the Framework 7 program under the project KESTCELLS (FP7-PEOPLE-2012-ITN-316488), by MINECO (Ministerio de Economía y Competitividad de España) under the SUNBEAM project (ENE2013–49136-C4–1-R) and NOVACOST project (PCIN-2013–128-C02–01), and by European Regional Development Funds (ERDF, FEDER Programa Competitivitat de Catalunya 2007–2013). Authors from IREC and the University of Barcelona belong to the M-2E (Electronic Materials for Energy) Consolidated Research Group and the XaRMAE Network of Excellence on Materials for Energy of the "Generalitat de Catalunya." S.G. thanks the Government of Spain for the FPI fellowship (BES-2014–068533), Y.S. for the PTA fellowship (PTA2012–7852-A), M.P.

ADVANCED ENERGY MATERIALS
www.advenergymat.de

www.MaterialsViews.com

for the MINECO postdoctoral fellowship (FPDI-2013–18968), and E.S. for the "Ramón y Cajal" fellowship (RYC-2011–09212). H.X. thanks the "China Scholarship Council" fellowship (CSC No. 201206340113). P.P. thanks the European Union for the JUMPKEST Marie Curie Individual Fellowship (FP7-PEOPLE-2013-IEF-625840).

Received: May 31, 2015
Revised: July 21, 2015
Published online:

[1] S. Siebentritt, S. Schorr, *Prog. Photovoltaics* **2012**, *20*, 512.
[2] D. B. Mitzi, O. Gunawan, T. K. Todorov, D. A. R. Barkhouse, *Philos. Trans. R. Soc., A* **2013**, *371*, 20110432.
[3] Y. S. Lee, T. Gershon, O. Gunawan, T. K. Todorov, T. Gokmen, Y. Virgus, S. Guha, *Adv. Energy Mater.* **2014**, *5*, 1401372.
[4] T. K. Todorov, K. B. Reuter, D. B. Mitzi, *Adv. Mater.* **2010**, *22*, 1.
[5] S. Bag, O. Gunawan, T. Gokmen, Y. Zhu, D. B. Mitzi, *Chem. Mater.* **2012**, *24*, 4588.
[6] C. J. Hages, S. Levcenco, C. K. Miskin, J. H. Alsmeier, D. Abou-Ras, R. G. Wilks, M. Bär, T. Unold, R. Agrawal, *Prog. Photovoltaics* **2013**, *23*, 376.
[7] I. Kim, K. Kim, Y. Oh, K. Woo, G. Cao, S. Jeong, J. Moon, *Chem. Mater.* **2014**, *26*, 3957.
[8] T. J. Huang, X. Yin, G. Qi, H. Gong, *Phys. Status Solidi RRL* **2014**, *8*, 735.
[9] K. Biswas, S. Lany, A. Zunger, *Appl. Phys. Lett.* **2010**, *96*, 201902.
[10] A. Fairbrother, X. Fontané, V. Izquierdo-Roca, M. Placidi, D. Sylla, M. Espindola-Rodriguez, S. López-Mariño, F. A. Pulgarín, O. Vigil-Galán, A. Pérez-Rodríguez, E. Saucedo, *Prog. Photovoltaics* **2014**, *22*, 479.
[11] M. Grossberg, K. Timmo, T. Raadik, E. Kärber, V. Mikli, J. Krustok, *Thin Solid Films* **2014**, *582*, 176.
[12] V. Fthenakis, *Renewable Sustainable Energy Rev.* **2009**, *13*, 2746.
[13] M. Neuschitzer, Y. Sánchez, S. López-Marino, H. Xie, A. Fairbrother, M. Placidi, S. Haass, V. Izquierdo-Roca, A. Pérez-Rodríguez, E. Saucedo, *Prog. Photovoltaics* **2015**, DOI: 10.1002/pip.2589.
[14] G. Brown, V. Faifer, A. Pudov, S. Anikeev, E. Bykov, M. Contreras, J. Wu, *Appl. Phys. Lett.* **2010**, *96*, 022104.
[15] a) T. K. Todorov, J. Tang, S. Bag, O. Gunawan, T. Gokmen, Y. Zhu, D. B. Mitzi, *Adv. Energy Mater.* **2012**, *3*, 34; b) W. Wang, M. T. Winkler, O. Gunawan, T. Gokmen, T. K. Todorov, Y. Zhu, D. B. Mitzi, *Adv. Energy Mater.* **2014**, *4*, 1301465.
[16] R. F. Egerton, *Electron Energy-Loss Spectroscopy in the Electron Microscope*, Springer, New York **2011**.
[17] K. Riegler, G. Kothleitner, *Ultramicroscopy* **2010**, *110*, 1004.
[18] S. Stølen, H. B. Johnsen, C. S. Bøe, O. B. Karlsen, T. Grande, *J. Phase Equilib.* **1999**, *20*, 17.
[19] A. Redinger, D. M. Berg, P. J. Dale, S. Siebentritt, *J. Am. Chem. Soc.* **2011**, *133*, 3320.
[20] D. B. Khadka, J. Kim, *J. Phys. Chem. C* **2015**, *119*, 1706.
[21] M. Dimitrievska, A. Fairbrother, A. Pérez-Rodríguez, E. Saucedo, V. Izquierdo-Roca, *Acta Mater.* **2014**, *70*, 272.
[22] R. Caballero, J. M. Cano-Torres, E. Garcia-Llamas, X. Fontané, A. Pérez-Rodríguez, D. Greiner, C. A. Kaufmann, J. M. Merino, I. Victorov, G. Baraldi, M. Valakh, I. Bodnar, V. Izquierdo-Roca, M. León, *Sol. Energy Mater. Sol. Cells* **2015**, *139*, 1.
[23] A. Kolmakov, S. Potluri, A. Barinov, T. O. Mentes, L. Gregoratti, M. A. Niño, A. Locatelli, M. Kiskinova. *ACS Nano* **2008**, *10*, 1993.
[24] S. López-Marino, Y. Sánchez, M. Placidi, A. Fairbrother, M. Espindola-Rodríguez, X. Fontané, V. Izquierdo-Roca, J. López-García, L. Calvo-Barrio, A. Pérez-Rodríguez, E. Saucedo, *Chem. - Eur. J.* **2013**, *19*, 14814.
[25] H. Xie, Y. Sánchez, S. López-Marino, M. Espíndola-Rodríguez, J. López-García, M. Neuschitzer, D. Sylla, A. Fairbrother, A. Pérez-Rodríguez, E. Saucedo, *ACS Appl. Mater. Interfaces* **2014**, *6*, 12744.

SUPPORTING INFORMATION

Large efficiency improvement in $Cu_2ZnSnSe_4$ solar cells by introducing a superficial Ge nanolayer

*Sergio Giraldo, Markus Neuschitzer, Thomas Thersleff, Simón López-Marino, Yudania Sánchez, Haibing Xie, Mónica Colina, Marcel Placidi, Paul Pistor, Victor Izquierdo-Roca, Klaus Leifer, Alejandro Pérez-Rodríguez, and Edgardo Saucedo**

To optimize the Ge quantities required to achieve high efficiency devices, a rational design of experiments was performed introducing different Ge thicknesses on top of the metallic precursor stack as was described in the Experimental Section (from 0 to 25 nm). From this preliminary optimization, we conclude that 10 nm of Ge is the optimized quantity to achieve the highest efficiency with this methodology. In **Table S1** a summary of the optoelectronic parameters of these experiments is presented, where a maximum efficiency is obtained for the Ge10 sample. By using Ge nano-layer thicknesses between 2 nm to 15 nm, the V_{OC} of the devices is clearly improved, with a maximum reported in **Table S1** of 452.8 mV. As was demonstrated in the Communication the absorber can be considered almost Ge free, in agreement with the results presented in **Table S1** where the band gap of the material is barely affected. If we compare this value with the reported ones for pure CZTSe, we see that this V_{OC} is the highest reported for this absorber to the best of our knowledge.[S1-S3] The absorber preparation with optimized Ge content (10 nm of Ge) was repeated several times in order to confirm its reproducibility: in six independent experimental runs, the maximum efficiency for reference cells (no Ge added) was in the range of 7.0-8.2%; while when 10 nm of Ge were applied onto the surface of the precursor stack, the maximum efficiencies were in the range of 9.2-10.1% (without anti-reflective coating and metallic grids). To better support the relevance of these results, a statistical study is presented in **Table S2**, where average and standard deviation of the most relevant optoelectronic parameters are presented, confirming the clear tendency observed in **Table S1**. More notably, some of these devices achieve unexpected high open circuit voltages with values as high as 469 mV, as is presented in **Figure S1**. This represents a paramount result in CZTSe based technologies.

Table S1. Summary of the experimental optimization of the Ge upmost layer thickness.

Sample	Ge thick. (nm)	Nominal Ge/(Ge+Sn)	Eff. (%)	V_{OC} (mV)	J_{SC} (mA.cm^{-2})	F.F. (%)	R_S (Ω.cm^2)	R_{SH} (Ω.cm^2)	E_G (eV)
Ref	0	0%	7.0	408.7	29.1	59.2	0.23	265	1.04
Ge1	1	0.44%	6.8	407.9	29.2	56.8	0.50	260	1.05
Ge2	2	0.87%	8.3	414.7	31.5	63.3	0.33	399	1.05
Ge5	5	2.2%	8.5	431.2	30.7	64.3	0.61	335	1.05
Ge10	10	4.4%	**10.1**	452.8	33.3	66.8	0.52	712	1.04
Ge15	15	6.6%	8.1	412.4	32.6	59.8	1.04	156	1.03
Ge25	25	10.9%	8.2	410.7	33.5	59.9	0.98	131	1.02

Table S2. Summary of the average and standard deviation of the main optoelectronic parameters for the different devices (based in the average of 9 representative cells).

Sample	Aver. Eff. (%)	Std. Dev. Eff. (%)	Aver. F.F. (%)	Std. Dev. F.F. (%)	Aver. V_{OC} (mV)	Std. Dev. V_{OC} (mV)	Aver. J_{SC} (mA/cm^{-2})	Std. Dev. J_{SC} (mA/cm^{-2})
Ref	6.6	0.3	57.3	1.8	398	10	28.8	1.0
Ge1	6.6	0.1	56.3	1.4	401	11	29.1	1.0
Ge2	7.7	0.4	60.7	2.4	413	7	30.7	1.0
Ge5	8.3	0.2	63.9	1.4	428	4	30.3	1.1
Ge10	9.8	0.2	66.3	0.3	447	6	33.0	0.5
Ge15	7.5	0.2	60.0	1.2	415	4	31.2	1.0
Ge25	6.8	0.2	57.1	1.3	405	5	31.4	1.1

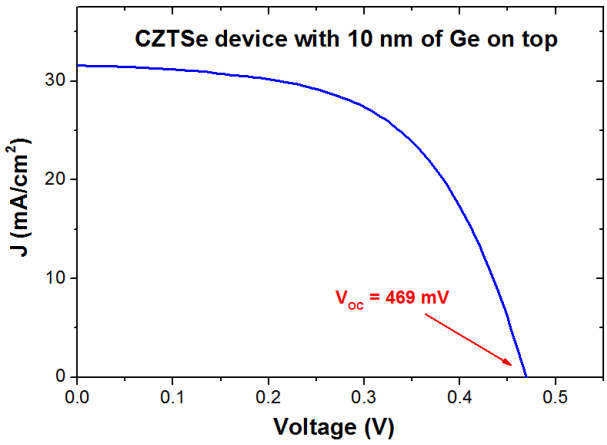

Figure S1. Solar cell showing 469 mV of V_{OC}.

Table S1 presents the band-gap of the different absorbers estimated by means the EQE plots, where almost the same value is obtained independently on the Ge quantity. Nevertheless, this value represents the effective minimum E_G value. To corroborate that the E_G is not changing with the Ge quantity, complementary PL measurements were performed on the same samples and is shown in Figure S2 (using 785 nm as excitation wavelength, with an estimated penetration depth ~ 200 nm). All the spectra look very similar, indicating no drastic changes in the defect structure on the

surface. The estimation of the energy position of the maxima of the PL spectra leads to very similar values, suggesting that the band-gap is almost unaffected by the inclusion of Ge, in agreement with the values obtained by EQE.

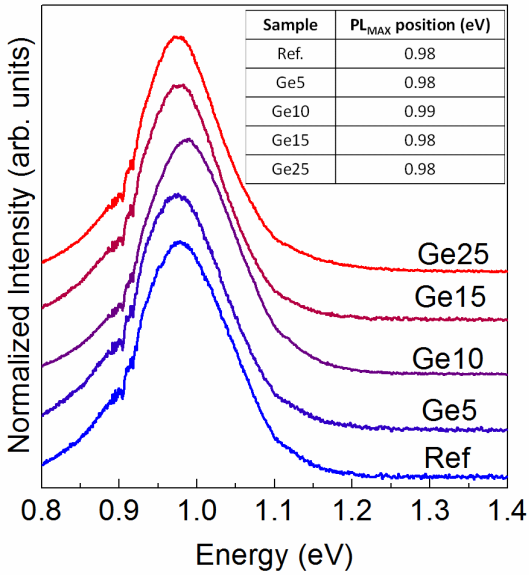

Figure S2. Room temperature PL of the different samples, including the energy position of the maximum of the PL peak.

This unexpected large improvement was accompanied by a very small quantity of Ge incorporated in the absorber. Further evidence for the lack of Ge within the absorber layer is presented in **Figure S3**. In this figure, the elemental map of Ge from **Figure 2** of the manuscript was used to generate a "mask" which allows for the spectra present within this region to be selectively summed. As a comparison, a neighboring "reference" region containing the same number of pixels was also summed. Both of the regions are depicted as an inset to **Figure S3**, and the summations are plotted on the graph without any further data treatment. There are striking differences between the resulting two energy-loss spectra. For the spectra summed over the Ge mask, a clear Ge signal is observed with an onset of 1217 eV. This is sufficiently distant from the Zn L1 edge to be distinguishable. This edge is completely absent from the reference region, indicating that any Ge in this region must be below the detection limit, which we estimate to be 0.2 at% under these conditions (see the manuscript text). There are additional features observable in the Energy-Loss Near Edge Fine Structure (ELNES) features. In particular, for the Ge-mask spectra, an additional edge is present at 1060 eV that is absent in the reference spectra, as denoted by the red arrow. This likely represents an additional electronic transition within the Zn atoms present in this region and its origin is currently under investigation. There is also an apparent white-line ratio change in the Cu edge that could be indicative of a modified valence state.

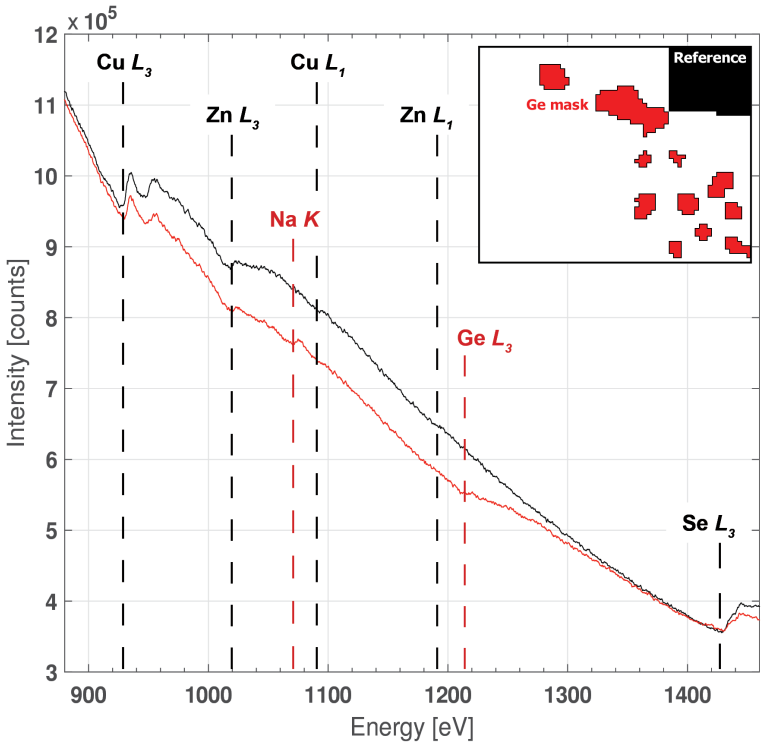

Figure S3. EELS map with Ge mask (right hand) and corresponding spectra in the reference areas (black line) and Ge nano-inclusions (red line) (left hand).

As was highlighted in the main manuscript, the rather small quantities of Ge employed in this work significantly improve the crystalline quality of CZTSe absorber. **Figure S4** shows additional SEM cross sectional images of layers with lower and higher Ge quantities than the optimized one (Ge10), to support the Ge assisted grain growth reported in the manuscript. As is clear, the higher the Ge thickness used in the precursor, the bigger the uppermost grain sizes in the absorber.

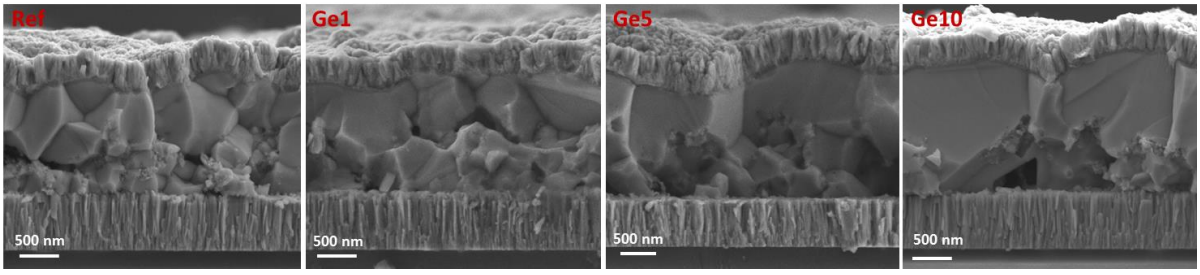

Figure S4. Cross sectional SEM images of reference CZTSe sample (left hand image) and Ge10 sample (right hand image).

To analyze the back region of the samples, these were lifted-off from the substrate. **Table S3** presents the detailed analysis of the Raman spectra presented in **Figure S5**, where the Raman shift and FWHM of the main A^1 mode of CZTSe are summarized. The slight differences at the front can be explained by a crystalline quality improvement for the Ge10 sample as has been proposed before. At the back region,

there are no remarkable differences between both samples. Additionally, Raman analysis before and after the surface etchings employed in this work (see Experimental Section) does not show evidences of the possible formation of $GeSe_2$ secondary phases at the surface, in agreement with its volatility.

Table S3. Summary of the main Raman parameters extracted from spectra presented in Figure 3 of the manuscript.

Sample	Region	Raman shift A^1 CZTSe (cm^{-1})	FWHM A^1 CZTSe (cm^{-1})
Ref	Front	195.26 ± 0.05	6.1 ± 0.1
Ref	Back	194.20 ± 0.05	6.8 ± 0.1
Ge10	Front	195.52 ± 0.05	5.8 ± 0.1
Ge10	Back	194.21 ± 0.05	6.5 ± 0.1

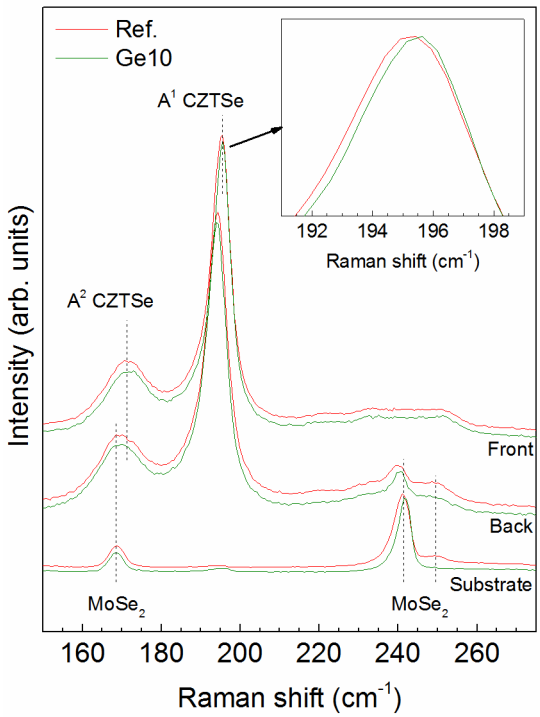

Figure S5. Front, back and substrate spectra of Ref. and Ge10 absorbers.

Finally, **Figure S6** shows the XPS analysis of Ref. and Ge10 samples where in particular, the Sn3d5 peak of Sn in shown. As is presented in **Figure S6b**, the peak can be fitted by two Gaussian contributions (after baseline subtraction) that can be assigned to Sn^{+2} and Sn^{+4} oxidation states [S4], allowing for a quantification of each of them (one Gaussian peak centered at 485.85 eV for Sn^{+2} and the other Gaussian peak centered at 486.61 eV for Sn^{+4}). Whiles in **Figure S6a** the shift of the XPS peak towards higher biding energies for Ge10 sample suggests a higher contribution of Sn^{+4} state [S4], **Figure S6b**

clearly demonstrates an increase of this contribution. It is important to remark that a direct evaluation of the concentration of each Sn species was not possible due to the unknown sensitivity factor for each Sn oxidation state in these samples, and in consequence, their quantity cannot be determined with these measurements. Nevertheless, an increase of the relative intensity of one of the oxidation states means that this particular state is enhanced with respect to the other. In fact, the inset of **Figure S6a** corroborates the increase of the Sn^{+4} signal when Ge is added to the layers, demonstrating a higher contribution of the high oxidation state of Sn on this sample, supporting that Ge enhance the presence of Sn^{+4} at the very surface, probably contributing to the improvement of the optoelectronic parameters of the devices [S5].

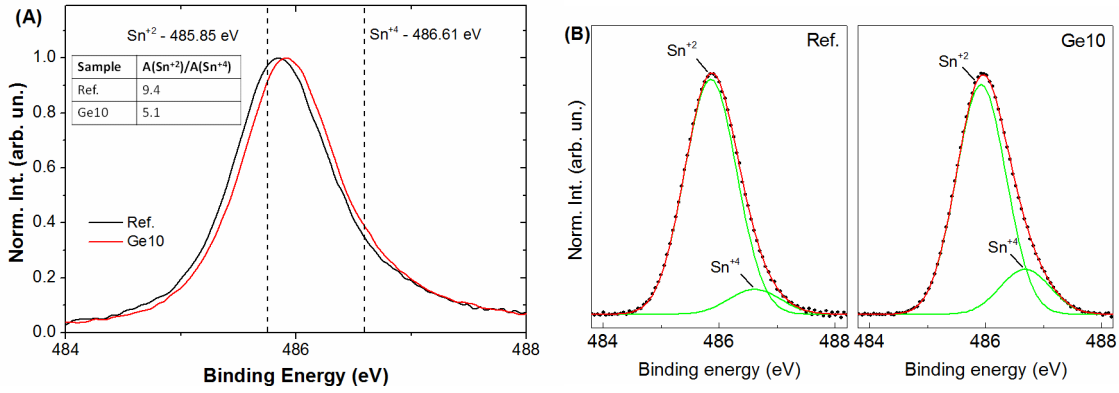

Figure S6. XPS spectra corresponding to the Sn3d5 transition, showing the Sn+2 and Sn+4 states for the Ref. and Ge10 layers (a). Gaussian fitting of the two spectra presented in the previous figure (b).

Additional References

[S1] Y. S. Lee, T. Gershon, O. Gunawan, T. K. Todorov, T. Gokmen, Y. Virgus, S. Guha, *Adv. Energy Mater.* **2014**, *5*, 1401372.

[S2] I. Repins, C. Beall, N.Vora, C. De Hart, D. Kuciauskas, P. Dippo, B. To, J. Mann, W-C. Hsu, A. Goodrich, R. Noufi, *Solar Ener. Mater. Solar Cells* **2012**, *101*, 154.

[S3] M. Buffière, G. Brammertz, M. Batuk, C. Verbist, D. Mangin, C. Koble, J. Hadermann, M. Meuris, J. Poortmans. *Appl. Phys. Lett.* **2013**, *103*, 163904.

[S4] A. Kolmakov, S. Potluri, A. Barinov, T. O. Mentes, L. Gregoratti, M. A. Niño, A. Locatelli, M. Kiskinova. *ACS Nano* **2008**, *10*, 1993.

[S5] C. J. Hages, S. Levcenco, C. K. Miskin, J. H. Alsmeier, D. Abou-Ras, R. G. Wilks, M. Bär, T. Unold, R. Agrawal, *Prog. Photovolt. Res. Appl.* **2013**, *23*, 376.

Progress in PHOTOVOLTAICS

PROGRESS IN PHOTOVOLTAICS: RESEARCH AND APPLICATIONS
Prog. Photovolt: Res. Appl. 2016; **24**:1359–1367
Published online 6 July 2016 in Wiley Online Library (wileyonlinelibrary.com). DOI: 10.1002/pip.2797

RESEARCH ARTICLE

$Cu_2ZnSnSe_4$ solar cells with 10.6% efficiency through innovative absorber engineering with Ge superficial nanolayer

Sergio Giraldo[1]*, Thomas Thersleff[2], Gerardo Larramona[3], Markus Neuschitzer[1], Paul Pistor[1], Klaus Leifer[2], Alejandro Pérez-Rodríguez[1,4], Camille Moisan[3], Gilles Dennler[3] and Edgardo Saucedo[1]

[1] Catalonia Institute for Energy Research (IREC), Jardins de les Dones de Negre 1, 08930 Sant Adrià de Besòs (Barcelona), Spain
[2] The Ångström Laboratory, Department of Engineering Sciences, Uppsala University, Box 534, Uppsala, Sweden
[3] IMRA Europe S.A.S., 220 rue Albert Caquot, F-06904 Sophia Antipolis, France
[4] IN2UB, Universitat de Barcelona, c. Martí i Franquès 1, 08028 Barcelona, Spain

ABSTRACT

In our recently published work, the positive effect of a Ge nanolayer introduced into the processing of $Cu_2ZnSnSe_4$ absorbers (CZTSe) was demonstrated. In this contribution, the complete optimization of this new approach is presented for the first time. Hence, the optimum Ge nanolayer thickness range is defined in order to achieve an improved performance of the devices, obtaining a record efficiency of 10.6%. By employing this optimized approach, the open-circuit voltage (V_{OC}) is boosted for our pure selenide CZTSe up to 489 mV, leading to V_{OC} deficit among the lowest reported so far in kesterite technology. Additionally, two important effects related to the Ge are unambiguously demonstrated that might be the origin of the V_{OC} boost: the improvement of the grain size and the corresponding crystalline quality, and the interaction between Ge and Na that allows for dynamic control over the CZTSe doping. Finally, evidences pointing to the origin of the deterioration of devices properties for large Ge concentrations are presented. Copyright © 2016 John Wiley & Sons, Ltd.

KEYWORDS

$Cu_2ZnSnSe_4$; kesterite; germanium; Na doping; thin-film photovoltaics

***Correspondence**

Sergio Giraldo, Catalonia Institute for Energy Research (IREC), Jardins de les Dones de Negre 1, 08930 Sant Adrià de Besòs (Barcelona), Spain.

E-mail: sgiraldo@irec.cat

Received 4 February 2016; Revised 13 May 2016; Accepted 9 June 2016

1. INTRODUCTION

Nowadays, the use of absorbers based on earth abundant, non-critical elements in thin-film photovoltaics is essential in order to guarantee their long-term sustainability. In this sense, $Cu_2ZnSn(S,Se)_4$ (CZTSSe) kesterites have been studied in the last decade showing large potential as absorber material for high-performance photovoltaic devices [1,2]. Nevertheless, considering that these materials are only very recently under intensive research, kesterites still have some way to go to achieve the efficiency values of the conventional thin-film materials like CdTe and $Cu(In,Ga)Se_2$ (CIGSe) [3]. As it is widely known, the reduction of the large voltage deficit is one of the major challenges that kesterite-based solar cell devices have to overcome in the next years in order to reach the performance levels of the more mature technologies [4]. The main reasons for this large voltage deficit are not yet understood, but possible candidates are the short minority carrier lifetime related to the high concentration of bulk defects, the grain boundary (GB) characteristics, and the interfacial defects affecting the quality of the hetero-junction as well as the back contact [5]. In particular, the modification of the interfaces has proven to be very promising for increasing the voltage and, in general, the device performance [6–10]. For example, the use of surface chemical etchings combined with subsequent post-deposition annealings has proven useful for passivating the surface of the absorber and achieving beneficial grain boundaries composition. The optimization of the CdS buffer layer growth has also been shown to improve the quality of the CZTSe/CdS interface resulting in an efficiency increase [9,11]. On that topic, Messaoud

et al. studied the impact of modifying the properties of the CZTSe/CdS layer interface by using a Cd^{2+} treatment before the buffer layer deposition, leading to an improvement of the efficiency from 8.3% to 9.0% mainly due to a series resistance (R_S) decrease [12]. In addition, other Cd introduction approaches in Cu_2ZnSnS_4 (CZTS) showed impressive performance improvements obtaining solar cells over 9% efficiency [13].

In order to address the large voltage deficit of this technology, some key issues are as follows: (i) very good absorber crystalline quality; (ii) an accurate control of intrinsic and extrinsic doping; and (iii) an effective passivation of interfaces, including grain boundaries, the CZTSe/CdS interface, and the CZTSe/Mo interface. In this regard, several strategies have been investigated in the literature. Regarding the improvement of the crystalline quality, several works have shown that well-crystallized absorbers can be obtained by taking advantage of the formation of liquid copper-rich selenide phases during the reactive annealing that acts as fluxing agent [14–16]. Other successful approaches, mostly reported for the CIGSe thin-film technology, are based on the use of impurity elements promoting an improved crystallization and grain growth. For example, the introduction of antimony in CZTSe as well as in CIGSe films has demonstrated a remarkable enlargement of the crystals [17,18]. Following the same strategy, Nakada *et al.* discovered the same crystal growth enhancement when bismuth is used, besides corroborating the beneficial effect of antimony. Additionally, a synergistic effect together with sodium was observed because this seemed to be necessary for obtaining the beneficial effect of bismuth and antimony doping [19]. Nevertheless, these approaches have shown, at best, rather small improvements in the efficiency of devices. In the kesterite systems, sodium incorporation has demonstrated numerous beneficial properties at different levels, such as enhanced grain growth, and effective GB and interface passivation, reducing interfacial recombination and leading to several performance improvements [20–22]. Similarly, other alkali dopants like lithium have been investigated in kesterite solar cells giving successful results by improving the electronic quality of the absorber [23].

Regarding the passivation of interfaces, in particular the passivation of grain boundaries, several works have shown that the presence of oxygen or SnO_X and sodium, along with Cu-poor composition, is beneficial for device performance, avoiding the appearance of recombination centers and promoting carrier separation by the formation of electrical potentials [24–26]. Using Ge, we observe several improvements, including better crystalline quality as it has been demonstrated in other works, an optimized doping level, and probably a more effective passivation of interfaces by the formation of small amounts of oxide compounds like GeO_X and SnO_X present in the absorber material [27–29].

In this work, following the recently published positive effect of a Ge nanolayer introduced on CZTSe absorbers, we present for the first time the complete optimization of this new approach, based on the introduction of an extremely thin Ge layer, allowing a remarkable V_{OC} increase (from about 400 mV for Ge-free absorbers to values around 490 mV for Ge-containing ones) [27]. Additionally, this leads to efficiencies exceeding 10% with V_{OC} deficit values among the lowest reported so far for kesterite solar cells.

2. RESULTS

In our previous work, we demonstrated that the application of rather small quantities of Ge onto Cu–Zn–Sn precursors dramatically increases voltage and efficiency of the resulting devices [27]. Despite the very low Ge incorporation corroborated by different advanced sensitive techniques in the previous study, several reasons were provided to explain the large improvement, including the formation of a Ge_3Se_7 phase during the reactive annealing that incongruently decomposes into $GeSe_2$ (which has a non-negligible vapor pressure at high temperatures, as does SnSe) and a Se-rich Ge_xSe_y liquid phase. The formation of such liquid phase is expected to assist the grain growth, improving the crystalline quality. Furthermore, the presence of Ge seems to reduce the probability of formation of Sn-reduced species, mainly Sn^{+2}, that are associated with deep defects deteriorating the voltage. Finally, the hypothesis that the GeO_X nanoparticles associated with the presence of SnO_X might act as electron back reflectors enhancing the voltage of the devices was presented as possible explanations for the observed performance improvement. Therefore, in this study, we investigated an extensive range of Ge thickness with the aim of determining the optimum Ge content to obtain the best performance on the resulting devices, along with additional characterizations leading to a better understanding of the beneficial effects of a few nanometers layer of Ge as well as the detrimental effect of higher Ge quantities.

In order to optimize the Ge quantity, we performed a detailed study of different Ge thicknesses in the range from 0 to 50 nm. Figure 1 shows the evolution of the different photovoltaic parameters with increasing Ge concentration, corroborating the efficiency maximums around 7.5–12.5 nm of Ge, with values up to 10.6% efficiency for the sample containing 12.5 nm of Ge. Considering that the material is pure selenide kesterite, the devices reported in this work are probably the most efficient ones fabricated by a sequential process from sputtered precursors and are only 1% (absolute) below the efficiency record values reported so far for CZTSe regardless of the fabrication method [30,31]. After several runs of samples using this approach, it seems that there is a relatively narrow Ge thickness range from 7.5 to 12.5 nm that results in high efficiencies with a significant increase compared with the reference cells (without Ge). Furthermore, a clear trend is visible with efficiency beginning to increase from 2 nm, reaching the maximum around 10 nm, and then decreasing beyond 15 nm, with the lowest overall efficiency occurring when

Prog. Photovolt: Res. Appl. 2016; **24**:1359–1367 © 2016 John Wiley & Sons, Ltd.
DOI: 10.1002/pip

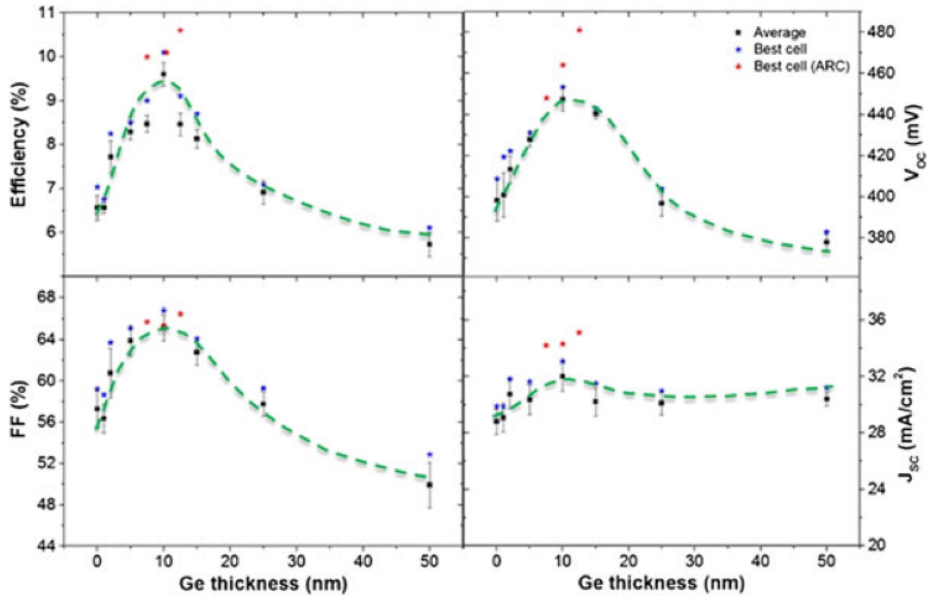

Figure 1. Photovoltaic parameters analysis of devices fabricated from absorbers with different Ge contents.

higher Ge quantities are used. Regarding the fill factor (FF) and the open-circuit voltage (V_{OC}), they show exactly the same trend, obtaining for the latter values around 490 mV, which means a V_{OC} increase of more than 22% with respect to the reference cell. Despite this, the short-circuit current (J_{SC}) slightly increases with Ge concentration, although it does not seem to degrade for the highest Ge quantities. The series resistance (R_S) and shunt resistance (R_{Sh}) extracted from J–V curves were remarkably lower and higher, respectively, possibly because of improved GB passivation, for the cells containing an optimized Ge quantity compared with the reference cells and those with high Ge content (see Figure S1, Supporting Information). Hence, these improved resistances contribute to a high FF, around 67%, which is comparable with the 11.6% efficiency record CZTSe device with 67.3% FF [31].

The optoelectronic characterization was complemented with spectral response measurements of the complete set of samples in the whole range of Ge thicknesses. Figure 2(a) shows the plots of the external quantum efficiency (EQE). For wavelengths between 300 and 600 nm, the results seem to be barely affected by the Ge quantity. However, increasing Ge quantities lead to a clear collection improvement for longer wavelengths, which

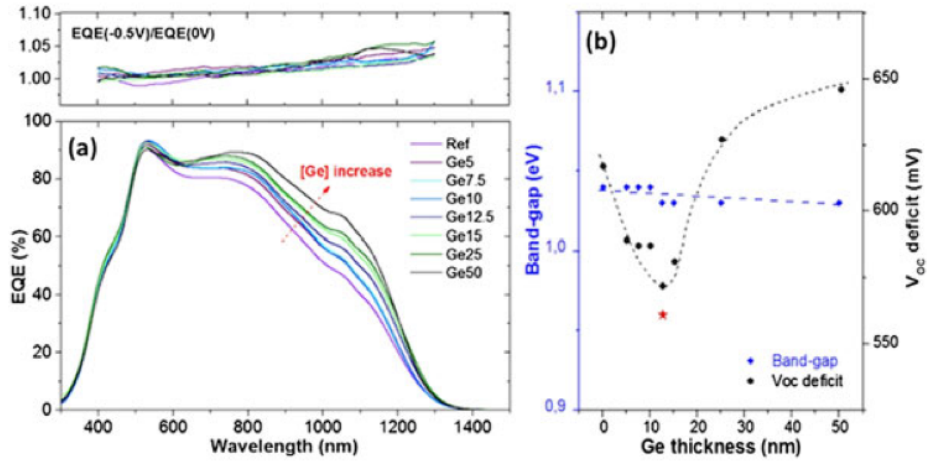

Figure 2. (a) EQE of solar cells synthesized with different Ge thicknesses from 0 (Ref.) to 50 nm (Ge50); in the upper part, the ratio EQE(−0.5 V)/EQE(0 V) is displayed. (b) Bandgap and V_{OC} deficit evolution with increasing Ge layer thickness; in red, the record V_{OC} deficit value achieved is shown.

correspond to charge carriers generated in and collected from the depth of the absorber bulk. Interestingly, the EQE in this range keeps increasing continuously as more Ge is introduced, in line with the general trend of a slightly increasing J_{SC} in the measured J–V curves. This indicates an improvement of the effective collection length that is commonly approximated by the sum of the space charge region width and the diffusion length of the minority charge carriers. Generally speaking, the effective carrier collection length is quite low for our samples and limits further performance improvement. As the EQE improvement through Ge addition is not correlated with the doping density (Figure 3) or the measurement of the EQE under bias voltage (Figure 2(a), upper part), we expect it to be originated in an improvement of the diffusion length of the minority charge carriers. However, further investigation is needed to corroborate on this.

The bandgap values for the complete set of samples were estimated from the EQE measurements by the derivative method and, to our surprise, showed no remarkable changes. In all samples, the bandgap oscillated between 1.03 and 1.04 eV, even for the samples containing up to 50 nm of Ge confirming the very low incorporation of this element into the absorber. Figure 2(b) shows the evolution of the bandgap value along with the V_{OC} deficit with increasing Ge concentration. Impressive V_{OC} deficit values down to 561 mV were achieved for the best cells in the range between 7.5 and 12.5 nm of Ge. Recently, Kim *et al.* showed similar studies, where adding of Ge to pure selenide-based kesterite absorbers led to significant performance improvements achieving efficiencies around 10%, although with V_{OC} deficit values of 647 mV that remained rather high compared with the values reported here [32].

In Table I, most of the recent records for kesterite solar cells are summarized and listed together with their corresponding V_{OC} deficit. The record cell for the pure $CuInSe_2$ chalcopyrite solar cell is also demonstrated for comparison. Analyzing the V_{OC} of the different cells, the values we report here around 490 mV result a breakthrough for Ge-doped CZTSe, being even comparable with solid solution sulfo-selenide compounds (CZTSSe) with much higher bandgap. Thereby, taking into account a bandgap value of 1.05 eV, this leads with 560 mV to V_{OC} deficits unprecedented for kesterites.

The Time-of-Flight Secondary Ion Mass Spectrometry (ToF-SIMS) in-depth profiles were performed to assess possible composition variations due to Ge incorporation. As is widely known, sodium plays a crucial role in the doping of kesterites, being essential to obtain high-performance devices. In Figure 3, the Na content of samples with 0, 1, 5, 10, and 25 nm of Ge (i.e., Ref, Ge1, Ge5, Ge10, and Ge25, respectively) is analyzed, showing a clear gradual increase from the reference to the Ge10 sample and a decrease for the Ge25 sample till values around the reference. This is further confirmed by capacitance–voltage (C–V) measurements, whereby the doping level (N_{CV}, at 0 V) increases for the samples containing 5, 10, and 15 nm of Ge (i.e., Ge5, Ge10, and Ge15, respectively) with values around $3–4 \times 10^{16}\,cm^{-3}$ and drastically decreases for the samples with higher Ge quantity (Ge25 and Ge50), showing an order of magnitude less. The N_{CV} values found in the literature for the best CZTSe devices exhibit a wide range of doping level with a difference of an order of magnitude between them [30,31]. Recently, a detailed study of the Sn content in CZTSSe has shown a similar decrease of the charge carrier density with increasing Sn concentration [37]. As mentioned before, there seems to be an interaction between Ge and Na (some evidences are shown in Figure S3 of the Supporting Information of the previous study [27]), regulating their incorporation into absorber material. As we have speculated previously, Ge can form Ge–Se liquid phases during the reactive annealing with high content of Se (about 85 at.%), which in turn could dissolve Na-related liquid compounds like liquid sodium polyselenide phases (Na_2Se_X) that are formed at temperatures around 300 °C [21]. The presence of Ge could lead to more Na in the absorber owing to its reaction with Ge–Se liquid phases.

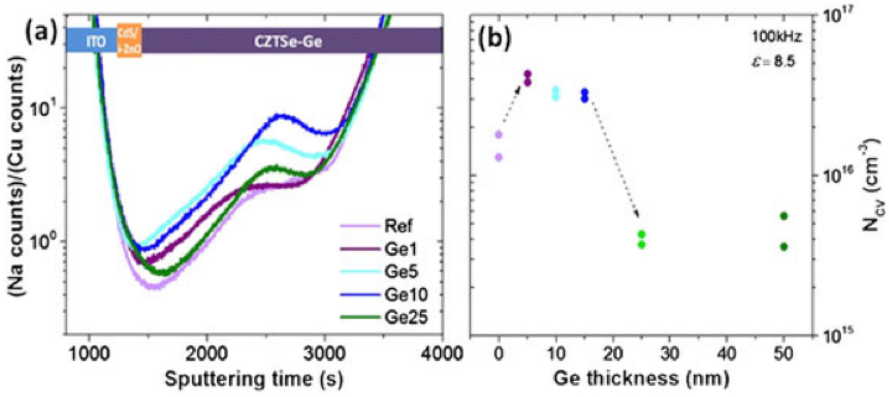

Figure 3. (a) Na/Cu ToF-SIMS in-depth profiles of samples fabricated with different Ge concentrations. (b) Charge carrier density (at 0 V) at 300 K characterized by C–V measurements of devices produced using different Ge quantities (measurements of two different cells are displayed for each sample).

Prog. Photovolt: Res. Appl. 2016; **24**:1359–1367 © 2016 John Wiley & Sons, Ltd.
DOI: 10.1002/pip

Table I. Summary of selected photovoltaic parameters of some of the best kesterite devices reported in the literature.

Material	Institution	Eff. (%)	V_{OC} (mV)	Bandgap (eV)	V_{OC} deficit (V)	Ref.
CISe	NREL	15.0	491	1.00	0.51	[33]
CZTS	Solar Frontier	9.2	708	1.45	0.74	[34]
CZTSSe	IBM	12.6	513	1.13	0.62	[35]
CZTSSe	EMPA	11.2	479	1.05	0.57	[36]
CZTSSe	IMRA	10.8	510	1.18	0.67	[37]
CZTSe	IBM	11.6	423	1.00	0.58	[31]
CZTSe	IMEC	10.4	395	~1	0.61	[30]
CZTSe	Nexcis + IREC	8.2	440	1.05	0.61	[38]
Best eff.—this work (CZTSe)	IREC	10.6	473	1.05	0.58	—
Best V_{OC}—this work (CZTSe)	IREC	9.6	489	1.05	0.56	—

Record CISe cell parameters are also included for comparison.

In addition, the Ge nanolayer is expected to be partly oxidized because of the short air exposure, and the presence of GeOx nanoclusters within the absorber has been demonstrated in our previous publication. It is known that the presence of oxygen attracts Na and a strong link between Na and oxygen has been repeatedly reported for chalcopyrite absorbers in the past as well as for kesterite absorbers [39–42]. Nevertheless, when high Ge quantities are introduced, this sodium seems to be somehow extracted to the surface of the absorber: needle-like Na/O precipitates were observed by Scanning Electron Microscopy/Energy-Dispersive X-ray Spectroscopy (SEM/EDX) analysis of the as-annealed Ge25 and Ge50 samples before the etching (Figure S2, Supporting Information). The different chemical etchings during the further solar cell processing remove these Na/O phases on the surface of the absorber, as was also confirmed by SEM/EDX.

To better understand the efficiency drop when Ge quantities higher than 15 nm are introduced, Transmission Electron Microscopy/Electron Energy-Loss Spectrometry (TEM/EELS) advanced characterization was performed to the sample Ge25 (containing 25 nm of Ge), as shown in Figure 4. A detailed analysis at nanoscale level of the lamella revealed the presence of ZnSe and Cu-related secondary phases at the CdS/CZTSe interface. The most reasonable explanation for the Zn and Cu-related secondary phases encountered is the Sn loss that could happen during the reactive annealing. However, we observe this phenomenon only when we apply high Ge concentrations (≥25 nm), suggesting an interaction between Sn and Ge. This can be explained by considering that Ge and Sn are expected to be interchangeable in the kesterite lattice, and both are likely to have similar chemical behavior. Therefore, during the formation of the Ge–Se liquid phase, Sn is probably incorporated into this phase as well, leading to a lack of Sn (Table S2, Supporting Information) in the kesterite structure and to the consequent formation of secondary phases. Interestingly, Kim *et al.* investigated the effects of the annealing environment in Ge-incorporated CZTSe showing kesterite decomposition at temperatures

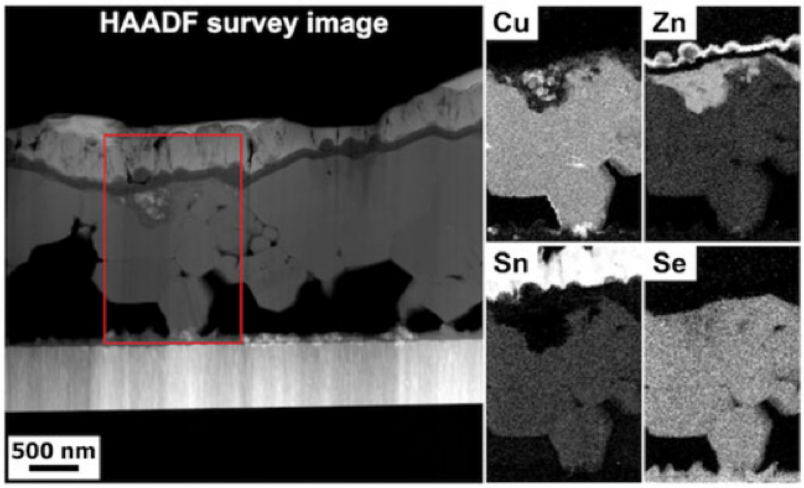

Figure 4. TEM/EELS analysis of Ge25 device. At left, a high-angle annular dark field (HAADF) survey image presents an overview of the solar cell stack. The contrast mechanism is predominately atomic mass. At right, qualitative elemental EELS maps extracted from the boxed region are presented for Cu, Zn, Sn, and Se.

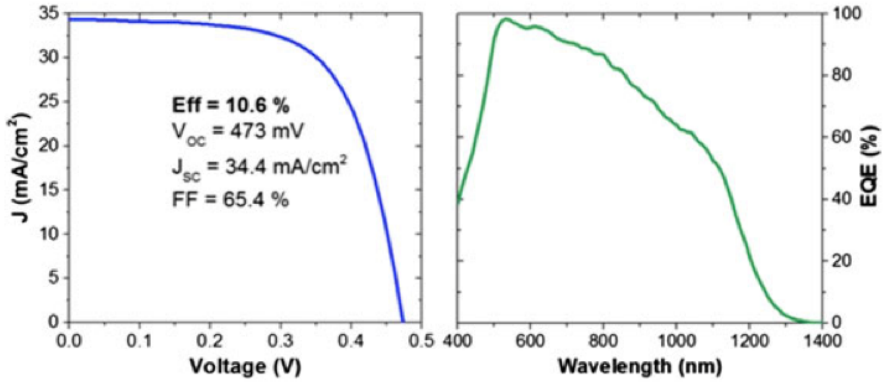

Figure 5. J–V curve of the record CZTSe-Ge device (with Ni/Al metallic grid and MgF_2 anti-reflective coating) under 1-Sun illumination conditions (left) and the corresponding EQE plot (right). Cell area = 0.228 cm^2.

higher than 500 °C when Sn and Ge are not introduced in the reactive annealing environment, confirming the presence of Cu and Zn secondary phases [32]. It is important to note that none of these secondary phases were detected in the sample Ge10 (containing 10 nm of Ge). This means that, for samples with thicker Ge top layers (Ge25 and Ge50), the large Ge–Se liquid phase quantity that is formed possibly reacts and decomposes the main kesterite phase, leading to the Sn(Ge) loss and the concomitant formation of Cu–Se-related and Zn–Se-related secondary phases. Together with the observed strong decrease of the Na doping level and the carrier concentration, a partial decomposition of the kesterite at the surface due to the presence of high quantities of the Ge–Se liquid phase can contribute to the observed drastic drop of the efficiency for samples Ge25 and Ge50.

Finally, in Figure 5, the illuminated J–V curve of one of our best solar cells is reported with an efficiency of 10.6% (with metallic grid and anti-reflective coating) and the corresponding EQE spectrum used to estimate the bandgap and the V_{OC} deficit. In this case, the absorber was produced with a 12.5 nm thick superficial Ge layer.

3. CONCLUSION

In this work, we presented a complete optimization of this new approach using a nanometric layer of Ge, showing an optimum Ge thickness about 10 nm, although remarkable performance improvements are obtained with Ge thicknesses in the range from 7.5 to 12.5 nm. We found a strong interaction between Ge and Na, which can further influence the electrical properties of the absorbers. Furthermore, performance deterioration when higher Ge amounts are introduced has been identified, and we attribute this to a decrease of the charge carrier density along with the presence of secondary phases. Based on these observations, we propose a decomposition mechanism of the kesterite. The presented optimization has allowed achieving efficiencies as high as 10.6% for the best devices reported in this study and impressive V_{OC} values around 490 mV for the pure selenide CZTSe compound. All this leads to reach V_{OC} deficits among the lowest reported in the literature for kesterite technology.

4. EXPERIMENTAL SECTION

The CZTSe films were prepared by a sequential process onto Mo-coated soda lime glass substrates. For this purpose, Zn-rich and Cu-poor Cu/Sn/Cu/Zn multi-stacks (Cu/(Zn + Sn) = 0.75 and Zn/Sn = 1.20 determined with calibrated X-ray fluorescence (Fischerscope XVD)) were deposited using direct-current magnetron sputtering (Alliance Ac450). Additionally, different Ge thicknesses were thermally evaporated on top of the precursors (from 0 to 50 nm, Oerlikon Univex 250). Then, the whole precursor stack was subsequently annealed in a Se + Sn atmosphere (100 mg of Se (Alfa-Aesar powder, 200 mesh, 99.999%, Thermo Fisher Scientific Chemicals Inc., Ward Hill, Massachusetts, USA) and 5 mg of Sn (Alfa-Aesar powder, 100 mesh, 99.995%)), using graphite boxes (69 cm^3 in volume) in a conventional tubular furnace. The selenization was performed in a two-step process: the first one at 400 °C (heating ramp of 20 °C/min) during 30 min and 1.5 mbar of Ar pressure, followed by the second step at 550 °C (heating ramp of 20 °C/min) during 15 min and 1 bar of Ar pressure, with a natural cooling down to room temperature. To complete the devices, a CdS buffer layer (50 nm) was grown by chemical bath deposition, preceded by several chemical etchings in order to remove secondary phases on the surface of the absorber and to passivate it. First, an oxidizing etching was performed by using $KMnO_4 + H_2SO_4$ solution, followed by a chemical etching in $(NH_4)_2S$ solution, and finally, a diluted KCN solution was used to etch the absorber [7,8]. Immediately after CdS growth, the solar cells were completed by DC-pulsed sputtering deposition of i-ZnO (50 nm) and In_2O_3-SnO_2 (ITO, 350 nm) as transparent conductive window layer (Alliance CT100). Afterwards, for

Prog. Photovolt: Res. Appl. 2016; **24**:1359–1367 © 2016 John Wiley & Sons, Ltd.
DOI: 10.1002/pip

the standard optoelectronic characterization, $3 \times 3\,mm^2$ of cells were mechanically scribed using a manual microdiamond scriber (MR200, OEG Optical Metrology, Frankfurt, Germany). Additionally, selected cells of $5 \times 5\,mm^2$ in area were fabricated using Ni/Al metallic grids and MgF_2 anti-reflective coating.

Dark and illuminated J–V curves were measured using a calibrated Sun 3000 class AAA solar simulator (Abet Technologies, Milford, Connecticut, USA). Measurements were carried out at 25 °C, under AM1.5G 1-Sun illumination conditions (uniform illumination area of $15 \times 15\,cm^2$). The spectral response was measured using a Bentham PVE300 system calibrated with Si and Ge photodiodes, in order to obtain the EQE of the solar cells. TEM analysis were carried out using a Tecnai F30 from FEI company (Hillsboro, Oregon, USA) operated at 300 kV and equipped with a Tridiem image filter from Gatan Inc. (Abingdon, UK) for EELS measurements. The elemental EELS maps were generated by first decomposing the raw EELS hyperspectral datacube into its components of highest variance using the weighted principal component analysis algorithm as implemented in the MATLAB programming language. The first six components were found to explain approximately 99.8% of the spectral variance in the raw data and were used to reconstruct the data before extracting the elemental maps. A gamma curve was subsequently applied to the Zn and Sn maps to enhance visibility of the low intensity signal. The lamellae were prepared for TEM investigation using the focused ion beam *in situ* lift-out method and thinned to a final thickness of less than 100 nm using a 5-kV Ga+ beam. SEM images were obtained with a ZEISS (Carl Zeiss AG, Jena, Germany) Series Auriga microscope using 5 kV of accelerating voltage. ToF-SIMS measurements were performed with ION-TOF IV equipment, equipped with 25 kV of Bi cluster primary ion gun for analysis, and O2 and Cs ion guns for sputtering in depth profiling modes. The analyzed area was $50 \times 50\,\mu m$ with a cycle time of 100 µs and a time-to-digital converter resolution of 200 ps. C–V measurements were performed in the dark at room temperature with a frequency of 100 kHz and a modulation voltage of 50 mV using an impedance analyzer from Novocontrol Technologies (Montabaur, Germany). From C–V measurements, charge carrier concentration profiles were calculated assuming a relative dielectric permittivity of $\varepsilon = 8.5$ for CZTSe.

ACKNOWLEDGEMENTS

This research was supported by the Framework 7 program under the project KESTCELLS (FP7-PEOPLE-2012-ITN-316488), by Ministerio de Economía y Competitividad de España under the SUNBEAM project (ENE2013-49136-C4-1-R) and NOVACOST project (PCIN-2013-128-C02-01), and by the European Regional Development Funds (Fondo Europeo de Desarollo Regional (FEDER) Programa Competitivitat de Catalunya 2007–2013). Authors from IREC and the University of Barcelona belong to the M-2E (Electronic Materials for Energy) Consolidated Research Group and the XaRMAE Network of Excellence on Materials for Energy of the "Generalitat de Catalunya." S. G. thanks the Government of Spain for the Formación de Personal Investigador (FPI) fellowship (BES-2014-068533), and E. S. for the "Ramón y Cajal" fellowship (RYC-2011-09212). P. P. thanks the European Union for the JUMPKEST Marie Curie Individual Fellow (FP7-PEOPLE-2013-IEF- 625840).

REFERENCES

1. Todorov TK, Tang J, Bag S, Gunawan O, Gokmen T, Zhu Y, Mitzi DB. Beyond 11% efficiency: characteristics of state-of-the-art $Cu_2ZnSn(S,Se)_4$ solar cells. *Advanced Energy Materials* 2013; **3**: 34–38. DOI:10.1002/aenm.201200348.
2. Huang TJ, Yin X, Qi G, Gong H. CZTS-based materials and interfaces and their effects on the performance of thin film solar cells. *Physica Status Solidi - Rapid Research Letters* 2014; **8**: 735–762. DOI:10.1002/pssr.201409219.
3. Green MA, Emery K, Hishikawa Y, Warta W, Dunlop ED. Solar cell efficiency tables (version 46). *Progress in Photovoltaics: Research and Applications* 2015; **23**: 805–812. DOI:10.1002/pip.2637.
4. Mitzi DB, Gunawan O, Todorov TK, Barkhouse DAR. Prospects and performance limitations for Cu–Zn–Sn–S–Se photovoltaic technology. *Philosophical Transactions of the Royal Society A: Mathematical, Physical and Engineering Sciences* 2013; **371**: . DOI:10.1098/rsta.2011.0432.
5. Siebentritt S, Schorr S. Kesterites-a challenging material for solar cells. *Progress in Photovoltaics: Research and Applications* 2012; **20**: 512–519. DOI:10.1002/pip.2156.
6. Fairbrother A, García-Hemme E, Izquierdo-Roca V, Fontané X, Pulgarín-Agudelo FA, Vigil-Galán O, Pérez-Rodríguez A, Saucedo E. Development of a selective chemical etch to improve the conversion efficiency of Zn-rich Cu_2ZnSnS_4 solar cells. *Journal of the American Chemical Society* 2012; **134**: 8018–8021. DOI:10.1021/ja301373e.
7. Xie H, Sánchez Y, López-Marino S, Espíndola-Rodríguez M, Neuschitzer M, Sylla D, Fairbrother A, Izquierdo-Roca V, Pérez-Rodríguez A, Saucedo E. Impact of Sn(S,Se) secondary phases in $Cu_2ZnSn(S,Se)_4$ solar cells: a chemical route for their selective removal and absorber surface passivation. *ACS Applied Materials and Interfaces* 2014; **25**: 2–6. DOI:10.1021/am502609c.
8. López-Marino S, Sánchez Y, Placidi M, Fairbrother A, Espindola-Rodríguez M, Fontané X, Izquierdo-Roca

V, López-García J, Calvo-Barrio L, Pérez-Rodríguez A, Saucedo E. ZnSe etching of Zn-rich $Cu_2ZnSnSe_4$: an oxidation route for improved solar-cell efficiency. *Chemistry - A European Journal* 2013; **19**: 14814–14822. DOI:10.1002/chem.201302589.

9. Neuschitzer M, Sanchez Y, Olar T, Thersleff T, Lopez-Marino S, Oliva F, Espindola-Rodriguez M, Xie H, Placidi M, Izquierdo-Roca V, Lauermann I, Leifer K, Pérez-Rodríguez A, Saucedo E. The complex surface chemistry of kesterites: Cu/Zn re-ordering after low temperature post deposition annealing and its role in high performance devices. *Chemistry of Materials* 2015; **27**: 5279–5287. DOI:10.1021/acs.chemmater.5b01473.
10. Furuta K, Sakai N, Kato T, Sugimoto H, Kurokawa Y, Yamada A. Improvement of $Cu_2ZnSn(S,Se)_4$ solar cell efficiency by surface treatment. *Physica Status Solidi C* 2015; **12**: 704–707. DOI:10.1002/pssc.201400309.
11. Neuschitzer M, Sanchez Y, López-Marino S, Xie H, Fairbrother A, Placidi M, Haass S, Izquierdo-Roca V, Perez-Rodriguez A, Saucedo E. Optimization of CdS buffer layer for high-performance $Cu_2ZnSnSe_4$ solar cells and the effects of light soaking: elimination of crossover and red kink. *Progress in Photovoltaics: Research and Applications* 2015; **23**: 1660–1667. DOI:10.1002/pip.2589.
12. Messaoud KB, Buffiere M, Brammertz G, ElAnzeery H, Oueslati S, Hamon J, Kniknie BJ, Meuris M, Amlouk M, Poortmans J. Impact of the Cd^{2+} treatment on the electrical properties of $Cu_2ZnSnSe_4$ and Cu(In, Ga)Se_2 solar cells. *Progress in Photovoltaics: Research and Applications* 2015; **23**: 1608–1620. DOI:10.1002/pip.2599.
13. Su Z, Tan JMR, Li X, Zeng X, Batabyal SK, Wong LH. Cation substitution of solution-processed Cu_2ZnSnS_4 thin film solar cell with over 9% efficiency. *Advanced Energy Materials* 2015; **4**: 1500682. DOI:10.1002/aenm.201500682.
14. Gabor AM, Tuttle JR, Albin DS, Contreras MA, Noufi R, Hermann AM. High-efficiency $CuIn_xGa_{1-x}Se_2$ solar cells made from $(In_x,Ga_{1-x})_2Se_3$ precursor films. *Applied Physics Letters* 1994; **65**: 198–200. DOI:10.1063/1.112670.
15. Albin DS, Mooney GD, Duda A, Tuttle J, Matson R, Noufi R. Enhanced grain growth in polycrystalline $CuInSe_2$ using rapid thermal processing. *Solar Cells* 1991; **30**: 47–52. DOI:10.1016/0379-6787(91)90036-O.
16. Mousel M, Schwarz T, Djemour R, Weiss TP, Sendler J, Malaquias JC, Redinger A, Cojocaru-Mirédin O, Choi PP, Siebentritt S. Cu-rich precursors improve kesterite solar cells. *Advanced Energy Materials* 2014; **4**: 1300543. DOI:10.1002/aenm.201300543.
17. Carrete A, Shavel A, Fontané X, Montserrat J, Fan J, Ibáñez M, Saucedo E, Pérez-Rodríguez A, Cabot A. Antimony-based ligand exchange to promote crystallization in spray-deposited $Cu_2ZnSnSe_4$ solar cells. *Journal of the American Chemical Society* 2013; **135**: 15982–15985. DOI:10.1021/ja4068639.
18. Yuan M, Mitzi DB, Liu W, Kellock AJ, Chey SJ, Deline VR. Optimization of CIGS-based PV device through antimony doping. *Chemistry of Materials* 2010; **22**: 285–287. DOI:10.1021/cm903428f.
19. Nakada T, Honishi Y, Yatsushiro Y, Nakakoba H. Impacts of Sb and Bi incorporations on CIGS thin films and solar cells. *IEEE Photovoltaic Specialists Conference* 2011; 3527–3531. DOI:10.1109/PVSC.2011.6186709.
20. Zhou H, Song T, Hsu W, Luo S, Ye S, Duan H, Hsu C, Yang W, Yang Y. Rational defect passivation of $Cu_2ZnSn(S,Se)_4$ photovoltaics with solution-processed Cu_2ZnSnS_4 :Na nanocrystals. *Journal of the American Chemical Society* 2013; **135**: 15998–16001. DOI:10.1021/ja407202u.
21. Sutter-Fella CM, Stückelberger JA, Hagendorfer H, Mattina FL, Kranz L, Nishiwaki S, Uhl AR, Romanyuk YE, Tiwari AN. Sodium assisted sintering of chalcogenides and its application to solution processed $Cu_2ZnSn(S,Se)_4$ thin film solar cells. *Chemistry of Materials* 2014; **26**: 1420–1425. DOI:10.1021/cm403504u.
22. Li JV, Kuciauskas D, Young MR, Repins IL. Effects of sodium incorporation in Co-evaporated $Cu_2ZnSnSe_4$ thin-film solar cells. *Applied Physics Letters* 2013; **102**: 163905. DOI:10.1063/1.4802972.
23. Xin H, Vorpahl SM, Collord AD, Braly IL, Uhl AR, Krueger BW, Ginger DS, Hillhouse HW. Lithium-doping inverts the nanoscale electric field at the grain boundaries in $Cu_2ZnSn(S,Se)_4$ and increases photovoltaic efficiency. *Physical Chemistry Chemical Physics* 2015; **17**: 23859–23866. DOI:10.1039/C5CP04707B.
24. Yan Y, Jiang CS, Noufi R, Wei SH, Moutinho HR, Al-Jassim MM. Electrically benign behavior of grain boundaries in polycrystalline $CuInSe_2$ films. *Physical Review Letters* 2007; **99**: 235504. DOI:10.1103/PhysRevLett.99.235504.
25. Rau U, Taretto K, Siebentritt S. Grain boundaries in Cu(In, Ga)$(Se, S)_2$ thin-film solar cells. *Applied Physics A* 2009; **96**: 221–234. DOI:10.1007/s00339-008-4978-0.
26. Yin WJ, Wu Y, Wei SH, Noufi R, Al-Jassim MM, Yan Y. Engineering grain boundaries in $Cu_2ZnSnSe_4$ for better cell performance: a first-principle study. *Advanced Energy Materials* 2014; **4**: 1300712. DOI:10.1002/aenm.201300712.
27. Giraldo S, Neuschitzer M, Thersleff T, López-Marino S, Sánchez Y, Xie H, Colina M, Placidi M, Pistor P, Izquierdo-Roca V, Leifer K, Pérez-Rodríguez A, Saucedo E. Large efficiency improvement in $Cu_2ZnSnSe_4$ solar cells by introducing a superficial Ge nanolayer. *Advanced Energy Materials* 2015; **5**: 1501070. DOI:10.1002/aenm.201501070.

28. Bag S, Gunawan O, Gokmen T, Zhu Y, Mitzi DB. Hydrazine-processed Ge-substituted CZTSe solar cells. *Chemistry of Materials* 2012; **24**: 4588–4593. DOI:10.1021/cm302881g.
29. Khadka DB, Kim J. Band gap engineering of alloyed $Cu_2ZnGe_xSn_{1-x}Q_4$ (Q = S,Se) films for solar cell. *The Journal of Physical Chemistry C* 2015; **119**: 1706–1713. DOI:10.1021/jp510877g.
30. Oueslati S, Brammertz G, Buffière M, ElAnzeery H, Touayar O, Köble C, Bekaert J, Meuris M, Poortmans J. Physical and electrical characterization of high-performance $Cu_2ZnSnSe_4$ based thin film solar cells. *Thin Solid Films* 2015; **582**: 224–228. DOI:10.1016/j.tsf.2014.10.052.
31. Lee YS, Gershon T, Gunawan O, Todorov TK, Gokmen T, Virgus Y, Guha S. $Cu_2ZnSnSe_4$ thin-film solar cells by thermal co-evaporation with 11.6% efficiency and improved minority carrier diffusion length. *Advanced Energy Materials* 2015; **5**: 1401372. DOI:10.1002/aenm.201401372.
32. Kim S, Kim KM, Tampo H, Shibata H, Matsubara K, Niki S. Ge-incorporated $Cu_2ZnSnSe_4$ thin-film solar cells with efficiency greater than 10%. *Solar Energy Materials and Solar Cells* 2016; **144**: 488–492. DOI:10.1016/j.solmat.2015.09.039.
33. AbuShama JAJ, Noufi R, Johnston S, Ward S, Wu X. Improved performance in $CuInSe_2$ and surface-modified $CuGaSe_2$ solar cells. *IEEE Photovoltaic Specialists Conference* 2005; 299–302. DOI:10.1109/PVSC.2005.1488128.
34. Kato T, Hiroi H, Sakai N, Muraoka S, Sugimoto H. Characterization of front and back interfaces on Cu_2ZnSnS_4 thin-film solar cells. *European Photovoltaic Solar Energy Conference and Exhibition* 2012; 2236–2239. DOI:10.4229/27thEUPVSEC2012-3CO.4.2.
35. Wang W, Winkler MT, Gunawan O, Gokmen T, Todorov TK, Zhu Y, Mitzi DB. Device characteristics of CZTSSe thin-film solar cells with 12.6% efficiency. *Advanced Energy Materials* 2014; **4**: 1301465. DOI:10.1002/aenm.201301465.
36. Haass SG, Diethelm M, Werner M, Bissig B, Romanyuk YE, Tiwari AN. 11.2% efficient solution processed kesterite solar cell with a low voltage deficit. *Advanced Energy Materials* 2015; **5**: 1500712. DOI:10.1002/aenm.201500712.
37. Larramona G, Levcenko S, Bourdais S, Jacob A, Choné C, Delatouche B, Moisan C, Just J, Unold T, Dennler G. Fine-tuning the Sn content in CZTSSe thin films to achieve 10.8% solar cell efficiency from spray-deposited water-ethanol-based colloidal inks. *Advanced Energy Materials* 2015; **5**: 1501404. DOI:10.1002/aenm.201501404.
38. Vauche L, Risch L, Sánchez Y, Dimitrievska M, Pasquinelli M, Monsabert TG, Grand PP, Jaime-Ferrer S, Saucedo E. 8.2% pure selenide kesterite thin-film solar cells from large-area electrodeposited precursors. *Progress in Photovoltaics: Research and Applications* 2016; **24**: 38–51. DOI:10.1002/pip.2643.
39. Heske C, Richter G, Chen Z, Fink R, Umbach E, Riedl W, Karg F. Influence of Na and H_2O on the surface properties of $Cu(In,Ga)Se_2$ thin films. *Journal of Applied Physics* 1997; **82**: 2411–2420. DOI:10.1063/1.366096.
40. Kronik L, Cahen D, Schock HW. Effects of sodium on polycrystalline $Cu(In,Ga)Se_2$ and its solar cell performance. *Advanced Materials* 1998; **10**: 31–36. DOI:10.1002/(SICI)1521-4095(199801)10:1<31::AID-ADMA31>3.0.CO;2-3.
41. Zellner MB, Birkmire RW, Eser E, Shafarman WN, Chen JG. Determination of activation barriers for the diffusion of sodium through CIGS thin-film solar cells. *Progress in Photovoltaics: Research and Applications* 2003; **11**: 543–548. DOI:10.1002/pip.515.
42. Haight R, Shao X, Wang W, Mitzi DB. Electronic and elemental properties of the $Cu_2ZnSn(S,Se)_4$ surface and grain boundaries. *Applied Physics Letters* 2014; **104**: 033902. DOI:10.1063/1.4862791.

SUPPORTING INFORMATION

Supporting information may be found in the online version of this article.

SUPPORTING INFORMATION

10.6% efficiency Cu2ZnSnSe4 solar cells through innovative absorber engineering with Ge superficial nanolayer

Sergio Giraldo, Thomas Thersleff, Gerardo Larramona, Markus Neuschitzer, Paul Pistor, Klaus Leifer, Alejandro Pérez-Rodríguez, Camille Moisan, Gilles Dennler, and Edgardo Saucedo*

This Supporting Information section contains important materials to support the main hypotheses raised in the main manuscript. Table S1 summarizes the J_{SC} values obtained from both, illuminated J-V curves and EQE spectra. Notably, the difference between the J_{SC} obtained from integrating the EQE and the one directly measured under the Sun simulator tends to increase with increasing Ge content. This suggests some correlation between the Ge application and the existence of some light-dependent effect on the carrier collection, which is under further investigation.

Table S1. J_{SC} extracted from J-V illuminated curves, from EQE and difference between both values.

Sample	J_{SC} from J-V (mA cm^{-2})	J_{SC} from EQE (mA cm^{-2})	ΔJ_{SC} (mA cm^{-2})
Ref	27.5	31.7	4.2
Ge5	29.2	33.3	4.1
Ge7.5	29.0	33.6	4.6
Ge10	29.5	33.5	4.0
Ge12.5	29.7	34.4	4.7
Ge15	29.7	35.1	5.4
Ge25	30.9	35.4	4.5
Ge50	30.6	36.1	5.5

In Figure S1, the evolution of the series resistance and the shunt resistance of the devices presented in Figure 1 of the manuscript is presented. According to this figure the R_{Sh} strongly increases in the Ge thickness range where the maximum efficiency is obtained. This suggests that Ge could contribute to some grain boundary passivation among other effects. For higher Ge thicknesses the R_{Sh} is decreased and is probably related to the observed formation of secondary phases due to the decomposition of the main kesterite phase when in contact with the excess of Ge-Se liquid phase. On the contrary, the R_S slightly decreases in the Ge-thickness optimum region, and then considerably increases in agreement with the general deterioration of the devices properties.

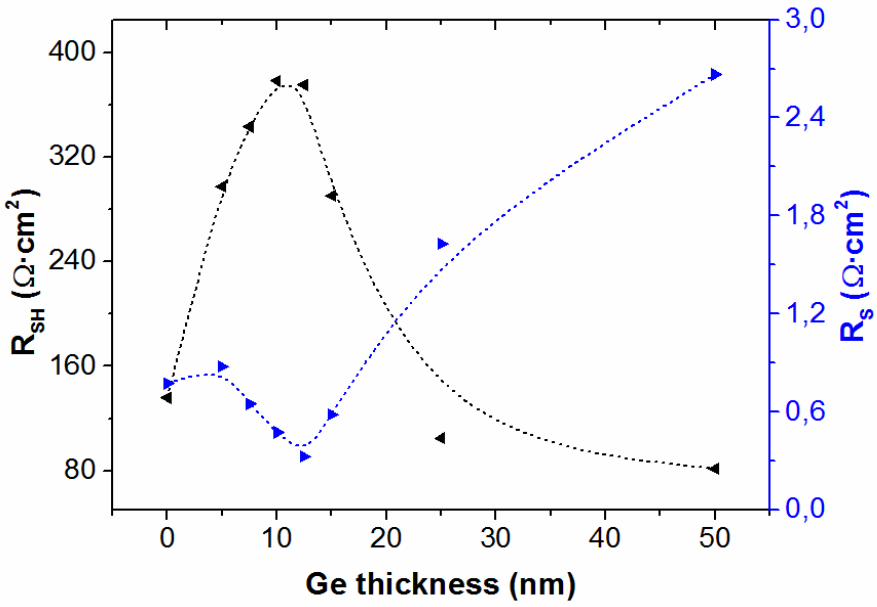

Figure S1. Evolution of the R_S and R_{Sh} with the Ge thickness.

In Figure S2, one of the typical superficial morphologies that are clearly detected at the CZTSe surface for high Ge thicknesses (Ge25 and Ge50 samples), with a needle-like aspect. Preliminary EDX analysis shows that these structures are made at least of Na and O, supporting the idea that are formed during the crystallization process, due to the dissolution of Na-species at the grain boundaries in the Ge-Se liquid phase. During the cooling-down process, these Na-containing structures are crystallized at the surface, explaining the lower Na content, and concomitantly the lower carrier concentration of the Ge25 and Ge50 absorbers.

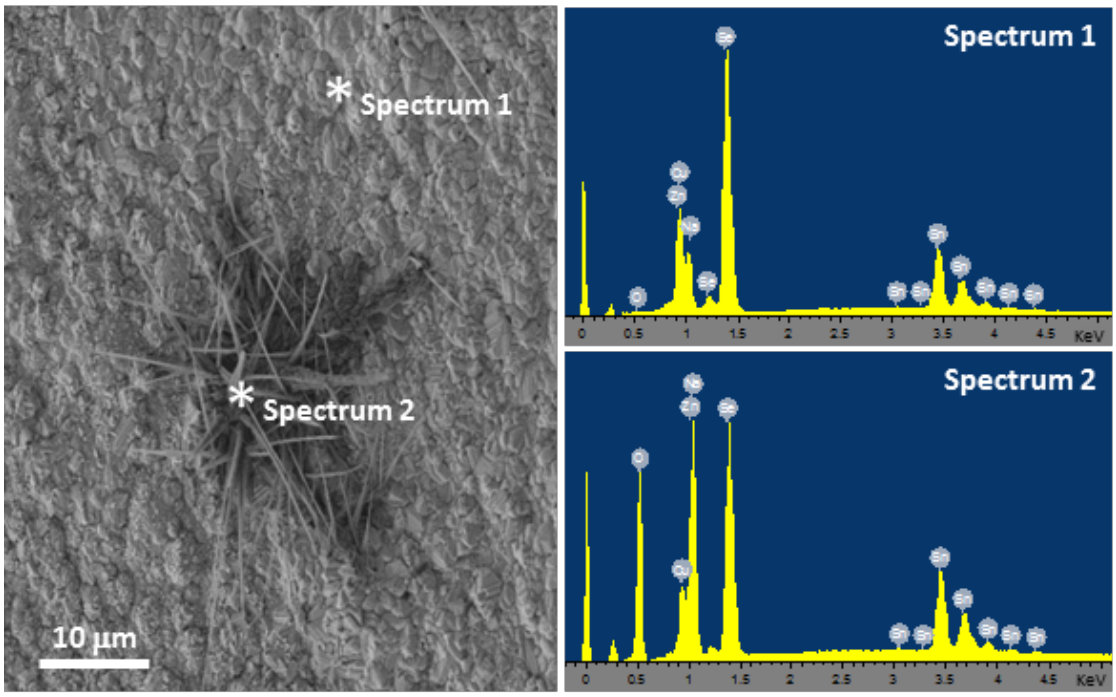

Figure S2. SEM image of a typical needle-like morphology observed in the as-annealed absorbers of the samples Ge25 and Ge50, before any chemical etching (left-side). EDX spectra showing that these structures are mainly formed by Na and O (right-side).

Finally, Table S2 shows the composition of the absorbers synthesized with different Ge thicknesses, corroborating the significant Sn-loss when large amounts of Ge are introduced, as is proposed in the manuscript.

Table S2. Compositional XRF measurements of absorbers produced with different Ge thicknesses.

Sample	Cu (%)	Zn (%)	Sn (%)	Ge (%)	Se (%)
Ref	21.94	15.34	11.97	0.00	50.75
Ge10	21.97	15.23	11.67	<0.1*	51.12
Ge25	21.95	15.65	10.06	1.35	50.99

*Ge is detected, but the concentration is below the quantification limit.

Chapter 3

Exploring the role of Ge doping in high efficiency solar cells

In line with the previous chapter focused on the use of Ge as an effective dopant in CZTSe, and after proving its significant beneficial effect, the aim of this chapter is to shed light on the origin and the mechanisms involved in this approach, and to further explore the role of this element in high performing CZTSe solar cells.

In the literature, the incorporation of Ge in kesterite-based solar cells has led to several important improvements. First Ge-alloyed CZTSSe device was reported in 2012 by IBM, with a 40% Ge-substituted absorber, showing a higher V_{OC}, although very subtle impact on power conversion efficiency (from 9.07% to 9.14%) and no improvement of the V_{OC} deficit.[92] In any case, these were promising results indicating an alternative way to tailor the band-gap of CZTSSe absorber layers, and demonstrated compatibility of Ge with kesterite state-of-the-art processes. Derived from this band-gap tuning properties arises the possibility of using Ge to achieve graded band-gap absorbers, like in CIGS with the use of Ga or S gradients. This was demonstrated by Kim et al., who fabricated Ge-alloyed CZTS with a variation of the band-gap from 1.85 eV (back) to 1.62 eV (front), leading to higher J_{SC} (23.3 mA/cm^2 vs 19.5 mA/cm^2) and V_{OC} (0.52 V vs 0.48 V) compared to the constant flat band-gap case.[95] At the same time, Hages et al. reported nanocrystal-based CZTGeSSe absorbers with tunable band-gap, combining for the first time Sn/Ge and S/Se alloying.[93] In that study, maximum conversion efficiencies of up to 9.4% were achieved (8.4% efficiency for reference CZTSSe) with a Ge content of 30 at.%, allowing for increased minority charge carrier lifetimes as well as reduced voltage-dependent charge carrier collection, also pointing out the potential impact of Ge on annihilation of deep levels (likely related to Sn). More recently, Hillhouse's group at the University of Washington performed a complete study of CZTGeSSe devices as function of Ge/(Ge+Sn) ratio in a broad composition range (from 0% to 90%), using spray coated absorbers and molecular inks.[55] Best results were obtained with 25% Ge relative content leading to an 11.0% efficiency (band-gap of about 1.2 eV), with a remarkable reduction of the V_{OC} deficit. In parallel, and corroborating some of the findings reported in the publications presented in Chapter 2, AIST researchers in Japan synthesized Ge-alloyed CZTSe with efficiencies above 10%, through sequential process (co-evaporation followed by thermal annealing).[94] Similar to the enhanced crystallization showed in our previous papers, in this work the annealing environment containing $GeSe_2$ led to substantially improved morphological properties, obtaining flat surfaces, dense morphologies and large grains. Following the same approach, just some months later, the same group demonstrated a Ge-incorporated CZTSe solar cell with a conversion efficiency of 12.3%.[54] The most noteworthy results included an improvement of the V_{OC} deficit by reducing band tailing, and a reduced carrier recombination at the absorber/buffer interface and/or in the space-charge region, leading to high FF values. Additionally, Khadka and colleagues also corroborated the improved grain growth, compactness of film texture and crystallinity, together with a remarkable efficiency improvement, and showed a decrease in diode ideality factor, suppression of crossover effect (between white and dark J-V curves), and reduction of defects level in Ge-

incorporated CZTSSe solar cell devices.[96]

In summary, Ge incorporation has demonstrated: the possibility to increase the V_{OC} by widening the band-gap; the potential for graded band-gap concepts; a remarkable improvement of grain growth and crystallinity; increased minority charge carrier lifetimes; and large potential to reduce the V_{OC} deficit in current kesterite technology. But, with the drawback of relying on large amounts of Ge (20-40% Ge-substitution), compromising the sustainability of the technology, since it is considered a critical raw material by the European Commission.

In this context, the study of alternative approaches using small amounts of Ge becomes crucial to further develop long-term sustainable technologies based mainly on earth-abundant elements. Regarding the origin of the positive effect of Ge doping in CZTSe solar cells, several hypotheses have been formulated and are presented below:

- Surface modification: the initial idea behind the use of Ge superficial nanolayers on top of the precursors was to incorporate Ge at the very surface of the absorbers, leading to a graded band-gap towards the absorber surface. Higher band-gap values at the surface are expected to lower the interface recombination and, thus, increasing the open-circuit voltage. This effect has been widely demonstrated in CIGS technology by using In/Ga or S/Se alloying to increase the band-gap towards the absorber surface.[97,98] Nevertheless, in previously presented publications, we already demonstrated that almost no traceable amounts of Ge are detected when adding such small quantities in the precursors, and no changes neither in the band-gap nor in the absorber surface structure are observed.
- Formation of a flux agent: as shown in the previous chapter, the formation of Ge-Se phases that decompose incongruently into Ge_xSe_y (Se 85%) liquid phase, and volatile $GeSe_2$ gas phase has been proposed explaining both, the low Ge incorporation in the CZTSe, and the notably improved crystallinity (as illustrated in Figure 3.1).

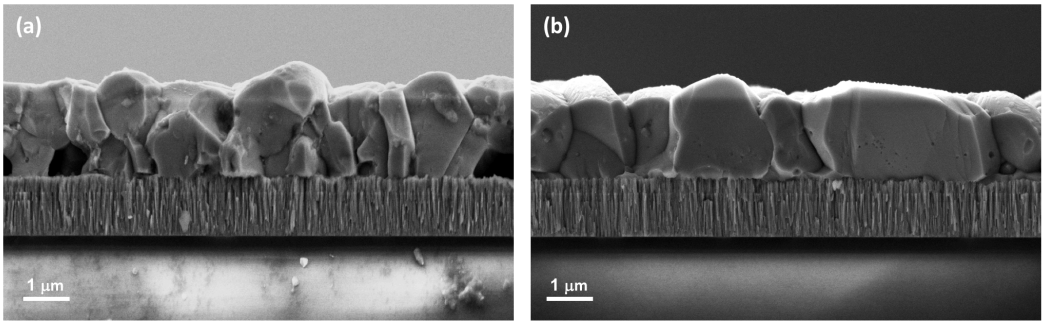

Figure 3.1. Cross-sectional SEM pictures of (a) reference CZTSe sample without Ge; (b) 10 nm Ge-containing CZTSe sample.

- Defect levels modification: the impact of small amounts of Ge on the defects formation has been demonstrated, showing the beneficial effect of about 10 nm of Ge by making shallower the shallow defect present in reference CZTSe samples, and annihilating (or strongly reducing) a deep defect, as can be seen in Figure 3.2. In that work, Neuschitzer et al. also proved the formation of a deep defect when higher amounts of Ge (50 nm) are used, proposing a dynamic defect model to explain this behavior, and emphasizing the importance of a careful control of the composition of group IV elements as a key factor to achieve high performance kesterite devices.[99]

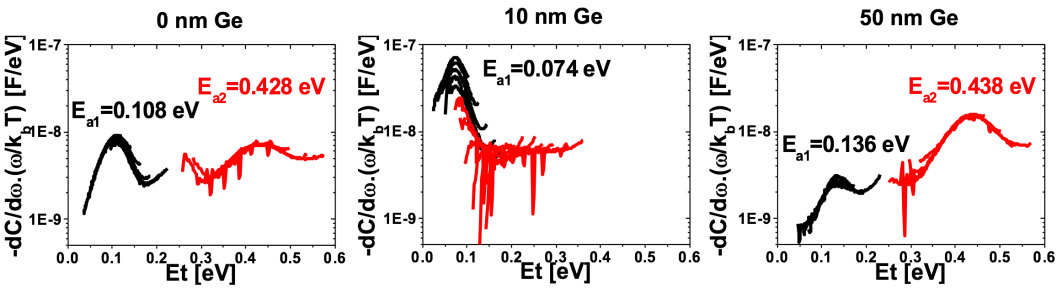

Figure 3.2. Defect spectra derived from C-f measurements for samples fabricated with 0 nm Ge (reference CZTSe), 10 nm Ge, and 50 nm Ge.

- Interaction with Na: strong interaction between Ge and Na has been observed during the thermal annealing process, with a clear impact on the Na content and thus on the doping level of the absorbers, indicating that Ge could help to control the alkali concentration in kesterite bulk and surface. Moreover, this might correlate with the idea that Ge is forming Ge-Se liquid phases at the surface during the selenization process that can act as a flux agent and, at the same time, control the doping level of the CZTSe absorber. This point will be further discussed in the following chapter.
- Impact on grain boundaries: the presence of two distinct types of grain boundaries has been revealed by a detailed microstructural analysis of high efficiency Ge-doped samples, as presented in one of the following publications included in this chapter. The chemistry of these different grain boundaries has been studied in detail using electron energy loss spectroscopy (EELS) and energy dispersive X-ray spectroscopy (EDX). Further discussion on the nature of and possible technological implications of these characteristic grain boundaries can be found throughout the paper.

In this chapter, we investigate in depth mechanisms underlying the Ge boost on CZTSe solar cells and suggest alternative mechanism based on the reaction scheme

during the annealing process. Differences in the reaction schemes during selenization for samples with and without Ge are analyzed in detail by EDX, XRF, XRD and Raman spectroscopy with multi-wavelength excitation, demonstrating how rather small amounts of Ge modify the reaction pathways of CZTSe. Ultimately, after optimizing a new approach using Ge nanolayers below and above metallic stack precursors, a record 11.8% efficiency is achieved. On the whole, here we present a detailed study of grain boundaries nature in Ge-doped CZTSe solar cells, completed with a deep investigation of the mechanisms behind the use of small quantities of Ge and a new approach to eliminate potentially detrimental grain boundaries, leading to high performance kesterite solar cells, which are among the best reported in the literature for CZTSe.

This chapter includes the following two publications: "Chemically and morphologically distinct grain boundaries in Ge-doped $Cu_2ZnSnSe_4$ solar cells revealed with STEM-EELS", and "How small amounts of Ge modify the formation pathways and crystallization of kesterites" with a detailed investigation of grain boundaries nature in Ge-doped CZTSe, the mechanisms underlying the Ge boost and how Ge affects the formation pathways of kesterite CZTSe.

Materials and Design 122 (2017) 102–109

Contents lists available at ScienceDirect

Materials and Design

journal homepage: www.elsevier.com/locate/matdes

Chemically and morphologically distinct grain boundaries in Ge-doped $Cu_2ZnSnSe_4$ solar cells revealed with STEM-EELS

Thomas Thersleff [a,*], Sergio Giraldo [b], Markus Neuschitzer [b], Paul Pistor [b], Edgardo Saucedo [b], Klaus Leifer [a]

[a] Department of Engineering Sciences, Uppsala University, Box 534, 75121 Uppsala, Sweden
[b] Catalonia Institute for Energy Research (IREC), 08930 Sant Adrià del Besòs, Barcelona, Spain

HIGHLIGHTS

- Advanced analytical STEM investigation of a Ge-doped CZTSe film with 10.1% efficiency performed
- Two types of grain boundaries identified
- Chemical segregation of absorber layer into two stoichiometrically-distinct layers observed
- Lower grain boundaries are poorly connected, propagate parallel to the back contact, and have SnO nanoinclusions
- Well-connected, straight grain boundaries are Cu-rich and appear in the upper half of the film

GRAPHICAL ABSTRACT

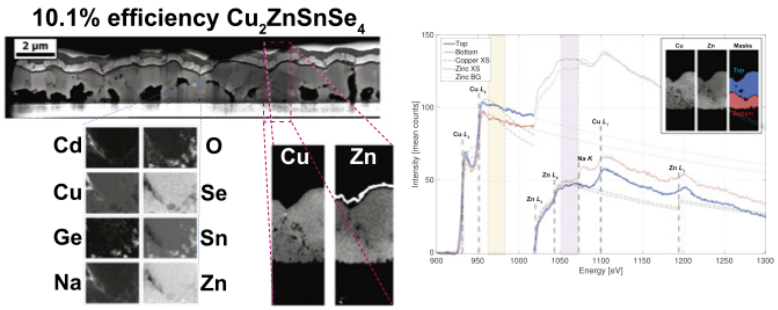

ARTICLE INFO

Article history:
Received 9 December 2016
Received in revised form 8 February 2017
Accepted 23 February 2017
Available online 24 February 2017

Keywords:
$Cu_2ZnSnSe_4$ (CZTSe)
Kesterites
Thin film solar cell
Scanning Transmission Electron Microscopy (STEM)
Electron Energy-Loss Spectroscopy (EELS)
Grain boundary

ABSTRACT

Critical to the future development of $Cu_2ZnSnSe_4$ (CZTSe) materials is a comprehensive understanding of the underlying nanoscale mechanisms responsible for reduced performance. Investigating these mechanisms is challenging since they arise on the nanoscale, yet manifest themselves over macroscopic regions. Here, we present an analytical study combining Scanning Transmission Electron Microscopy (STEM), sample preparation, and hyperspectral Electron Energy Loss Spectroscopy (EELS) mapping techniques to meet this challenge. We apply our method to a Ge-doped CZTSe sample with a measured efficiency of 10.1%, revealing that its microstructure is dominated by two distinct types of grain boundaries. The first type appears in the upper half of the absorber separating large grains. These are Cu-enriched, Se-poor, and have varying amounts of O. The second type of grain boundary is largely parallel to the substrate and appears predominately in the lower half of the absorber where the Cu/Zn ratio of the kesterite material is slightly lower. These grain boundaries contain voids and Sn oxide nanoparticles, exhibit high concentrations of Na, Cd, and S, and Cu assumes a higher valence state. We conclude with a discussion on the nature of and possible technological implications of these grain boundaries in this system.

1. Introduction

Recent progress in solar cells based on earth abundant kesterite absorbers ($Cu_2ZnSnSe_4$ – CZTSe or Cu_2ZnSnS_4 – CZTS as well as their solid solutions), has been mainly driven by the optimization of the current density and the fill factor of the devices [1]. The currently published record devices evidence that the low open circuit voltage is the main

* Corresponding author at: Department of Materials and Environmental Chemistry (MMK), Stockholm University, SE-10691 Stockholm, Sweden.
E-mail address: thomas.thersleff@mmk.su.se (T. Thersleff).

http://dx.doi.org/10.1016/j.matdes.2017.02.077
0264-1275/

obstacle impeding competitive efficiency levels in comparison to more mature chalcogenide technologies, like CdTe and Cu(In,Ga)Se_2 (CIGS) [2–4]. The most commonly cited causes for this deficit are Cu/Zn order-disorder [5,6] compositional/electrostatic/band-gap fluctuations [5,7], and grain boundary characteristics [8,9]. Studying these effects directly is challenging due to the complexity of the CZTSe absorber, which consists of an intricate interplay with the heterojunction [10–12], grain boundaries [9,10,12–14], and the back contact interface [15,16].

The grain boundaries in particular have been extensively studied in recent years, as their pervasiveness and complex chemistry is believed to have an enormous impact on overall efficiency. Yin et al. used first-principle density functional calculations to propose that some defects types such as Zn_{Sn}, Na^{+}_{i} and O_{Se} located at the grain boundaries, could be beneficial for the device efficiency, as they might eliminate deep gap states and create hole barriers and electron sinks at the grain boundaries [13]. Kim et al. used atomic scale observation to demonstrate that partial substitution of Se by O at the grain boundaries efficiently inhibits electron-hole recombination and, in consequence, blocks hole transport [9]. Sardashti et al., proposed a grain boundary passivation mechanism by correlating photovoltaic devices with high performance and the presence of Cu-depleted and SnO_x rich grain boundaries [12]. Xin et al. proposed that the presence of alkaline atoms at the grain boundaries (in this case Li), can invert the polarity of the electric field in this region, repelling the minority carrier electrons through the compensation of copper vacancies (Li_{Cu} defects) and the reduction of Zn_{Cu} donors [14]. Xu et al. used spatially mapped Raman spectroscopy and scanning probe microscopy to reveal that deviations in Cu stoichiometry can be found in the grain boundaries [17]. They also observed horizontal grain boundaries, and, although their chemical nature was not studied, they proposed that these grain boundaries could act as barriers against the transportation of minority carriers. Finally, Schwarz et al. reported a complete nanoscale characterization of grain and grain boundaries using atomic probe microscopy [18]. They observe that either Cu-enriched or Cu-poor grains can exist in kesterites depending on the thermal history of the sample. ZnSe was also detected in the vicinity of these grain boundaries and is dissolved after an annealing at 500 °C, together with the diffusion of Na and K towards the interfaces.

All of these works underscore the complexity of grain boundaries in kesterites, suggesting that a deeper understanding will require investigating the nanoscale compositional fluctuations and applying the results to the grain boundary networks observed on the absorber layer macroscale. Experimentally, this is a daunting task, as it requires the combination of techniques having a nanoscale spatial resolution with a field of view that is at least on the micron scale. For these reasons, many previous investigations on high efficiency systems have limited the field of view [19] or use a sampling rate that precludes the identification of nanoscale fluctuations [20]. Consequently, despite the considerable progress represented by these studies, the exact nature and chemistry of the grain boundaries in kesterites remains an open question.

In this report, we address this challenge by presenting a refined methodological approach for analytical Scanning Transmission Electron Microscopy (STEM) analysis of thin film solar cells in the kesterite family. The methodology first uses the sample preparation of a large sample area with the Focused Ion Beam (FIB) to classify the observed grain boundaries in terms of their morphology. The chemistry of these different grain boundaries is then studied in detail using Electron Energy Loss Spectroscopy (EELS) and Energy Dispersive X-ray Spectroscopy (EDX). In all cases, we acquire analytical datasets with a wide field of view to guide further experiments with a higher resolution.

Using this methodology, we report a detailed analysis of structural, morphological, and compositional trends in a Ge-doped CZTSe sample with an efficiency of 10.1% (among the state-of-the-art efficiencies for this fabrication route). Our findings reveal that there are at least two morphologically and distinct types of grain boundaries present in this system. These are concentrated in the upper and lower portions of the absorber layer, and the subsequent analytical STEM investigation reveals that they have very different chemical compositions. The more detailed EELS analysis of the lower grain boundaries shows that they contain large amounts of tin oxide and that copper assumes a higher valence state, whereas the upper grain boundaries are slightly Cu-enriched and contain trace amounts of oxygen. We can also link the extent of these grain boundaries to a change in the overall composition of the absorber layer, which appears to have different stoichiometries in the upper and lower halves. Finally, the potential impact of both types of grain boundaries on the device performance and fabrication is discussed.

2. Results

2.1. Overview of $Cu_2ZnSnSe_4$ solar cell: revealing the grain structure

The subject of this investigation is a Ge-doped CZTSe solar cell with an efficiency of 10.1%. The main optoelectronic characteristics such as IV-curves and external quantum efficiency as well as a cross-sectional scanning electron micrograph of the solar cell can be found in Giraldo et al. [19], where this specific solar cell is denoted as Ge10. An overview of the full TEM lamella is presented in Fig. 1. In Fig. 1a, a series of bright field (BF) TEM images are stitched together. The contrast generation mechanism for this image is primarily diffraction contrast, and it reveals that the absorber layer is polycrystalline with an average grain diameter on the order of hundreds of nanometers. The lamella is suspended in a vacuum, which appears bright in this image, clearly demonstrating a number of pores which appear in proximity to the Mo back contact layer (at the bottom of the image). The through-thickness of the lamella is presented in Fig. 1b. Here, a series of energy filtered BF images were used to separate out the elastic and inelastic contributions to scattering, allowing for a measurement of the number of inelastic scattering events

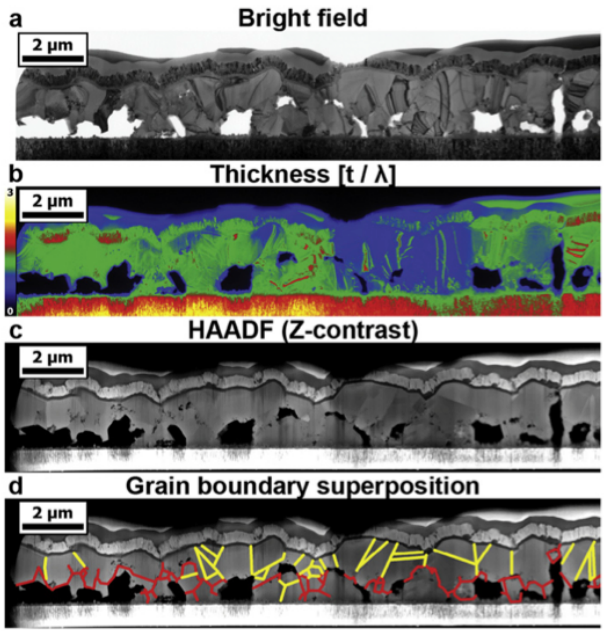

Fig. 1. In (a), the bright field panorama of the Ge10 sample is presented. In (b), the thickness map of the entire lamella is shown in values of t/lambda, as denoted on the color bar at left. In (c), the HAADF overview is presented, showing a strong Z-contrast. Finally, (d) shows an estimation of the propagation of the two types of grain boundaries discussed in this work. The upper grain boundaries are yellow while the lower grain boundaries are red.

undergone by the traversing electrons. The probability of such an event increases as a function of both thickness t and the mean free path λ, which is material dependent. The color scale in Fig. 1b is presented on a scale of 0–3 t/λ, and the regions of blue correspond to an absolute thickness of <50 nm in the CZTSe absorber layer for the acceleration voltage used. Fig. 1c shows the same overview acquired in Scanning TEM (STEM) mode using a High Angle Annular Dark Field (HAADF) detector. The dominant contrast mechanism for this method is mass thickness, and a clear distinction between the individual layers of the solar cell stack can be made in this image.

A critical observation that is particularly evident in Fig. 1c is that the absorber film can be described as having an upper and lower layer. The upper layer is dense and consists of larger, rounded grains while the lower layer contains numerous pores and smaller grains. Intriguingly, the grain boundaries in the upper layer are predominately straight and appear to propagate along well-defined crystallographic planes largely perpendicular to the substrate, while the grains in the lower layer propagate largely parallel to the substrate and are more meandering in nature, even exhibiting micropores. This relationship is emphasized by tracing these grain boundaries onto the HAADF overview, which is presented in Fig. 1d. In this text, we will refer to the mainly straight grain boundaries in the upper layer as "upper GBs" and accordingly the mainly horizontal and more meandering grain boundaries in the lower part "lower GBs".

To assess the overall composition of the film, EELS was performed in STEM mode to acquire a hyperspectral datacube containing information on all of the elements of interest, a technique known as Electron Spectrum Imaging (ESI) [21]. The results of this analysis are presented in Fig. 2. The pixel sampling size in this dataset is 12 nm, allowing for a detailed overview but at the cost of deeper analysis of smaller features such as grain boundaries. The X-ray yield of the electron/sample interaction was simultaneously acquired and dispersed with Energy Dispersive X-ray Spectroscopy (EDX). However, the count rates for EDX in the equipment used for this experiment are significantly lower than what is possible for EELS, yielding very noisy real-space maps. Of note is that the Se edge was only partially captured in EELS due to technical constraints. Accordingly, the EELS map for Se in Fig. 2 is replaced with EDX. The very low count rate in this map makes it impossible to accurately remove the background, so the intensity values contain both background and Se information in summation.

The EELS maps at first suggest that the stoichiometry of the absorber layer is largely invariant over the scanning region, as little variation above the noise level for the different elements can be observed. The lower grain boundaries are visible in these maps and appear to be largely deficient in Cu and Zn, while a slight Sn enrichment is observed. The Sn-rich regions correlate to O enrichment as well. No significant amounts of Cd or Mo were observed within the absorber layer. S is present in trace amounts within the lower grain boundaries and evidence for it is also seen in the $MoSe_2$ reaction layer. It was also attempted to make maps of Na and Ge. However, Ge was not observed due to the large lateral sampling size of the electron probe and its low inelastic scattering cross section, while the Na map was too noisy to confidently describe its spatial distribution.

To better assess compositional variations within the film on this dataset, the EELS datacube was compressed using Principal Component Analysis (PCA). The resulting maps from Cu and Zn are shown in the Fig. 3b and c. The contrast in these maps has also been steeply enhanced to distinguish between very small compositional variations. Using this technique, it was observed that the upper and lower layers of the CZTSe film do, indeed, have slightly different Cu:Zn stoichiometry. To better quantify these small variations, we segmented the Zn map presented in Fig. 3 by using contrast thresholding to yield two separate binary masks representing the upper and the lower layers. The exact extent of these binary masks is presented in Fig. 3d, where blue represents the upper layer and red represents the lower layer. These masks were then applied to the raw EELS datacube and the mean of the spectra from each mask was computed. The resulting two spectra are presented in Fig. 3a for the energy range 900–1300 eV, covering the Cu, Zn, Na, and Ge edges. Prior to plotting, the pre-edge background was modeled using an inverse power law fit in the range 900–925 eV and extrapolated under the ionization edges before subtraction. Subsequently, the individual spectra were deconvolved using the EELS low-loss spectra acquired from the exact same region [22]. The amounts of Cu and Zn were quantified by generating Hartree-Slater cross sections (denoted XS) for each of these ionization edges under the experimental conditions and scaling these to the experimental data within the shaded windows shown in Fig. 3a. Care was taken to avoid the EELS fine structure features such as the L_3 and L_2 ionization edges as well as the Na K edge that appears at 1172 eV. The energy offsets and widths of the scaling windows were 31 eV and 20 eV, respectively. Under these conditions, the Cu:Zn ratio was observed to be 1.49 ± 0.03 and 1.40 ± 0.03 for the top and bottom layers, respectively. The error bars represent the estimated statistical error caused by choosing both the background and quantification intervals, and were determined by varying these over an energy range of 20 eV. These films were purposefully produced to be Cu-poor, and the targeted Cu:Zn ratio of the metallic precursor is 1.38 [19]. This was confirmed by X-ray Fluorescence (XRF) measurements, which determined the Cu:Zn ratio of the metallic precursor to

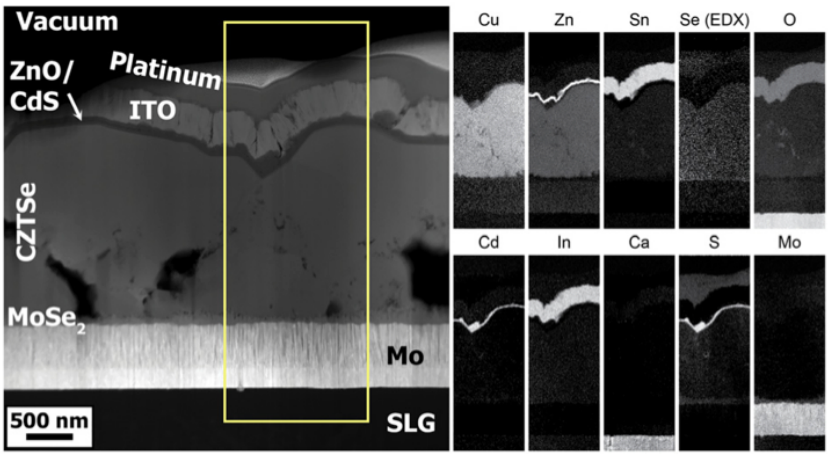

Fig. 2. Hyperspectral EELS maps taken over a large field of view on the prepared lamella capturing a meandering grain boundary. The Se map has been replaced by the EDX results since the EELS results are only partially available due to descan effects. The elemental maps were generated over an area of 1.57 × 4.32 μm. These maps were generated from the raw EELS data.

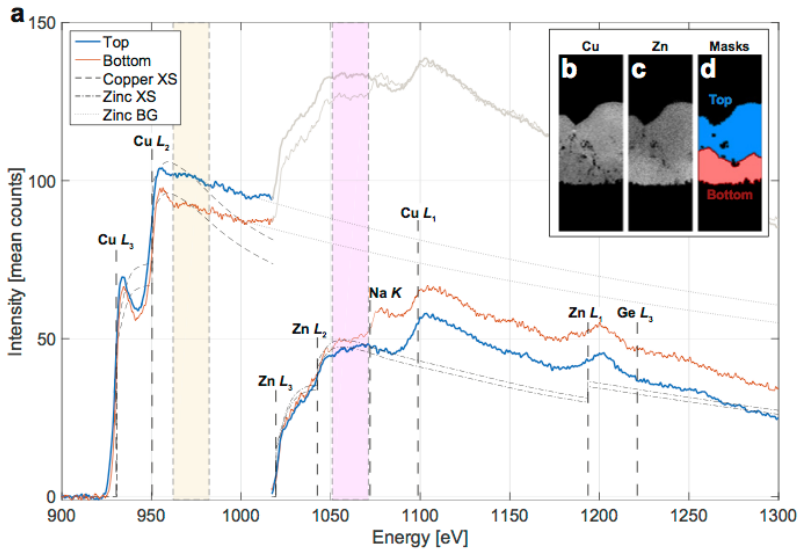

Fig. 3. Inset: PCA-treated and contrast-enhanced maps from the data presented in Fig. 2 (dimensions 1.57 × 4.32 μm) showing the spatial distribution of Cu (b) and Zn (c). These maps were used to generate the binary masks for the top and bottom layers presented in (d). The mean spectra from these regions are plotted in (a). Hartree-Slater cross-sections (XS) were scaled in the windows denoted by the shaded boxes. The spectra were background (BG) subtracted prior to the Cu and Zn edges. The energy ranges chosen for the BG models were 900–930 eV for Cu and 975–1005 eV for Zn. The models for the Zn pre-edge BG are shown along with the subtracted spectra.

be 1.39. Following selenization, XRF measurements indicate that the ratio increased to 1.46. This value is in close agreement with the average ratio over the entire lamella as determined by EELS. This suggests that the bottom layer retains the nominal stoichiometry whereas the Cu:Zn ratio in the upper layer is slightly increased.

In addition to the Cu:Zn ratio, the spectra from these two regions reveal that Na is readily incorporated into the lower layer, while it is completely absent from the upper layer. The data acquired with a higher spatial resolution (see Figs. 4 and 5 below) suggest that Na may be concentrated at pore edges and grain boundaries, which are more prominent in the lower layer, in agreement with previous studies [18,23]. A similar observation can be made for the ratio between the Cu L_3 and L_2 edges. This ratio, known as the "white-line ratio" appears to differ significantly between the two layers, with the more pronounced edges in the bottom layer indicating that the Cu *d*-shell is partially emptied. This can be caused by electron charge transfer and implies that the valence state of the copper in the lower layer is slightly higher than in the upper layer [24]. Finally, the conditions used for this dataset were not optimized for the detection of Ge, making it thus difficult to detect in the spectra from Fig. 3a. However, a very slight onset can be observed in the upper film, consistent with the finding that Ge tends to remain in the upper region of these films [19]. The presence of Ge is explored more thoroughly in the high resolution datasets below as well as previous studies [19].

2.2. Lower grain boundaries

To better understand the composition of the two different types of grain boundaries, higher resolution EELS and EDX ESI maps of both of these grain boundaries were acquired. In Fig. 4, qualitative elemental maps from a meandering grain boundary connecting two pores are presented. For this grain boundary, the sample was tilted such that the EDX collection efficiency was maximized. The same region was scanned four separate times to acquire all of the elements of interest in the energy loss spectrum. The EDX maps were generated by adding all of the individual EDX datacubes, whereas the EELS maps are generated from single scans. The EELS maps were also denoised using PCA, as described below.

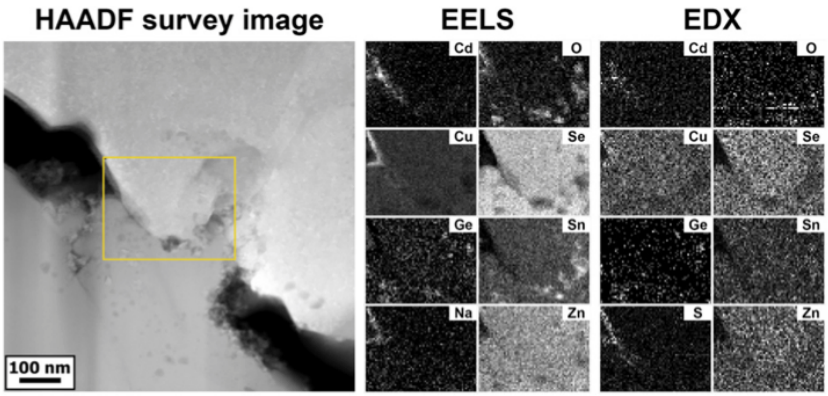

Fig. 4. Elemental maps from a meandering grain boundary. At left, the survey region acquired with the HAADF detector is shown and the scanning region measuring 321 × 250 nm is indicated with a box. EELS and EDX elemental maps for 8 individual elements are presented at right. The EELS maps are generated following PCA decomposition.

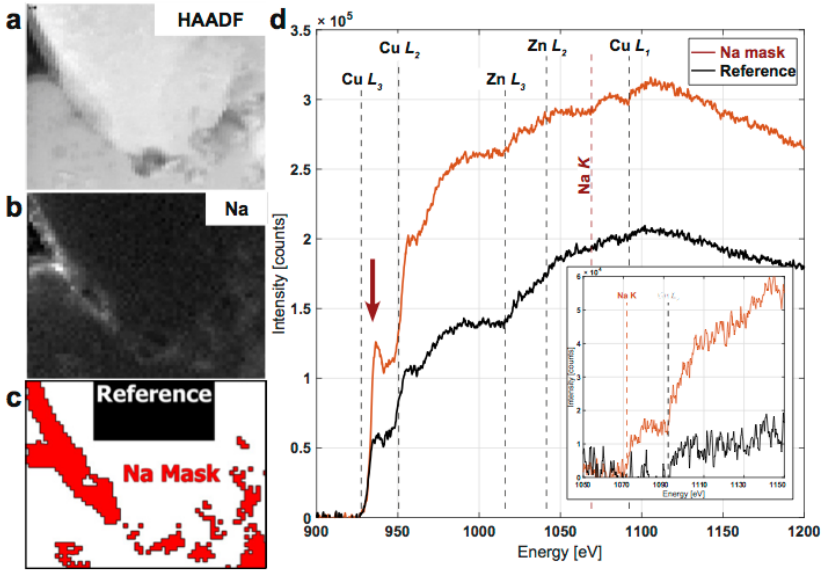

Fig. 5. In (a), the HAADF scan region (321 × 250 nm) is presented along with the map for Na (b), generated using PCA. This map was thresholded to create a binary mask shown below in (c). A reference region formed with the same number of pixels is also provided in black. This mask was used to select the spectra from the raw data to sum over, and the result is presented in (d) following background subtraction. A zoomed in graph from the Na region is inset in (d), following background subtraction directly preceding the edge onset.

The maps reveal that the grain boundary itself consists of a large number of Sn and O rich inclusions. A small number of Ge-rich nanoinclusions are observed here as well, and their spatial positions correlate well with the presence of O and Sn. Critically, these SnO_x particles appear to incorporate Na. There is some evidence that these particles are also rich in Zn; however, they appear to be quite poor in Cu and Se.

In contrast to the grain boundary, the sides of the pores appear to have a very different composition. These regions appear to be relatively rich in Cu, somewhat rich in O, Cd, and S, and poor in Zn, Sn, and Se. The Cd and S are presumably sourced from the thin CdS heterojunction.

While these maps are generated by statistically treating the raw data, it is very instructive to use them as a guide for exploring the raw data. In Fig. 5c, the Na map was thresholded to generate a mask from which the raw spectra can be summed. This allows a direct comparison between the EELS spectra from the Na-rich regions to that of the bulk absorber, and the comparison between these two spectra is presented in Fig. 5d. The Na edge is clearly visible in the EELS data from the Na mask as a low intensity edge approximately 20 eV prior to the Cu L_1 edge. This indicates that the Na observed in Fig. 3a is largely confined to the lower grain boundaries and is less prominent in the absorber itself. Of additional interest with these spectra is the variation in the electronic fine structure of the Cu edge. The Cu present in the Na-mask exhibits a strongly enhanced L_3 peak with respect to L_2, indicating a change in the white line ratio. This is a consequence of a reduction in the Cu *d*-shell occupancy, which is consistent with a modification of the chemical environment [24,25]. In this case, it is likely caused by the formation of CuO or Cu_2O. Hence, this variation of the EELS near edge structure suggests that the electrical conductivity of these grain boundaries is reduced, indicating a passivation effect.

2.3. Upper grain boundaries

A detailed compositional analysis of the straight grain boundaries is more complex than the meandering grain boundaries because they can be atomically sharp, thereby requiring a much higher spatial resolution. Moreover, the grain boundary must be oriented nearly perpendicular to the electron beam to ensure accurate detection, necessitating very thin TEM lamellae. For randomly oriented grain boundaries, it is not always obvious when it is oriented perpendicular to the electron beam, and some meandering throughout the lamella thickness is common.

A grain boundary running parallel to the film normal that propagates from an internal pore was chosen for this analysis. The grain on the "right" side (referred to as "Grain 1") was tilted to the zone axis [8 −2 −1] to which the grain boundary appeared to be largely parallel. The grain on the left side (referred to as "Grain 2") was indexed as lying close to the [−2 1 2] zone axis, meaning that the two grains are rotated 84.17° from each other. This region has a thickness of below 50 nm, as measured from the EELS low-loss spectra.

The composition of this grain boundary and the surrounding regions was investigated using the same STEM-ESI methods as previously. The region was scanned twice, providing both a wide field of view to analyze the entire grain boundary as well as a higher resolution scan from a selected region. Both scans are presented in Fig. 6. The first scan probed a small area with a pixel sample size of 5 Å, and this region is marked with the green box. The second scan covered the entire grain boundary using a pixel sample size of 15 Å and is marked with the red box. The probe diameter in both instances was kept under 2 Å, and the probe position was varied in a mosaic pattern within each individual pixel (known as sub-pixel scanning). The dispersion was set to 0.5 eV/channel to cover a sufficiently large energy range for the Cd and Se edges. The spectral data were treated by PCA before the maps in Fig. 6 were generated.

The larger scan region reveals that this straight grain boundary is clearly Cu enriched with respect to the grain volume, along its entire length from the pore to the heterojunction. It also appears to be largely Zn and Sn neutral and Se poor. O in this scan was difficult to detect, but its presence is made clearer in the higher resolution scan. In this case, oxygen-rich nanoinclusions are observed to be strung along the grain boundary. These do not appear to be directly correlated to any of the other elements observed, raising the possibility that an additional undetected secondary phase is present, or that the O is mainly combined with Cu. In the larger map, O becomes deficient in the grain boundary towards the bottom in the region that is closely connected to the SnO_x nanoparticles, which appear within a lower grain boundary. This gives the impression that the presence of the Sn generates a chemical potential along the grain boundary that causes residual O to diffuse outwards. Neither Ge nor Na was detected within the meandering grain boundary

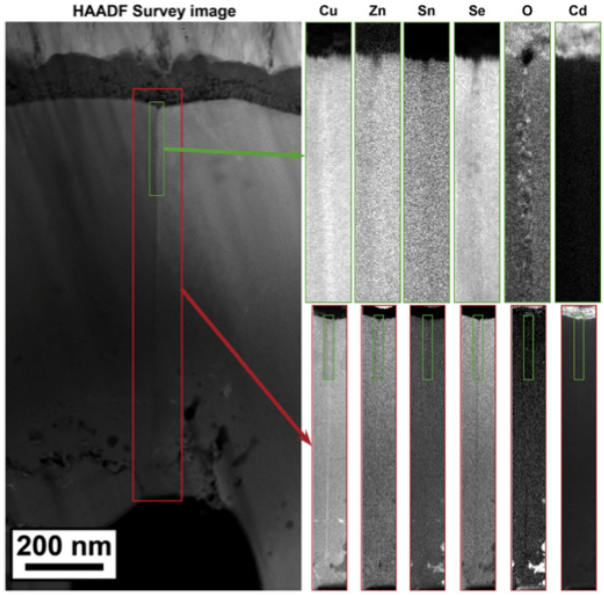

Fig. 6. At left, the HAADF survey image of a grain boundary in the upper film is presented. Two scanning regions were acquired, denoted by the red and green boxes. The elemental maps from these regions are presented at right. The smaller scan region has a sampling size of 8 Å and dimensions 32 × 200 nm, while the larger scan region has a sample size of 5 nm and has dimensions 400 × 3395 nm. Gamma curves have been applied to the lower O and Cd maps to enhance the visualization of low contrast regions.

in this dataset; however, this is expected from the much larger probe diameter that was used compared to Figs. 4 and 5. Finally, Cd is clearly observed within the edges of the large internal pores at the bottom of the larger map. However, there is no clear evidence for its presence within the grain boundary itself, despite being a potential diffusion path for Cd to follow from the heterostructure into the pores.

3. Discussion

These results clearly demonstrate that the kesterite absorber layer in this high efficiency solar cell stack consists of two morphologically and chemically distinct regions. The lower region close to the back contact appears to retain the target Cu:Zn stoichiometry and morphologically consists of small grains and large voids, whereas the upper layer appears slightly richer in Cu and morphologically is dominated by large grains, fewer pores, and straight grain boundaries. The natural frontier between these two regions is delineated by microporous "meandering" grain boundaries which propagate largely parallel to the substrate. While our previous interpretation of this system was based on time-of-flight secondary ion mass spectrometry (TOF-SIMS) measurements that appear to show an increase in both the Cu and Zn concentrations in proximity to the back contact [19], these new results allow us to refine our interpretation of the formation and growth of the absorber layer, and we discuss this here.

The similarity of the Cu:Zn stoichiometry to the target stoichiometry near the back contact indicates that the target chemistry is successfully transferred to the substrate during the metallic precursor deposition process. Subsequently, when the Ge nanolayer is deposited on the surface and the entire film is exposed to air, it appears that a thin oxide layer forms. It is presently unclear how this oxide layer propagates into the absorber layer. The oxide nanoinclusions found in the lower grain boundaries might be a relic of this thin germanium oxide layer. In this picture, the compact upper part of the absorber is formed by an up-diffusion of the metals through this layer and their consequent reaction with the selenium during the reactive annealing, while the lower layer is formed by a downward diffusion of selenium. Previously we have published evidence in favor of the formation of a liquid Ge-Se phase at the surface of metallic precursor during the selenization [19]. In this tentative description of the selenization reaction, the liquid phase acts as a crystallization flux agent, explaining the larger, more equiaxed grains present in the upper layer as well as the straight grain boundaries.

Oxygen likely reacts with the kesterite at this stage, forming SnO_x. These SnO_x deposits precipitate out at the meandering grain boundary, where they disrupt the target stoichiometry and form the meandering, porous grain boundaries we observe largely parallel to the substrate. The removal of Sn results in a concentration of Cu, Zn, and Se in the upper layer. Zn and Se react to form ZnSe, and this segregates to the surface, as seen in other Ge-doped samples [26]. This detrimental secondary phase is subsequently removed through the etching process [27]. The formation and elimination of ZnSe means that the Cu:Zn ratio in the upper region is increased, and excess Cu accumulates at the grain boundaries, as observed in Fig. 6. This hypothesis supports the conclusion that the composition of the absorber layer is at least partially controlled by the lower grain boundaries, and that their composition can be mediated by controlling the Ge nanolayer content. Hence, this appears to be a means for gaining enhanced control over the absorber layer chemistry.

The diverse morphology and stoichiometry of this system is somewhat surprising given the high efficiency of 10.1% measured from this sample. First, while the potentially beneficial passivating effect of O at the grain boundaries has previously been discussed in the literature [9,12,13], the tin oxide rich boundaries observed in this work are mainly found to be parallel to the substrate (horizontal). They are microporous and are aligned perpendicular to the current flow from the front to the back electrode. As a consequence, they can be expected to act as a current barrier and severely increase the series resistance of the device, consequently lowering the fill factor and device efficiency. The fact that the efficiency is so high despite these shortcomings leads us to believe that there is a complex trade-off between the beneficial growth properties imparted by the presence of these grain boundaries and their detrimental morphology and chemistry. Second, all the previous complete chemical analysis indicate that the Cu-enriched upper layer and straight grain boundaries should also be detrimental for high efficiency devices [18], which is also contradicted by the properties of this device. To explain this possible discrepancy, we examine the particular process that kesterites devices use to employ, which includes an oxidation step. We note that, immediately after fabrication, the solar cells exhibit rather low efficiencies (<4%). It is only following a post-fabrication thermal treatment of the complete devices under air at 250 °C for 20 min that the solar cells are "activated," increasing the efficiency towards values higher than 10% [11,19]. On average, after the soft annealing of the complete device in air, the V_{OC} increases 30–40%, the J_{SC} between 40 and 50%, and the FF 50–60% (all values in relative), and the efficiency 4–5 times. This impressive improvement has previously been associated with the diffusion of Cu into the CdS heterojunction, improving band matching [11]. Nevertheless the impact on the grain boundary properties has been not described up to now. It appears that mainly the shunt resistance is improved during the soft annealing. We connect this feature with the oxidation of the grain boundaries, creating oxides species (in this case for the upper grain boundaries with Cu-related oxides), allowing these samples to achieve excellent efficiencies even in the presence of Cu-enriched grain boundaries. Hence, we conclude that the detrimental properties of a Cu-enriched upper layer and grain boundaries can be at least partially mitigated through controlled oxidation, thereby ameliorating the imbalance in stoichiometry caused by the presence of the SnO_x-rich grain boundaries. Both of these hypotheses are being tested with future experiments in an attempt to identify the most efficient means of gaining control over the device morphology, chemistry, and ultimately performance.

4. Conclusions

In summary, we have presented a detailed microstructural analysis of one Ge-doped CZTSe thin film solar cell device with an efficiency of 10.1%. The wide field of view afforded by the sample preparation technique reveals the presence of two distinct types of grain boundaries that extend over the length of the entire lamella. One of these grain boundary types is meandering in nature and grows largely parallel to the substrate, and denotes the boundary between two CZTSe layers with differing Cu:Zn ratios. The second type of grain boundary is Cu-enriched and more straight, and this appears predominately in the Cu-enriched upper layer. While these grain boundaries may act as a limitation to device efficiency, it appears that this can be at least partially ameliorated through their controlled oxidation during the soft post-deposition annealing in air. We are currently investigating whether these grain boundaries can provide a way to tune the composition of the absorber layer and can thus improve control over device fabrication.

5. Experimental section

The CZTSe absorber was prepared onto a glass/Mo substrate using a sequential process. In the first step, Cu/Sn/Cu/Zn metallic precursor stacks are sputtered fixing the following metallic ratios: Cu/(Sn + Zn) = 0.75 and Zn/Sn = 1.20. On top of the metallic precursors, a 10 nm thick Ge layer is deposited by evaporation, which helps crystallization and improves the photovoltaic parameters of the devices [19]. In the second step, the precursors are annealed under Se and Sn atmosphere in a graphite box, using the conditions reported elsewhere [19]. Then, the absorber is sequentially etched in $KMnO_4$ acidic solution and $(NH_4)_2S$ in order to remove possible ZnSe phase at the surface [27,28], and finally in KCN solution (2% w/v, room temperature, 2 min). Immediately after, CdS (50 nm thick) is deposited by chemical bath deposition [29], and the device is completed by i-ZnO (50 nm) and ITO (250 nm). Using this procedure, devices with efficiency exceeding 10% are routinely obtained at IREC.

For the preparation of the TEM samples, a cross-sectional lamella was thinned to electron transparency over a lateral span of 20 μm using the Focused Ion Beam (FIB) In-Situ Lift-out method [30,31], permitting the observations of morphological and microstructural trends over a large field of view with nanometer resolution. The TEM investigations were carried out on a Tecnai F30 TEM from FEI Company operated at 300 kV. Bright field images and thickness maps in Fig. 1 were acquired on a 2K UltraScan 1000 CCD camera from Gatan, Inc. EELS data were acquired using a post-column Tridiem energy filter from Gatan, Inc. The TEM was operated in STEM Nanodiffraction mode for the acquisition of the EELS and ESI data presented in Figs. 2–6. The collection angle for these datasets was 32 mrad while the convergence angle was either 28 mrad for wide field of view maps or 9 mrad for higher resolution (reducing the blurring effect caused by spherical aberration, which is not corrected in this microscope). The Z-contrast imaging data was acquired using a High Angle Annular Dark Field (HAADF) detector by Gatan, Inc. with a minimum collection angle of 64 mrad.

The ESI datasets from Figs. 2–6 were treated post-acquisition to extract the elemental maps. This was done by extrapolating a pre-edge inverse power law background underneath the ionization edge of interest and subtracting it [22]. An example of this is provided in Fig. 3a. One exception to this was the isolation of O, as this strongly overlaps with the Sn ionization edge. Accordingly, the Sn edge was modeled using a 2nd order log polynomial model and subtracted instead of the simple inverse power law. With the exception of the data in Fig. 3, this workflow yields a qualitative assessment of the spatial distribution of the individual elements. The maps in Figs. 3–6 were generated after compressing the data using Principal Component Analysis (PCA). The algorithm used for this comes from the Matlab statistics toolbox. Care was taken to ensure that the data were not overcompressed, and the treated maps were consistently compared to maps generated from the raw data to ensure this. For EELS quantification or detailed analysis of the spectral shapes (Figs. 3 and 5), PCA was only used to generate spatial maps identifying regions of interest. The spectra themselves are not compressed and have the same noise characteristics as the raw data.

Author contributions

T.T. primarily designed and executed the TEM experiments, performed the analysis, wrote the paper, and prepared the figures. S.G., M.N., P.P., and E.S. were responsible for the fabrication of the sample and the experimental design to achieve high efficiencies. S.G., E.S., and K.L. assisted with the TEM experimental design. E.S., P.P., and K.L contributed to the structure of the manuscript. K.L. further assisted with the analysis of the TEM results. All authors read and commented on the manuscript.

Abbreviations

EELS	Electron Energy-Loss Spectroscopy
ESI	Electron Spectrum Imaging
PCA	Principal Component Analysis
HAADF	High Angle Annular Dark Field
TEM	Transmission Electron Microscopy
STEM	Scanning Transmission Electron Microscopy
EDX	Energy Dispersive X-ray Spectroscopy
XS	(scattering) cross Section
BF	Bright Field
TOF-SIMS	Time-Of-Flight Secondary Ion Mass Spectrometry

Acknowledgement

FEI Company is acknowledged for the preparation of a second TEM lamella that was used for the acquisition of the data in Fig. 6.

This research was supported by Seventh Framework Programme under the project KESTCELLS (FP7-PEOPLE-2012-ITN-316488) and by MINECO (Ministerio de Economía y Competitividad de España) under the NASCENT project (ENE2014-56237-C4-1-R) and NOVACOST project (PCIN-2013-128-C02-01). Authors from IREC and the University of Barcelona belong to the M-2E (Electronic Materials for Energy) Consolidated Research Group and the XaRMAE Network of Excellence on Materials for Energy of the "Generalitat de Catalunya". SG thanks the Government of Spain for the FPI fellowship (BES-2014-068533) and E.S. for the "Ramón y Cajal" fellowship (RYC-2011-09212). P.P. thanks the European Union for the JUMPKEST Marie Curie Individual Fellow (FP7-PEOPLE-2013-IEF-625840).

References

[1] X. Liu, Y. Feng, H. Cui, F. Liu, X. Hao, G. Conibeer, D.B. Mitzi, M. Green, The current status and future prospects of kesterite solar cells: a brief review, Prog. Photovolt. Res. Appl. 24 (2016) 879–898, http://dx.doi.org/10.1002/pip.2741.

[2] Y.S. Lee, T. Gershon, O. Gunawan, T.K. Todorov, T. Gokmen, Y. Virgus, S. Guha, $Cu_2ZnSnSe_4$ thin-film solar cells by thermal co-evaporation with 11.6% efficiency and improved minority carrier diffusion length, Adv. Energy Mater. 5 (2015) 1401372, http://dx.doi.org/10.1002/aenm.201401372.

[3] T.K. Todorov, J. Tang, S. Bag, O. Gunawan, T. Gokmen, Y. Zhu, D.B. Mitzi, Beyond 11% efficiency: characteristics of state-of-the-art $Cu_2ZnSn(S,Se)_4$ solar cells, Adv. Energy Mater. 3 (2013) 34–38, http://dx.doi.org/10.1002/aenm.201200348.

[4] W. Wang, M.T. Winkler, O. Gunawan, T. Gokmen, T.K. Todorov, Y. Zhu, D.B. Mitzi, Device characteristics of CZTSSe thin-film solar cells with 12.6% efficiency, Adv. Energy Mater. 4 (2014) 1301465, http://dx.doi.org/10.1002/aenm.201301465.

[5] G. Rey, T.P. Weiss, J. Sendler, A. Finger, C. Spindler, F. Werner, M. Melchiorre, M. Hála, M. Guennou, S. Siebentritt, Ordering kesterite improves solar cells: a low temperature post-deposition annealing study, Sol. Energy Mater. Sol. Cells 151 (2016) 131–138, http://dx.doi.org/10.1016/j.solmat.2016.02.014.

[6] S. Bourdais, C. Choné, B. Delatouche, A. Jacob, G. Larramona, C. Moisan, A. Lafond, F. Donatini, G. Rey, S. Siebentritt, A. Walsh, G. Dennler, Is the Cu/Zn disorder the main culprit for the voltage deficit in kesterite solar cells? Adv. Energy Mater. 6 (2016) 1502276, http://dx.doi.org/10.1002/aenm.201502276.

[7] T. Gokmen, O. Gunawan, T.K. Todorov, D.B. Mitzi, Band tailing and efficiency limitation in kesterite solar cells, Appl. Phys. Lett. 103 (2013) 103506, http://dx.doi.org/10.1063/1.4820250.
[8] T.J. Huang, X. Yin, G. Qi, H. Gong, CZTS-based materials and interfaces and their effects on the performance of thin film solar cells, Phys. Status Solidi RRL 08 (2014) 735–762, http://dx.doi.org/10.1002/pssr.201409219.
[9] J.H. Kim, S.-Y. Choi, M. Choi, T. Gershon, Y.S. Lee, W. Wang, B. Shin, S.-Y. Chung, Atomic-scale observation of oxygen substitution and its correlation with hole-transport barriers in $Cu_2ZnSnSe_4$ thin-film solar cells, Adv. Energy Mater. 6 (2016) 1501902, http://dx.doi.org/10.1002/aenm.201501902.
[10] R. Haight, X. Shao, W. Wang, D.B. Mitzi, Electronic and elemental properties of the $Cu_2ZnSn(S,Se)_4$ surface and grain boundaries, Appl. Phys. Lett. 104 (2014) 033902, http://dx.doi.org/10.1063/1.4862791.
[11] M. Neuschitzer, Y. Sanchez, T. Olar, T. Thersleff, S. Lopez-Marino, F. Oliva, M. Espindola-Rodriguez, H. Xie, M. Placidi, V. Izquierdo-Roca, I. Lauermann, K. Leifer, A. Pérez-Rodriguez, E. Saucedo, Complex surface chemistry of kesterites: Cu/Zn reordering after low temperature postdeposition annealing and its role in high performance devices, Chem. Mater. 27 (2015) 5279–5287, http://dx.doi.org/10.1021/acs.chemmater.5b01473.
[12] K. Sardashti, R. Haight, T. Gokmen, W. Wang, L.-Y. Chang, D.B. Mitzi, A.C. Kummel, Impact of nanoscale elemental distribution in high-performance kesterite solar cells, Adv. Energy Mater. 5 (2015) 1402180, http://dx.doi.org/10.1002/aenm.201402180.
[13] W.-J. Yin, Y. Wu, S.-H. Wei, R. Noufi, M.M. Al-Jassim, Y. Yan, Engineering grain boundaries in $Cu_2ZnSnSe_4$ for better cell performance: a first-principle study, Adv. Energy Mater. 4 (2014) 1300712, http://dx.doi.org/10.1002/aenm.201300712.
[14] H. Xin, S.M. Vorpahl, A.D. Collord, I.L. Braly, A.R. Uhl, B.W. Krueger, D.S. Ginger, H.W. Hillhouse, Lithium-doping inverts the nanoscale electric field at the grain boundaries in $Cu_2ZnSn(S,Se)_4$ and increases photovoltaic efficiency, Phys. Chem. Chem. Phys. 17 (2015) 23859–23866, http://dx.doi.org/10.1039/C5CP04707B.
[15] S. López-Marino, M. Placidi, A. Pérez-Tomás, J. Llobet, V. Izquierdo-Roca, X. Fontané, A. Fairbrother, M. Espíndola-Rodríguez, D. Sylla, A. Pérez-Rodríguez, E. Saucedo, Inhibiting the absorber/Mo-back contact decomposition reaction in $Cu_2ZnSnSe_4$ solar cells: the role of a ZnO intermediate nanolayer, J. Mater. Chem. A 1 (2013) 8338, http://dx.doi.org/10.1039/c3ta11419h.
[16] J.J. Scragg, J.T. Wätjen, M. Edoff, T. Ericson, T. Kubart, C. Platzer-Björkman, A detrimental reaction at the molybdenum back contact in $Cu_2ZnSn(S,Se)_4$ thin-film solar cells, J. Am. Chem. Soc. 134 (2012) 19330–19333, http://dx.doi.org/10.1021/ja308862n.
[17] M. Xu, B. Liu, G. Graham, X. Pan, High resolution characterization of grain boundaries in $Cu_2ZnSnSe_4$ solar cells synthesized by nanoparticle selenization, Sol. Energy Mater. Sol. Cells 157 (2016) 171–177, http://dx.doi.org/10.1016/j.solmat.2016.05.020.
[18] T. Schwarz, O. Cojocaru-Mirédin, P. Choi, M. Mousel, A. Redinger, S. Siebentritt, D. Raabe, Atom probe tomography study of internal interfaces in $Cu_2ZnSnSe_4$ thin-films, J. Appl. Phys. 118 (2015) 095302, http://dx.doi.org/10.1063/1.4929874.
[19] S. Giraldo, M. Neuschitzer, T. Thersleff, S. López-Marino, Y. Sánchez, H. Xie, M. Colina, M. Placidi, P. Pistor, V. Izquierdo-Roca, K. Leifer, A. Pérez-Rodríguez, E. Saucedo, Large efficiency improvement in $Cu_2ZnSnSe_4$ solar cells by introducing a superficial Ge nanolayer, Adv. Energy Mater. (2015) 1501070, http://dx.doi.org/10.1002/aenm.201501070.
[20] M. Werner, D. Keller, S.G. Haass, C. Gretener, B. Bissig, P. Fuchs, F. La Mattina, R. Erni, Y.E. Romanyuk, A.N. Tiwari, Enhanced carrier collection from CdS passivated grains in solution-processed $Cu_2ZnSn(S,Se)_4$ solar cells, ACS Appl. Mater. Interfaces 7 (2015) 12141–12146, http://dx.doi.org/10.1021/acsami.5b02435.
[21] C. Jeanguillaume, C. Colliex, Spectrum-image: the next step in EELS digital acquisition and processing, Ultramicroscopy 28 (1989) 252–257, http://dx.doi.org/10.1016/0304-3991(89)90304-5.
[22] R.F. Egerton, Electron Energy-Loss Spectroscopy in the Electron Microscope, Springer, 2011http://dx.doi.org/10.1007/978-1-4419-9583-4.
[23] T. Gershon, B. Shin, N. Bojarczuk, M. Hopstaken, D.B. Mitzi, S. Guha, The role of sodium as a surfactant and suppressor of non-radiative recombination at internal surfaces in Cu_2ZnSnS_4, Adv. Energy Mater. 5 (2015) 1400849, http://dx.doi.org/10.1002/aenm.201400849.
[24] D.H. Pearson, C.C. Ahn, B. Fultz, Measurements of 3*d* occupancy from Cu $L_{2,3}$ electron-energy-loss spectra of rapidly quenched CuZr, CuTi, CuPd, CuPt, and CuAu, Phys. Rev. B 50 (1994) 12969–12972, http://dx.doi.org/10.1103/PhysRevB.50.12969.
[25] D.H. Pearson, B. Fultz, C.C. Ahn, Measurements of 3d state occupancy in transition metals using electron energy loss spectrometry, Appl. Phys. Lett. 53 (1988) 1405–1407, http://dx.doi.org/10.1063/1.100457.
[26] S. Giraldo, T. Thersleff, G. Larramona, M. Neuschitzer, P. Pistor, K. Leifer, A. Pérez-Rodríguez, C. Moisan, G. Dennler, E. Saucedo, $Cu_2ZnSnSe_4$ solar cells with 10.6% efficiency through innovative absorber engineering with Ge superficial nanolayer, Prog. Photovolt. Res. Appl. (2016)http://dx.doi.org/10.1002/pip.2797.
[27] S. López-Marino, Y. Sánchez, M. Placidi, A. Fairbrother, M. Espindola-Rodríguez, X. Fontané, V. Izquierdo-Roca, J. López-García, L. Calvo-Barrio, A. Pérez-Rodríguez, E. Saucedo, ZnSe etching of Zn-rich $Cu_2ZnSnSe_4$: an oxidation route for improved solar-cell efficiency, Chem. Eur. J. 19 (2013) 14814–14822, http://dx.doi.org/10.1002/chem.201302589.
[28] H. Xie, Y. Sánchez, S. López-Marino, M. Espíndola-Rodríguez, M. Neuschitzer, D. Sylla, A. Fairbrother, V. Izquierdo-Roca, A. Pérez-Rodríguez, E. Saucedo, Impact of Sn(S,Se) secondary phases in $Cu_2ZnSn(S,Se)_4$ solar cells: a chemical route for their selective removal and absorber surface passivation, ACS Appl. Mater. Interfaces 6 (2014) 12744–12751, http://dx.doi.org/10.1021/am502609c.
[29] M. Neuschitzer, Y. Sanchez, S. López-Marino, H. Xie, A. Fairbrother, M. Placidi, S. Haass, V. Izquierdo-Roca, A. Perez-Rodriguez, E. Saucedo, Optimization of CdS buffer layer for high-performance $Cu_2ZnSnSe_4$ solar cells and the effects of light soaking: elimination of crossover and red kink, Prog. Photovolt. Res. Appl. 23 (2015) 1660–1667, http://dx.doi.org/10.1002/pip.2589.
[30] R.M. Langford, C. Clinton, In situ lift-out using a FIB-SEM system, Micron 35 (2004) 607–611, http://dx.doi.org/10.1016/j.micron.2004.03.002.
[31] M. Schaffer, B. Schaffer, Q. Ramasse, Sample preparation for atomic-resolution STEM at low voltages by FIB, Ultramicroscopy 114 (2012) 62–71, http://dx.doi.org/10.1016/j.ultramic.2012.01.005.

Energy & Environmental Science

PAPER

How small amounts of Ge modify the formation pathways and crystallization of kesterites

Cite this: DOI: 10.1039/c7ee02318a

S. Giraldo,[a] E. Saucedo,[*a] M. Neuschitzer,[a] F. Oliva,[a] M. Placidi,[a] X. Alcobé,[b] V. Izquierdo-Roca,[a] S. Kim,[c] H. Tampo,[c] H. Shibata,[c] A. Pérez-Rodríguez[ad] and P. Pistor[ae]

The inclusion of Ge into the synthesis of $Cu_2ZnSn(S,Se)_4$ absorbers for kesterite solar cells has been proven to be a very efficient way to boost the device efficiency in a couple of recent publications. This highlights the importance to elucidate the mechanisms by which Ge improves the kesterite solar cells properties to such a large extent. In this contribution, we first show how controlling the position and thickness of a very thin (10–15 nm) layer of Ge greatly influences the crystallization of kesterite thin films prepared in a sequential process. Typically, $Cu_2ZnSnSe_4$ (CZTSe) films form in a bi-layer structure with large grains in the upper region and small grains at the back. By introducing Ge nanolayers below our precursors, we observe that large CZTSe grains extending over the whole absorber thickness are formed. Additionally, we observe that Ge induces fundamental changes in the formation mechanism of the kesterite absorber. In a detailed analysis of the phase evolution with and without Ge, we combine the results of X-ray fluorescence, X-ray diffraction and Raman spectroscopy to demonstrate how the Ge influences the preferred reaction scheme during the selenization. We reveal that the presence of Ge causes a large change in the in-depth elemental distribution, induces a stabilizing Cu–Sn intermixing, and thus prevents drastic compositional fluctuations during the annealing process. This finally leads to a change from a tri-molecular towards, mainly, a bi-molecular CZTSe formation mechanism. Kesterite thin films with surprisingly large crystals of several microns in diameter can be fabricated using this approach. The results are related to the increase in device performance, where power conversion efficiencies of up to 11.8% were obtained. Finally, the consequences of the disclosed crystallization pathways and the extension to other chalcogenide technologies are discussed.

Received 14th August 2017,
Accepted 25th October 2017

DOI: 10.1039/c7ee02318a

rsc.li/ees

Broader context

Direct solar energy conversion into electricity (photovoltaic energy, PV), is probably the most relevant renewable energy source for the future sustainable development of humanity. In order to provide a significant share of the increasing global electricity demand in the short- to midterm, a mass deployment of PV installations in the TW regime will be needed. Ramping up the PV production to these large scales calls for the development of cheap PV technologies using earth abundant elements with low toxicity. Kesterite ($Cu_2ZnSn(S,Se)_4$-CZTS) thin film solar cells fulfil these criteria and are at the forefront of abundant inorganic materials for PV applications due to their intrinsic characteristics. Nevertheless, the performance of these device has so far been limited, mainly by their low open circuit voltage (V_{OC}). The partial substitution of Sn by Ge has been shown as one of the most promising routes to boost the V_{OC}, and has recently been demonstrated by several research groups around the world. Additionally, Ge is one of the most relevant candidates for the implementation of band-gap graded concepts in kesterites, similar to the grading strategies successfully implemented with In and Ga in high efficiency $Cu(In,Ga)Se_2$ devices. However, the reasons behind the strong impact of relatively small quantities of Ge are still obscure. Herein we report our fundamental analysis of the impact of Ge on the phases formed during the reactive selenization, and the consequences these changes have on the absorber morphology and device performance. A change in the kesterite formation mechanism is observed from a tri-molecular pathway involving the binary selenides without Ge, to a bi-molecular one involving Cu–Sn alloys with Ge. This strongly modifies the main characteristics of the synthesized layer, above all the homogeneity, morphology and opto-electronic properties. Our findings explain how Ge avoids the formation of the segregated bi-layered structures traditionally observed in kesterite devices and provide hope that Ge might have beneficial effects on other chalcogenide thin film technologies, too.

[a] Catalonia Institute for Energy Research (IREC), Jardins de les Dones de Negre 1, 08930 Sant Adrià de Besòs, Barcelona, Spain. E-mail: esaucedo@irec.cat; Tel: +34933562615
[b] Centres Científics i Tecnològics de la Universitat de Barcelona (CCiTUB), Lluís Solé i Sabarís 1-3, 08028 Barcelona, Spain
[c] Research Center for Photovoltaics, National Institute of Advanced Industrial Science and Technology (AIST), 1-1-1 Umezono, Tsukuba, Ibaraki, 305-8568, Japan
[d] IN2UB, Departament d'Electrònica, Universitat de Barcelona, Martí i Franquès, 1-11, 08028, Barcelona, Spain
[e] Institut für Physik, Martin-Luther-Universität Halle-Wittenberg, Halle, Germany

1. Introduction

Kesterite thin film photovoltaics (PV) based on $Cu_2ZnSn(S,Se)_4$ (CZTSSe) absorbers offer the same advantages as other large scale thin film production technologies such as CdTe or $Cu(In,Ga)Se_2$ (CIGSe), being potentially capable of high throughput at large scale and enabling stable module performance, monolithic integration, aesthetic design and allowing the manufacturer to choose a suitable substrate (*e.g.* glass, flexible metal or polyimide foils). Kesterite PV is still much younger and has so far demonstrated a 12.6% record efficiency.[1] Therefore, there is still a long way of technological engineering to go in order to catch up with its older chalcogenide cousins having already surpassed power conversion efficiencies of 20%.[2]

The clear advantages of kesterites – cheap, earth-abundant and non-toxic constituents – make it a very attractive alternative absorber material, but these assets may only translate into industrial success if high efficiencies (towards 20%) can also be achieved. Main limitation for the performance in current kesterite solar cells is the relatively low open circuit voltage in comparison to other technologies.[3–5] As the open circuit voltage of a given semiconductor is limited by its band gap, an adequate measure for comparing technologies with different band gaps is the voltage loss, defined as the difference between the band gap potential and the open circuit voltage. While for high efficiency CIGS and CdTe voltage losses of <0.4 V can be achieved, the best kesterite devices exhibit voltage losses of around 550–600 mV.[5] Different origins for these voltage losses in kesterite solar cells have been proposed and are currently under discussion, among others strong potential fluctuations, band tailing, Cu/Zn disorder effects, interface recombination and/or the influence of secondary phases and compositional inhomogeneities.[6–8]

Recently, we have reported the great beneficial impact that nanometric Ge layers have on the performance and especially on the open circuit voltage of sequentially processed $Cu_2ZnSnSe_4$ (CZTSe) solar cells.[9–11] In these cases, Ge thicknesses between 1–25 nm had been deposited on top of metallic Cu/Sn/Cu/Zn precursor stacks, which were then subjected to a reactive thermal treatment in order to selenize the precursors to CZTSe absorbers. A surprisingly large increase in the open circuit voltage up to 489 mV (compared to reference values, *i.e.* without Ge, around 400 mV) has been reported for an optimum Ge thickness of 10–15 nm, leading to an outstanding low voltage loss of only 0.56 V.[11] The beneficial effect of incorporating small amounts of Ge has been reproduced afterwards in several other works.[12,13] Kim *et al.*[12] and Neuschitzer *et al.*[14] have independently reported strongly enlarged grain sizes for $Cu_2Zn(Sn,Ge)Se_4$ absorbers that had been reannealed in an Ge containing atmosphere. However, the main lever of interaction underlying the "Ge boost" has not been clarified in detail. Several hypotheses have been formulated, as recapitulated in brief in the following:

(1) Surface modification: the initial idea behind the application of the Ge layers was to incorporate the Ge into the absorber and hence introduce a band gap grading towards the absorber surface. A graded absorber with higher band gap at the surface is expected to lower the interface recombination resulting in higher open circuit voltages. This effect can be observed in CIGS solar cells, where a gradient with increasing band gap towards the absorber surface is obtained through In/Ga or S/Se alloying.[15,16] However, in ref. 9 we showed, that for these small amounts of Ge no traceable amounts of Ge are incorporated into the absorber, no change in the absorber surface structure and no increase in the band gap is observed.

(2) Formation of a flux agent: the formation of Ge–Se phases that decompose incongruently into a Ge_xSe_y (Se $\sim$85%) liquid, and volatile $GeSe_2$ gas phase has been proposed explaining both, the low Ge incorporation in the CZTSe when small amounts of this element are used, and the observed improved crystallinity.[9]

(3) Interaction with Na: strong interaction between Ge and Na has been observed during the crystallization process, indicating that somehow Ge can help to control the Na content in kesterite bulk and surface. Additionally, this combines well with the idea that Ge is forming Ge–Se liquid phases at the surface during the annealing process that can act as crystallization flux and, at the same time, control the doping level of the absorber.[10]

(4) Improvement of transport charge properties: apparently Ge has a beneficial effect on the transport charge properties of kesterites, in particular increasing the carrier life-time, most probably interrelated to all the previously described improvements.[17]

Nevertheless, the reasons behind these improvements induced by Ge are still a matter of controversy. In this contribution, we investigate in depth the mechanisms underlying the Ge boost on kesterite solar cells and suggest an alternative mechanism based on the reaction scheme during selenization. For this purpose, kesterite absorbers are prepared in the standard sequential baseline process established at IREC, which is described in more detail in the experimental section. In this work, the amount and position (below and/or above the precursors) of deposited Ge is varied and correlated with the optoelectronic performance of the resulting devices. Differences in the reaction schemes during the selenization with and without Ge will be analyzed in detail with the help of energy-dispersive X-ray spectroscopy (EDX), X-ray fluorescence (XRF), X-ray diffraction (XRD) and Raman spectroscopy with multi-wavelength excitation for samples where the reactive annealing treatment had been interrupted at different points in time. It will be demonstrated that Ge has multiple effects on kesterites and that most of them are connected with the observation of a change in the synthesis mechanisms, together with the presence of Ge–Se liquid phases. Finally, we will show how this type of assisted crystallization can be extended in the future to other chalcogenide compounds with technological relevance.

2. Results

2.1. Effect on the phase formation and reaction schemes during selenization

Ge has shown to assist the crystallization of CZTSe, improving the morphology and electro-optical properties of this material.

This is a recurrent observation in the literature, where several works have reported an increased grain growth for Ge containing absorbers.[9,12,14] In spite of this, still a bilayer structure is frequently observed, with very big crystallites at the surface and smaller ones at the back, and the actual role of Ge in this system is still a matter of intense research.

In this section, we will try to elucidate the role of Ge during the reactive thermal annealing process and how it assists the formation of large crystallites. The phases formed during the different steps of the reactive thermal annealing under selenium atmosphere will be compared for samples with and without Ge. For this purpose, ultrathin layers of Ge (10–25 nm) were deposited below the CTZ precursor (between the Mo back contact and precursors) and selenized in a specially designed "break-off" experiment. In order to better describe the design of the "break-off" experiment, the temperature profile of our standard process is depicted in Fig. 1. It consists of two stages: in the first stage, the pressure within the tubular furnace is set to 1 mbar (0 min, t0). The furnace is then heated at a rate of 20 K min^{-1}. Once the set temperature of 400 °C is reached (18.5 min, t1), the temperature is hold for 30 min (48.5 min, t2). In the second stage, the pressure is increased to 1000 mbar through the inlet of Ar gas, and the temperature is increased to 550 °C (at 20 K min^{-1}) (56 min, t3). This temperature is kept for 15 min (71 min, t4). After this, the system cools down naturally. At the times t1, t2, t3, t4 we have interrupted the reactive annealing process in order to investigate differences in the reaction schemes for the samples with/without Ge, and characterized the layers at different stages by SEM, EDX, XRD and Raman spectroscopy.

In the same Fig. 1, cross-sectional micrographs of the different samples are depicted. In Fig. 2–4 samples with and without Ge are compared just after reaching the first temperature plateau at 400 °C (t1) using different characterization techniques. In Fig. 2 in-depth compositional maps of cross-sections obtained with EDX are displayed, while Fig. 3 and 4 show XRD diffractograms and Raman spectra, respectively. In the following, the results concerning the sample without Ge (0/CTZ/0) will be presented and then compared with the results obtained on the samples with Ge below the CTZ precursor (10/CTZ/0 and 25/CTZ/0). The nomenclature for the sample description is detailed in the experimental section at the end of this manuscript.

Sample without Ge. At time t1, the sample without Ge (0/CTZ/0) exhibits a bi-layer structure with fine grains and several voids at the bottom, and a relatively dense and rough structure at the top. Interestingly, the EDX in-depth compositional map (Fig. 2) reveals very different elemental compositions in both regions. In particular, the bottom structure is mainly formed by Zn, Sn and some Se, while the top and denser structure predominantly consists of Cu and Se. This suggests a very fast Cu-out diffusion to the surface, as has already been observed for other sequential processes,[21] while Zn diffuses at the same time towards the bottom. A complete demixing of Cu and Sn is observed, indicating that at least at this stage Cu–Sn–Se phases and/or Cu–Sn alloys are probably not present at all. At this point it seems natural to think that the observed Cu-out diffusion, together with the high probability to form binary volatile Sn–Se species (and the consequent loss of Sn) are the origin of the voids at the back region.

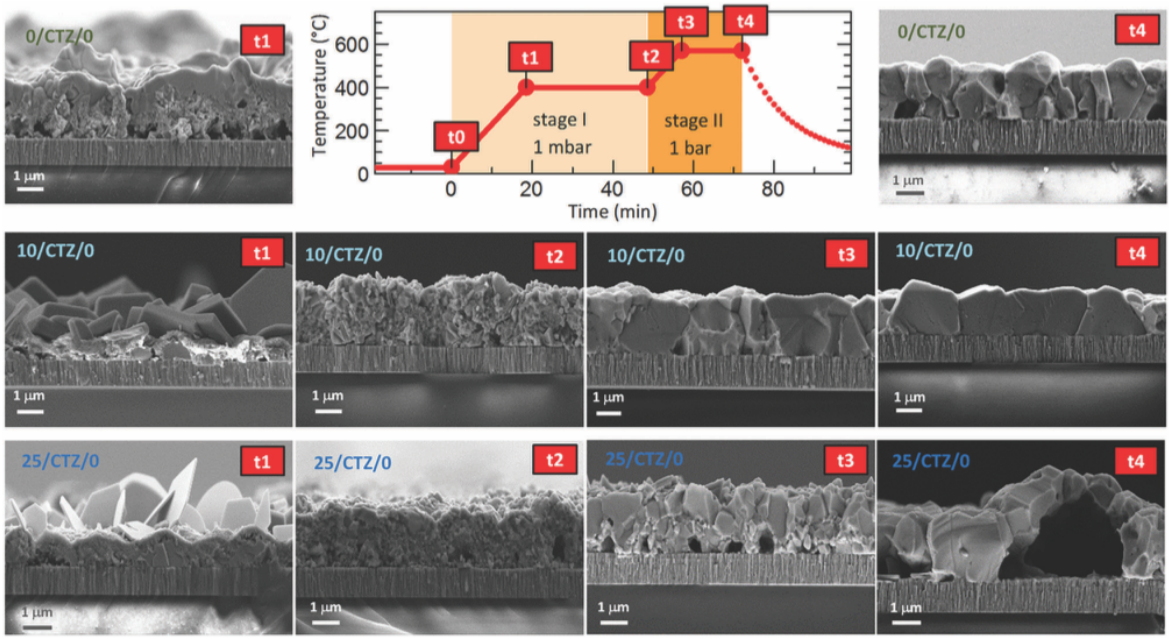

Fig. 1 Cross-sectional SEM micrographs of the CZTSe absorbers with different amounts of Ge (0 nm, 10 nm, 25 nm) deposited below the CTZ precursors (see Experimental section for a detailed nomenclature description). For these samples, the reactive annealing was interrupted after different times t1, t2, t3, t4, as marked in the temperature profile.

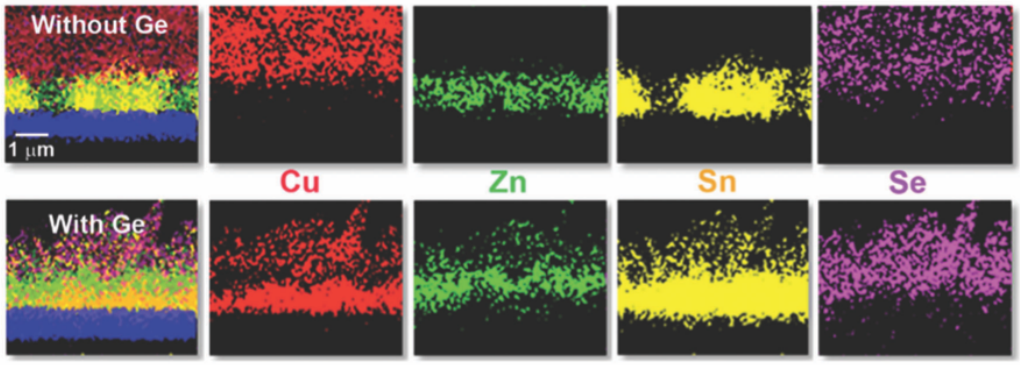

Fig. 2 Cross-sectional elemental distribution of samples with and without Ge (25 nm below the CTZ precursor) after reaching the first temperature plateau (t1) determined by EDX (Cu, Zn, Sn and Se. Mo is depicted in blue just in the overlapped mapping for guidance).

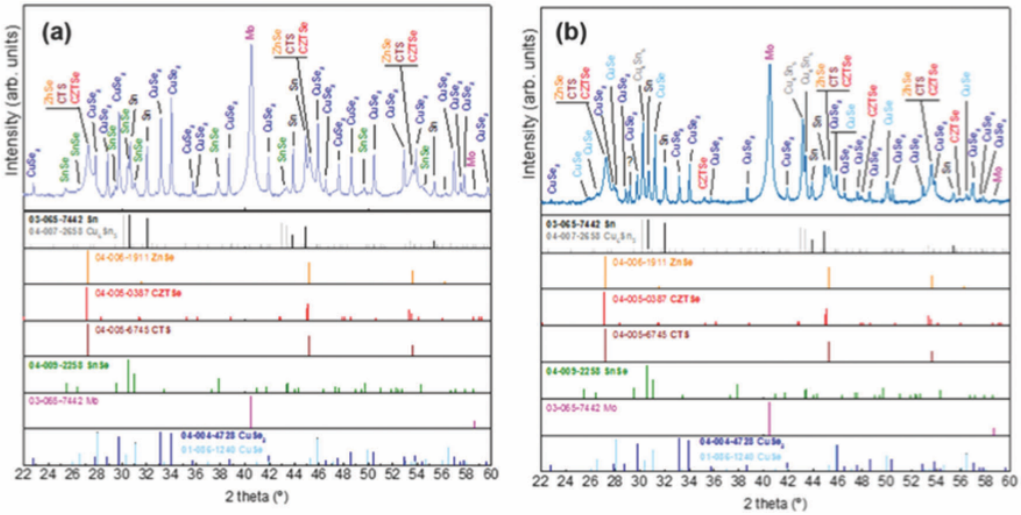

Fig. 3 XRD diffractograms of samples without Ge at t1 (a) and with Ge (25 nm below the CTZ precursor) at t1 (b).

At t1 we expect that the simplest compounds (binary or ternary) will be formed that will then react during the t1–t2 dwell time in order to form the quaternary kesterite. In this sense, it is very relevant to identify which phases actually form at t1 since it will bring first-hand information about the reaction pathway. In Fig. 3a, an XRD diffractogram of the sample without Ge (0/CTZ/0) at t1 is shown. The XRD analysis provides evidence that elemental Sn is the only metallic phase, suggesting that Cu and Zn have already reacted completely with Se. In fact, $CuSe_2$ is clearly identified in the XRD diffractogram together with some SnSe. Additionally, diffraction peaks are observed that can correspond either to ZnSe, Cu_2SnSe_3 and/or $Cu_2ZnSnSe_4$, confirming that one or more of these phases are present. However, characteristic further peaks corresponding to the lowered symmetry of the tetragonal phase of CZTSe are absent, excluding the presence of significant amounts of crystalline CZTSe. In order to support the XRD analysis, Raman spectra measured with different excitation wavelengths (633 nm, 532 nm, 488 nm) at the surface of this sample and (after lift-off) at the back side of the absorber are shown in Fig. 4a. At the surface, Cu_xSe is clearly detected with all three excitation wavelengths,[22] in agreement with the EDX and XRD analysis. At the back side, ZnSe is observed when using 488 nm excitation[23] together with Sn–Se phases,[24] and a very weak and broad band that is tentatively attributed to amorphous CZTSe. In any case, no evidences of Cu–Sn–Se phases are present, in agreement with the in-depth physical separation of Cu and Sn observed by EDX.

This strongly suggests that the kesterite formation proceeds *via* the reaction of binary compounds (Cu, Zn and Sn selenides) as has been reported for the sulphide kesterite compound Cu_2ZnSnS_4.[21] The presence of the $CuSe_2$ phase indicates that the reaction is in fact much more complex than previously believed. $CuSe_2$ is the phase with the lowest formation energy in the complex Cu–Se system.[25] In our annealing conditions, a high Se overpressure builds up at the very beginning. These two

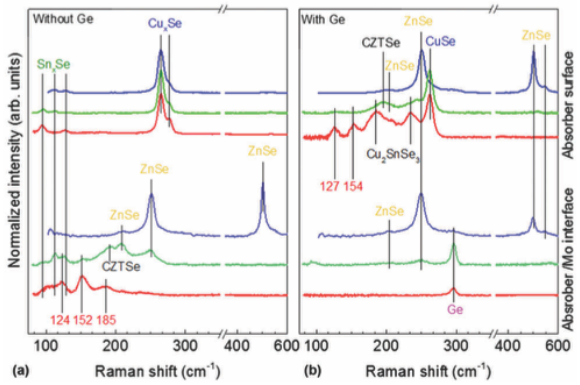

Fig. 4 Raman spectra using three different excitation wavelengths at the absorber surface and absorber back side for the sample without Ge at t1 and with Ge (25 nm below the CTZ precursor) at t1. Red: 633 nm, green: 532 nm and blue: 488 nm.

conditions together explain the formation of $CuSe_2$. Nevertheless, above a temperature of 332 °C this phase decomposes into CuSe, and then into Cu_2Se above 382 °C[25], following the reactions below:

$$CuSe_{2(s)} \xrightarrow{T > 332°C} CuSe_{(s)} + \frac{1}{2}Se_{2(g)}$$

$$2CuSe_{(s)} \xrightarrow{T > 382°C} Cu_2Se_{(s)} + \frac{1}{2}Se_{2(g)}$$

Then, Cu_2Se is expected to react with SnSe and ZnSe to form the kesterite through the following reaction:

$$Cu_2Se_{(s)} + SnSe_{(s)} + ZnSe_{(s)} + \frac{1}{2}Se_{2(g)} \xrightarrow{T\sim400°C} Cu_2ZnSnSe_{4(s)}$$

This reaction mechanism is firmly supported by the EDX, XRD and Raman analysis presented up to now. It implies another important point: the presence of SnSe at the beginning of the process, as is clearly evidenced by both the XRD and Raman analysis. The volatility of SnSe bears the high risk of Sn-loss during the reaction, a fact that is corroborated by a look at the analysis of the compositional ratios by X-ray fluorescence (XRF): While the initial precursor has a C/ZT of 0.76 and Z/T = 1.20, at t1 these have increased to C/ZT = 0.99 and Z/T = 1.68 as a result of substantial Sn loss. Therefore, the overall composition of the reference layer without Ge at t1 is in fact notably poorer in Sn than the initial precursors as a result of the uncontrolled Sn-loss.

The presence of almost all the Cu at the front might be the origin of the large grains formed at the surface of the absorbers, where the kesterite is growing under Cu-rich conditions from Cu_xSe. On the contrary, the low Cu concentration at the back (Cu-poor conditions) prevents the formation of large grains, as is commonly observed. The morphology of these layers, in particular the bi-layered structure and the formation of voids at the back side can therefore be explained as a result of this tri-molecular reaction mechanism (with three binary selenide compounds) and the involved Cu-out diffusion and segregation of Cu and Sn/Zn selenides. Intriguingly, Thersleff *et al.* have reported in a detailed analysis of a similar bi-layered structure that the back region in the final CZTSe made up by small grains is still Cu-poorer than the region with larger grains at the surface, supporting our model of differential grain growth at back and front.[26] In the next sub-section we will show how this story drastically changes, once Ge is introduced below the CTZ precursor.

Sample with Ge. As is clearly observed in Fig. 1 at t1, the morphology of the precursor is radically changed when Ge is introduced below the CTZ precursors, even for rather small quantities (10 nm). After heating the system initially to 400 °C (t1), samples with Ge show a peculiar morphology with three different regions, where in particular large hexagonal platelets (up to approximately 100 nm thick, several microns in lateral dimensions) have formed at the surface. Below these structures, a mix of relatively small and fine grains is observed. These morphological differences correspond to variations in the in-depth compositional distribution. The EDX mapping shown in Fig. 2 reveals that the platelets are formed by Cu, Se and probably small amounts of Sn, although Cu–Se is predominant.

Zn remains mainly in the middle-bottom part of the layer. Interestingly, at the back region still huge Cu quantities are observed, and are very well mixed with Sn. Apparently, the presence of Ge prevents a fast Cu-out diffusion and stimulates a very good mixing between Cu and Sn from the very beginning. The Cu–Sn alloy at the back is only partially selenized at this stage. The hypothesis of Cu–Sn alloying is well supported by the XRD analysis of the Ge-containing sample, where, in contrast to the Ge-free reference, metallic Cu–Sn alloys are observed in addition to metallic Sn. This means that already the presence of very small amounts of Ge can dramatically influence the evolution of phases during selenization.

One of the first consequences is the drastic reduction of Sn-loss in this first stage (t1). XRF measurements reveal that the C/ZT and Z/T ratios remain almost the same after t1 (0.78 and 1.27, respectively) as compared to the initial precursor composition (0.76 and 1.20) for the samples with Ge. This means that practically no Sn is lost to the annealing atmosphere, again in contrast to the Ge-free sample.

It is important to remark that the presence of Ge seems to minimize or even avoid two important issues affecting the morphology of CZTSe layers: the fast Cu-out diffusion and the uncontrolled Sn-loss. This notably also impacts on the final absorber morphology as is clearly observed in Fig. 1 for the samples with Ge at t4. For the sample 10/CTZ/0, already at t3 a nice morphology is observed, while at t4 (end of the annealing process), huge grains extending over the whole absorber thickness are obtained (even substantially wider than high), and with no observable voids or imperfections at the back interface. In consequence, we claim that the Ge containing samples are capable of holding the Sn within the precursors at the beginning of the selenization and avoid/minimize the fast Cu-out diffusion and Cu/Sn segregation observed for Ge-free samples. This is crucial for the improved selenization reaction, as will be discussed in Section 3.

The further characterization by XRD and Raman spectroscopy of the Ge-containing samples completely support this picture. As is observed in Fig. 3b, the XRD pattern of the sample containing Ge at t1 is very different to the sample without Ge. As stated earlier, two metallic phases are clearly detected: Sn and Cu_6Sn_5, confirming that somehow the presence of Ge at the back stabilizes the Cu–Sn alloys. Additionally, the presence of CuSe and $CuSe_2$ are confirmed, and once again the diffraction peaks corresponding to CZTSe and/or Cu_2SnSe_3 and/or ZnSe. However, in this case the low intensity diffraction peaks corresponding to the tetragonal phases can clearly be identified, proving an early formation of the quaternary kesterite and/or ternary Cu_2SnSe_3 tetragonal phase.

Further differences are revealed by the Raman analysis (Fig. 4b). As expected, ZnSe is detected at both, the back and front side of the layer. On the other hand, Cu–Se is also detected at the front together with evidence for the formation of a Cu_2SnSe_3 phase, and a small quantity of a nanocrystalline or amorphous kesterite phase. But most relevant, the characteristic peaks of the Sn–Se phases are absent. This means that the pathway for kesterite formation mechanism has now changed and seems not occur *via* the binary Sn, Cu and Zn selenide phases as before.

The confirmed presence of Cu_6Sn_5 and Sn metallic phases suggests that the first step in this case is related to the formation and maybe already decomposition of bronze at temperatures close to 400 °C through:[27]

$$Cu_6Sn_{5(s)} \xrightarrow{T\sim400^\circ C} 2Cu_3Sn_{(s)} + 3Sn_{(l)}$$

Then, the Cu_3Sn phase can immediately react with $Se_{2(g)}$ to form:

$$Cu_3Sn_{(s)} + \frac{5}{2}Se_{2(g)} \rightarrow Cu_2SnSe_{3(s)} + CuSe_{2(s)}$$

After that, the $CuSe_2$ phase can follow a similar pathway to the proposed above for the sample without Ge as a competitive mechanism to form kesterite, or react with the free elemental Sn as follows:

$$2CuSe_{2(s)} + Sn_{(s)} \rightarrow Cu_2SnSe_{3(s)} + \frac{1}{2}Se_{2(g)}$$

Finally, the ternary Cu–Sn–Se compound can react with ZnSe to form the CZTSe kesterite:

$$Cu_2SnSe_{3(s)} + ZnSe_{(s)} \rightarrow Cu_2ZnSnSe_{4(s)}$$

This implies the change from a tri-molecular reaction pathway as observed for the samples without Ge, towards a bimolecular one when using Ge. Additionally, this pathway does not involve the formation of a Sn–Se phase in any step, in line with the XRF, XRD and Raman spectroscopy results.

To summarize, the presence of very small amounts of Ge drastically modifies the reaction pathway in which the kesterite is formed. This notably impacts on the absorber morphology, the Sn loss and consequently on the devices properties, as will be further demonstrated in the following sections. It is worth to mention that we cannot rule out that Ge is assisting the crystallization also through the formation of Ge–Se liquid phases as has been reported elsewhere.[9] Nevertheless, this alternative explanation is also not necessarily in contradiction with the mechanisms proposed in this paper.

2.2. Effect on the solar cell devices

Now, the question is what happens when these improved layers are implemented as photovoltaic absorbers. In order to analyze this question, series with CZTSe absorbers with different amounts of Ge deposited on top and below the CTZ precursors were prepared. Fig. 5 shows the evolution of the average solar cell parameters of a series were varying amounts of Ge (0–25 nm) were deposited below the metallic precursors, in addition to a 5 nm Ge layer on top.

The average efficiency (6 cells) increases from 8.6% to 9.5% if a thin (5 nm) Ge layer is deposited below the CTZ in addition to the top 5 nm Ge layer. If the thickness of the bottom layer is increased to 10 nm, the efficiency remains high (9.4%). This efficiency increase is mainly achieved by an enhanced short circuit current density, while the open circuit voltage remains at the same high value for these three samples, at 450–460 mV. The inset of Fig. 5 shows the external quantum efficiency of devices with different amounts of Ge below the CTZ, and elucidates that the origin of the J_{SC} improvement is found in the longer wavelength range, related to collection of charge carriers from regions deep within the absorber.

We associate these improvements to a better charge carrier collection due to the better crystallinity as shown in the micrographs in Fig. 6. These micrographs again confirm the substantially improved morphology, especially towards the back contact, for the samples where the Ge was deposited between the back contact and precursors. Similar to the case of Ge layers deposited on top, a too thick Ge layer (25 nm) below the CTZ results in severe losses in fill factor (FF) and open circuit voltage (V_{OC}).

For this sample, the absorber layer is forming "dome"-like features all over the substrate. We interpret these as bubbles that form during the absorber formation by uncontrolled evaporation of volatile Ge–Se species. A close examination of Fig. 1 reveals similar features for the sample with 25 nm Ge below the precursors presented there, however less pronounced.

In our previous work, where Ge was only deposited on top of the precursors, we found an optimal Ge thickness of 5–15 nm.[11] Varying the Ge thickness above and below the CTZ precursors, we find the optimum for the global (sum of above and below) Ge thickness to be the same: 10–15 nm. The outcomes of the Ge variations above and below the precursors are summarized in Table 1 and Fig. 5, and clearly show:

(1) All devices with an overall Ge thickness of 10–15 nm reproducibly lead to an improved V_{OC} of 450–470 mV and efficiencies above 9.3%, while the reference values (*i.e.* without Ge) remain below 430 mV and below 9% respectively.

(2) Adding 25 nm Ge or more below or above the CTZ annihilates the beneficial effect of Ge and severely degrades the device performance.

(3) A slight increase in the short circuit current density is consistently observed for devices with Ge, up to 32.3–32.5 mA cm^{-2} for samples with small amounts of Ge introduced below

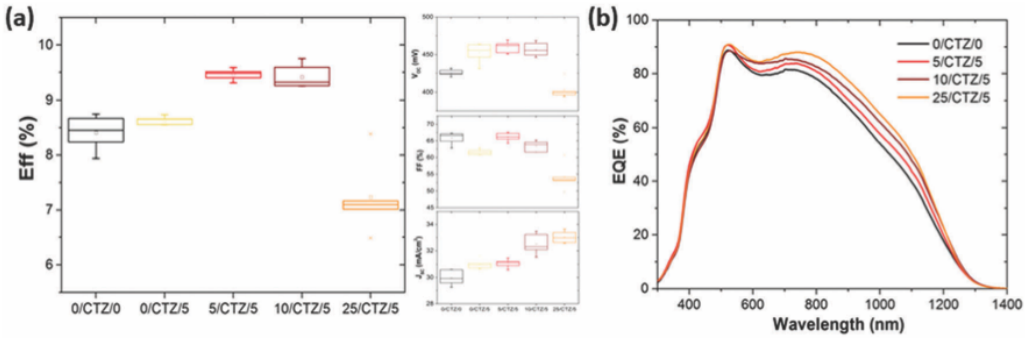

Fig. 5 Effect of depositing a Ge layer of varying thickness prior to the metallic precursor deposition on (a) the solar cells parameters, and (b) the external quantum efficiency. All samples had additionally 5 nm Ge layer on top of the precursors, except for the reference sample (without Ge). The samples nomenclature is detailed in the Experimental section.

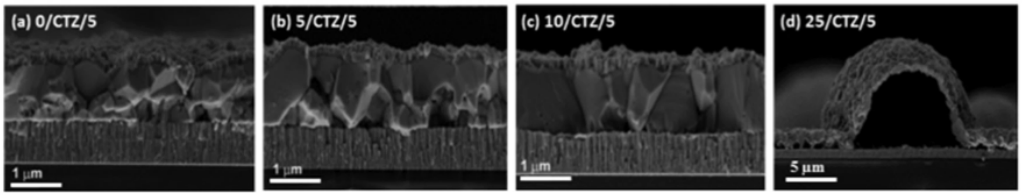

Fig. 6 Cross-sectional SEM micrographs of the completed CZTSe solar cells with different amounts of Ge deposited below the metallic Cu/Sn/Cu/Zn precursor stack: (a) 0 nm Ge below, (b) 5 nm Ge below, (c) 10 nm Ge below, (d) 25 nm Ge below. All precursors had deposited a 5 nm Ge layer on top.

Table 1 Average solar cells parameters (6 cells, error indicates the standard deviation) of $Cu_2ZnSnSe_4$ solar cells with Ge layers of different thickness deposited before (below) and after (on top) the deposition of the metallic Cu/Sn/Cu/Zn precursor stack

	Ge layer (nm)					
Sample	Below	On top	Eff. (%)	V_{OC} (mV)	J_{SC} (mA cm^{-2})	FF (%)
0/CTZ/0	—	—	8.4 ± 0.3	426 ± 5	30.0 ± 0.6	65.9 ± 1.8
0/CTZ/5	—	5	8.6 ± 0.1	453 ± 13	31.0 ± 0.4	61.6 ± 0.8
0/CTZ/10	—	10	9.3 ± 0.1	455 ± 12	30.7 ± 0.6	66.6 ± 1.3
5/CTZ/5	5	5	9.5 ± 0.1	460 ± 8	31.1 ± 0.4	66.2 ± 1.3
10/CTZ/0	10	—	9.6 ± 0.2	466 ± 7	32.3 ± 0.7	64.1 ± 0.8
5/CTZ/10	5	10	9.4 ± 0.2	461 ± 7	30.9 ± 0.3	65.9 ± 1.2
10/CTZ/5	10	5	9.4 ± 0.3	457 ± 9	32.5 ± 0.8	63.5 ± 1.6

the CTZ, while the reference values (*i.e.* without Ge) remain below 31.0 mA cm^{-2}.

We therefore conclude that the positive effect of the Ge on the V_{OC} (the V_{OC} boost) is achieved for Ge thicknesses of 5–15 nm regardless of the position of the Ge nanolayer (below and/or above the CTZ precursor). This implies that the beneficial effect of the Ge is not limited to some surface modifications as previously suggested, but rather affects the whole bulk of the absorber. The best solar cell of this series reached an efficiency of 9.9% (V_{OC} of 453 mV, FF of 67.1%, J_{SC} of 32.5 mA cm^{-2}), with 10 nm Ge below and 5 nm on top of the precursor (no anti-reflective coating applied).

3. Discussion

In a detailed high-resolution transmission electron microscopy (HR TEM) analysis it has been previously shown how the addition of 10 nm Ge on top of the precursors leads to a bi-layered absorber morphology and two distinct types of grain boundaries.[26] These were denominated "straight" and potentially malign "meandering" grain boundaries. The bi-layer structure consisted of large grains and vertical "straight" grain boundaries near the surface, separated from the lower part towards the back side of the absorber, which was characterized by voids, horizontal "meandering" grain boundaries and a slightly lower (1.40 ± 0.03) Cu/Zn ratio than the top part (1.49 ± 0.03). Large grains stretching over the complete absorber thickness can be observed for the sample where the 10 nm Ge have been deposited below the precursor. In this sample, the increased crystallization enabled to completely remove the "meandering" horizontal grain boundaries from the sample, with an absorber built up by large grains and straight, vertical grain boundaries. Huge grains with lateral extensions exceeding 4 microns were found. As a matter fact, we have never

observed or found evidence for comparable grain sizes and morphologies in prior work. The absence of the meandering grain boundaries in this type of samples might be an explanation for the improved charge collection, as resistive barriers and recombination centers at the bottom part of the absorber are removed.

Based on the presented results we suggest a fundamental difference in the reaction schemes for the samples containing Ge and the Ge-free ones. Scheme 2 depicts a schematic representation of the proposed model. For the Ge-free reference sample, Cu out-diffuses rapidly to the surface and forms Cu–Se as a dense, compact film on top of the Sn–Zn precursor. Se diffuses into the film and forms a porous region consisting of Sn–Se and Zn–Se. The reaction occurs predominantly *via* the formation of the binaries Zn–Se, Sn–Se and Cu–Se. As the Sn–Se phases have very high vapor pressures, a substantial loss of Sn occurs in the initial stage of the process. The loss of Sn–Se is a commonly observed issue in the synthesis of kesterites,[28] and in fact is the reason for incorporating an additional amount of Sn within the graphite box during processing. Thus, the evaporation of this Sn during the further evolution of the process causes a high Sn–Se partial pressure in the graphite box, which in turn leads to a re-incorporation of Sn into the absorber at later stages.[29] This self-regulation of the Sn content of the absorber is a well-known feature of the regular sequential processing and has been repeatedly observed. It is also reported in ref. 30 for sulphur-based kesterites. The Sn content, or the Cu/Sn ratio of the samples has been found to be crucial for the crystal growth and absorber quality in the past. A lower Cu/Sn ratio significantly enhances the crystallization and formation of large grains as is reported for example in ref. 31. Furthermore, Sugimoto *et al.* have shown that a lower Cu/Sn ratio in the absorbers is linked to increased charge carrier lifetimes and open circuit voltages.[32]

On the other hand, we could now demonstrate that the incorporation of Ge into the CTZ precursor prevents the Sn loss to some extent, firstly because Sn remains mainly fixed into a Cu–Sn–Se ternary phase, and additionally because a quaternary kesterite phase is formed much earlier. Here, during the heating, a Cu–Sn alloy is formed near the bottom region, close to the back contact. Se is diffusing into the precursor forming Zn–Se nano-crystals and large Cu–Se platelets at the surface, which also contain some Sn. In this case, the formation of Cu–Sn–Se ternary and Cu–Zn–Sn–Se phases already during the very first stages of the process effectively limits the Sn loss. There are two possible mechanisms how the Ge may assist the formation of the ternary phases and enlarged crystals. In the first model, small amounts of Ge incorporated into the Cu/Cu–Se might substantially increase the solubility of Sn within these phases and in consequence facilitate the crystallization and the formation of Cu–Sn–Se ternary phases. A similar effect is found for In and CZTSe: adding small amounts of In into the kesterite structure greatly increases the solubility of Zn in the kesterite phase.[33] This is *e.g.* used to prevent the segregation of ZnSe secondary phases during the absorber synthesis. A second plausible mechanism is the formation of a liquid Ge–Se phase that acts as a flux agent for the formation of the Cu–Sn–Se and Cu–Zn–Sn–Se phases, similar to the effect that Cu–Se has on the growth of chalcopyrite $Cu(In,Ga)Se_2$.[34] In chalcopyrite synthesis, a Cu-rich growth phase leads to a substantial improvement of the grain size and absorber quality. The generally accepted model for this growth mechanism implies the formation of Cu–Se phases on the surface of the absorber once the Cu/(In + Ga) ratio surpasses 1 (Cu-rich growth phase). Then, the Cu–Se phase acts as a flux agent for the growth of large chalcopyrite crystals with a low defect density. The small amount of Ge present during the synthesis in our case makes its detection and location rather difficult, which in turn, at this moment, represents an obstacle for the distinction whether the Ge is incorporated into the Cu–Sn–Se phases or is present in a separate Ge–Se liquid phase. Further investigations to clarify these details are under way.

Ultimately, after optimizing all the processes presented here and implementing MgF_2 anti-reflective coating as well as Ag grids to a CZTSe (+12.5 nm Ge) device, we achieved a record solar cell with an efficiency (illuminated area, not including the contact grid) of 11.8% with a V_{OC} of 463 mV, FF of 66.3% and J_{SC} of 38.3 mA cm^{-2}. Referring to the total area (cell area of 0.522 cm^2, including the contact grid) this measurement corresponds an efficiency of 11.0% and a J_{SC} of 36.0 mA cm^{-2}. The *JV*-curve corresponding to this device is shown in Fig. 7a. A comparison with literature data for the best devices with pure selenide-based kesterite absorbers shows that this is among the highest efficiencies reported for this type of absorber. The best efficiency so far has been reported by IBM, with a remarkably lower V_{OC} (423 mV), and higher J_{SC} (40.6 mA cm^{-2}), but resulting in a similar efficiency (total area efficiency of 11.6%) and FF (67.3%) for a slightly smaller device area (0.43 cm^2).[35] Other high performance devices reported by IMEC[36] and Nankai University[37] exhibit remarkably lower V_{OC} (between 390–420 mV) and efficiencies (both 10.4%). Devices reported previously by IREC show systematically higher V_{OC} values (typically between 460–490 mV).[9,11,18] This emphasizes the impact that Ge has on the improved voltage deficit in kesterite solar cells.

Fig. 7b shows a V_{OC} *vs.* temperature plot of two representative cells, one without Ge and one with 10 nm of Ge deposited on top of the precursors prior to selenization. The V_{OC} of our CZTSe devices generally does not extrapolate at 0 K to the band gap energy (roughly 1.05 eV), but rather 150–220 mV below it (780–820 mV). As Fig. 7 shows, this is not significantly changed upon the addition of Ge. Both devices show a fairly linear increase of the V_{OC} with decreasing temperature, as is expected for one dominant recombination mechanism which is thermally activated. The activation energy E_a of the recombination can in this case be extracted by an extrapolation of the V_{OC} to 0 K (V_{OC} (0 K)). For a dominant recombination in the bulk, the activation energy is generally expected to coincide with the band gap. As can be seen, the V_{OC} of both samples evolve very similar, with the device without Ge extrapolating to 789 mV, and the sample with Ge to 808 mV. The case of V_{OC} (0 K) $< E_G$ is generally associated with interface recombination, where a lowered interface band gap (*e.g.* due to band misalignments)

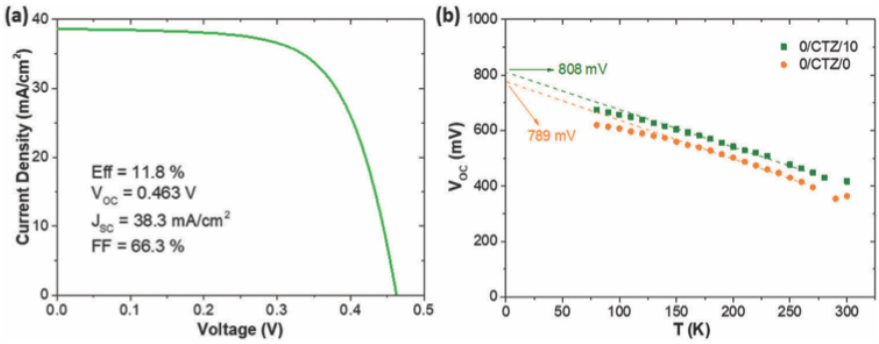

Fig. 7 (a) J–V curve corresponding to the best solar cell obtained in this work. (b) V_{OC} *vs.* T plot of a reference sample without Ge and a sample with 10 nm of Ge deposited on top of the CTZ precursors.

determines the activation energy of the dominant recombination path.[38] However, for CZTSe the interface band gap is reported not to be significantly lowered,[39] in contrast to CZTS, and other origins for a reduced E_a are also possible, *e.g.* high densities of tail states within the band gap, recombination *via* grain boundaries/secondary phase inclusions with reduced band gap or fermi level pinning.[38] The preliminary results presented here do not allow a clear location of the dominant recombination mechanism yet. However, the rather similar behaviour of the V_{OC} (T) does not indicate a fundamental change in the recombination mechanism (*e.g.* from interface to bulk). We therefore do not expect the observed improvement to be located at the absorber/buffer interface, but rather in the absorber bulk, *e.g.* due to an increased charge carrier lifetime.

For a deeper understanding of the effect of Ge on the intrinsic electronic properties of the absorbers and corresponding solar cells, a more complete characterization of a broad set of devices is required, together with an analysis of possible changes in the absorber surface and the absorber/buffer interface properties. This work is currently under way and will be published elsewhere.

Finally, an interesting question remains. Is the beneficial effect of Ge restricted to the synthesis of kesterites, or can it be applied to other chalcogenides used for photovoltaics? In order to test the impact of Ge on chalcopyrites, $CuInSe_2$ (CISe) was synthesized without and with a 25 nm Ge nanolayer below the precursor by a sequential process similar to the one used for kesterite absorbers (sputtering of Cu and In metallic stacks, followed by selenization in a graphite box). Fig. 8 shows the cross-sectional and surface SEM images of the resulting CISe layers. Surprisingly, the application of nanometric Ge layers also leads to significantly enlarged grains in this case. While we cannot answer the question of the global impact of Ge on chalcopyrites satisfactorily at the moment, our preliminary results at least strongly encourage a further investigation of the impact of Ge on the growth, crystallization, morphology and devices for other chalcogenides.

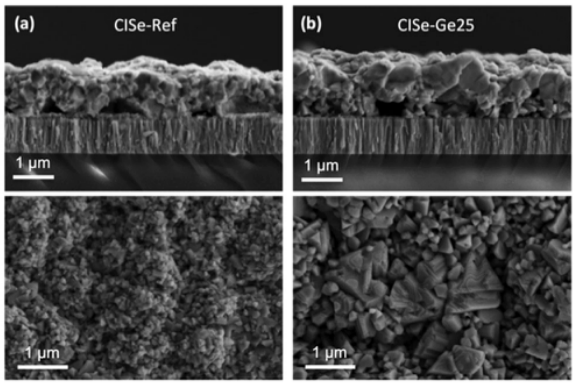

Fig. 8 SEM micrographs of CISe layers without Ge (a) and with 25 nm Ge (b), selenized at 450 °C for 30 min at 1 mbar Ar pressure.

4. Conclusions

Here we present a new concept for obtaining high quality CZTSe layers, by introducing an extremely thin Ge nanolayer at the back region, studying the impact and the origin of the recurrently observed positive effect of Ge in the kesterite system. We observe that the presence of Ge strongly affects the in-depth elemental distribution, delaying and minimizing the fast Cu-out diffusion and the formation of Sn–Se volatile species, and consequently avoiding Sn losses to a large extent. This allows modifying the reaction pathways of CZTSe from a tri-molecular mechanism for the layers without Ge, towards a mainly bi-molecular one for the samples containing Ge. The immediate effect is the large improvement of the CZTSe morphology, where very well crystallized layers with grains extending over the whole thickness are easily obtained. The main role of Ge seems to be related to the stabilization of Cu–Sn phases, impacting in the elemental in-depth distribution and ultimately in the reaction pathways of the kesterite. Through the optimization of the quantity of Ge together with the location of this element, we succeed to achieve a device that can be considered almost pure $Cu_2ZnSnSe_4$ and with 11.8% conversion efficiency.

5. Experimental

Kesterite absorbers were prepared on soda-lime glass substrates with an optimized tri-layer Mo back contact of

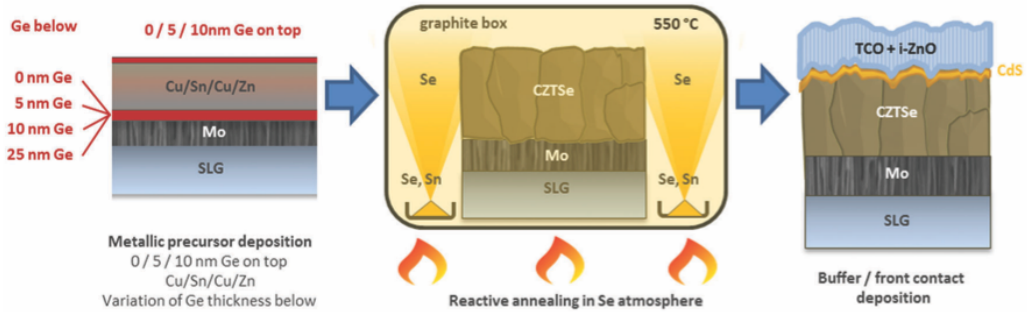

Scheme 1 Sketch of the CZTSe absorber preparation: (1) deposition of Cu/Sn/Cu/Zn metallic precursors by magnetron sputtering. Nanometric Ge layers are evaporated onto the substrate before and/or after the precursors. (2) Reactive annealing with elemental Se (and Sn) in a semi-closed graphite box. (3) Completed CZTSe solar cell structure.

approximately 800 nm. Details on the Mo back contact optimization can be found in ref. 18. The absorber synthesis is schematized in Scheme 1 and consisted of a sputter-deposition of metallic Cu(4 nm)/Sn(245 nm)/Cu(182 nm)/Zn(168 nm) precursors. These precursors usually yield suitable kesterite absorbers after selenization with Cu/(Zn + Sn) (C/ZT) ratios of 0.75–0.77 and Zn/Sn (Z/T) of 1.20–1.22. In the current variations, Ge layers of thicknesses between 5–25 nm were thermally evaporated onto the substrates before and/or after the metallic precursors, resulting in stacks were the Ge layers were situated below and/or above the metallic precursors. In the following, samples will be denominated by the thickness (in nm) and position of the deposited Ge layer, for example: CTZ/5 stands for 5 nm Ge on top of the metallic precursors, 10/CTZ corresponds to 10 nm Ge below the precursors, 25/CTZ/5 means 25 nm Ge below and 5 nm Ge on top and so on.

The metallic CTZ precursors (with and without Ge) where then placed in a graphite box together with 100 mg of Se and 5 mg of Sn for the reactive thermal annealing. The reactive thermal annealing was realized in a tubular furnace and Ar atmosphere by a first heating step at 400 °C for 30 min (1 mbar) and a second step at 550 °C for 15 min (1000 mbar). The temperature profile of the reactive thermal annealing is depicted in Fig. 1. More details on the baseline absorber synthesis can be found in ref. 9. For the analysis of the reaction pathways, the annealing process was stopped at different relevant points as will be schematized in the Fig. 1.

Following the baseline routine established at IREC, the samples were then subjected to a wet-chemical etching/passivation step in $(NH_4)_2S$ (22% v/v, for 2 min),[19] a chemical bath for the deposition of CdS[20] before the devices were finished by sputter-depositing an i-ZnO/ITO window layer. For IV and EQE-characterization, the devices were mechanically scribed into cells with a size of 3 mm × 3 mm and measured under simulated AM1.5 illumination from an AAA solar simulator (Abet Technologies). With the best samples, devices of 0.5 cm^2 in area and including MgF_2 anti-reflective coating and Ag metallic grids were fabricated. Finished devices were post-deposition annealed in air on a hot plate for 15 min at a temperature of 250 °C.

X-ray fluorescence (XRF, Fischerscope XVD) was used to determine the overall composition and thickness of the different precursor and absorber layers. Scanning electron microscopy (SEM) images were obtained with a ZEISS Series Auriga microscope using 5 kV accelerating voltage. Energy dispersive X-ray spectroscopy (EDX) analysis was performed with a 20 kV acceleration voltage using an INCA 250 series EDS detector from Oxford Instruments on the cross-sections of selected

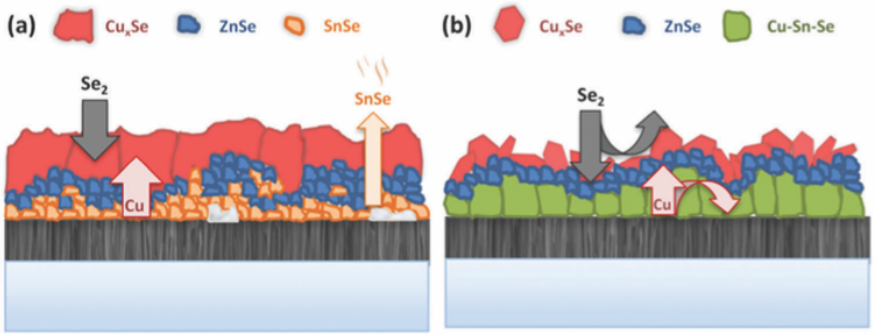

Scheme 2 Schematic sketches of the different intermediate steps and reaction mechanisms involved in the formation of CZTSe during the selenization of metallic Cu–Zn–Sn precursors: (a) reference sample without Ge, and (b) Ge-containing sample.

samples, with and without Ge. X-ray diffraction (XRD) was carried out using a PANalytical X'Pert PRO MPD Alpha1 powder diffractometer in Bragg–Brentano $\theta/2\theta$ geometry, from 4 to 145° with step size of 0.017° and integration time of 200 s per step, using Cu $K_{\alpha 1}$ radiation (λ1/41.5406 Å). Raman spectroscopy was performed with an iHR320 Horiba-Jobin Yvon spectrometer coupled to a Raman probe developed at IREC and a CCD detector, using three different excitation wavelengths (red: 633 nm, green: 532 nm, and blue: 488 nm).

Conflicts of interest

Acknowledgements

This research was supported by the H2020 Programme under the project STARCELL (H2020-NMBP-03-2016-720907), by MINECO (Ministerio de Economía y Competitividad de España) under the NASCENT project (ENE2014-56237-C4-1-R), by the European Regional Development Funds (ERDF, FEDER Programa Competitivitat de Catalunya 2007–2013) and CERCA Programme/Generalitat de Catalunya. Authors from IREC and the University of Barcelona belong to the M-2E (Electronic Materials for Energy) Consolidated Research Group and the XaRMAE Network of Excellence on Materials for Energy of the "Generalitat de Catalunya". SG thanks the Government of Spain for the FPI fellowship (BES-2014-068533). P. P. thanks the European Union for a Marie Curie Individual Fellowship ("JUMPKEST", FP7-PEOPLE-2013-IEF- 625840) and his wife for her continuous support.

References

1 W. Wang, M. T. Winkler, O. Gunawan, T. Gokmen, T. K. Todorov, Y. Zhu and D. B. Mitzi, Device Characteristics of CZTSSe Thin-Film Solar Cells with 12.6% Efficiency, *Adv. Energy Mater.*, 2014, **4**(7), 1301465.

2 P. Jackson, R. Wuerz, D. Hariskos, E. Lotter, W. Witte and M. Powalla, Effects of Heavy Alkali Elements in Cu(In,Ga)Se_2 Solar Cells with Efficiencies up to 22.6%, *Phys. Status Solidi RRL*, 2016, **10**(8), 583–586.

3 K. Kaur, N. Kumar, M. Kumar, Q. Guo, L. K. Johnson, R. S. Mclean, I. Malajovich, K. R. Choudhury, P. Scardi and A. Mittiga, Strategic Review of Interface Carrier Recombination in Earth Abundant Cu–Zn–Sn–S–Se Solar Cells: Current Challenges and Future Prospects, *J. Mater. Chem. A*, 2017, **5**(7), 3069–3090.

4 A. Polman, M. Knight, E. C. Garnett, B. Ehrler and W. C. Sinke, Photovoltaic Materials: Present Efficiencies and Future Challenges, *Science*, 2016, **352**, 6283.

5 J. Kim and B. Shin, Strategies to Reduce the Open-Circuit Voltage Deficit in Cu2ZnSn(S,Se)$_4$ Thin Film Solar Cells, *Electron. Mater. Lett.*, 2017, 1–20.

6 T. Gokmen, O. Gunawan, T. K. Todorov and D. B. Mitzi, Band Tailing and Efficiency Limitation in Kesterite Solar Cells, *Appl. Phys. Lett.*, 2013, **103**(10), 103506.

7 S. Bourdais, C. Choné, B. Delatouche, A. Jacob, G. Larramona, C. Moisan, A. Lafond, F. Donatini, G. Rey, S. Siebentritt, A. Walsh and G. Dennler, Is the Cu/Zn Disorder the Main Culprit for the Voltage Deficit in Kesterite Solar Cells?, *Adv. Energy Mater.*, 2016, **6**(12), 1–21.

8 M. Kumar, A. Dubey, N. Adhikari, S. Venkatesan and Q. Qiao, Strategic Review of Secondary Phases, Defects and Defect-Complexes in Kesterite CZTS–Se Solar Cells, *Energy Environ. Sci.*, 2015, **8**(11), 3134–3159.

9 S. Giraldo, M. Neuschitzer, T. Thersleff, S. López-Marino, Y. Sánchez, H. Xie, M. Colina, M. Placidi, P. Pistor, V. Izquierdo-Roca, K. Leifer, A. Pérez-Rodríguez and E. Saucedo, Large Efficiency Improvement in $Cu_2ZnSnSe_4$ Solar Cells by Introducing a Superficial Ge Nanolayer, *Adv. Energy Mater.*, 2015, **5**(21), 1501070.

10 S. Giraldo, M. Neuschitzer, M. Placidi, P. Pistor, A. Pérez-Rodríguez and E. Saucedo, $Cu_2ZnSnSe_4$-Based Solar Cells With Efficiency Exceeding 10% by Adding a Superficial Ge Nanolayer: The Interaction Between Ge and Na, *IEEE J. Photovoltaics*, 2016, **6**(3), 754–759.

11 S. Giraldo, T. Thersleff, G. Larramona, M. Neuschitzer, P. Pistor, K. Leifer, A. Pérez-rodríguez, C. Moisan, G. Dennler and E. Saucedo, $Cu_2ZnSnSe_4$ Solar Cells with 10.6% Efficiency through Innovative Absorber Engineering with Ge Superficial Nanolayer, *Prog. Photovoltaics*, 2016, **24**(10), 1359–1367.

12 S. Kim, K. M. Kim, H. Tampo, H. Shibata and S. Niki, Improvement of voltage deficit of Ge-incorporated kesterite solar cell with 12.3% conversion efficiency, *Appl. Phys. Express*, 2016, **9**(10), 102301.

13 D. B. Khadka, S. Y. Kim and J. H. Kim, Effects of Ge Alloying on Device Characteristics of Kesterite-Based CZTSSe Thin Film Solar Cells, *J. Phys. Chem. C*, 2016, **120**(8), 4251–4258.

14 M. Neuschitzer, J. Marquez, S. Giraldo, M. Dimitrievska, M. Placidi, I. Forbes, V. Izquierdo-Roca, A. Pérez-Rodriguez and E. Saucedo, V_{OC} Boosting and Grain Growth Enhancing Ge-Doping Strategy for $Cu_2ZnSnSe_4$ Photovoltaic Absorbers, *J. Phys. Chem. C*, 2016, **120**, 9661–9670.

15 E. Avancini, R. Carron, B. Bissig, P. Reinhard, R. Menozzi, G. Sozzi, S. Di Napoli, T. Feurer, S. Nishiwaki, S. Buecheler and A. N. Tiwari, Impact of compositional grading and overall Cu deficiency on the near-infrared response in Cu(In,Ga)Se_2 solar cells, *Prog. Photovoltaics*, 2017, **25**(3), 233–241.

16 T. Kato, Cu(In,Ga)(Se,S)$_2$ solar cell research in Solar Frontier: Progress and current status, *Jpn. J. Appl. Phys.*, 2017, **56**(4), 04CA02.

17 C. J. Hages, S. Levcenco, C. K. Miskin, J. H. Alsmeier, D. Abou-Ras, R. G. Wilks, M. Bär, T. Unold and R. Agrawal, Improved performance of Ge-alloyed CZTGeSSe thin-film solar cells through control of elemental losses, *Prog. Photovoltaics*, 2013, **23**(3), 376–384.

18 S. Lopez-Marino, M. Espíndola-Rodríguez, Y. Sánchez, X. Alcobé, F. Oliva, H. Xie, M. Neuschitzer, S. Giraldo,

M. Placidi, R. Caballero, V. Izquierdo-Roca, A. Pérez-Rodríguez and E. Saucedo, The importance of back contact modification in $Cu_2ZnSnSe_4$ solar cells: The role of a thin MoO_2 layer, *Nano Energy*, 2016, **26**, 708–721.

19 H. Xie, Y. Sánchez, S. López-Marino, M. Espíndola-Rodríguez, M. Neuschitzer, D. Sylla, A. Fairbrother, V. Izquierdo-Roca, A. Pérez-Rodríguez and E. Saucedo, Impact of Sn(S,Se) Secondary Phases in $Cu_2ZnSn(S,Se)_4$ Solar Cells: a Chemical Route for Their Selective Removal and Absorber Surface Passivation, *ACS Appl. Mater. Interfaces*, 2014, **6**, 12744–12751.

20 M. Neuschitzer, Y. Sanchez, S. López-Marino, H. Xie, A. Fairbrother, M. Placidi, S. Haass, V. Izquierdo-Roca, A. Perez-Rodriguez and E. Saucedo, Optimization of CdS buffer layer for high-performance $Cu_2ZnSnSe_4$ solar cells and the effects of light soaking: elimination of crossover and red kink, *Prog. Photovoltaics*, 2015, **23**, 1660–1667.

21 A. Fairbrother, X. Fontané, V. Izquierdo-Roca, M. Espíndola-Rodríguez, S. López, M. Placidi, L. Calvo-Barrio, A. Pérez-Rodríguez and E. Saucedo, On the Formation Mechanisms of Zn-rich Cu_2ZnSnS_4 Films Prepared by Sulfurization of Metallic Stacks, *Sol. Energy Mater. Sol. Cells*, 2013, **112**, 97–105.

22 V. Izquierdo-Roca, E. Saucedo, C. M. Ruiz, X. Fontané, L. Calvo-Barrio, J. Álvarez-Garcia, P.-P. Grand, J. S. Jaime-Ferrer, A. Pérez-Rodríguez, J. R. Morante and V. Bermudez, Raman scattering and structural analysis of electrodeposited $CuInSe_2$ and S-rich quaternary $CuIn(S,Se)_2$ semiconductors for solar cells, *Phys. Status Solidi A*, 2009, **206**(5), 1001–1004.

23 M. Dimitrievska, H. Xie, A. J. Jackson, X. Fontané, M. Espíndola-Rodríguez, E. Saucedo, A. Pérez-Rodríguez, A. Walsh and V. Izquierdo-Roca, Resonant Raman scattering of ZnS_xSe_{1-x} solid solutions: the role of S and Se electronic states, *Phys. Chem. Chem. Phys.*, 2016, **18**(11), 7632–7640.

24 A. Fairbrother, L. Fourdrinier, X. Fontané, V. Izquierdo-Roca, M. Dimitrievska, A. Pérez-Rodríguez and E. Saucedo, Precursor Stack Ordering Effects in $Cu_2ZnSnSe_4$ Thin Films Prepared by Rapid Thermal Processing, *J. Phys. Chem. C*, 2014, **118**, 17291–17298.

25 D. J. Chakrabarti and D. E. Laughlin, *Bull. Alloy Phase Diagrams*, 1981, **2**(3), 305–315.

26 T. Thersleff, S. Giraldo, M. Neuschitzer, P. Pistor, E. Saucedo and K. Leifer, Chemically and morphologically distinct grain boundaries in Ge-doped $Cu_2ZnSnSe_4$ solar cells revealed with STEM-EELS, *Mater. Des.*, 2017, **122**, 102–109.

27 S. Fürtauer, D. Li, D. Cupid and H. Flandorfer, The Cu–Sn phase diagram, Part I: New experimental results, *Intermetallics*, 2013, **34**, 142–147.

28 A. Weber, H. Krauth, S. Perlt, B. Schubert, I. Kötschau, S. Schorr and H. W. Schock, Multi-stage evaporation of Cu_2ZnSnS_4 thin films, *Thin Solid Films*, 2009, **517**(7), 2524–2526.

29 A. Redinger, D. M. Berg, P. J. Dale and S. Siebentritt, The consequences of kesterite equilibria for efficient solar cells, *J. Am. Chem. Soc.*, 2011, **133**(10), 3320–3323.

30 M. C. Johnson, C. Wrasman, X. Zhang, M. Manno, C. Leighton and E. S. Aydil, Self-Regulation of Cu/Sn Ratio in the Synthesis of Cu_2ZnSnS_4 Films, *Chem. Mater.*, 2015, **27**(7), 2507–2514.

31 G. Larramona, S. Levcenko, S. Bourdais, A. Jacob, C. Choné, B. Delatouche, C. Moisan, J. Just, T. Unold and G. Dennler, Fine-tuning the Sn content in CZTSSe thin films to achieve 10.8% solar cell efficiency from spray-deposited water-ethanol-based colloidal inks, *Adv. Energy Mater.*, 2015, **5**, 1501404.

32 H. Sugimoto; C. Liao; H. Hiroi; N. Sakai and T. Kato, Life-time improvement for high efficiency Cu_2ZnSnS_4 submo-dules, Proceedings of 2013 IEEE 39th Photo-voltaic Specialists Conference (PVSC), 2013, 3208–3211.

33 S. Hartnauer, S. Körbel, M. A. L. Marques, S. Botti, P. Pistor and R. Scheer, Stable single-phase Zn-rich $Cu_2ZnSnSe_4$ through In doping, *APL Mater.*, 2016, **4**, 070701.

34 A. Han, Y. Huang, X. Liu, W. Xian, F. Meng and Z. Liu, Morphology, structure, and properties of Cu-poor and Cu-rich $Cu(In,Ga)Se_2$ films partially selenized using H_2Se gas, *Jpn. J. Appl. Phys.*, 2016, **55**(11), 115502.

35 Y. S. Lee, T. Gershon, O. Gunawan, T. K. Todorov, T. Gokmen, Y. Virgus and S. Guha, $Cu_2ZnSnSe_4$ thin-film solar cells by thermal co-evaporation with 11.6% efficiency and improved minority carrier diffusion length, *Adv. Energy Mater.*, 2015, **5**(7), 1401372.

36 S. Oueslati, G. Brammertz, M. Buffière, H. ElAnzeery, O. Touayar, C. Köble, J. Bekaert, M. Meuris and J. Poortmans, Physical and electrical characterization of high-performance $Cu_2ZnSnSe_4$ based thin film solar cells, *Thin Solid Films*, 2015, **582**, 224–228.

37 J. Li, H. Wang, L. Wu, C. Chen, Z. Zhou, F. Liu, Y. Sun, J. Han and Y. Zhang, Growth of $Cu_2ZnSnSe_4$ film under controllable Se vapor composition and impact of low Cu content on solar cell efficiency, *ACS Appl. Mater. Interfaces*, 2016, **8**(16), 10283–10292.

38 R. Scheer and H. W. Schock, *Chalcogenide Solar Cells*, Wiley-VCH, ISBN: 978-3-527-31459.

39 A. Crovetto and O. Hansen, What is the band alignment of $Cu_2ZnSn(S,Se)_4$ solar cells?, *Sol. Energy Mater. Sol. Cells*, 2017, **169**, 177–194.

Chapter 4

Interaction of Ge with Na and Post-Deposition Treatment

Among the most well-known factors that can notably impact on device performance, post-deposition treatments (PDT) and the presence and control of alkali elements during thermal processes are of key importance to obtain high efficiency solar cells. However, there is some discrepancy in the literature about PDT temperatures and different alkalis efficacy, therefore additional studies are needed for a better understanding.

Regarding alkali doping, especially Na, and more recently K and heavier Rb and Cs, have been proven to be of paramount importance in the field of CIGS technology to obtain the highest efficiencies.[19,98,100–102] In the case of Na, it naturally out-diffuses from the soda-lime glass substrate to the absorber during the thermal annealing process, although it can also be supplied extrinsically through Na compound precursors.[103,104] For CIGS, the effects of Na are commonly associated with an increase in p-type conductivity (by reducing the donor density), increasing net hole concentration,[105,106] enhanced grain growth and surface morphology,[107] and reduced interdiffusion of In and Ga helping the formation of the graded band-gap.[108] Furthermore, in terms of device electrical properties, all the studies report an increase in V_{OC} and FF.[88,109,110]

However, when it comes to kesterites, the influence of Na on CZTSSe-based solar cells has been less thoroughly investigated. In the available literature, similarly to the case of CIGS, Na incorporation has demonstrated to substantially improve the device efficiency, enhancing the V_{OC} and FF by increasing the hole density and shifting the acceptor level closer to the conduction band, also reducing the concentration of certain deep recombination centers.[81] Likewise, a significant improvement in grain growth and crystallinity has been reported by several groups.[82,111] But these advantageous effects of alkalis in kesterite are not limited to Na; first studies on the effect of K addition have confirmed similar beneficial effects on kesterite absorber growth and electrical properties.[112,113] Additionally, several recent studies have analyzed and compared different alkali elements and their impact on solar cell properties and device performance, although no consistent experimental results have been obtained.[50,114–117] In particular, in the work of Haass et al., a very interesting relationship between alkali metals and Sn concentrations has been found, revealing a complex dependency of metal ratios, alkali elements, and alkali concentration on the device performance in high efficiency kesterite solar cells.[50] Table 4.1 presents some characteristics of the most relevant works reported in the literature, highlighting the conclusions about the effect of alkali doping.

Table 4.1. Summary of relevant studies about the impact of different alkalis on kesterite solar cells performance.

Reference	Absorber material	Relevant features	Order of performance improvement
Mule et al.[117] Thin Solid Films 2016	CZTSe	Spin coated alkali elements on evaporated metal precursor stack. Best efficiency of 8.3% for Na+K combined doping.	Na > Cs > K > Rb > Li
Hsieh et al.[114] Adv. Energy Mater. 2016	CZTSSe	Alkali metal-containing molecular precursor. Best efficiency of 8.0% for K doping.	K > Rb > Na > Li > Cs
Altamura et al.[116] Scientific Reports 2016	CZTSSe	Electrostatic spray-assisted vapor deposition method. Best efficiency of 6.4% for Rb doping.	Rb > Na > Li
López-Marino et al.[115] J. Mater. Chem A 2016	CZTSe	Flexible ferritic steel substrates. Evaporated alkali metals / sputtered Mo:Na. Best efficiency of 6.1% for Na doping (Mo:Na).	Na > K
Haass et al.[50] Adv. Energy Mater. 2017	CZTSSe	Solution-based process + alkali chlorides. Best efficiency of 11.5% for Li incorporation.	Li > Na > K > Rb > Cs

In the same vein, one of the publications included in this chapter confirms the strong interaction between group IV elements (Ge, Sn) and alkalis. In particular, we investigate the complex Na-Ge interaction in a detailed analysis of Ge-doped CZTSe devices, revealing significant differences between low Ge content (~10 nm, and high efficiency) and higher Ge contents (≥25 nm, and degraded performance). In this study, we explain how Ge concentration can notably impact on the Na content and, thus, modify the doping level of the kesterite absorber. In addition, a possible mechanism underlying this interaction and the implication on the formation of point defects are presented, highlighting the importance of accurately controlling alkali and group IV elements concentration to achieve high performing kesterite solar cells.

Closely related to alkalis interaction and diffusion are the widely used post-deposition treatments, especially low temperature post-deposition annealings (PDA). These treatments are known to have a clear influence on Na diffusion mechanisms and distribution throughout the device structure.[118] In general, low temperature PDA either in air or inert atmosphere have been reported by several groups as beneficial to increase device efficiency.[119–121] In fact, already in other chalcogenide thin film solar cells, the use of PDA treatments have shown clear improvements of device performance.[122–124] Moreover, for kesterites, these low temperature treatments are especially interesting since they can impact on the well-documented Cu-Zn disorder. Some studies have determined the order-disorder transition temperature around 200°C, for CZTSe,[125] and 260°C, for CZTS,[126] although this phenomenon has not been yet clearly associated with the formation of point defects and their influence on device performance. Recently, Neuschitzer et al. have presented an optimization of different PDA treatments for CZTSe bare absorbers, CZTSe/CdS heterojunctions and full devices, and its impact on solar cell performance, interestingly revealing the formation of a Cu-depleted and Zn-enriched absorber surface, which has proven to be mandatory for high device efficiency.[127]

In the work presented in the last publication of this chapter, we go a step further and investigate in detail diffusion and recrystallization phenomena at the absorber/buffer interface during PDA performed at different temperatures (from RT to 350°C, in air atmosphere), correlating Raman spectroscopy analysis with optoelectronic characterization of full CZTSe devices. Additionally, we comment on the formation and evolution of defects due to Cu-Zn redistribution within the surface and bulk of the absorber. This study opens the possibility of tuning the number of defects in the kesterite absorber by choosing the suitable PDA temperature. Figure 4.1 shows preliminary results of the impact of PDA temperatures on different photovoltaic parameters. Interestingly, two different temperatures can be chosen to maximize device conversion efficiency: 175°C, by enhancing J_{SC}, or 250°C, by enhancing V_{OC}; further characterization results and discussion can be found in the corresponding publication.

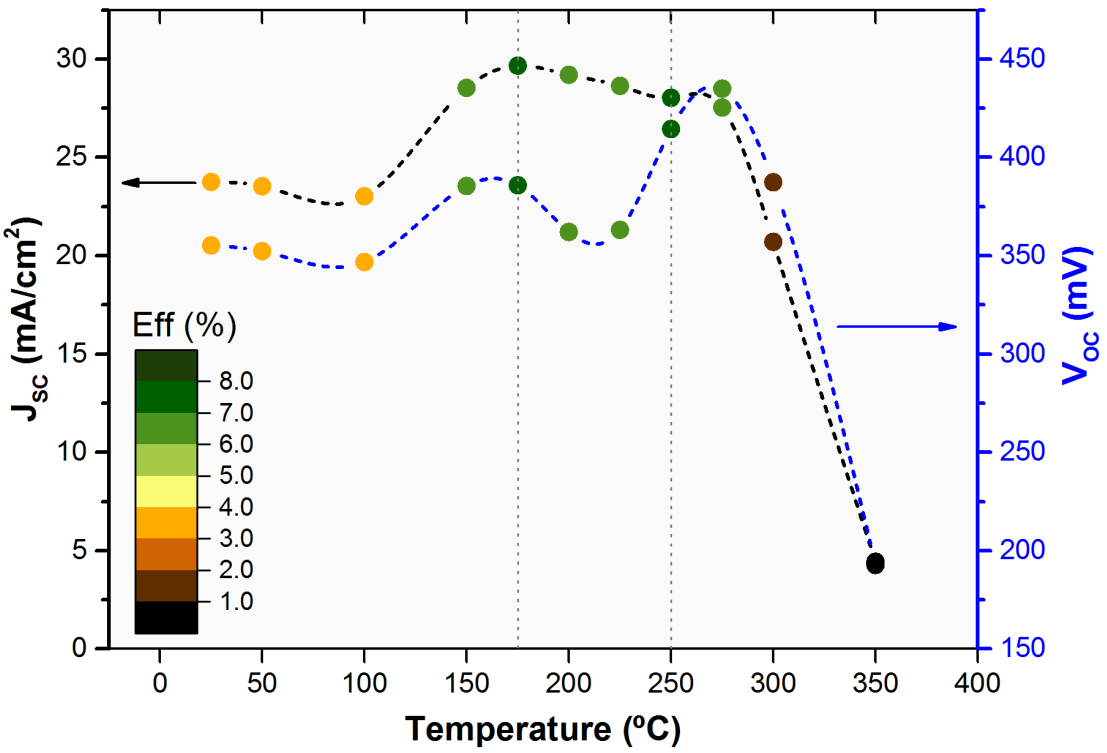

Figure 4.1. Impact of PDA temperature on different photovoltaic parameters (J_{SC}, V_{OC} and conversion efficiency). Vertical dashed lines mark two different efficiency maximums.

This chapter includes the following two publications: "$Cu_2ZnSnSe_4$-based solar cells with efficiency exceeding 10% by adding a superficial Ge nanolayer: The interaction between Ge and Na", and "Raman scattering analysis of the surface chemistry of kesterites: Impact of post-deposition annealing and Cu/Zn reordering on solar cell performance" in which detailed information about the mentioned results is presented.

$Cu_2ZnSnSe_4$-Based Solar Cells With Efficiency Exceeding 10% by Adding a Superficial Ge Nanolayer: The Interaction Between Ge and Na

Sergio Giraldo, Markus Neuschitzer, Marcel Placidi, Paul Pistor, Alejandro Pérez-Rodríguez, and Edgardo Saucedo

***Abstract*—Recently, beneficial effects of the incorporation of small amounts of Ge into $Cu_2ZnSnSe_4$ (CZTSe)-based solar cells have been reported, showing that the presence of Ge can enhance the crystalline properties of CZTSe, assisting the grain growth, leading to high-efficiency devices. In this study, we prepare CZTSe layers by a sequential process consisting of the sputtering of metallic stacks followed by a reactive annealing under Se atmosphere, previously adding different Ge nanolayers on top (from 0 to 50 nm). The present work is focused on the study of the interaction between germanium and sodium. As is widely known, Na is a very important dopant in kesterite, which plays an essential role in the doping level control. We demonstrate that during the annealing process, a Ge–Se liquid phase is formed which dissolves preferably Na-related phases modifying the content of this last element in the CZTSe absorber and impacting notably on the electrical properties of the layers and, concomitantly, on the performance of the devices. We support our Ge–Na interaction model with experiments using Na-free substrates, showing the importance of accurately controlling the Na content when Ge is used to increase the efficiency of CZTSe-based solar cells.**

***Index Terms*—Deposition and characterization of thin-film photovoltaic (PV) absorbers, PV cells, semiconductor device doping, thin-film devices.**

I. Introduction

$Cu_2ZnSn(S,Se)_4$ photovoltaic (PV) material (CZTSSe, known as kesterites, their structure) has attracted recently a lot of attention as possible candidate for replacing $Cu(In,Ga)Se_2$ (CIGSe) and CdTe in thin-film PV technologies [1], [2]. This is mainly because of In, Ga, and Te scarcity, as well as Cd toxicity [3]. On the contrary, CZTSSe is formed only by earth-abundant elements with low toxicity, ensuring the sustainability and large-scale viability of kesterite technologies. Nevertheless, although the material exhibits relatively high efficiencies, these are still far from those reported for more mature CIGSe and CdTe technologies, owing to the large voltage deficit of kesterites [4]. Among the possible origins for this voltage deficit, the short minority carrier lifetime of the bulk, the interfaces properties (the buffer/window and the rear contact interfaces), the passivation of the grain boundaries, etc., can have a strong impact on this important device parameter [4], [5].

In this sense, strategies to increase the V_{OC} in CdTe and CIGS technologies have been widely explored. These include, for example, the design of the back contact [6], the use of bandgap gradients [7], and the control of surface doping to implement "buried junction" concepts [8]. In kesterites and due to the lower maturity of the materials, these advanced concepts have yet to be developed. Additionally, alkaline doping in chalcopyrites, as well as in kesterites, has shown to be crucial for the absorber doping level control, being a determinant factor in order to achieve high efficiencies, mainly impacting on the voltage and fill factor [9], [10].

On the other hand, recently, it was shown that introducing very small quantities of Ge (between 5 and 15 nm) in the CZTSe surface, a large improvement of the V_{OC} is achieved, leading to an impressive efficiency increase of more than 3% in absolute, allowing to achieve efficiencies easily exceeding 10% [5]. Among other possible factors, it has been observed that during the reactive annealing process, a $Ge_3Se_{7(s)}$ phase is formed, which decomposes incongruently into volatile $GeSe_{2(v)}$ and a Ge–Se liquid phase, acting as a crystallization flux and assisting the grain growth [5]. On the contrary, when thicker Ge nanolayers (>15 nm) are used, a general deterioration of the material and device properties is observed, whose origin is not clear, although it could be related to the interaction of the Ge–Se liquid phase with the kesterite absorber.

In this work, we present a detailed comparative analysis of CZTSe:Ge devices fabricated with low Ge content (∼10 nm) and high efficiency, together with devices made using higher Ge contents (≥25 nm) showing deteriorated conversion efficiencies, with the aim to understand the dynamics of Ge incorporation into the CZTSe lattice and its interaction with the kesterite matrix. We show that during the reactive annealing, there is a strong interaction between Ge and Na, which controls the doping level of the absorber and, consequently, their electrical properties and the performance of the solar cells. This interaction between

Manuscript received December 23, 2015; revised February 9, 2016; accepted February 18, 2016. Date of publication March 10, 2016; date of current version April 19, 2016. This work was supported by the Framework 7 program under the Project KESTCELLS (FP7-PEOPLE-2012-ITN-316488), by the Ministerio de Economía y Competitividad de España (MINECO) under the SUNBEAM Project (ENE2013-49136-C4-1-R), and by European Regional Development Funds (ERDF, FEDER Programa Competitivitat de Catalunya 2007–2013). The work of S. Giraldo was supported by the Government of Spain through the FPI fellowship (BES-2014-068533). The work of M. Placidi was supported through the MINECO postdoctoral fellow (FPDI-2013-18968). The work of E. Saucedo was supported through the "Ramón y Cajal" fellowship (RYC-2011-09212). The work of P. Pistor was supported by the European Union through the JUMPKEST Marie Curie Individual fellowship (FP7-PEOPLE-2013-IEF-625840).

S. Giraldo, M. Neuschitzer, M. Placidi, P. Pistor, and E. Saucedo are with the Catalonia Institute for Energy Research (IREC), 08930 Barcelona, Spain (e-mail: sgiraldo@irec.cat; mneuschitzer@irec.cat; mplacidi@irec.cat; ppistor@irec.cat; esaucedo@irec.cat).

A. Pérez-Rodríguez is with the Catalonia Institute for Energy Research (IREC), 08930 Barcelona, Spain, and also with the IN2UB, Universitat de Barcelona, 08028 Barcelona, Spain (e-mail: aperezr@irec.cat).

Color versions of one or more of the figures in this paper are available online at http://ieeexplore.ieee.org.

Digital Object Identifier 10.1109/JPHOTOV.2016.2535236

Ge and Na leads to achieve efficiencies in the 10–10.6% level when Ge and Na quantities are the optimum ones, while the use of higher Ge quantities results in degraded devices exhibiting low efficiencies due to, among others, the high solubility of Na species in the larger amount of Ge–Se liquid phase, ultimately leading to a reduced Na concentration in these samples. The understanding of the interaction between both elements can help to further increase the efficiency of kesterite-based devices by using advanced technological concepts.

II. Experimental Details

A. Solar Cell Fabrication

CZTSe absorbers were synthesized by a sequential process onto Mo-coated soda-lime glass substrates, in which a metallic stack was deposited followed by a reactive annealing process. Cu/Sn/Cu/Zn metallic stacks were produced by DC magnetron sputtering (Alliance Ac450), carefully tailoring each metal thickness in order to obtain Cu-poor (Cu/(Zn + Sn) = 0.75) and Zn-rich (Zn/Sn = 1.20) absorbers, determined with calibrated X-ray fluorescence (XRF, Fischerscope XVD) [11]. Prior to the selenization process, different Ge thicknesses were thermally evaporated on top of the precursors (Oerlikon Univex 250). In this study, we compare the reference sample (without Ge) with the ones produced with 10 nm of Ge (the optimum Ge quantity) and with 25 nm of Ge (exceeding the optimum Ge quantity). Other Ge quantities (5, 12.5, 15, and 50 nm) were also included in the XRF compositional analysis for a more reliable and detailed study. A conventional tubular furnace was used to perform the reactive annealing under Se + Sn atmosphere, together with graphite boxes (69 cm^3 in volume) containing 100 mg of Se (Alfa-Aesar powder, 200 mesh, 99.999%) and 5 mg of Sn (Alfa-Aesar powder, 100 mesh, 99.995%). The selenization consisted in a two-step process: first, 400 °C during 30 min and 1.5-mbar Ar pressure, and second, 550 °C during 15 min and 1-bar Ar pressure. Both heating ramps were set at 20 °C/min, and with a natural cooling down to room temperature. The as-annealed absorbers were chemically etched in order to remove secondary phases on the surface and to passivate it by using three different solutions: first, in a $KMnO_4 + H_2SO_4$ solution, then in a $(NH_4)_2S$ solution, and finally, in a diluted KCN solution [11]–[13]. Immediately after the chemical etchings, a 50-nm-thick CdS buffer layer was deposited by chemical bath deposition, followed by a DC-pulsed sputtering deposition of i-ZnO (50 nm) and In_2O_3–SnO_2 (ITO, 350 nm) as transparent conductive window layer (Alliance CT100). The finished samples were mechanically scribed in 3 × 3 mm^2 cells using a manual microdiamond scriber (MR200 OEG) and, finally, subjected to a 250 °C postdeposition annealing in air atmosphere on a hot plate for 15 min.

B. Sample Characterization

XRF spectroscopy was used to measure the composition of the absorbers made with different Ge quantities using a Fischerscope XVD equipment. In order to assess possible compositional variations due to the several chemical etchings, XRF analyses were performed to the as-annealed absorbers, before any chemical etching, and afterward to the as-etched absorbers. Additionally, scanning electron microscope/energy-dispersive X-ray spectroscopy (SEM/EDX) analysis was carried out before and after the chemical etchings. SEM images were obtained with a ZEISS Series Auriga microscope using 5-kV accelerating voltage, while EDX (Oxford Instruments, XMax) was performed using 20-kV accelerating voltage. Time-of-flight secondary ion mass spectrometry (TOF-SIMS) measurements were performed in an ION-TOF IV equipment, using a 25-kV Bi cluster primary ion gun for analysis, and O_2 and Cs ion guns for sputtering in depth profiling modes. The analyzed area was 50 μm × 50 μm with a cycle time of 100 μs and a time-to-digital converter resolution of 200 ps. Capacitance–voltage (C–V) measurements were performed in the dark at room temperature with a frequency of 100 kHz and a modulation voltage of 50 mV using an impedance analyzer (Novocontrol Technologies). From C–V measurements, charge carrier concentration (N_{CV}) and space charge region width (SCR) were calculated assuming a relative dielectric permittivity of $\varepsilon = 8.5$ for CZTSe. Finally, the resulting devices were characterized using a calibrated Sun 3000 class AAA solar simulator (Abet Technologies) to obtain dark and illuminated J–V curves. Measurements were carried out at 25 °C, under AM1.5G 1-sun illumination conditions (uniform illumination area of 15 × 15 cm^2).

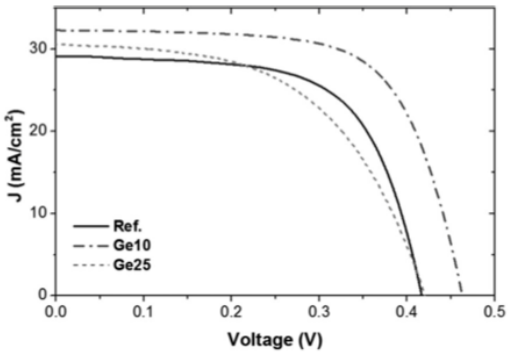

Sample	Eff. (%)	V_{OC} (mV)	J_{SC} (mA.cm^{-2})	FF (%)	R_S (Ω.cm^2)	R_{Sh} (Ω.cm^2)	N_{CV} (cm^{-3})	SCR (μm)
Ref	7.7	417	29.1	63.8	0.7	333	2x10^{16}	0.15
Ge10	10.0	463	32.3	66.9	0.9	734	3x10^{16}	0.10
Ge25	6.9	420	30.5	53.6	1.3	252	4x10^{15}	0.32

Fig. 1. Illuminated J–V curves of the reference, Ge10, and Ge25 devices. In the corresponding table, the optoelectronic parameters extracted from the J–V curves and the N_{CV} (charge carriers density) and SCR extracted from the C–V measurements are displayed.

III. Results and Discussion

Fig. 1 shows the comparison of the illuminated J–V curves of the reference (without Ge), the Ge10, and the Ge25 samples. When Ge is incorporated into the absorber using thicknesses about 10 nm, a general improvement of all the optoelectronic parameters is observed, as has been reported before [5]. In particular, V_{OC} values around 450–490 mV are easily achieved, leading to efficiencies exceeding 10%, and one of

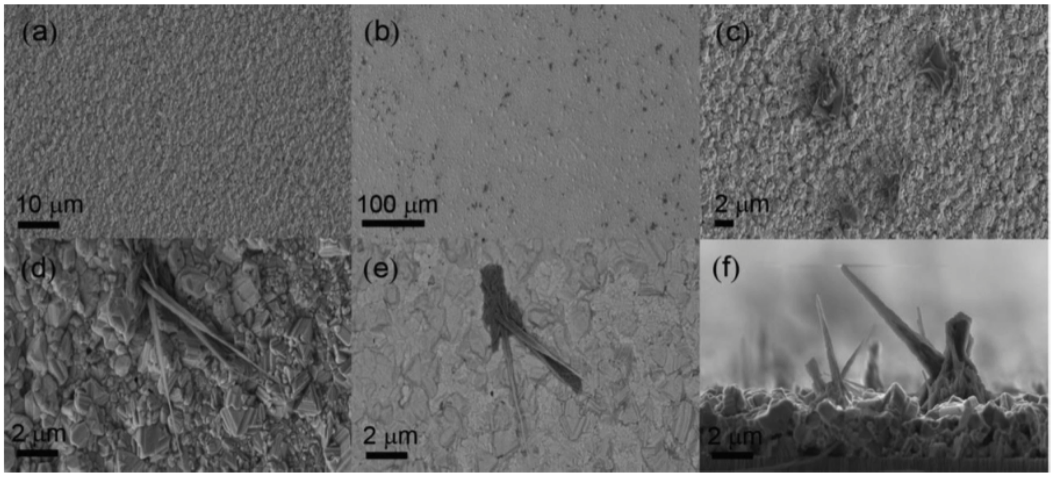

Fig. 2. SEM images of different samples. (a) Surface overview of Ge10 absorber. (b) Surface overview of Ge50 absorber. (c) Detail of the surface morphologies observed in low density in Ge10 layer. (d) Detail of the surface morphologies observed in Ge50 layers. (e) Backscattered electron image of the previous figure. (f) Cross-sectional image of a Ge25 layer showing in detail the observed surface morphologies.

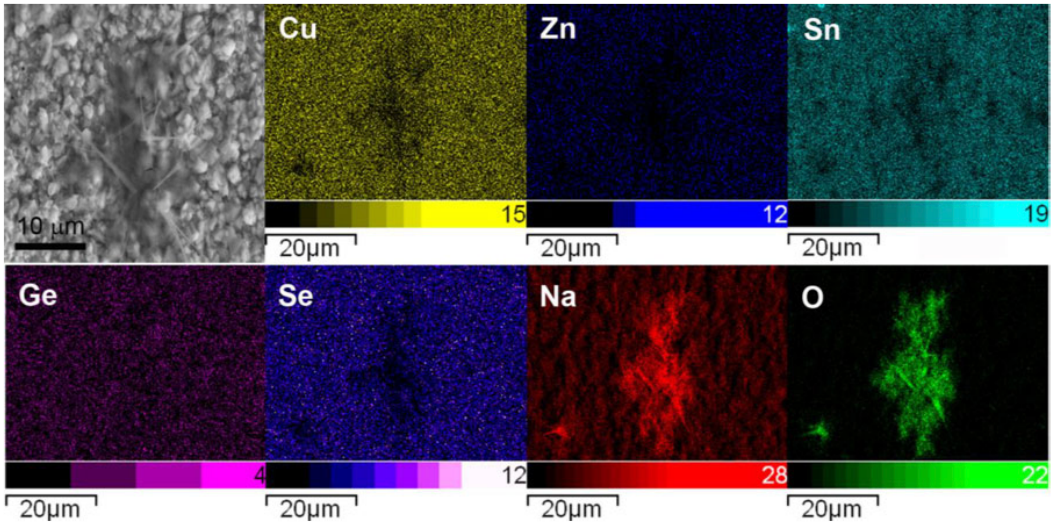

Fig. 3. Top-view SEM image of the typical morphologies observed in layers made using high Ge content and the corresponding Cu, Zn, Sn, Ge, Se, Na, and O compositional mappings obtained by EDX.

the lowest V_{OC} deficits reported for this material [5]. Nonetheless, if thicker Ge layers are used (Ge thickness $\geq$ 25 nm), a fast deterioration of the solar cell properties is clearly observed. Interestingly, besides the drop of the V_{OC} value, the FF of the devices is largely affected, obtaining values well below those typical for the reference material (without Ge). Conversely, the current density of the devices is less affected when compared with the previous two parameters.

Through a deep electrical characterization of the devices by *C–V* measurements, we can obtain two important parameters related to the quality of the devices under study: the absorber's carrier concentration (N_{CV}) and the SCR. N_{CV} is almost invariable for the Ge10 sample with respect to the reference one, while it decreases one order of magnitude for the Ge25. On the other hand, the SCR is slightly reduced and then remarkably increases. It is possible to correlate the behavior of these two parameters with those observed for the solar cell devices. It was demonstrated that for the Ge10 sample, the grain size and the crystalline quality are improved [5]. Then, considering that the SCR decreases while the doping level is almost constant or only slightly increases, this feature can contribute to boost the internal electric field at the SCR and then the V_{OC}. Together with this, the proved better crystalline quality of the Ge10 can imply the reduction of the defects density in the bulk inducing less recombination in the material, thus improving the diffusion length and/or carrier life time, positively impacting in the voltage [14].

On the contrary, the devices behave differently when the Ge nanolayer thickness is increased. Notably, the current density

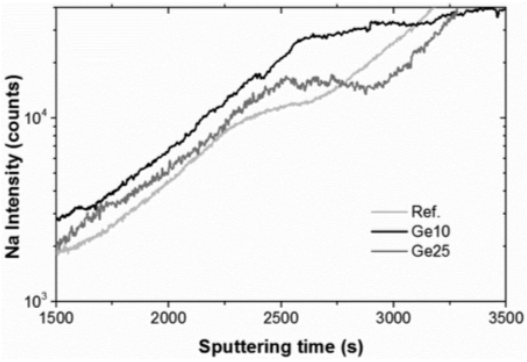

Fig. 4. TOF-SIMS in-depth profile of Na for samples Ge10, Ge25, and the reference one (no Ge added in the system). Na intensity was corrected using Cu-intensity signal (considering that Cu concentration is the same in both samples, since they were prepared from the same precursor and same conditions).

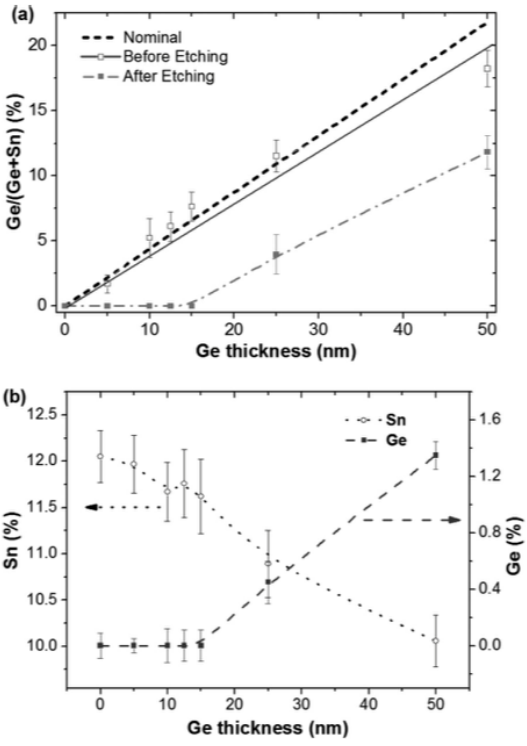

Fig. 5. (a) Nominal, before, and after etching Ge/(Ge+Sn) ratio as a function of Ge thickness. Last two values have been obtained by XRF. (b) Ge and Sn concentration after etching as a function of Ge thickness obtained by XRF.

is only slightly reduced, suggesting a limited impact of the Ge concentration on this parameter, i.e., a decent charge collection is kept. Whereas the SCR increases and the N_{CV} diminishes, the V_{OC} and, mainly, the FF are strongly reduced. This can be related to several complex issues but most probably to the deterioration of the transport properties of the material, either for the reduction of the carrier's life time in the bulk or for the deterioration of the quality of the interfaces (back and rear

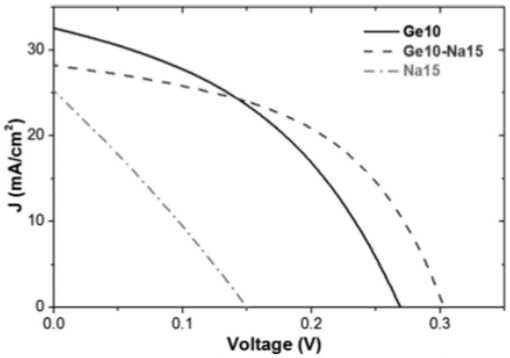

Sample	Eff. (%)	V_{OC} (mV)	J_{SC} (mA.cm^{-2})	FF (%)	R_S (Ω.cm^2)	R_{Sh} (Ω.cm^2)
Ge10	3.6	269	32.3	41.7	1.8	26
Ge10-Na15	4.2	303	28.2	49.1	0.7	47
Na15	1	149	24.8	27.7	1	7

Fig. 6. Illuminated *J–V* curves and the corresponding optoelectronic parameters for CZTSe-based devices prepared onto Na-free substrates (Si/SiO_2). Ge10—absorber synthesized including 10 nm of Ge. Ge10-Na15—absorber synthesized including 10 nm of Ge and 15 nm of NaF. Na15—absorber synthesized including 15 nm of NaF.

interfaces, grain boundaries, etc.). Both can be associated with the formation of defects that increase the recombination, related to the remarkable change in the charge carrier density that is induced by the change in the doping level of the material, driven by the presence of Ge.

Fig. 2 displays a detailed SEM analysis of the Ge10 and Ge25 as-annealed absorbers. The Ge10 absorber top view [see Fig. 2(a)] shows the typical uniform appearance with grains in the order of 1–2 μm. Nevertheless, taking a look at the Ge25 absorber [see Fig. 2(b)], a lot of dark morphologies are clearly observed. These morphologies seem to be needle-like structures with a different composition than the absorber, as shown in more detail in Fig. 2(d)–(f). In particular, backscattered electron image of Fig. 2(e) highlights the different composition of the absorber surface and the needle-like structures. In addition, in the case of the Ge10 absorber, some small dark crystals start to appear along the surface, which could be the beginning of formation of these needle-like structures in the Ge25 sample. Therefore, the use of higher Ge quantities seems to be somehow affecting the synthesis reaction of the kesterite, inducing the formation of additional compounds remaining on the surface. It is important to note that all these superficial morphologies were only observed in the as-annealed absorbers, since they are removed during the chemical etching processes, as corroborated by SEM.

In order to assess the composition of the observed morphologies and further investigate their origin, Fig. 3 shows the EDX mappings of some of these needle-like structures, revealing that they are made mainly of Na and O. This suggests that the presence of higher Ge concentrations in the absorbers induces Na extraction toward the surface, forming Na–O-related compounds. Of course, as is well known, the Na excess comes from the

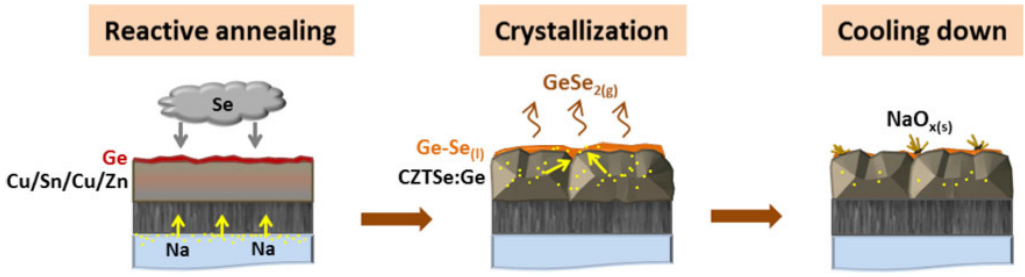

Fig. 7. Schematic representation of the interaction between Ge and Na in the CZTSe absorber.

outdiffusion of this element from the substrate (soda-lime glass) during the annealing process. The involved mechanism could be associated with the formation of relatively large amounts of Ge–Se liquid phase during the annealing stage, inducing the Na dissolution in this phase. In the further crystals growth stage, the excess of these liquid phase would come out toward the surface and, finally, during the cooling down process, forming the observed morphologies. Logically, we would expect to find Ge associated with these superficial morphologies, although it was not detected by EDX probably because it is below the detection limit. Furthermore, with this explanation, a decrease in the Na concentration is expected for the samples with higher Ge content, which could be clearly linked to the remarkable decrease of the doping level estimated by the *C–V* measurements (see the table in Fig. 1).

To demonstrate the expected decrease of the Na concentration, TOF-SIMS analysis was performed for the samples Ge10, Ge25, and the reference one without Ge. Fig. 4 depicts the Na in-depth profiles corresponding to the absorber region, corroborating an increase of the Na concentration for the Ge10 sample with respect to the reference one, in agreement with the doping level (N_{CV}) increase presented in Fig. 1 (see the table in this figure). Further increase of the Ge content (Ge25 sample) leads to the reduction of the Na quantity in the layer. Overall, the Na concentration diminishes in the whole CZTSe absorber, from the surface to the back region, but mainly in this last part, because it is also in agreement with the doping level reported in Fig. 1. This could demonstrate that the Ge–Se liquid phase is very effective in dissolving and removing Na from the complete absorber, controlling the alkaline doping level of the CZTSe layer.

In order to investigate in more detail possible compositional variations due to the Ge incorporation, additional XRF analyses were performed on a complete set of samples with different Ge content. Fig. 5(a) shows the Ge/(Ge + Sn) ratio of the as-annealed absorbers (before any etching) and the Ge/(Ge + Sn) ratio of the same samples after the different chemical etchings, together with the expected nominal ratio with increasing Ge thickness. From these results, a Ge loss after the etching processes is clearly observed , which would mean that most of the Ge remains on the absorber surface. In the case of Ge thicknesses below 15 nm, it seems that almost all the Ge is removed after etching, although it is important to take into consideration the error of the measurements. Thus, these observations would support our explanation since most of the Ge has to be in the absorbers surface and possibly associated with the already analyzed Na–O morphologies. On the other hand, Fig. 5(b) shows the evolution of Ge and Sn concentrations after etching as a function of Ge thickness, demonstrating a significant Ge incorporation in the material as we introduce Ge thicknesses over 15 nm. In fact, the appearance of large amounts of Na–O needle-like structures on the CZTSe absorber surface corresponds well with the inflection point of the Ge incorporation curve in Fig. 5, corroborating that their formation is associated with the Ge quantity in the samples. As was highlighted before, this Ge and Na interaction controls the doping level in CZTSe, as was presented by *C–V* measurements, impacting the formation of intrinsic and extrinsic defects in the system.

Besides this, the composition of our samples is in the Zn-rich part of the so-called A-type compositional line of CZTSe, i.e., with Sn-stoichiometric and Cu-poor conditions [15]. Under this composition, the expected main defects are [$Zn_{Cu} + V_{Cu}$], together with the possible formation of an extrinsic Na_{Cu} defect due to the Na doping of the absorber [16]. After germanium doping, the incorporation of this element in Sn position could lead to slightly Sn(Ge)-rich absorbers; thus, we would be moving above the A-type compositional line, to a certain extent, toward the E-type one [17]. In this case, we promote the possibility that Sn goes to Cu position, increasing the probability of formation of Sn_{Cu} defects, forcing the break of the extrinsic Na_{Cu} defects, and, then, releasing Na in the matrix, which could be dissolved in the Ge–Se liquid phase, explaining the consequent formation of the Na–O needle-like structures. In summary, we can propose a phenomenological Ge–Na dynamics reaction for the formation of point defects in kesterites and the releasing of Na, as follows:

$$Sn_{Sn} + Na_{Cu} + Ge \rightarrow Ge_{Sn} + Sn_{Cu} + Na. \quad (1)$$

To further explore how Na and Ge concentrations and their interaction can have an impact on the device performance, Fig. 6 shows the optoelectronic characterization of different solar cells fabricated varying the content of these two elements. The devices produced for this experiment were fabricated onto Si/SiO_2 Na-free substrates, instead of soda-lime glass substrates, to ensure the absence of any interference due to the Na contained in the glass. Additionally, 15 nm of NaF as alkaline source was used to ensure a large excess of this doping element. The PV parameters extracted from the *J–V* curves corroborate a significant drop of the device performance when an excess of Na is introduced

in the absorbers (Na15), as is already expected for highly doped absorbers [18]. Nevertheless, the additional introduction of Ge in samples with an excess of Na (Ge10-Na15) shows a strong performance recovery, reaching even higher efficiency values than using only Ge without Na (Ge10). From this study, it is possible to confirm that the addition of Ge is able to control/regulate to some extent the Na content in the absorber layer through their interaction, resulting in an important impact on the performance of solar cells.

As a summary of the proposed explanation, Fig. 7 illustrates the mechanism by which Na and Ge could probably interact when high Ge thicknesses are used. In this process, during reactive annealing, the Na would be dissolved in the Ge–Se liquid phase, and due to the growth of crystals, it would come out toward the absorbers surface, ultimately forming the observed solid morphologies during the cooling down process. Therefore, the presence of large amounts of Ge–Se liquid phase could lead to the extraction of too much Na, explaining the remarkable drop of the devices performance using Ge thicknesses higher than 15 nm.

IV. Conclusion

In this work, we have investigated the complex Na–Ge interaction, which has allowed obtaining solar cells with efficiencies exceeding 10%. The interaction involving these two elements has been shown to be crucial to understand why the performance of devices is strongly affected when thick Ge nanolayers are introduced in the absorbers. In the present study, we explained how Ge concentration can have a remarkable impact on the Na content and, thus, modifying the doping level of the kesterite, as well as the possible mechanism by which this interaction occurs and, concomitantly, the formation of point defects. Hence, the control of Na and Ge content is something to take into consideration in order to properly regulate the doping level and obtain the optimum composition in the absorbers.

Acknowledgment

The authors from the Catalonia Institute for Energy Research and the University of Barcelona belong to the M-2E (Electronic Materials for Energy) Consolidated Research Group and the XaRMAE Network of Excellence on Materials for Energy of the "Generalitat de Catalunya."

References

[1] W. Wang *et al.*, "Device characteristics of CZTSSe thin-film solar cells with 12.6% efficiency," *Adv. Energy Mater.*, vol. 4, no. 7, p. 1301465, 2014.

[2] A. Fairbrother *et al.*, "Development of a selective chemical etch to improve the conversion efficiency of Zn-rich Cu_2ZnSnS_4 solar cells," *J. Amer. Chem. Soc.*, vol. 134, no. 19, pp. 8018–8021, 2012.

[3] C. Wadia, A. P. Alivisatos, and D. M. Kammen, "Materials availability expands the opportunity for large-scale photovoltaics deployment," *Environ. Sci. Technol.*, vol. 43, no. 6, pp. 2072–2077, Mar. 2009.

[4] D. B. Mitzi, O. Gunawan, T. K. Todorov, and D. A. R. Barkhouse, "Prospects and performance limitations for Cu–Zn–Sn–S–Se photovoltaic technology," *Philos. Trans. R. Soc. London A Math. Phys. Eng. Sci.*, vol. 371, no. 1996, p. 20110432, Jul. 2013.

[5] S. Giraldo *et al.*, "Large efficiency improvement in $Cu_2ZnSnSe_4$ solar cells by introducing a superficial ge nanolayer," *Adv. Energy Mater.*, vol. 5, no. 21, art. no. 1501070, 2015.

[6] B. Vermang *et al.*, "Employing Si solar cell technology to increase efficiency of ultra-thin Cu(In,Ga)Se_2 solar cells," *Prog. Photovoltaics, Res. Appl.*, vol. 22, no. 10, pp. 1023–1029, Oct. 2014.

[7] S. H. Sohn *et al.*, "Band gap grading and photovoltaic performance of solution-processed Cu(In,Ga)S_2 thin-film solar cells," *Phys. Chem. Chem. Phys.*, vol. 16, no. 48, pp. 27112–27118, Dec. 2014.

[8] C. S. Jiang *et al.*, "Direct evidence of a buried homojunction in Cu(In,Ga)Se_2 solar cells," *Appl. Phys. Lett.*, vol. 82, no. 1, p. 127, 2003.

[9] A. D. Collord, H. Xin, and H. W. Hillhouse, "Combinatorial exploration of the effects of intrinsic and extrinsic defects in $Cu_2ZnSn(S,Se)_4$," *IEEE J. Photovoltaics*, vol. 5, no. 1, pp. 288–298, Jan. 2015.

[10] P. M. P. Salome *et al.*, "Incorporation of Na in cu(In,Ga)Se_2 thin-film solar cells: A statistical comparison between Na from soda-lime glass and from a precursor layer of NaF," *IEEE J. Photovoltaics*, vol. 4, no. 6, pp. 1659–1664, Nov. 2014.

[11] M. Neuschitzer *et al.*, "Optimization of CdS buffer layer for high-performance $Cu_2ZnSnSe_4$ solar cells and the effects of light soaking: elimination of crossover and red kink," *Prog. Photovoltaics, Res. Appl.*, vol. 23, no. 11, pp. 1660–1667, 2015.

[12] S. López-Marino *et al.*, "ZnSe etching of zn-rich $Cu_2ZnSnSe_4$: An oxidation route for improved solar-cell efficiency," *Chem. A Eur. J.*, vol. 19, no. 44, pp. 14814–14822, 2013.

[13] H. Xie *et al.*, "Impact of Sn(S,Se) secondary phases in $Cu_2ZnSn(S,Se)_4$ solar cells: A chemical route for their selective removal and absorber surface passivation," *ACS Appl. Mater. Interfaces*, vol. 25, pp. 2–6, 2014.

[14] C. J. Hages *et al.*, "Improved performance of Ge-alloyed CZTGeSSe thin-film solar cells through control of elemental losses," *Prog. Photovoltaics, Res. Appl.*, vol. 23, no. 3, pp. 376–384, Mar. 2015.

[15] M. Paris *et al.*, "Solid-state NMR and raman spectroscopy to address the local structure of defects and the tricky issue of the Cu/Zn Disorder in Cu-Poor, Zn-rich CZTS materials," *Inorg. Chem.*, vol. 53, no. 16, pp. 8646–8653, Jul. 2014.

[16] B. T. Gershon *et al.*, "The impact of sodium on the sub-bandgap states in CZTSe and CZTS," *Appl. Phys. Lett.*, vol. 106, no. 12, p. 123905, Mar. 2015.

[17] L. E. Valle Rios, K. Neldner, G. Gurieva, and S. Schorr, "Existence of off-stoichiometric single phase kesterite," *J. Alloys Compounds*, vol. 657, pp. 408–413, Sep. 2015.

[18] P. M. P. Salome´ *et al.*, "Cu(In,Ga)Se_2 solar cells with varying Na content prepared on nominally alkali-free glass substrates," *IEEE J. Photovoltaics*, vol. 3, no. 2, pp. 852–858, Apr. 2013.

Authors' photographs and biographies not available at the time of publication.

Solar Energy Materials & Solar Cells 157 (2016) 462–467

Contents lists available at ScienceDirect

Solar Energy Materials & Solar Cells

journal homepage: www.elsevier.com/locate/solmat

Raman scattering analysis of the surface chemistry of kesterites: Impact of post-deposition annealing and Cu/Zn reordering on solar cell performance

Mirjana Dimitrievska [a,*], Sergio Giraldo [a], Paul Pistor [a], Edgardo Saucedo [a], Alejandro Pérez-Rodríguez [a,b], Victor Izquierdo-Roca [a]

[a] Catalonia Institute for Energy Research (IREC), Jardins de les Dones de Negre 1 2pl., 08930 Sant Adrià del Besòs, Barcelona, Spain
[b] IN2UB, Departament d'Electrònica, Universitat de Barcelona, C. Martí i Franquès 1, 08028 Barcelona, Spain

ARTICLE INFO

Article history:
Received 13 June 2016
Accepted 8 July 2016

Keywords:
Kesterite
Defects
Solar cells
Raman spectroscopy
Optoelectronic properties

ABSTRACT

Post-deposition annealing (PDA) of chalcogenide-based solar cells has shown to enhance optoelectronic properties, though the mechanism for such improvement is still poorly understood. In this work $Cu_2ZnSnSe_4$ kesterite-based solar cells are fabricated and subjected to different PDA temperatures in order to study the structure/function relationships and explain the responsible mechanisms. Diffusion and recrystallization phenomena at the absorber/buffer interface during the PDA are investigated using multiwavelength Raman spectroscopy and photoluminescence, and correlated to the optoelectronic properties. By using varying laser excitations (442, 532, 785 nm), the selective acquisition of structural information at different depths is obtained, thus providing insights of the differences in the composition and defect concentration in the device cross section. The results show that PDA treatments of completed devices induce a redistribution of atoms (Cu and Zn) within the surface and sub-surface of the absorber layer. The absorber surface becomes more Cu-depleted and Zn-enriched, creating optoelectronically beneficial defects V_{Cu} and Zn_{Cu}, which are partly responsible for the performance improvement. Recrystallization effects of the CdS layer are observed, leading to a better absorber-buffer interface and potentially a better band alignment. Additionally, this work opens the possibility of tuning the defect concentration in the absorber with the PDA temperature.

1. Introduction

In order to achieve high performance photovoltaics based on emerging earth-abundant $Cu_2ZnSnSe_4$ (CZTSe) thin film solar cells, significant effort has been placed on phase purification and grain size enhancement [1–7]. Less explored, but nevertheless highly crucial for the device performance is the structural and compositional constitution of the CZTSe surface and the CZTSe/buffer interface, the most important part of the p-n junction. Here, the majority of the charged carriers are generated and have to be separated before they recombine. Post-deposition soft annealing (PDA) processes on finished devices are known to improve the characteristics of chalcogenide thin film solar cells [8–10].

In the case of kesterite-based solar cells, PDA is expected to have a strong influence on the surface region of the absorber (CZTSe) layer, as well as the interface between the buffer (CdS) and absorber layer, and the buffer layer in general. Currently in our lab a combination of improved preparation methods and the application of an optimized PDA process has produced CZTSe-based solar cells with efficiencies of up to 10.6%, and open circuit voltages (V_{OC}) of 473 mV, among the highest V_{OC} value reported for this compound [11]. However, the origin of the behavior of the devices upon annealing is still not completely resolved, and deeper understanding of the PDA process is needed for further optimization and improvement of the device efficiency. In principle, PDA in air can contribute to the device improvement in a variety of ways: interdiffusion of elements within the device, recrystallization processes and oxidation. As annealing of devices in inert gas atmosphere or vacuum is known to also improve device performance, oxidation cannot be the only explanation for device improvement. For example, Neuschitzer et al. have measured a Cu depleted and Zn enrichment surface of bare absorbers annealed in vacuum by X-ray photoelectron spectroscopy [12]. In the present study, diffusion and recrystallization phenomena at the absorber/

* Corresponding author.
E-mail addresses: mira.dimitreivska@gmail.com, mdimitrievska@irec.cat (M. Dimitrievska).

http://dx.doi.org/10.1016/j.solmat.2016.07.009
0927-0248/

buffer interface during PDA performed at different temperatures will be investigated in detail with Raman spectroscopy and optoelectronic characterization.

Raman spectroscopy has proven to be a suitable characterization tool for obtaining deeper insights into the CdS/kesterite interface, and recently its capability to identify and monitor defects in these materials has been shown [13,14]. Additionally, different penetration depths of varying laser excitation energies enable the selective acquisition of structural information from varying depths of the layers, thus providing insights on the differences in composition and defect concentration throughout the device cross section. On the other side, Raman spectroscopy is a very attractive technique from the industrial point of view, as it is non-destructive, non-contact and does not require any special sample preparation. As such it is an ideal tool for process and quality control monitoring [15]. An additional advantage is also the possibility of non-destructive assessment of the different layers of the solar cells, which can be achieved by using different laser excitations. This allows simultaneous monitoring of both structural and optoelectronic properties.

In that sense, the main goal of this work is the application of correlated Raman spectroscopy and optoelectronic characterization techniques to study the structure/function relationships in $Cu_2ZnSnSe_4$ (CZTSe) kesterite based solar cells in an attempt to resolve and explain the mechanisms behind the effect of PDA treatments on the device performance.

2. Materials and methods

CZTSe device grade layers were synthesized on Mo coated soda lime glass by annealing of Cu/Sn/Cu/Zn metallic multi-stacks with an additional 10 nm Ge nanolayer, deposited by DC magnetron sputtering technique, under a Se+Sn atmosphere, as described in Ref. [11]. As prepared absorbers were then subjected to several etching processes in order to remove secondary phases and to passivate the surface [16,17]. A CZTSe-based device was fabricated by chemical bath deposition of a CdS buffer layer (60 nm), followed immediately by pulsed DC-magnetron sputtering deposition of ZnO/In_2O_3–Sn_2O window layer (CT100 Alliance Concepts) [18]. The devices were mechanically scribed into 3×3 mm^2 cells, forming approximately 12–15 individual solar cells per sample. One sample with completed solar cell devices was then subsequently annealed on a hot plate in air for 5 min at temperatures ranging from 50 to 350 °C. After each PDA treatment, the different devices of the same sample were characterized by illuminated J-V, external quantum efficiency (EQE), photoluminescence (PL) and Raman measurements. Raman scattering and PL measurements were performed in back scattering configuration with iHR320 Horiba Jobin Yvon system [19]. In all cases, and to avoid the presence of thermal effects in the spectra, the power excitation density was around 50 W/cm^2. To ensure the analysis of a representative area of each sample, measurements were made in macro configuration (light spot size on the sample of ≥ 100 μm). Illuminated J-V measurements were performed with ABET3000 Solar Simulator with AM1.5 conditions, while the EQE measurements were obtained using Bentham PVE300 characterization system.

A detailed analysis of the surface region was achieved using multiwavelength excitation Raman measurements combining blue (442 nm), green (532 nm) and near-infrared (785 nm) excitation lines. This has allowed in-depth characterization of the CdS layer, as well as surface and sub-surface regions of CZTSe (Fig. 1). The approximate penetration depths of each excitation, presented in Fig. 1, were calculated based on the absorption curves measured for this compound.

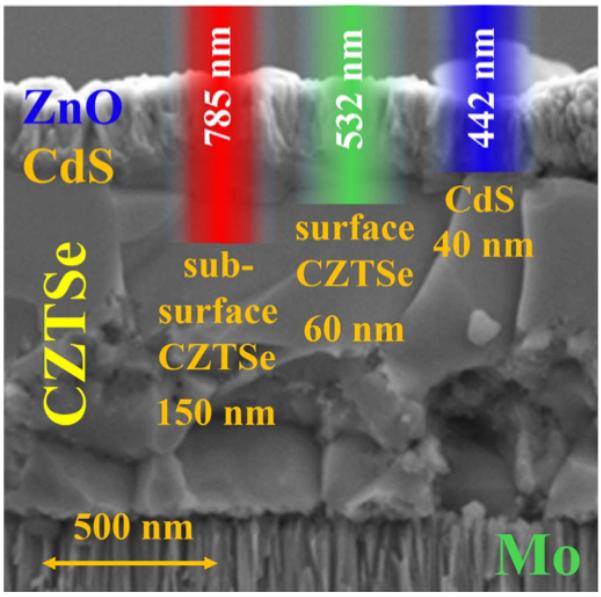

Fig. 1. Cross section of the CZTSe-based solar cell device with relative penetration depths of different lasers used for defect characterization with Raman spectroscopy. (For interpretation of the references to color in this figure, the reader is referred to the web version of this article.)

3. Results and discussion

Fig. 2 presents the dependence of device efficiency, V_{OC}, short-circuit current density (J_{sc}), and fill factor (FF) on the PDA temperature. It is observed that the maximum J_{SC} and maximum V_{OC} are obtained at two different temperatures, 175 °C and 250 °C, respectively, leading to two local maxima in efficiency. Also the V_{OC} itself shows two distinct maxima (at 160 °C and 250 °C). Previously published results [20], have shown two distinct compositional processing conditions for which either V_{oc} or J_{sc} have been maximized. It was observed that the J_{sc} was maximized in Cu-poor and slightly Zn-rich compositions, where the occurrence of V_{Cu} and Zn_{Cu} point defects is expected, while the V_{oc} was maximized under more Zn-rich conditions with a high density of Zn_{Cu} and Zn_{Sn}. As defect types and density in the CZTSe compounds are governed by the chemical potential of component elements [21,22], it is assumed that the post-deposition annealing is inducing compositional changes and element dispersion in the surface and bulk region of the CZTSe absorber. The two maxima observed in this experiment could therefore well be originated from different local Cu/(Zn+Sn) and Zn/Sn compositions.

In order to better understand the effect of the PDA temperature on the element dispersion and optoelectronic properties a systematic study after each PDA treatment was performed on the devices using multi-wavelength Raman spectroscopy. Fig. 3 presents representative Raman spectra measured with 442, 532 and 785 nm excitations corresponding to the characterization of the CdS layer and surface and sub-surface kesterite layer for different PDA temperatures. Multiple changes with PDA temperature in the intensity and half-widths of peaks corresponding to CdS and CZTSe compounds are observed, as labeled with arrows in Fig. 3.

The most pronounced changes in the CZTSe phase are observed in the intensity of the Raman modes located around the 170 and 250 cm^{-1} spectral regions. Previous studies have shown that the relative intensity of the broad band at 170 cm^{-1} is inversely proportional to the concentration of $[V_{Cu}+Zn_{Cu}]$ defect clusters in CZTSe, while intensity of the band at around 250 cm^{-1} is directly

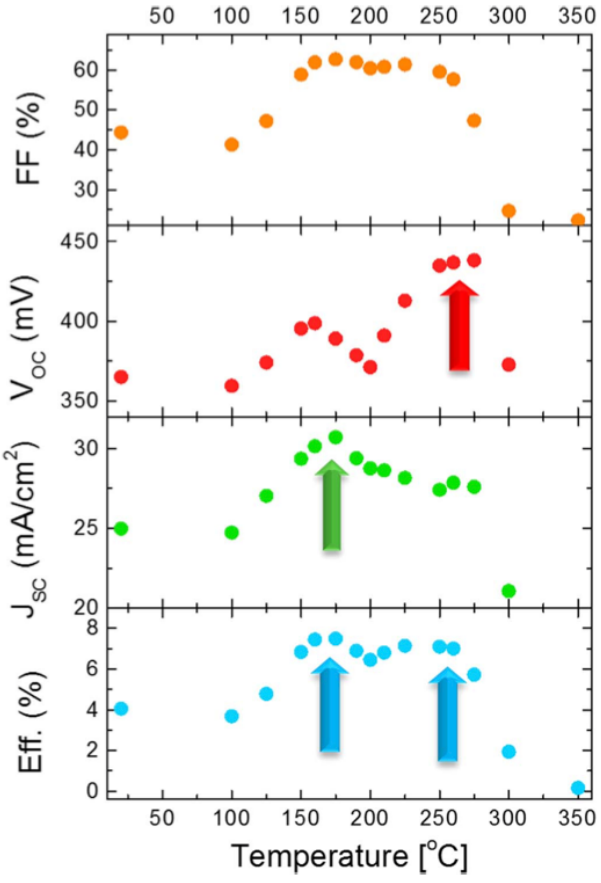

Fig. 2. Dependence of the optoelectronic properties: efficiency (Eff.), short-circuit current density (J_{SC}) open-circuit voltage (V_{OC}) and fill factor (FF) on the post-deposition annealing temperature.

proportional to the concentration of Zn_{Cu} and Zn_{Sn} defects [13,23]. In order to obtain a clear understanding of the changes in the defect concentration with the PDA temperature, deconvolution of the Raman spectra with Lorentzian curves was performed, from which the integral intensity of the bands at 170 and 250 cm^{-1} was determined. Comparison of the different spectra was enabled by the normalization of all bands to the most intense Raman mode observed at 196 cm^{-1}, which is identified as an A symmetry mode corresponding to solely Se anion vibrations. Changes in the intensity of the Raman peaks at 170 and 250 cm^{-1} with the changes in the PDA temperature obtained from the Raman spectra measured with 532 and 785 nm are presented in Fig. 4.

Based on the changes in the intensity of the 170 cm^{-1} mode, it can be concluded that with the increase in the PDA temperature up to 200 °C, Cu ions diffuse away from the surface to the bulk of CZTSe. This kind of diffusion creates a Cu depleted surface layer of the kesterite, which according to first principle calculations leads to a reduced formation energy of shallow V_{Cu} acceptor defects and inhibits the formation of the deeper and more detrimental Cu_{Zn} antisite defects [21]. Due to the high mobility of the Cu ions, it has been suggested that beneficial acceptor defects may form in the $MoSe_2$ layer from Cu diffusion towards the back contact, which would facilitate carrier transport by eliminating potential back contact barrier between the kesterite and $MoSe_2$ layer [24]. Furthermore, changes in the intensity of the 250 cm^{-1} mode for the same temperature region show an increase in Zn composition in the surface region, leading to diffusion of Zn ions from the bulk to the surface of CZTSe. These results suggest the PDA treatment at 200–250 °C creates an Zn enrichment and Cu depletion of the kesterite surface. This should reduce detrimental ($2Cu_{Zn}+Sn_{Zn}$) defect clusters in the sensitive interface region and lead to the formation of optoelectronically beneficial V_{Cu} and Zn_{Cu} point defects, which is expected to increase the performance of kesterite based solar cells.

For the PDA temperatures higher than 200 °C, only very small changes in the Cu concentration of the surface and the subsurface CZTSe layers are observed. However, a small additional increase in the Zn concentration of the surface region is detected, while no changes in the Zn concentration of the sub-surface region of CZTSe layer are observed, suggesting that Zn diffuses from the deeper region in the bulk. This behavior additionally increases the probability of forming of Zn_{Cu} and Zn_{Sn} defects in the CZTSe surface region, and based on the previous results [20], is probably partly responsible for the enhancement in the V_{OC} values which are observed at 250 °C. The other reason for this additional boosting in V_{OC}, is probably related to effects associated with the diffusion of Na, as diffusion of Na from the substrate towards the surface of the kesterite is expected in this temperature region [25,26]. Further studies regarding the effect of Na on the optoelectronic properties of these kind of CZTSe absorbers during the PDA process are underway in our laboratories.

The postulated increase in the point defect density concluded from the changes in the intensity of the modes is also confirmed by the increase in the full width at half maximum (FWHM) of the main A mode at 196 cm^{-1} ($\Gamma_{A\ mode}$). An increase of the FWHM and a decrease in the frequency of this mode are observed in the Raman spectra measured with both 532 and 785 nm excitation lines, as presented in Fig. 5. According to Ref. [27], both these effects indicate an increase in the defect concentration in the surface and subsurface region of the kesterite. Rey et al. also reported a broadening of the main A mode for CZTSe devices subjected to a PDA treatment in vacuum above a critical temperature of 200 °C, which they associated to an order-disorder transition of Cu-Zn atoms [28].

A systematic decrease in the band gap of CZTSe from 1.07 to 1.01 eV, as extracted from the onset of absorption in the EQE measurements, is observed when PDA temperature is increased (Fig. S1 in Supporting information). At first, it may appear that this is not consistent with the increase in the concentration of V_{Cu} and Zn_{Cu} defects in the surface region, since according to first principle calculations these defects should promote local increase in the band gap, by lowering the energy of the valance band edge and increasing the energy of the conduction band edge [21]. However, one has to bear in mind that the measured band gap from the EQE is effective band gap energy in the absorber bulk. This corresponds to the region within the absorber with lowest band gap energy from which photogenerated charge carriers can still be collected, which is not necessarily identical with the absorber surface. In fact, the Cu depletion and Zn enrichment at the absorber surface is expected to lead to a locally increased bandgap and lowered valence band. This positively suppresses recombination and increases the V_{OC}, as the valence band is moved away from the Fermi energy and in consequence photo-generated electrons (minority charge carriers in the p-type absorber) find less recombination partners (holes) at the interface. A band bending as additional effect of the formation of beneficial V_{Cu} and Zn_{Cu} defects can further facilitate the separation of photo-generated electron-hole pairs [29,30].

Besides the changes in the CZTSe layer during the PDA process, monotonous changes in the CdS layer were observed in both Raman and room temperature PL spectra. Fig. 6(a) presents the representative PL spectra measured with 442 nm excitation. One

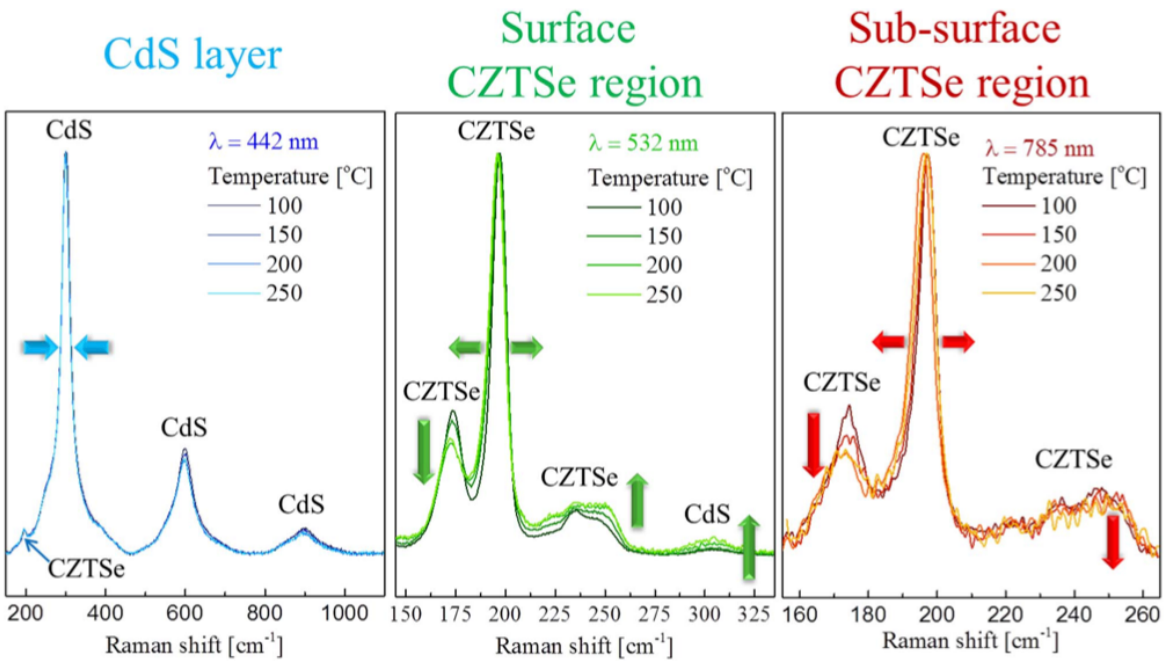

Fig. 3. Representative Raman spectra of the kesterite-based solar cell device after PDA treatment measured with 442, 532 and 785 nm excitation lines.

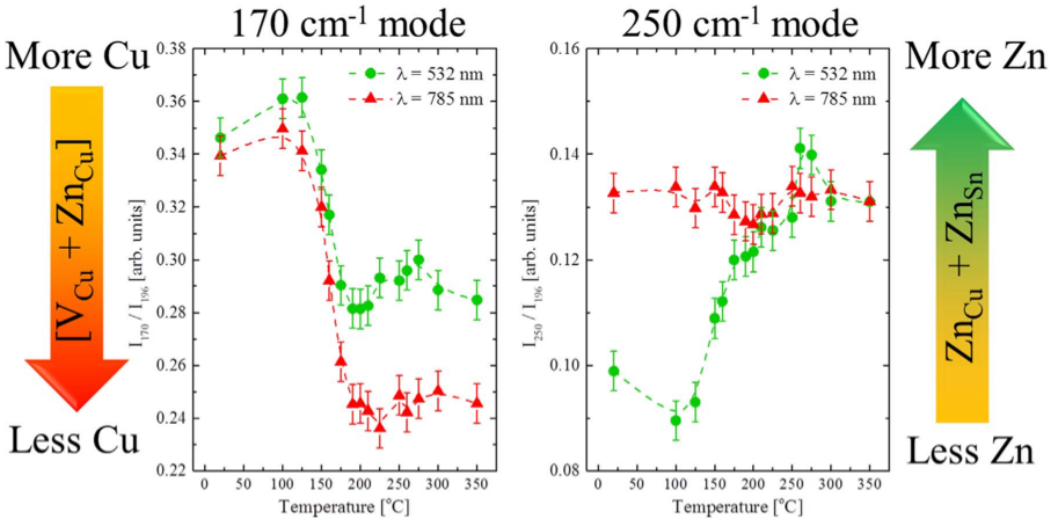

Fig. 4. PDA temperature dependent changes of the defect concentration in the surface (532 nm) and subsurface (785 nm) regions of the kesterite absorber layer. The arrows point the direction of the higher defect concentration.

broad green band centered at 490 nm (2.53 eV) is observed in the measured spectral region, for the CdS buffer layer before the PDA treatment. The three weak peaks visible in the region between 445 and 465 nm in the PL spectra are the 1LO, 2LO and 3LO Raman lines of CdS, which can clearly be seen when the intensity scale is expanded. Systematic shift of the green band towards higher wavelengths, i.e. lower photon energies with the increase in PDA temperature is observed, as presented in Fig. 6(b). It is reported that the green band in the PL spectra of CdS is originated from the transition of S-vacancy donors to the valence band and the recombination of donor–acceptor pairs [31–33]. The CdS layer is about 50 nm and is composed of mostly nanometric grains. The red energy shift of the green band with the PDA treatment is caused by the diffusion of Se from CZTSe layer into the CdS layer, creating a very S-rich CdSSe solid solution. Anion-mixed crystals generally show a large band-gap bowing because of a large difference in atomic size. The bowing parameter for CdSSe is known to be 0.7 eV [34], meaning that the band gap energy of CdS can decrease fast with the introduction of small amount of Se. Additionally, a reduction in the number of defects in the CdS layer upon the post-deposition annealing is also observed by Raman measurements, where a monotonous decrease in the FWHM of the CdS LO Raman band centered at 300 cm^{-1} is detected with the increase in PDA temperature, as shown in Fig. 6(c) [27].

This behavior of the CdS layer is improving the interface between the absorber and buffer layer leading to the reduction of the

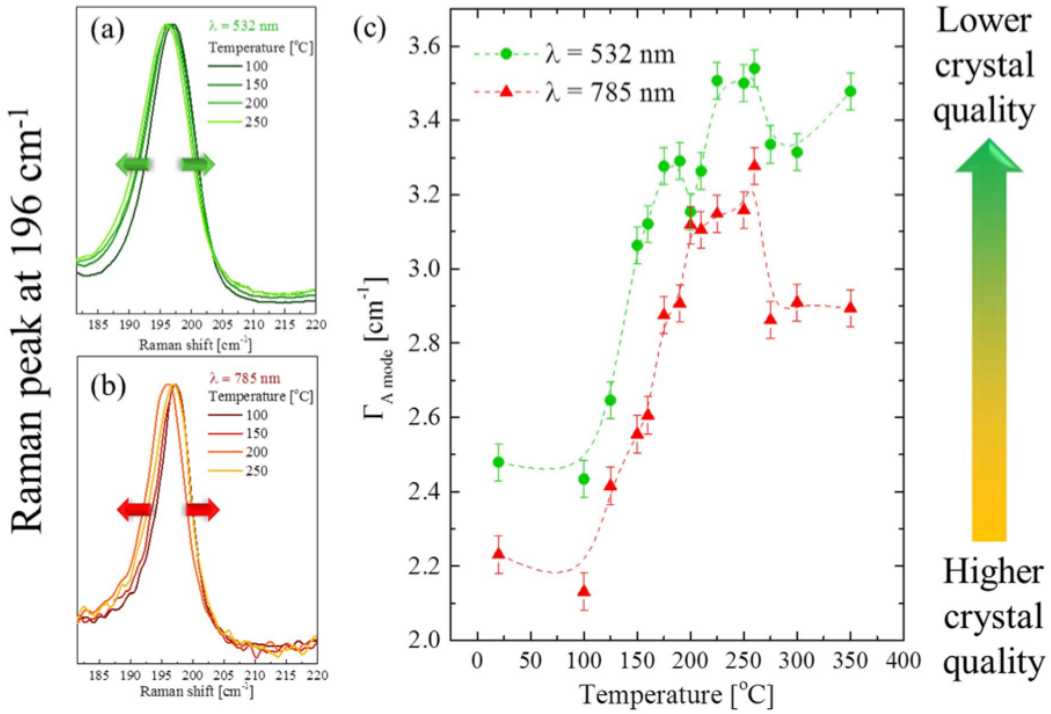

Fig. 5. Raman peak centered at 196 cm^{-1} and attributed to the A vibrational mode of kesterite structure measured with (a) 532 nm and (b) 785 nm excitation. (c) PDA temperature dependence of the A vibrational mode FWHM showing the reduction in the crystal quality with the increase in the temperature.

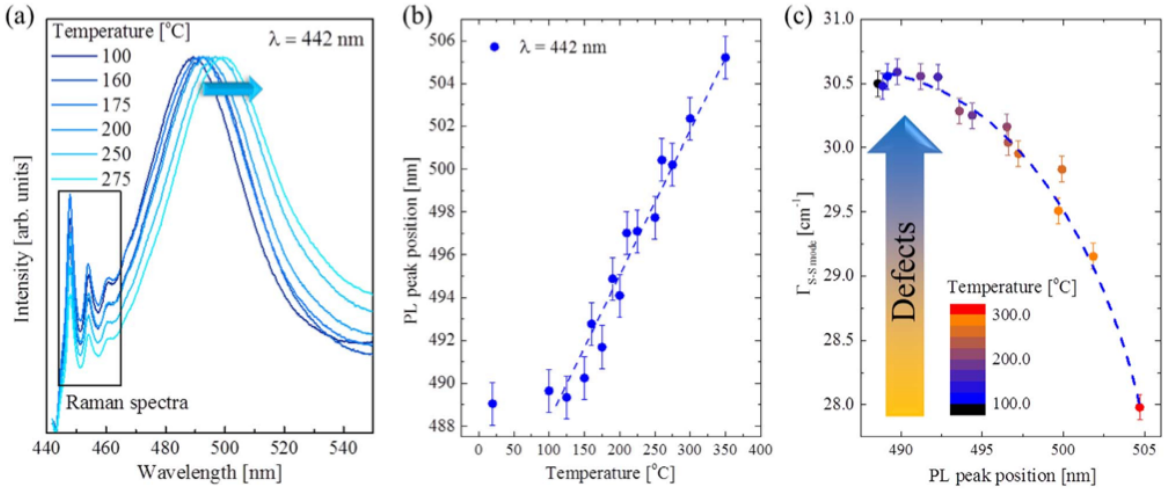

Fig. 6. (a) Room temperature photoluminescence (PL) spectra of CdS layer after different PDA treatments measured with 442 nm excitation. (b) PL peak position dependence of the post-deposition annealing temperature. (c) Variation in the FWHM of the main Raman modes ($\Gamma_{S\text{-}S\ mode}$) with the increase in PDA temperature. The arrow points the direction of higher defect concentration.

interfacial recombination, and is probably leading to better band alignment, which is also partly responsible for the improvement of the optoelectronic properties of the CZTSe-based device with the PDA treatment.

Finally, the strong decrease in all optoelectronic properties for the PDA temperatures higher than 260 °C is probably caused by the degradation and decomposition of the CZTSe and CdS layers originating from the inter-diffusion of elements. With greater diffusion between the layers, the p-n junction becomes more poorly defined, negatively affecting overall device performance. Thus it becomes clear that certain temperature induced effects are beneficial to the system, while above a certain temperature other changes occur which deteriorate optoelectronic properties.

4. Conclusions

In conclusion, with multi-wavelength Raman spectroscopy we find that low temperature PDA treatments of completed devices induce a redistribution of atoms (Cu and Zn) within the surface and bulk of the absorber. The absorber surface becomes more Cu-depleted and Zn-enriched, creating optoelectronically beneficial

defects V_{Cu} and Zn_{Cu}, which are partly responsible for the performance improvement of the CZTSe-based solar cells upon annealing. Furthermore, recrystallization effects of the CdS layer are observed, leading to a better absorber-buffer interface and potentially a better band alignment. Additionally, this work opens the possibility of tuning the amount of defects in the absorber by choosing the right PDA temperature.

Acknowledgments

The research leading to these results has received funding from the People Program (Marie Curie Actions) of the European Union's Seventh Framework Program FP7/2007–2013/ under REA grant agreement no. 316488 (KESTCELLS) and GA no. 625840 ("JumpKEST"), as well as by MINECO (Ministerio de Economía y Competitividad de España) under the NASCENT project (ENE2014-56237-C4-1-R). Authors from IREC and IN^{2}UB belong to the M-2E (Electronic Materials for Energy) Consolidated Research Group and the XaRMAE Network of Excellence on Materials for Energy of the "Generalitat de Catalunya". E.S. thanks the Government of Spain for the "Ramon y Cajal" fellowship (RYC-2011-09212).

Appendix A. Supplementary material

Supplementary data associated with this article can be found in the online version at http://dx.doi.org/10.1016/j.solmat.2016.07.009.

References

[1] X. Liu, Y. Feng, H. Cui, F. Liu, X. Hao, G. Conibeer, D.B. Mitzi, M. Green, The current status and future prospects of kesterite solar cells: a brief review, Prog. Photovolt. Res. Appl. (2016), http://dx.doi.org/10.1002/pip.2741, n/a-n/a.
[2] M. Johnson, S.V. Baryshev, E. Thimsen, M. Manno, X. Zhang, I.V. Veryovkin, C. Leighton, E.S. Aydil, Alkali-metal-enhanced grain growth in Cu_2ZnSnS_4 thin films, Energy Environ. Sci. 7 (2014) 1931–1938.
[3] X. Yin, C. Tang, L. Sun, Z. Shen, H. Gong, Study on Phase Formation Mechanism of Non- and Near-Stoichiometric $Cu_2ZnSn(S,Se)_4$ Film Prepared by Selenization of Cu–Sn–Zn–S Precursors, Chem. Mater. 26 (2014) 2005–2014.
[4] W.-C. Hsu, I. Repins, C. Beall, C. DeHart, B. To, W. Yang, Y. Yang, R. Noufi, Growth mechanisms of co-evaporated kesterite: a comparison of Cu-rich and Zn-rich composition paths, Prog. Photovolt. Res. Appl. 22 (2014) 35–43.
[5] I. Repins, C. Beall, N. Vora, C. DeHart, D. Kuciauskas, P. Dippo, B. To, J. Mann, W.-C. Hsu, A. Goodrich, R. Noufi, , Co-evaporated $Cu_2ZnSnSe_4$ films and devices, Sol. Energy Mater. Sol. Cells 101 (2012) 154–159.
[6] R. Mainz, A. Singh, S. Levcenko, M. Klaus, C. Genzel, K.M. Ryan, T. Unold, Phase-transition-driven growth of compound semiconductor crystals from ordered metastable nanorods, Nat. Commun. 5 (2014) 3133.
[7] J. Zhong, Z. Xia, M. Luo, J. Zhao, J. Chen, L. Wang, X. Liu, D.-J. Xue, Y.-B. Cheng, H. Song, J. Tang, Sulfurization induced surface constitution and its correlation to the performance of solution-processed $Cu_2ZnSn(S,Se)_4$ solar cells, Sci. Rep. 4 (2014) 6288.
[8] U. Rau, D. Braunger, R. Herberholz, H.W. Schock, J.-F. Guillemoles, L. Kronik, D. Cahen, Oxygenation and air-annealing effects on the electronic properties of $Cu(In,Ga)Se_2$ films and devices, J. Appl. Phys. 86 (1999) 497–505.
[9] I. Repins, M.A. Contreras, B. Egaas, C. DeHart, J. Scharf, C.L. Perkins, B. To, R. Noufi, 19.9%-efficient ZnO/CdS/$CuInGaSe_2$ solar cell with 81.2% fill factor, Prog. Photovolt. Res. Appl 16 (2008) 235–239.
[10] D. Hauschild, F. Meyer, A. Benkert, D. Kreikemeyer-Lorenzo, S. Pohlner, J. Palm, M. Blum, W. Yang, R.G. Wilks, M. Bär, C. Heske, L. Weinhardt, F. Reinert, Annealing-induced effects on the chemical structure of the In_2S_3/$CuIn(S,Se)_2$ thin-film solar cell interface, J. Phys. Chem. C 119 (2015) 10412–10416.
[11] S. Giraldo, M. Neuschitzer, T. Thersleff, S. López-Marino, Y. Sánchez, H. Xie, M. Colina, M. Placidi, P. Pistor, V. Izquierdo-Roca, K. Leifer, A. Pérez-Rodríguez, E. Saucedo, Large efficiency improvement in $Cu_2ZnSnSe_4$ solar cells by introducing a superficial Ge nanolayer, Adv. Energy Mater. (2015), http://dx.doi.org/10.1002/aenm.201501070, n/a-n/a.
[12] M. Neuschitzer, Y. Sanchez, T. Olar, T. Thersleff, S. Lopez-Marino, F. Oliva, M. Espindola-Rodriguez, H. Xie, M. Placidi, V. Izquierdo-Roca, I. Lauermann, K. Leifer, A. Pérez-Rodríguez, E. Saucedo, The complex surface chemistry of kesterites: Cu/Zn re-ordering after low temperature post deposition annealing and its role in high performance devices, Chem. Mater. 27 (2015) 5279–5287.
[13] M. Dimitrievska, A. Fairbrother, E. Saucedo, A. Pérez-Rodríguez, V. Izquierdo-Roca, Influence of compositionally induced defects on the vibrational properties of device grade $Cu_2ZnSnSe_4$ absorbers for kesterite based solar cells, Appl. Phys. Lett. 106 (2015) 73903.
[14] M. Dimitrievska, A. Fairbrother, E. Saucedo, A. Pérez-Rodríguez, V. Izquierdo-Roca, Secondary phase and Cu substitutional defect dynamics in kesterite solar cells: Impact on optoelectronic properties, Sol. Energy Mater. Sol. Cells 149 (2016) 304–309.
[15] F. Oliva, S. Kretzschmar, D. Colombara, S. Tombolato, C.M. Ruiz, A. Redinger, E. Saucedo, C. Broussillou, T.G. de Monsabert, T. Unold, P.J. Dale, V. Izquierdo-Roca, A. Pérez-Rodríguez, Optical methodology for process monitoring of chalcopyrite photovoltaic technologies: Application to low cost $Cu(In,Ga)(S,Se)_2$ electrodeposition based processes, Sol. Energy Mater. Sol. Cells. (n.d.). http://dx.doi.org/10.1016/j.solmat.2015.12.036http://dx.doi.org/10.1016/j.solmat.2015.12.036.
[16] H. Xie, Y. Sánchez, S. López-Marino, M. Espíndola-Rodríguez, M. Neuschitzer, D. Sylla, A. Fairbrother, V. Izquierdo-Roca, A. Pérez-Rodríguez, E. Saucedo, Impact of Sn(S,Se) secondary phases in $Cu_2ZnSn(S,Se)_4$ solar cells: a chemical route for their selective removal and absorber surface passivation, ACS Appl. Mater. Interfaces 6 (2014) 12744–12751.
[17] S. López-Marino, Y. Sánchez, M. Placidi, A. Fairbrother, M. Espindola-Rodríguez, X. Fontané, V. Izquierdo-Roca, J. López-García, L. Calvo-Barrio, A. Pérez-Rodríguez, E. Saucedo, ZnSe etching of Zn-rich $Cu_2ZnSnSe_4$: an oxidation route for improved solar-cell efficiency, Chem. – Eur. J. 19 (2013) 14814–14822.
[18] Y. Sánchez, M. Espíndola-Rodríguez, H. Xie, S. López-Marino, M. Neuschitzer, S. Giraldo, M. Dimitrievska, M. Placidi, V. Izquierdo-Roca, F.A. Pulgarín-Agudelo, O. Vigil-Galán, E. Saucedo, Ultra-thin CdS for highly performing chalcogenides thin film based solar cells, Sol. Energy Mater. Sol. Cells. (n.d.). http://dx.doi.org/10.1016/j.solmat.2015.12.037http://dx.doi.org/10.1016/j.solmat.2015.12.037.
[19] M. Dimitrievska, A. Fairbrother, X. Fontané, T. Jawhari, V. Izquierdo-Roca, E. Saucedo, A. Pérez-Rodríguez, Multiwavelength excitation Raman scattering study of polycrystalline kesterite Cu_2ZnSnS_4 thin films, Appl. Phys. Lett. 104 (2014) 21901.
[20] A. Fairbrother, M. Dimitrievska, Y. Sánchez, V. Izquierdo-Roca, A. Pérez-Rodríguez, E. Saucedo, Compositional paradigms in multinary compound systems for photovoltaic applications: a case study of kesterites, J. Mater. Chem. A 3 (2015) 9451–9455.
[21] S. Chen, A. Walsh, X.-G. Gong, S.-H. Wei, Classification of lattice defects in the kesterite Cu_2ZnSnS_4 and $Cu_2ZnSnSe_4$ earth-abundant solar cell absorbers, Adv. Mater. 25 (2013) 1522–1539.
[22] A. Polizzotti, I.L. Repins, R. Noufi, S.-H. Wei, D.B. Mitzi, The state and future prospects of kesterite photovoltaics, Energy Environ. Sci. 6 (2013) 3171–3182.
[23] J.M. Skelton, A.J. Jackson, M. Dimitrievska, S.K. Wallace, A. Walsh, Vibrational spectra and lattice thermal conductivity of kesterite-structured Cu_2ZnSnS_4 and $Cu_2ZnSnSe_4$, APL Mater. 3 (2015) 41102.
[24] T. Schnabel, M. Löw, E. Ahlswede, Vacuum-free preparation of 7.5% efficient $Cu_2ZnSn(S,Se)_4$ solar cells based on metal salt precursors, Sol. Energy Mater. Sol. Cells 117 (2013) 324–328.
[25] H. Xie, S. Lopez-Marino, T. Olar, Y. Sánchez González, M. Neuschitzer, F. Oliva, S. Giraldo, V. Izquierdo-Roca, I. Lauermann, A. Pérez-Rodríguez, E. Saucedo, On the impact of Na dynamics at the $Cu_2ZnSn(S,Se)_4$/CdS interface during post low temperature treatment of absorbers, ACS Appl. Mater. Interfaces 8 (2016) 5017–5024.
[26] C.M. Sutter-Fella, J.A. Stückelberger, H. Hagendorfer, F. La Mattina, L. Kranz, S. Nishiwaki, A.R. Uhl, Y.E. Romanyuk, A.N. Tiwari, Sodium assisted sintering of chalcogenides and its application to solution processed $Cu_2ZnSn(S,Se)_4$ thin film solar cells, Chem. Mater. 26 (2014) 1420–1425.
[27] M. Dimitrievska, A. Fairbrother, A. Pérez-Rodríguez, E. Saucedo, V. Izquierdo-Roca, Raman scattering crystalline assessment of polycrystalline Cu_2ZnSnS_4 thin films for sustainable photovoltaic technologies: Phonon confinement model, Acta Mater. 70 (2014) 272–280.
[28] G. Rey, A. Redinger, J. Sendler, T.P. Weiss, M. Thevenin, M. Guennou, B.E. Adib, S. Siebentritt, The band gap of $Cu_2ZnSnSe_4$: effect of order-disorder, Appl. Phys. Lett. 105 (2014) 112106.
[29] S. Chen, X.G. Gong, A. Walsh, S.-H. Wei, Defect physics of the kesterite thin-film solar cell absorber Cu_2ZnSnS_4, Appl. Phys. Lett. 96 (2010), 21902-21902–3.
[30] S. Chen, J.-H. Yang, X.G. Gong, A. Walsh, S.-H. Wei, Intrinsic point defects and complexes in the quaternary kesterite semiconductor Cu_2ZnSnS_4, Phys. Rev. B 81 (2010) 245204.
[31] M. Agata, H. Kurase, S. Hayashi, K. Yamamoto, Photoluminescence spectra of gas-evaporated CdS microcrystals, Solid State Commun. 76 (1990) 1061–1065.
[32] C.T. Tsai, D.S. Chuu, G.L. Chen, S.L. Yang, Studies of grain size effects in rf sputtered CdS thin films, J. Appl. Phys. 79 (1996) 9105–9109.
[33] A.E. Abken, D.P. Halliday, K. Durose, Photoluminescence study of polycrystalline photovoltaic CdS thin film layers grown by close-spaced sublimation and chemical bath deposition, J. Appl. Phys. 105 (2009) 64515.
[34] T. Sander, M.S. Rinn, P.J. Klar, Photoluminescence and Raman spectroscopy of Cd(S,Se) under hydrostatic pressure, Phys. Status Solidi B 250 (2013) 688–692.

Chapter 5

Conclusions and outlook

The main objective of this thesis was to develop high efficiency thin film solar cells based on kesterite CZTSe absorbers through the implementation of innovative doping strategies. Special focus is put on the optimization of reactive thermal processes, followed by the screening of possible doping elements and further analysis of the most promising ones. Additionally, deeper investigations were carried out in order to improve understanding of main loss mechanisms that can degrade device performance and the use of small amounts of Ge to mitigate some of them, including the possible interactions with alkali elements and the effect of post-deposition annealing treatments on devices properties. Most of the results obtained in this thesis have been published as articles in high impact peer-reviewed journals.

In the first part of the thesis, previous study and optimization of the thermal processes were presented, identifying and varying the most critical parameters in a conventional tubular furnace selenization. With this work, we demonstrated that the 2-step process, with a first stage at 400°C for 30 min (1.5 mbar) and a second stage at 550°C for 15 min (1 bar), both using 20°C/min as heating ramp rates, is the best performing treatment for our particular precursors and set-up, leading to high quality CZTSe absorber layers.

Following this, after a preliminary screening of possible doping elements in the CZTSe system (including Ag, In, Si, Ge and Pb), In and Ge were both selected as the most promising/interesting ones to further analyze their doping properties. Regarding the use of In, it was demonstrated that CZTSe absorbers can tolerate rather high quantities of this element without significant modifications of their properties, confirming the possibility of using In-containing layers (e.g. ITO as window layer or In_2S_3 as buffer layer) in kesterite CZTSe-based devices. Additionally, the observed deterioration of devices properties due to high In concentrations was tentatively explained with the presence of a conductive phase at the grain boundaries that we associate to the formation of SnO_2-In_2O_3 conductive compounds. However, with regard to Ge, a remarkable improvement of solar cells performance (from about 7% efficiency for Ge-free reference samples to more than 10% efficiency for Ge-doped ones) was presented, based on the introduction of nanometric Ge layers into the metallic stack precursors. Several reasons were proposed to explain the great efficiency improvement in spite of the observed Ge loss: (i) the formation of a Ge_3Se_7 phase that decomposes into volatile $GeSe_2$ and a Se-rich liquid phase that assists the crystallization of the CZTSe, improving the crystalline quality; (ii) the presence of Ge reduces the probability of formation of detrimental Sn +II species, commonly associated with deep defects; (iii) the presence of GeO_x nanoinclusions associated with SnO_2 inclusions, which might have a passivation or electron reflector effect, enhancing the cell voltage. In the following optimization, we determined a Ge thickness range from 7.5 to 12.5 nm for an optimum device performance, achieving a 10.6% efficiency and V_{OC} values around 490 mV for pure selenide CZTSe, leading to V_{OC} deficits around 0.56 V, which are among the best values

reported for kesterites. Furthermore, the performance deterioration observed for higher Ge concentrations was attributed to a decrease of the charge carrier density (evidences of a strong interaction with Na) along with the presence of secondary phases due to decomposition phenomena of the kesterite.

In the next part of the thesis, a detailed microstructural analysis of high efficiency Ge-doped CZTSe solar cells was presented, revealing the presence of two distinct types of grain boundaries: one type is meandering in nature and grows largely parallel to the substrate, and denotes the boundary between two CZTSe layers with differing Cu/Zn ratios; and the second type is Cu-enriched and more straight, and predominates in the upper layer. Whereas these grain boundaries might be limiting device efficiency, the controlled oxidation occurring during soft post-deposition annealings in air could significantly ameliorate their effect. After that, a new approach for obtaining high quality CZTSe layer was presented, by introducing extremely thin Ge nanolayers below and above metallic stack precursors. This strategy led to eliminate the previously characterized meandering horizontal grain boundaries and to obtain huge grains with lateral extensions exceeding 4 microns. In addition, a deep study of the effect of Ge on the selenization process and reaction pathways revealed that Ge strongly affects the in-depth elemental distribution, delaying and minimizing the typical fast Cu-out diffusion and the formation of Sn-Se volatile species, consequently avoiding Sn losses to a large extent. This allowed modifying the reaction pathways of CZTSe from a tri-molecular mechanism for layers without Ge, towards a mainly bi-molecular one for Ge-containing samples. Through the optimization of the quantity and location of Ge, a record efficiency of 11.8% was achieved.

In the last part of the thesis, the complex Ge-Na interaction was investigated, providing further insights into the impact of Ge concentration on the Na content, modifying the doping level of the kesterite, and the possible mechanisms by which this interaction occurs. Additionally, a phenomenological Ge-Na dynamics reaction for the formation of point defects and the releasing of Na was proposed. Finally, a detailed investigation of low temperature post-deposition annealings was presented. An exhaustive multi-wavelength Raman spectroscopy analysis of devices subjected to different post-deposition annealings revealed an induced redistribution of atoms (Cu and Zn) within the surface and bulk of the absorbers. In particular, the absorber surface becomes Cu-depleted and Zn-enriched, creating optoelectronically beneficial defects V_{Cu} and Zn_{Cu}, which are partly responsible for the performance improvement of the solar cells after PDA. Moreover, recrystallization effects of the CdS buffer layer were observed, leading to a better absorber/buffer interface. In addition, this work allows the possibility of tuning the number of defects in the absorber by choosing the right PDA temperature.

On the whole, the work presented in this thesis provides meaningful results and innovative (but also simple) strategies to boost the efficiency of kesterite solar cells, by tackling some limiting factors of this material. The presented doping strategies have led to a better crystalline quality of the absorbers, the avoidance of formation of detrimental point defects, the reduction and control of compositional fluctuations during the synthesis processes by modifying the reaction pathways, and the control/optimization of the doping level of the absorber. Overall, this has allowed a significant improvement of the cell voltage, leading to a reduced V_{OC} deficit and, ultimately, a remarkable performance improvement of kesterite solar cells.

The results presented so far have allowed a great improvement of IREC's kesterite baseline conversion efficiency as shown in Figure 5.1. Furthermore, the efficiencies, and especially the voltage values obtained in the best devices presented in this work are among the best reported in the literature, as presented in the comparative Table 5.1. This comparative analysis demonstrates a significant contribution of this thesis to reduce the voltage deficit in kesterite solar cells, which is considered one of the main problems of this technology.

Nevertheless, despite all the knowledge gained in recent years in the field of kesterites, there is still a large gap in performance between them and the closely related chalcopyrite CIGS. Since first kesterite devices were fabricated, the vast majority of research works have been limited to copy the methods, strategies, device architecture, back contact, buffers, window layer materials… from CIGS technologies and to apply them into kesterite technology. Although this is a good starting point, kesterites are similar but not the same material as CIGS, so they have particular features that have to be especially addressed. Therefore, customized strategies and solutions need to be designed in order to hopefully improve the performance of this promising photovoltaic material, and make it a real alternative for energy production in the near future.

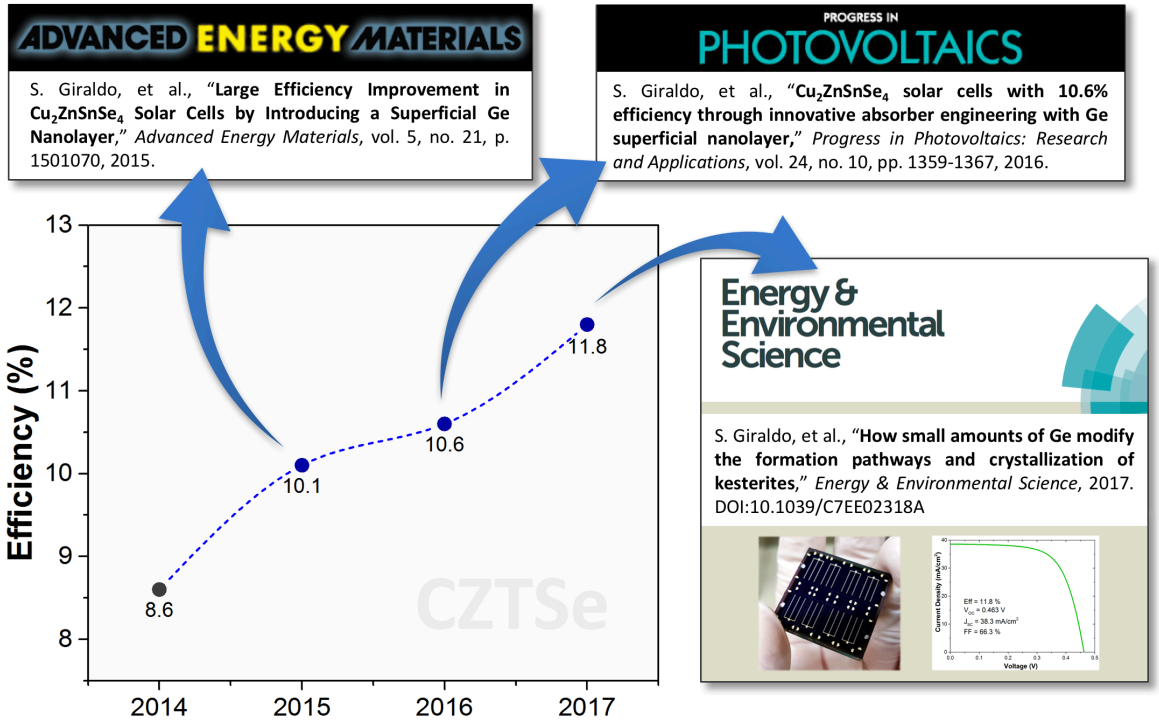

Figure 5.1. Evolution of IREC's record efficiencies of kesterite CZTSe solar cells, reflecting the most important milestones achieved during the PhD, reported in internationally renowned high impact journals.

Table 5.1. Comparative table of selected best kesterite devices reported in the literature, including the best device presented in this thesis.

Absorber (E_g, eV)	Eff (%)	V_{OC} (V)	V_{OC} deficit* (V)	Affiliation (Ref)
CZTSSe (1.13)	12.6	0.513	0.372	IBM[32]
CZTSe (1.0)	11.6	0.423	0.337	IBM[41]
CZTS (1.5)	11.0	0.731	0.504	UNSW[9]
CZTGSe (1.11)	12.3	0.527	0.337	AIST[54]
CZTSe (1.04)	11.8	0.463	0.335	IREC

* Calculated according to the Shockley-Queisser limit.

References

(1) IRENA; IEA. Perspectives for the Energy Transition: Investment Needs for a Low-Carbon Energy System. **2017**, 204.

(2) UNFCCC. 1992 United Nations Framework Convention on Climate. **2004**, 1–24.

(3) Nations, U. Resolution 48/189. United Nations Framework Convention on Climate Change. **1994**, No. Part II, 2–3.

(4) Nations, U. Kyoto Protocol To the United Nations Framework Kyoto Protocol To the United Nations Framework. *Rev. Eur. Community Int. Environ. Law* **1998**.

(5) UNFCCC. Paris Agreement. *Conf. Parties its twenty-first Sess.* **2015**.

(6) Ribera, T.; Sachs, J. Pathways to Deep Decarbonization (2015 Report). *DDPP* **2015**, 1–58.

(7) IRENA. *Renewable Power: Sharply Falling Generation Costs*; 2016.

(8) Fraunhofer Institute for Solar Energy Systems, I. *Photovoltaics Report*; 2017.

(9) Green, M. A.; Hishikawa, Y.; Warta, W.; Dunlop, E. D.; Levi, D. H.; Hohl-Ebinger, J.; Ho-Baillie, A. W. H. Solar Cell Efficiency Tables (Version 50). *Prog. Photovoltaics Res. Appl.* **2017**, *25* (7), 668–676.

(10) Yaroshevsky, A. A. Abundances of Chemical Elements in the Earth's Crust. *Geochemistry Int.* **2006**, *44* (1), 48–55.

(11) Green, M. A. Recent Developments in Photovoltaics. *Sol. Energy* **2004**, *76* (1–3), 3–8.

(12) Shockley, W.; Queisser, H. J. Detailed Balance Limit of Efficiency of P-N Junction Solar Cells. *J.Appl.Phys.* **1961**, *32* (3), 510–519.

(13) Rühle, S. Tabulated Values of the Shockley-Queisser Limit for Single Junction Solar Cells. *Sol. Energy* **2016**, *130*, 139–147.

(14) Yamaguchi, M.; Takamoto, T.; Araki, K. Super High-Efficiency Multi-Junction and Concentrator Solar Cells. *Sol. Energy Mater. Sol. Cells* **2006**, *90* (18–19), 3068–3077.

(15) Conibeer, G. Third-Generation Photovoltaics. *Mater. Today* **2007**, *10* (11), 42–50.

(16) Brown, G. F.; Wu, J. Third Generation Photovoltaics. *Laser Photonics Rev.* **2009**, *3* (4), 394–405.

(17) Chapin, D. M.; Fuller, C. S.; Pearson, G. L. A New Silicon P-N Junction Photocell for Converting Solar Radiation into Electrical Power. *J. Appl. Phys.* **1954**, *25* (5), 676–677.

(18) National Renewable Energy Laboratory (NREL). Best Research-Cell Efficiencies chart https://www.nrel.gov/pv/assets/images/efficiency-chart.png (accessed Nov 23, 2017).

(19) Jackson, P.; Wuerz, R.; Hariskos, D.; Lotter, E.; Witte, W.; Powalla, M. Effects of Heavy Alkali Elements in Cu(In,Ga)Se2 Solar Cells with Efficiencies up to 22.6%. *Phys. Status Solidi - Rapid Res. Lett.* **2016**, *10* (8), 583–586.

(20) Mitzi, D. B.; Gunawan, O.; Todorov, T. K.; Barkhouse, D. A. R. Prospects and Performance Limitations for Cu-Zn-Sn-S-Se Photovoltaic Technology. *Philos. Trans. R. Soc. A Math. Phys. Eng. Sci.* **2013**, *371* (1996), 20110432–20110432.

(21) Riha, S. C.; Parkinson, B. A.; Prieto, A. L. Compositionally Tunable Cu2ZnSn(S1-xSe x)4 Nanocrystals: Probing the Effect of Se-Inclusion in Mixed Chalcogenide Thin Films. *J. Am. Chem. Soc.* **2011**, *133* (39), 15272–15275.

(22) Green, M. A. Estimates of Te and In Prices from Direct Mining of Known Ores. *Prog. Photovoltaics Res. Appl.* **2009**, *17* (5), 347–359.

(23) Fthenakis, V. M.; Moskowitz, P. D. Photovoltaics: Environmental, Health and Safety Issues and Perspectives. *Prog. Photovoltaics Res. Appl.* **2000**, *8* (1), 27–38.

(24) Phipps, G.; Mikolajczak, C.; Guckes, T. Indium and Gallium: Long-Term Supply. *Renew. Energy Focus* **2008**, *9* (4), 56–59.

(25) Emsley, J. *The Elements*; Clarendon Press, 1998.

(26) USGS. USGS Minerals Information: Commodity Statistics and Information https://minerals.usgs.gov/minerals/pubs/commodity/ (accessed Dec 5, 2017).

(27) Ito, K.; Nakazawa, T. Electrical and Optical Properties of Stannite-Type Quaternary Semiconductor Thin Films. *Jpn. J. Appl. Phys.* **1988**, *27* (11R), 2094–2097.

(28) Katagiri, H.; Sasaguchi, N.; Hando, S.; Hoshino, S.; Ohashi, J.; Yokota, T. Preparation and Evaluation of Cu2ZnSnS4 Thin Films by Sulfurization of E-B Evaporated Precursors. *Sol. Energy Mater. Sol. Cells* **1997**, *49* (1–4), 407–414.

(29) Katagiri, H.; Jimbo, K.; Yamada, S.; Kamimura, T.; Maw, W. S.; Fukano, T.; Ito, T.; Motohiro, T. Enhanced Conversion Efficiencies of Cu2ZnSnS4-Based Thin Film Solar Cells by Using Preferential Etching Technique. *Appl. Phys. Express* **2008**, *1* (4), 0412011–0412012.

(30) Todorov, T. K.; Reuter, K. B.; Mitzi, D. B. High-Efficiency Solar Cell with Earth-Abundant Liquid-Processed Absorber. *Adv. Mater.* **2010**, *22* (20), E156–E159.

(31) Barkhouse, D. A. R.; Gunawan, O.; Gokmen, T.; Todorov, T. K.; Mitzi, D. B. Device Characteristics of a 10.1% Hydrazine-Processed Cu2ZnSn(Se,S)4 Solar Cell. *Prog. Photovoltaics Res. Appl.* **2012**, *20* (1), 6–11.

(32) Wang, W.; Winkler, M. T.; Gunawan, O.; Gokmen, T.; Todorov, T. K.; Zhu, Y.; Mitzi, D. B. Device Characteristics of CZTSSe Thin-Film Solar Cells with 12.6% Efficiency. *Adv. Energy Mater.* **2014**, *4* (7), 1301465.

(33) Seol, J.; Lee, S.; Lee, J.; Nam, H.; Kim, K. Electrical and Optical Properties of CuZnSnS Thin Films Prepared by Rf Magnetron Sputtering Process. *Sol. Energy Mater. Sol. Cells* **2003**, *75* (1–2), 155–162.

(34) He, J.; Sun, L.; Chen, S.; Chen, Y.; Yang, P.; Chu, J. Composition Dependence of Structure and Optical Properties of Cu2ZnSn(S,Se)4 Solid Solutions: An Experimental Study. *J. Alloys Compd.* **2012**, *511* (1), 129–132.

(35) Ahn, S.; Jung, S.; Gwak, J.; Cho, A.; Shin, K.; Yoon, K.; Park, D.; Cheong, H.; Yun, J. H. Determination of Band Gap Energy (Eg) of Cu2 ZnSnSe4 Thin Films: On the Discrepancies of Reported Band Gap Values. *Appl. Phys. Lett.* **2010**, *97* (2), 21905.

(36) Ford, G. M.; Guo, Q.; Agrawal, R.; Hillhouse, H. W. Earth Abundant Element Cu2Zn(Sn1-xGex)S4 Nanocrystals for Tunable Band Gap Solar Cells: 6.8% Efficient Device Fabrication. *Chem. Mater.* **2011**, *23* (10), 2626–2629.

(37) Xiao, Z.-Y.; Li, Y.-F.; Yao, B.; Deng, R.; Ding, Z.-H.; Wu, T.; Yang, G.; Li, C.-R.; Dong, Z.-Y.; Liu, L.; Zhang, L.-G.; Zhao, H.-F. Bandgap Engineering of Cu2CdxZn1−xSnS4 Alloy for Photovoltaic Applications: A Complementary Experimental and First-Principles Study. *J. Appl. Phys.* **2013**, *114* (18), 183506.

(38) Hages, C. J.; Koeper, M. J.; Agrawal, R. Optoelectronic and Material Properties of Nanocrystal-Based CZTSe Absorbers with Ag-Alloying. *Sol. Energy Mater. Sol. Cells* **2016**, *145*, 342–348.

(39) Lafond, A.; Guillot-Deudon, C.; Vidal, J.; Paris, M.; La, C.; Jobic, S. Substitution of Li for Cu in Cu2ZnSnS4: Toward Wide Band Gap Absorbers with Low Cation Disorder for Thin Film Solar Cells. *Inorg. Chem.* **2017**, *56* (5), 2712–2721.

(40) Lee, Y. S.; Gershon, T.; Gunawan, O.; Todorov, T. K.; Gokmen, T.; Virgus, Y.; Guha, S. Cu2ZnSnSe4 Thin-Film Solar Cells by Thermal Co-Evaporation with 11.6% Efficiency and Improved Minority Carrier Diffusion Length. *Adv. Energy Mater.* **2015**, *5* (7), 1401372.

(41) Oueslati, S.; Brammertz, G.; Buffière, M.; ElAnzeery, H.; Touayar, O.; Köble, C.; Bekaert, J.; Meuris, M.; Poortmans, J. Physical and Electrical Characterization of High-Performance Cu2ZnSnSe4 Based Thin Film Solar Cells. *Thin Solid Films* **2015**, *582*, 224–228.

(42) Li, J.; Wang, H.; Wu, L.; Chen, C.; Zhou, Z.; Liu, F.; Sun, Y.; Han, J.; Zhang, Y. Growth of Cu2ZnSnSe4 Film under Controllable Se Vapor Composition and Impact of Low Cu Content on Solar Cell Efficiency. *ACS Appl. Mater. Interfaces* **2016**, *8* (16), 10283–10292.

(43) Choi, S. G.; Kim, T. J.; Hwang, S. Y.; Li, J.; Persson, C.; Kim, Y. D.; Wei, S. H.; Repins, I. L. Temperature Dependent Band-Gap Energy for Cu2ZnSnSe4: A Spectroscopic Ellipsometric Study. *Sol. Energy Mater. Sol. Cells* **2014**, *130*, 375–379.

(44) Tampo, H.; Kim, K. M.; Kim, S.; Shibata, H.; Niki, S. Improvement of Minority Carrier Lifetime and Conversion Efficiency by Na Incorporation in Cu 2 ZnSnSe 4 Solar Cells. *J. Appl. Phys.* **2017**, *122* (2), 23106.

(45) Andres, C.; Haass, S. G.; Romanyuk, Y. E.; Tiwari, A. N. 9.4% Efficient Cu2ZnSnSe4 Solar Cells from Co-Sputtered Elemental Metal Precursor and Rapid Thermal Annealing. *Thin Solid Films* **2017**, *633*, 141–145.

(46) Hages, C. J.; Carter, N. J.; Agrawal, R. Generalized Quantum Efficiency Analysis for Non-Ideal Solar Cells: Case of Cu2ZnSnSe4. *J. Appl. Phys.* **2016**, *119* (1), 14505.

(47) Kim, J.; Hiroi, H.; Todorov, T. K.; Gunawan, O.; Kuwahara, M.; Gokmen, T.; Nair, D.; Hopstaken, M.; Shin, B.; Lee, Y. S.; Wang, W.; Sugimoto, H.; Mitzi, D. B. High Efficiency Cu2ZnSn(S,Se)4 Solar Cells by Applying a Double In2S3/CdS Emitter. *Adv. Mater.* **2014**, *26* (44), 7427–7431.

(48) Xin, H.; Vorpahl, S. M.; Collord, A. D.; Braly, I. L.; Uhl, A. R.; Krueger, B. W.; Ginger, D. S.; Hillhouse, H. W. Lithium-Doping Inverts the Nanoscale Electric Field at the Grain Boundaries in $Cu_2ZnSn(S,Se)_4$ and Increases Photovoltaic Efficiency. *Phys. Chem. Chem. Phys.* **2015**, *17* (37), 23859–23866.

(49) Hiroi, H.; Sakai, N.; Iwata, Y.; Kato, T.; Sugimoto, H. Impact of Buffer Layer on Kesterite Solar Cells. *2015 IEEE 42nd Photovolt. Spec. Conf.* **2015**, 1–4.

(50) Haass, S. G.; Andres, C.; Figi, R.; Schreiner, C.; Bürki, M.; Romanyuk, Y. E.; Tiwari, A. N. Complex Interplay between Absorber Composition and Alkali Doping in High-Efficiency Kesterite Solar Cells. *Adv. Energy Mater.* **2017**, 1701760.

(51) Bourdais, S.; Choné, C.; Delatouche, B.; Jacob, A.; Larramona, G.; Moisan, C.; Lafond, A.; Donatini, F.; Rey, G.; Siebentritt, S.; Walsh, A.; Dennler, G. Is the Cu/Zn Disorder the Main Culprit for the Voltage Deficit in Kesterite Solar Cells? *Adv. Energy Mater.* **2016**, *6* (12), 1–21.

(52) Schnabel, T.; Abzieher, T.; Friedlmeier, T. M.; Ahlswede, E. Solution-Based Preparation of Cu2ZnSn(S,Se)4 for Solar Cells - Comparison of SnSe2 and Elemental Se as Chalcogen Source. *IEEE J. Photovoltaics* **2015**, *5* (2), 670–675.

(53) Wu, S. H.; Chang, C. W.; Chen, H. J.; Shih, C. F.; Wang, Y. Y.; Li, C. C.; Chan, S. W. High-Efficiency Cu2ZnSn(S,Se)4 Solar Cells Fabricated through a Low-Cost Solution Process and a Two-Step Heat Treatment. *Prog. Photovoltaics Res. Appl.* **2017**, *25* (1), 58–66.

(54) Kim, S.; Kim, K. M.; Tampo, H.; Shibata, H.; Niki, S. Improvement of Voltage Deficit of Ge-Incorporated Kesterite Solar Cell with 12.3% Conversion Efficiency. *Appl. Phys. Express* **2016**, *9* (10), 1–5.

(55) Collord, A. D.; Hillhouse, H. W. Germanium Alloyed Kesterite Solar Cells with Low Voltage Deficits. *Chem. Mater.* **2016**, *28* (7), 2067–2073.

(56) Yan, C.; Sun, K.; Huang, J.; Johnston, S.; Liu, F.; Veettil, B. P.; Sun, K.; Pu, A.; Zhou, F.; Stride, J. A.; Green, M. A.; Hao, X. Beyond 11% Efficient Sulfide Kesterite Cu 2 Zn X Cd 1– X SnS 4 Solar Cell: Effects of Cadmium Alloying. *ACS Energy Lett.* **2017**, *2* (4), 930–936.

(57) Su, Z.; Tan, J. M. R.; Li, X.; Zeng, X.; Batabyal, S. K.; Wong, L. H. Cation Substitution of Solution-Processed Cu2ZnSnS4 Thin Film Solar Cell with over 9% Efficiency. *Adv. Energy Mater.* **2015**, *5* (19), 1500682.

(58) Qi, Y.; Tian, Q.; Meng, Y.; Kou, D.; Zhou, Z.; Zhou, W.; Wu, S. Elemental Precursor

Solution Processed (Cu1-xAgx)2ZnSn(S,Se)4Photovoltaic Devices with over 10% Efficiency. *ACS Appl. Mater. Interfaces* **2017**, *9* (25), 21243–21250.

(59) Gershon, T.; Lee, Y. S.; Antunez, P.; Mankad, R.; Singh, S.; Bishop, D.; Gunawan, O.; Hopstaken, M.; Haight, R. Photovoltaic Materials and Devices Based on the Alloyed Kesterite Absorber (AgxCu1-x)2ZnSnSe4. *Adv. Energy Mater.* **2016**, *6* (10), 1–7.

(60) Hall, S. R.; Szymanski, J. T.; Stewart, J. M. Kesterite, Cu2(Zn,Fe)SnS4 and Stannite Cu2(Fe,Zn)SnS4, Structurally Similar but Distinct Minerals. *Can. Mineral.* **1978**, *16* (2), 131–137.

(61) Nakamura, S.; Maeda, T.; Wada, T. Phase Stability and Electronic Structure of In-Free Photovoltaic Materials Cu2IISnSe4 (II: Zn, Cd, Hg). *Jpn. J. Appl. Phys.* **2011**, *50*, 6.

(62) Camps, I.; Coutinho, J.; Mir, M.; Cunha, A. F. da; Rayson, M. J.; Briddon, P. R. Elastic and Optical Properties of Cu2ZnSn(SexS1−x)4 Alloys: Density Functional Calculations. *Semicond. Sci. Technol.* **2012**, *27* (11), 115001.

(63) Zhang, Y.; Sun, X.; Zhang, P.; Yuan, X.; Huang, F.; Zhang, W. Structural Properties and Quasiparticle Band Structures of Cu-Based Quaternary Semiconductors for Photovoltaic Applications. *J. Appl. Phys.* **2012**, *111* (6).

(64) Schorr, S. The Crystal Structure of Kesterite Type Compounds: A Neutron and X-Ray Diffraction Study. *Sol. Energy Mater. Sol. Cells* **2011**, *95* (6), 1482–1488.

(65) Schorr, S.; Hoebler, H.-J.; Tovar, M. A Neutron Diffraction Study of the Stannite-Kesterite Solid Solution Series. *Eur. J. Mineral.* **2007**, *19* (1), 65–73.

(66) Nam, D.; Kim, J.; Lee, J. U.; Nagaoka, A.; Yoshino, K.; Cha, W.; Kim, H.; Hwang, I. C.; Yoon, K. B.; Cheong, H. Polarized Raman Spectroscopy of Cu-Poor and Zn-Rich Single-Crystal Cu2ZnSnSe4. *Appl. Phys. Lett.* **2014**, *105* (17), 0–5.

(67) Persson, C. Electronic and Optical Properties of Cu2ZnSnS4 and Cu2ZnSnSe4. *J. Appl. Phys.* **2010**, *107* (5), 53710.

(68) Paris, M.; Choubrac, L.; Lafond, A.; Guillot-Deudon, C.; Jobic, S. Solid-State NMR and Raman Spectroscopy to Address the Local Structure of Defects and the Tricky Issue of the Cu/Zn Disorder in Cu-Poor, Zn-Rich CZTS Materials. *Inorg. Chem.* **2014**, *53* (16), 8646–8653.

(69) Kobayashi, T.; Jimbo, K.; Tsuchida, K.; Shinoda, S.; Oyanaoi, T.; Katagiri, H. Investigation of Cu2ZnSnS4-Based Thin Film Solar Cells Using Abundant Materials. *Jpn. J. Appl. Phys.* **2005**, *44* (1 B), 783–787.

(70) Fairbrother, A.; Dimitrievska, M.; Sánchez, Y.; Izquierdo-Roca, V.; Pérez-Rodríguez, A.; Saucedo, E. Compositional Paradigms in Multinary Compound Systems for Photovoltaic Applications: A Case Study of Kesterites. *J. Mater. Chem. A* **2015**, *3* (18), 9451–9455.

(71) Romero, M. J.; Du, H.; Teeter, G.; Yan, Y.; Al-Jassim, M. M. Comparative Study of the Luminescence and Intrinsic Point Defects in the Kesterite Cu2ZnSnS4 and Chalcopyrite Cu(In,Ga)Se 2 Thin Films Used in Photovoltaic Applications. *Phys. Rev. B - Condens. Matter Mater. Phys.* **2011**, *84* (16), 165324.

(72) Gokmen, T.; Gunawan, O.; Todorov, T. K.; Mitzi, D. B. Band Tailing and Efficiency Limitation in Kesterite Solar Cells. *Appl. Phys. Lett.* **2013**, *103* (10), 103506.

(73) Shin, D.; Saparov, B.; Mitzi, D. B. Defect Engineering in Multinary Earth-Abundant Chalcogenide Photovoltaic Materials. *Adv. Energy Mater.* **2017**, *7* (11).

(74) Chen, S.; Yang, J. H.; Gong, X. G.; Walsh, A.; Wei, S. H. Intrinsic Point Defects and Complexes in the Quaternary Kesterite Semiconductor Cu2 ZnSnS4. *Phys. Rev. B - Condens. Matter Mater. Phys.* **2010**, *81* (24), 35–37.

(75) Chen, S.; Walsh, A.; Gong, X. G.; Wei, S. H. Classification of Lattice Defects in the Kesterite Cu2ZnSnS4 and Cu2ZnSnSe4 Earth-Abundant Solar Cell Absorbers. *Adv. Mater.* **2013**, *25* (11), 1522–1539.

(76) Biswas, K.; Lany, S.; Zunger, A. The Electronic Consequences of Multivalent Elements in Inorganic Solar Absorbers: Multivalency of Sn in Cu2ZnSnS4. *Appl. Phys. Lett.* **2010**, *96* (20), 2012–2015.

(77) Antunez, P. D.; Bishop, D. M.; Luo, Y.; Haight, R. Efficient Kesterite Solar Cells with High Open-Circuit Voltage for Applications in Powering Distributed Devices. *Nat. Energy* **2017**, *2* (11), 1–7.

(78) Ashworth, C. Photovoltaics: Voltage Victory for Kesterite Solar Cells. *Nat. Rev. Mater.* **2017**, *2* (12), 17079.

(79) Schleussner, S. M.; Törndahl, T.; Linnarsson, M.; Zimmermann, U.; Wätjen, T.; Edoff, M. Development of Gallium Gradients in Three-Stage Cu(In,Ga)Se2 Co-Evaporation Processes. *Prog. Photovoltaics Res. Appl.* **2012**, *20* (3), 284–293.

(80) Zhao, Z.-Y.; Zhao, X. First-Principles Study on Doping Effects of Sodium in Kesterite Cu2ZnSnS4. *Inorg. Chem.* **2014**, *53* (17), 9235–9241.

(81) Li, J. V.; Kuciauskas, D.; Young, M. R.; Repins, I. L. Effects of Sodium Incorporation in Co-Evaporated Cu2ZnSnSe4 Thin-Film Solar Cells. *Appl. Phys. Lett.* **2013**, *102* (16), 163905.

(82) Sutter-Fella, C. M.; Stückelberger, J. A.; Hagendorfer, H.; La Mattina, F.; Kranz, L.; Nishiwaki, S.; Uhl, A. R.; Romanyuk, Y. E.; Tiwari, A. N. Sodium Assisted Sintering of Chalcogenides and Its Application to Solution Processed Cu2ZnSn(S,Se)4 Thin Film Solar Cells. *Chem. Mater.* **2014**, *26* (3), 1420–1425.

(83) Sun, Y.; Lin, S.; Li, W.; Cheng, S.; Zhang, Y.; Liu, Y.; Liu, W. Review on Alkali Element Doping in Cu(In,Ga)Se2 Thin Films and Solar Cells. *Engineering* **2017**, *3* (4), 452–459.

(84) Yuan, Z. K.; Chen, S.; Xiang, H.; Gong, X. G.; Walsh, A.; Park, J. S.; Repins, I.; Wei,

S. H. Engineering Solar Cell Absorbers by Exploring the Band Alignment and Defect Disparity: The Case of Cu- and Ag-Based Kesterite Compounds. *Adv. Funct. Mater.* **2015**, *25* (43), 6733–6743.

(85) Shu, Q.; Yang, J.-H.; Chen, S.; Huang, B.; Xiang, H.; Gong, X.-G.; Wei, S.-H. Cu2Zn(Sn,Ge)Se4 and Cu2Zn(Sn,Si)Se4 Alloys as Photovoltaic Materials: Structural and Electronic Properties. *Phys. Rev. B* **2013**, *87*, 115208.

(86) Vauche, L.; Risch, L.; Sánchez, Y.; Dimitrievska, M.; Pasquinelli, M.; Goislard De Monsabert, T.; Grand, P. P.; Jaime-Ferrer, S.; Saucedo, E. 8.2% Pure Selenide Kesterite Thin-Film Solar Cells From Large-Area Electrodeposited Precursors. *Prog. Photovoltaics Res. Appl.* **2016**, *24* (1), 38–51.

(87) Yan, C.; Liu, F.; Sun, K.; Song, N.; Stride, J. A.; Zhou, F.; Hao, X.; Green, M. Boosting the Efficiency of Pure Sulfide CZTS Solar Cells Using the In/Cd-Based Hybrid Buffers. *Sol. Energy Mater. Sol. Cells* **2016**, *144*, 700–706.

(88) Caballero, R.; Kaufmann, C. A.; Eisenbarth, T.; Unold, T.; Klenk, R.; Schock, H.-W. High Efficiency Low Temperature Grown Cu(In,Ga)Se2 Thin Film Solar Cells on Flexible Substrates Using NaF Precursor Layers. *Prog. Photovoltaics Res. Appl.* **2011**, *19* (5), 547–551.

(89) Kuo, D. H.; Tsega, M. Electrical Conduction and Mobility Enhancement in P-Type In-Doped Cu2ZnSnSe4 Bulks. *Jpn. J. Appl. Phys.* **2014**, *53* (3), 35801.

(90) Grossberg, M.; Timmo, K.; Raadik, T.; Kärber, E.; Mikli, V.; Krustok, J. Study of Structural and Optoelectronic Properties of Cu2Zn(Sn1 - XGex)Se4(x = 0 to 1) Alloy Compounds. *Thin Solid Films* **2015**, *582*, 176–179.

(91) Khadka, D. B.; Kim, J. H. Band Gap Engineering of Alloyed Cu2ZnGexSn1-xQ4 (Q = S,Se) Films for Solar Cell. *J. Phys. Chem. C* **2015**, *119* (4), 1706–1713.

(92) Bag, S.; Gunawan, O.; Gokmen, T.; Zhu, Y.; Mitzi, D. B. Hydrazine-Processed Ge-Substituted CZTSe Solar Cells. *Chem. Mater.* **2012**, *24* (23), 4588–4593.

(93) Hages, C. J.; Levcenco, S.; Miskin, C. K.; Alsmeier, J. H.; Abou-Ras, D.; Wilks, R. G.; Bär, M.; Unold, T.; Agrawal, R. Improved Performance of Ge-Alloyed CZTGeSSe Thin-Film Solar Cells through Control of Elemental Losses. *Prog. Photovoltaics Res. Appl.* **2015**, *23* (3), 376–384.

(94) Kim, S.; Kim, K. M.; Tampo, H.; Shibata, H.; Matsubara, K.; Niki, S. Ge-Incorporated Cu2ZnSnSe4 Thin-Film Solar Cells with Efficiency Greater than 10%. *Sol. Energy Mater. Sol. Cells* **2016**, *144* (4), 488–492.

(95) Kim, I.; Kim, K.; Oh, Y.; Woo, K.; Cao, G. Z.; Jeong, S.; Moon, J. Bandgap-Graded Cu2Zn(Sn1-xGex)S-4 Thin-Film Solar Cells Derived from Metal Chalcogenide Complex Ligand Capped Nanocrystals. *Chem. Mater.* **2014**, *26* (13), 3957–3965.

(96) Khadka, D. B.; Kim, S. Y.; Kim, J. H. Effects of Ge Alloying on Device Characteristics of Kesterite-Based CZTSSe Thin Film Solar Cells. *J. Phys. Chem. C* **2016**, *120* (8), 4251–4258.

(97) Avancini, E.; Carron, R.; Bissig, B.; Reinhard, P.; Menozzi, R.; Sozzi, G.; Di Napoli, S.; Feurer, T.; Nishiwaki, S.; Buecheler, S.; Tiwari, A. N. Impact of Compositional Grading and Overall Cu Deficiency on the near-Infrared Response in Cu(In,Ga)Se2 Solar Cells. *Prog. Photovoltaics Res. Appl.* **2017**, *25* (3), 233–241.

(98) Kato, T. Cu(In,Ga)(Se,S)2 Solar Cell Research in Solar Frontier: Progress and Current Status. *Jpn. J. Appl. Phys.* **2017**, *56* (4).

(99) Neuschitzer, M.; Marquez, J.; Giraldo, S.; Dimitrievska, M.; Placidi, M.; Forbes, I.; Izquierdo-Roca, V.; Pérez-Rodriguez, A.; Saucedo, E. Voc Boosting and Grain Growth Enhancing Ge-Doping Strategy for Cu2ZnSnSe4 Photovoltaic Absorbers. *J. Phys. Chem. C* **2016**, *120* (18), 9661–9670.

(100) Jackson, P.; Hariskos, D.; Wuerz, R.; Kiowski, O.; Bauer, A.; Friedlmeier, T. M.; Powalla, M. Properties of Cu(In,Ga)Se $_2$ Solar Cells with New Record Efficiencies up to 21.7%. *Phys. status solidi - Rapid Res. Lett.* **2015**, *9* (1), 28–31.

(101) Chirilă, A.; Reinhard, P.; Pianezzi, F.; Bloesch, P.; Uhl, A. R.; Fella, C.; Kranz, L.; Keller, D.; Gretener, C.; Hagendorfer, H.; Jaeger, D.; Erni, R.; Nishiwaki, S.; Buecheler, S.; Tiwari, A. N. Potassium-Induced Surface Modification of Cu(In,Ga)Se2 Thin Films for High-Efficiency Solar Cells. *Nat. Mater.* **2013**, *12* (12), 1107–1111.

(102) Ramanujam, J.; Singh, U. P. Copper Indium Gallium Selenide Based Solar Cells – a Review. *Energy Environ. Sci.* **2017**, *10* (6), 1306–1319.

(103) Zellner, M. B.; Birkmire, R. W.; Eser, E.; Shafarman, W. N.; Chen, J. G. Determination of Activation Barriers for the Diffusion of Sodium through CIGS Thin-Film Solar Cells. *Prog. Photovoltaics Res. Appl.* **2003**, *11* (8), 543–548.

(104) Salome, P. M. P.; Hultqvist, A.; Fjallstrom, V.; Edoff, M.; Aitken, B. G.; Zhang, K.; Fuller, K.; Kosik Williams, C. Incorporation of Na in Cu(In,Ga)Se2 Thin-Film Solar Cells: A Statistical Comparison between Na from Soda-Lime Glass and from a Precursor Layer of NaF. *IEEE J. Photovoltaics* **2014**, *4* (6), 1659–1664.

(105) Nakada, T.; Iga, D.; Ohbo, H.; Kunioka, A. Effects of Sodium on Cu(In,Ga)Se2-Based Thin Films and Solar Cells. *Jpn. J. Appl. Phys.* **1997**, *36* (Part 1, No. 2), 732–737.

(106) Cho, D.-H.; Lee, K.-S.; Chung, Y.-D.; Kim, J.-H.; Park, S.-J.; Kim, J. Electronic Effect of Na on Cu(In,Ga)Se2 Solar Cells. *Appl. Phys. Lett.* **2012**, *101* (2), 23901.

(107) Bodeg Ård, M.; Granath, K.; Stolt, L. Growth of Cu(In,Ga)Se2 Thin Films by Coevaporation Using Alkaline Precursors. *Thin Solid Films* **2000**, *361–362*, 9–16.

(108) Rudmann, D.; Brémaud, D.; da Cunha, A. F.; Bilger, G.; Strohm, A.; Kaelin, M.; Zogg, H. Sodium Incorporation Strategies for CIGS Growth at Different Temperatures. *Thin Solid Films* **2005**, *480–481*, 55–60.

(109) Salomé, P. M. P.; Hultqvist, A.; Fjällström, V.; Edoff, M.; Aitken, B.; Vaidyanathan, K.; Zhang, K.; Fuller, K.; Kosik Williams, C. Cu(In,Ga)Se2 Solar Cells with Varying Na Content Prepared on Nominally Alkali-Free Glass Substrates. *IEEE J. Photovoltaics*

2013, *3* (2), 852–858.

(110) Rudmann, D.; da Cunha, A. F.; Kaelin, M.; Kurdesau, F.; Zogg, H.; Tiwari, A. N.; Bilger, G. Efficiency Enhancement of Cu(In,Ga)Se2 Solar Cells due to Post-Deposition Na Incorporation. *Appl. Phys. Lett.* **2004**, *84* (7), 1129–1131.

(111) Johnson, M.; Baryshev, S. V.; Thimsen, E.; Manno, M.; Zhang, X.; Veryovkin, I. V.; Leighton, C.; Aydil, E. S. Alkali-Metal-Enhanced Grain Growth in Cu_2ZnSnS_4 Thin Films. *Energy Environ. Sci.* **2014**, *7* (6), 1931–1938.

(112) Li, W.; Su, Z.; Tan, J. M. R.; Chiam, S. Y.; Seng, H. L.; Magdassi, S.; Wong, L. H. Revealing the Role of Potassium Treatment in CZTSSe Thin Film Solar Cells. *Chem. Mater.* **2017**, *29* (10), 4273–4281.

(113) Tong, Z.; Yan, C.; Su, Z.; Zeng, F.; Yang, J.; Li, Y.; Jiang, L.; Lai, Y.; Liu, F. Effects of Potassium Doping on Solution Processed Kesterite Cu2ZnSnS4 Thin Film Solar Cells. *Appl. Phys. Lett.* **2014**, *105* (22), 223903.

(114) Hsieh, Y. T.; Han, Q.; Jiang, C.; Song, T. Bin; Chen, H.; Meng, L.; Zhou, H.; Yang, Y. Efficiency Enhancement of Cu2ZnSn(S,Se)4 Solar Cells via Alkali Metals Doping. *Adv. Energy Mater.* **2016**, *6* (7), 1502386.

(115) López-Marino, S.; Sánchez, Y.; Espíndola-Rodríguez, M.; Alcobé, X.; Xie, H.; Neuschitzer, M.; Becerril, I.; Giraldo, S.; Dimitrievska, M.; Placidi, M.; Fourdrinier, L.; Izquierdo-Roca, V.; Pérez-Rodríguez, A.; Saucedo, E. Alkali Doping Strategies for Flexible and Light-Weight Cu2ZnSnSe4 Solar Cells. *J. Mater. Chem. A* **2016**, *4* (5), 1895–1907.

(116) Altamura, G.; Wang, M.; Choy, K.-L. Influence of Alkali Metals (Na, Li, Rb) on the Performance of Electrostatic Spray-Assisted Vapor Deposited Cu2ZnSn(S,Se)4 Solar Cells. *Sci. Rep.* **2016**, *6* (1), 22109.

(117) Mule, A.; Vermang, B.; Sylvester, M.; Brammertz, G.; Ranjbar, S.; Schnabel, T.; Gampa, N.; Meuris, M.; Poortmans, J. Effect of Different Alkali (Li, Na, K, Rb, Cs) Metals on Cu2ZnSnSe4 Solar Cells. *Thin Solid Films* **2017**, *633*, 156–161.

(118) Xie, H.; López-Marino, S.; Olar, T.; Sánchez, Y.; Neuschitzer, M.; Oliva, F.; Giraldo, S.; Izquierdo-Roca, V.; Lauermann, I.; Pérez-Rodríguez, A.; Saucedo, E. Impact of Na Dynamics at the Cu2ZnSn(S,Se)4/CdS Interface during Post Low Temperature Treatment of Absorbers. *ACS Appl. Mater. Interfaces* **2016**, *8* (7), 5017–5024.

(119) Hironiwa, D.; Sakai, N.; Kato, T.; Sugimoto, H.; Tang, Z.; Chantana, J. Impact of Annealing Treatment before Buffer Layer Deposition on Cu2ZnSn(S,Se)4 Solar Cells. *Thin Solid Films* **2015**, *582*, 151–153.

(120) Repins, I.; Beall, C.; Vora, N.; Dehart, C.; Kuciauskas, D.; Dippo, P.; To, B.; Mann, J.; Hsu, W. C.; Goodrich, A.; Noufi, R. Co-Evaporated Cu2ZnSnSe4 Films and Devices. *Sol. Energy Mater. Sol. Cells* **2012**, *101*, 154–159.

(121) Sardashti, K.; Haight, R.; Gokmen, T.; Wang, W.; Chang, L. Y.; Mitzi, D. B.; Kummel, A. C. Impact of Nanoscale Elemental Distribution in High-Performance Kesterite

Solar Cells. *Adv. Energy Mater.* **2015**, *5* (10).

(122) Rau, U.; Braunger, D.; Herberholz, R.; Schock, H. W.; Guillemoles, J.-F.; Kronik, L.; Cahen, D. Oxygenation and Air-Annealing Effects on the Electronic Properties of Cu(In,Ga)Se2 Films and Devices. *J. Appl. Phys.* **1999**, *86* (1), 497–505.

(123) Hauschild, D.; Meyer, F.; Benkert, A.; Kreikemeyer-Lorenzo, D.; Pohlner, S.; Palm, J.; Blum, M.; Yang, W.; Wilks, R. G.; Bär, M.; Heske, C.; Weinhardt, L.; Reinert, F. Annealing-Induced Effects on the Chemical Structure of the In2S3/CuIn(S,Se)2 Thin-Film Solar Cell Interface. *J. Phys. Chem. C* **2015**, *119* (19), 10412–10416.

(124) Repins, I.; Contreras, M. A.; Egaas, B.; Dehart, C.; Scharf, J.; Perkins, C. L.; To, B.; Noufi, R. 19.9% Efficient ZnO/Cds/CuInGaSe2 Solar Cell with 81.2% Fill Factor. *Prog. Photovolt Res. Appl.* **2008**, *15* (February 2013), 659–676.

(125) Rey, G.; Redinger, A.; Sendler, J.; Weiss, T. P.; Thevenin, M.; Guennou, M.; El Adib, B.; Siebentritt, S. The Band Gap of Cu2ZnSnSe4: Effect of Order-Disorder. *Appl. Phys. Lett.* **2014**, *105* (11).

(126) Scragg, J. J. S.; Choubrac, L.; Lafond, A.; Ericson, T.; Platzer-Björkman, C. A Low-Temperature Order-Disorder Transition in Cu2ZnSnS4 Thin Films. *Appl. Phys. Lett.* **2014**, *104* (4), 41911.

(127) Neuschitzer, M.; Sanchez, Y.; Olar, T.; Thersleff, T.; Lopez-Marino, S.; Oliva, F.; Espindola-Rodriguez, M.; Xie, H.; Placidi, M.; Izquierdo-Roca, V.; Lauermann, I.; Leifer, K.; Pérez-Rodriguez, A.; Saucedo, E. Complex Surface Chemistry of Kesterites: Cu/Zn Reordering after Low Temperature Postdeposition Annealing and Its Role in High Performance Devices. *Chem. Mater.* **2015**, *27* (15), 5279–5287.

Appendix

Graphical Table of Contents & Covers

"Optical and electrical properties of In-doped $Cu_2ZnSnSe_4$"

S. Giraldo, C. M. Ruiz, M. Espíndola-Rodríguez, Y. Sánchez, M. Placidi, D. Cozza, D. Barakel, L. Escoubas, A. Pérez-Rodríguez, and E. Saucedo

Sol. Energy Mater. Sol. Cells, vol. 151, pp. 44–51, 2016

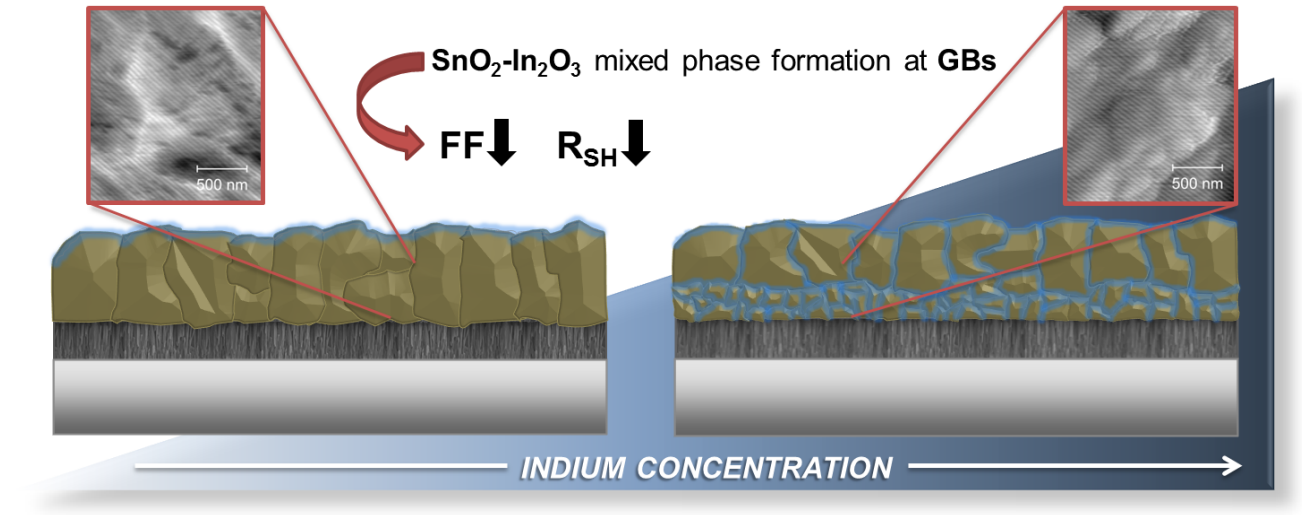

"Large Efficiency Improvement in $Cu_2ZnSnSe_4$ Solar Cells by Introducing a Superficial Ge Nanolayer"

S. Giraldo, M. Neuschitzer, T. Thersleff, S. López-Marino, Y. Sánchez, H. Xie, M. Colina, M. Placidi, P. Pistor, V. Izquierdo-Roca, K. Leifer, A. Pérez-Rodríguez, and E. Saucedo

Adv. Energy Mater., vol. 5, no. 21, p. 1501070, 2015

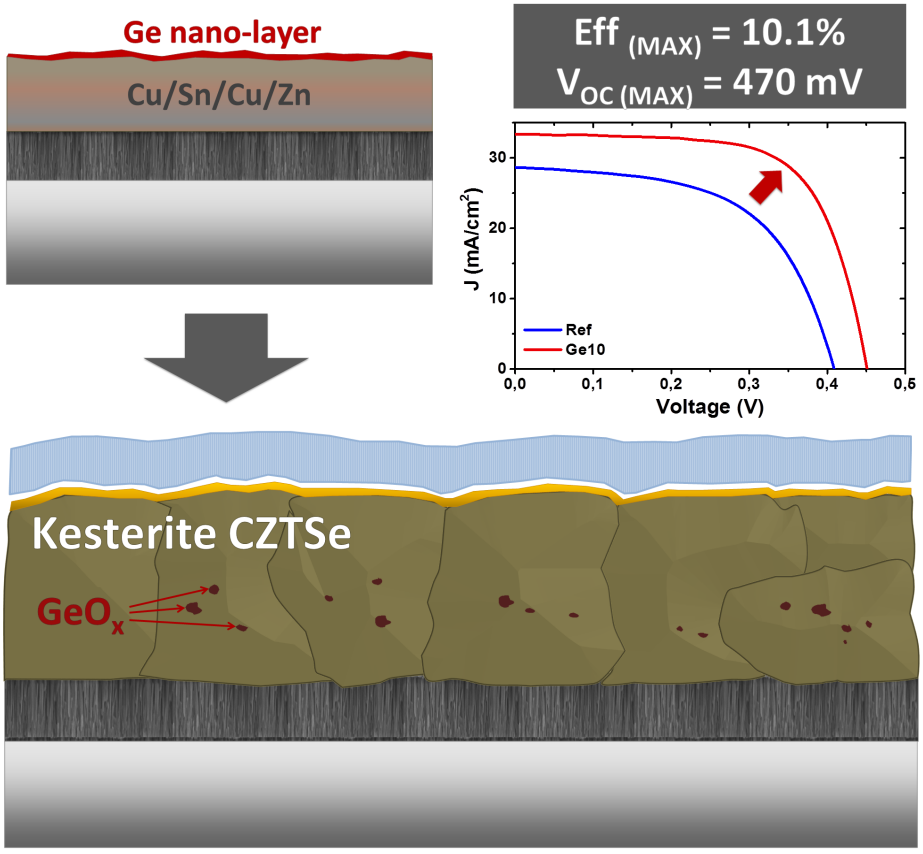

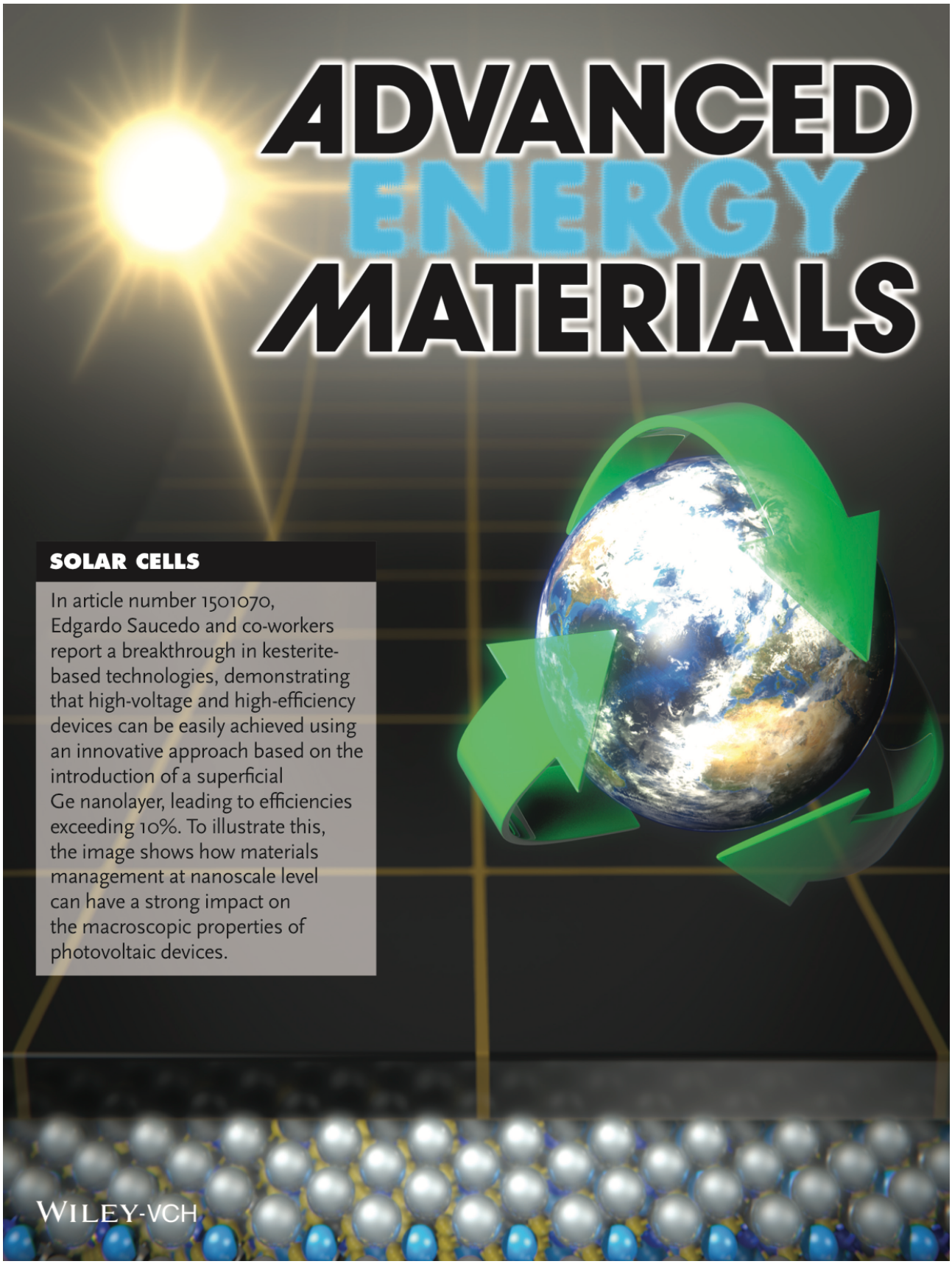
ADVANCED
ENERGY
MATERIALS
SOLAR CELLS
In article number 1501070, Edgardo Saucedo and co-workers report a breakthrough in kesterite-based technologies, demonstrating that high-voltage and high-efficiency devices can be easily achieved using an innovative approach based on the introduction of a superficial Ge nanolayer, leading to efficiencies exceeding 10%. To illustrate this, the image shows how materials management at nanoscale level can have a strong impact on the macroscopic properties of photovoltaic devices.
WILEY-VCH

"$Cu_2ZnSnSe_4$ solar cells with 10.6% efficiency through innovative absorber engineering with Ge superficial nanolayer"

S. Giraldo, T. Thersleff, G. Larramona, M. Neuschitzer, P. Pistor, K. Leifer, A. Pérez-Rodríguez, C. Moisan, G. Dennler, and E. Saucedo

Prog. Photovoltaics Res. Appl., vol. 24, no. 10, pp. 1359-1367, 2016

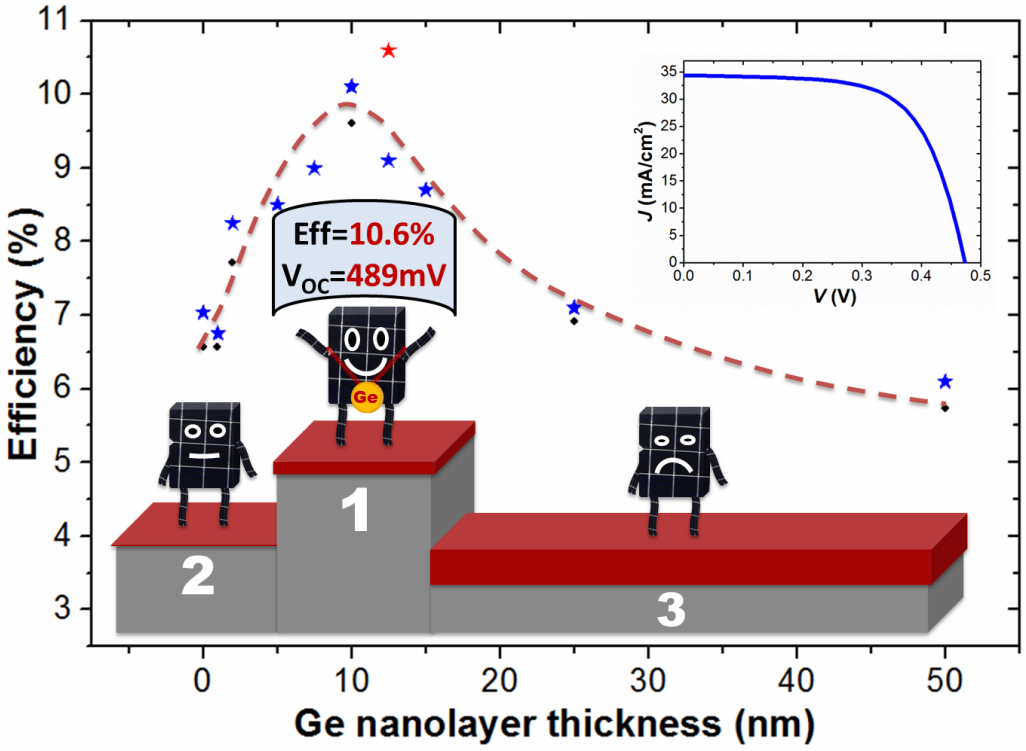

"Chemically and morphologically distinct grain boundaries in Ge-doped $Cu_2ZnSnSe_4$ solar cells revealed with STEM-EELS"

T. Thersleff, S. Giraldo, M. Neuschitzer, P. Pistor, E. Saucedo, and K. Leifer

Mater. Des., vol. 122, pp. 102-109, 2017

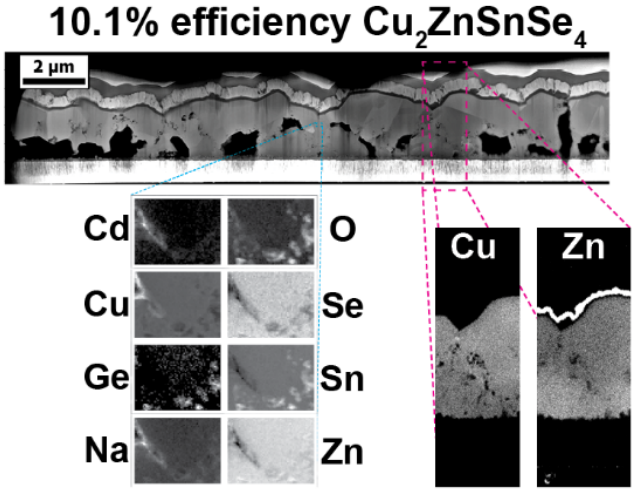

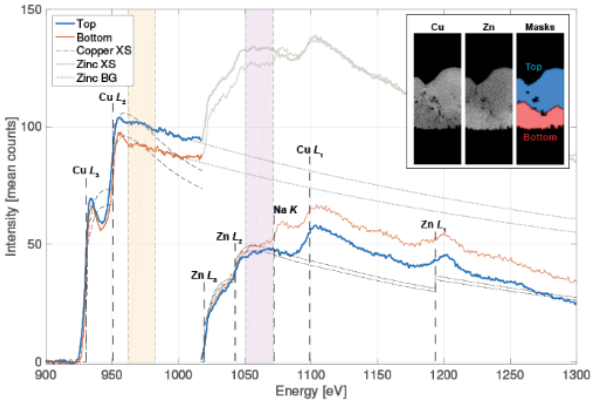

"How small amounts of Ge modify the formation pathways and crystallization of kesterites"

S. Giraldo, E. Saucedo, M. Neuschitzer, F. Oliva, M. Placidi, X. Alcobé, V. Izquierdo-Roca, S. Kim, H. Tampo, H. Shibata, A. Perez-Rodriguez, and P. Pistor

Energy Environ. Sci., 2017. DOI:10.1039/C7EE02318A

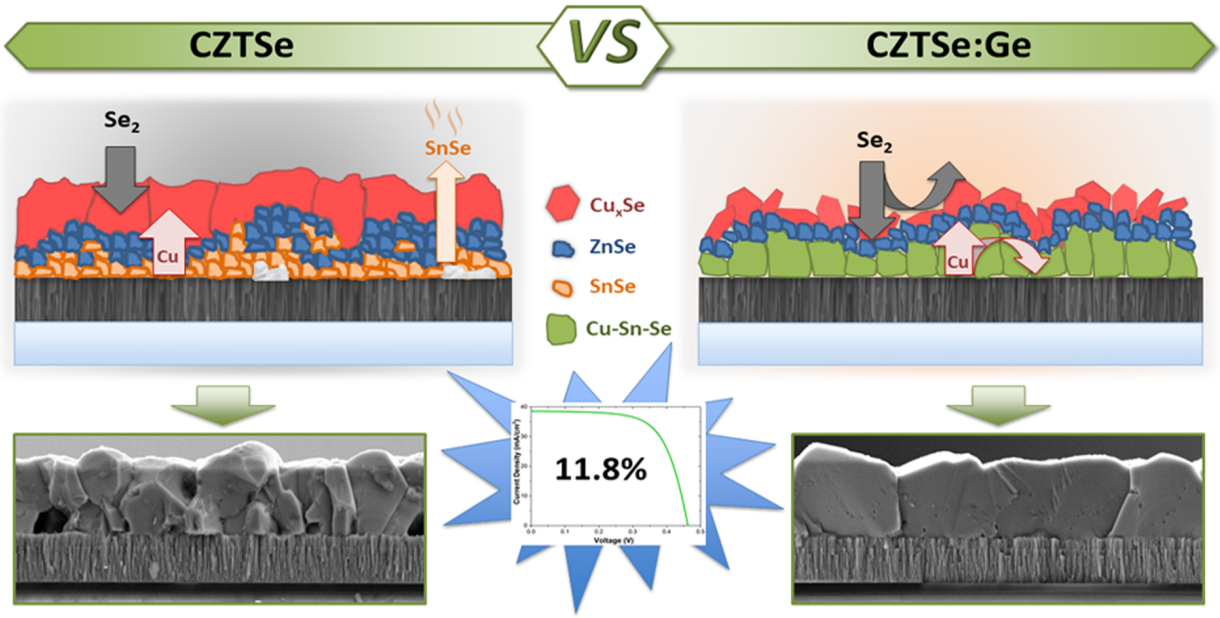

"Raman scattering analysis of the surface chemistry of kesterites: Impact of post-deposition annealing and Cu/Zn reordering on solar cell performance"

M. Dimitrievska, S. Giraldo, P. Pistor, E. Saucedo, A. Pérez-Rodríguez, and V. Izquierdo-Roca

Sol. Energy Mater. Sol. Cells, vol. 157, pp. 462–467, 2016